Experiments on Stratified Multiphase Plumes

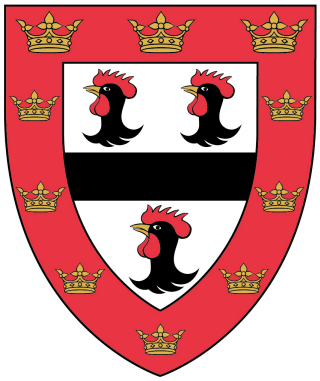

Jonathan Barnard

Department of Chemical Engineering and Biotechnology
University of Cambridge

This thesis is submitted for the degree of
Doctor of Philosophy

Jesus College June 2021

Declaration

This thesis is the result of my own work and includes nothing which is the outcome of work done in collaboration except as declared in the Introduction and specified in the text. I further state that no substantial part of my thesis has already been submitted, or, is being concurrently submitted for any such degree, diploma or other qualification at the University of Cambridge or any other University or similar institution except as declared in the Introduction and specified in the text. It does not exceed the prescribed word limit for the relevant Degree Committee.

Jonathan Barnard
June 2021

Experiments on Stratified Multiphase Plumes

Jonathan Barnard

Buoyant plumes are flows of great interest to engineers and geologists alike with applications varying from chemical engineering processes to explosive volcanic eruption columns. Single-phase plumes have been well studied and the flow's behaviour is generally well understood, however many examples in both industry and the natural world consist of a secondary dispersed phase of either bubbles or dense particles. The presence of multiple phases in a plume significantly complicates the flow dynamics, especially when rising through density stratified environments such as the ocean or the atmosphere. In this thesis, four experimental studies are presented investigating the dynamic behaviour of both particle-laden plumes and bubble plumes in stratified ambients. Experiments on stratified particle-laden plumes have enabled five steady-state flow regimes to be identified and subsequently characterised using a criterion for the onset of ambient convection and the ratio of particle to fluid buoyancy flux at the source. Measurements of plume height are compared to theoretical models within the literature and are shown to be successful for pure plumes rising through quiescent environments, however not for those rising through particle-induced convection. Through discrete measurements taken within the convection column surrounding the plume, predictions for the local values of density and particle concentration are produced allowing the plume heights to be predicted through only a minor adjustment to simple plume theory. Other models to predict the radial extent of ambient convection, secondary intrusion height and various particle concentrations are also presented. Weak bubble plumes were experimentally studied to understand both the dynamics of the spreading intrusions and the mass transfer of dissolved species to the environment. Bubble plumes with large non-dimensional slip velocities create multiple spreading events and upon comparison with well known scaling, were determined to spread three times slower than an isolated intrusion at large radial distances when viscosity is important. Measurements along the spreading intrusions showed the presence of a mixing region where concentration of dissolved species decays and a non-mixing region where concentration remains constant. A diffusion model is developed and successfully compared to both local measurements and experimental images.

I would like to dedicate this thesis to my family

Acknowledgements

Firstly, I would like to thank my supervisor, Professor Silvana Cardoso, for her unwavering support and guidance throughout my PhD.

Secondly, I would like to acknowledge my collaborators, most notably, Ms. Arna Sigurðardóttir. Our work together during the second year of my PhD lead to the publication of Chapter 5 in *Philosophical Transactions of the Royal Society A*, and preliminary results noted in her MPhil thesis provided the motivation for the work presented in Chapter 6. I would also like to thank IIB students Ms. Danielle Bullamore, Mr. Matthew Harris, Ms. Amy McCormick and Mr. Matthew Spry for their contributions to the experiments presented in Chapters 5 and 6.

Thanks to Dr. Nicola Mingotti for showing me the ropes in my first couple of terms transitioning from industry back into the lab, and also to Dr. Rajesh Bhagat, for our stimulating discussions later into my PhD. Thanks also goes to the other members of the Fluids and Environment group, Dr. Yang Ding and Mr. Luis Rocha, for their support and encouragement.

Also to the workshop in the Department of Chemical Engineering, specifically Mr. Lee Pratt and Mr. Andy Hubbard, thank you for building my various tanks and for fixing my pumps whenever something unexpected occurred.

Thank you to my funders, the Woolf Fisher Trust, for giving me the opportunity to conduct this research. I would specifically like to thank Dr. Nigel Evans for his support throughout this process.

Finally, I would like to thank my friends and family. My time in Cambridge certainly wouldn't have been as special without the people I met along the way. There are too many to name individually, but I would like to thank those who have been there since the beginning. Thanks to Dr. Victoria Tse for always being up for a chat and a coffee at Bould Brothers, and thank you to Liam and Stephanie Jolliffe for making home seem not so far away. To my family back in New Zealand, my quest to understand particles and bubbles is now coming to an end and I couldn't have done it without you. Last, but not least, I would like to thank my fiancée, Abbey Mayhead, for endlessly supporting me through both the highs and lows of my PhD journey.

Table of contents

List of figures

List of tables

Nomenclature

Roman Symbols

A	Absorbance
B	Plume buoyancy flux
$\hat{B}$	Dimensionless buoyancy flux
B_0	Source buoyancy flux
$B_{0,f}$	Source fluid buoyancy flux
$B_{0,p}$	Source particle buoyancy flux
$B_{0,ss}$	Source buoyancy flux at steady state
B_i	Intrusion buoyancy flux
b	Plume radius
b_0	Source radius
b_G	Gaussian plume radius
b_i	Inner plume radius
b_o	Outer plume radius
b_s	Plume radius at the spreading height
$b(z)$	Local plume radius
$c_{1/2/3}$	Constants
c_∞	Intrusion concentration beyond the mixing radius

c_I Inertia-buoyancy spreading constant

c_V Viscous-buoyancy spreading constant

c_a Concentration of attenuating species

c_e Ambient dissolved species concentration

c_{e0} Ambient concentration at the plume radius

c_i Intrusion dissolved species concentration

c_{i0} Intrusion concentration at the plume radius

c_{im} Average intrusion concentration within mixing radius

c_{max} Maximum intrusion concentration

c_n Concentration in the inner plume at the peel height

c_{n-1} Concentration in the inner plume at the trap height

D Diffusion coefficient

d_b Bubble diameter

d_n Nozzle diameter

d_p Particle diameter

f Peeling efficiency

F_B Intrusion buoyancy force

F_I Intrusion inertia force

F_V Intrusion viscous force

F_b Buoyancy force

G Spreading regime transition parameter

g Acceleration due to gravity

g' Reduced gravity

g'_0 Source reduced gravity

g'_G Gaussian reduced gravity

g'_s Suspension reduced gravity

$g'(z)$ Local reduced gravity

H Reservoir height

L Characteristic length scale

L_c Convection length scale

L_i Intrusion thickness

L_m Jet length scale

L_p Plume length scale

L_t Plume trough depth

l Optical length

l_p α-scaled plume length scale

M Plume momentum flux

$\hat{M}$ Dimensionless momentum flux

M_0 Source momentum flux

M_H Buoyancy to bubble velocity ratio

N Brunt-Väisälä frequency or ambient buoyancy frequency

N_s Suspension buoyancy frequency

n Number of submerged intrusions

P Buoyancy flux ratio

P_c Critical buoyancy flux ratio

P_N Plume number

p Pressure

p_0 Reference pressure

p_e	Ambient pressure
Q	Plume volume flux
$\hat{Q}$	Dimensionless volume flux
Q_0	Source volume flux
Q_b	Bubble volume flux
Q_e	Outer plume entrainment flux
Q_f	Peeling volume flux
Q_i	Intrusion volume flux
Q_n	Inner plume volume flux at the peel height
Q_{n-1}	Inner plume volume flux at the trap height
Q_r	Inner plume entrainment flux
Q_s	Plume volume flux at the spreading height
Q_t	Plume volume flux at theoretical neutral buoyancy height
R_c	Convection column radius
R_i	Intrusion radius
R_m	Critical mixing radius
R_r	Reference intrusion radius
r	Radius
r_c	Critical re-entrainment radius
T	Surface tension
t	Time
t_r	Reference time
U_c	Ambient convective velocity
U_N	Non-dimensional slip velocity

u	Radial velocity
u_b	Bubble slip velocity
u_e	Entrainment velocity
u_i	Intrusion velocity
u_{st}	Stokes settling velocity
V	Volume
V_f	Fluid volume
V_p	Particle volume
V_t	Total volume
x	Horizontal Cartesian coordinates
y	Vertical Cartesian coordinates
y_b	Intrusion half-width
y_{bm}	Intrusion mixing half-width
z	Height
$\hat{z}$	Dimensionless height
z_0	Initial plume height
z_∞	Steady-state plume height
$z_{B=0}$	Plume neutral buoyancy height
z_P	Plume peel height
z_T	Plume trap height
z_{avs}	Asymptotic virtual source
z_b	Tank base height
z_f	Fluid height
z_m	Maximum plume height above the virtual source

z_{max} Maximum plume height above the real source

z_s Plume spreading height

z_{si} Secondary intrusion height

z_v Virtual source

Greek Symbols

α Entrainment coefficient

α_i Inner plume entrainment coefficient

α_j Jet entrainment coefficient

α_o Outer plume entrainment coefficient

α_p Plume entrainment coefficient

$\Delta\rho$ Change in density

Δz Change in height

δ Dimensionless diffusion coefficient

ϵ Plume top entrainment coefficient

Γ_0 Scaled source Richardson number

γ Momentum scaling parameter

κ Molar absorptivity

μ Dynamic viscosity

ν Kinematic viscosity

ω Vertical velocity

ω_0 Source velocity

ω_G Gaussian plume velocity

$\omega(z)$ Local plume velocity

ϕ Particle volume fraction

ϕ_0 Source particle volume fraction

ϕ_e Ambient particle volume fraction

ϕ_s Particle volume fraction at spreading level

ρ Density

ρ_0 Reference density

$\rho_{0,ss}$ Reference density at steady state

ρ_b Bubble density

ρ_e Ambient density

ρ_f Fluid density

ρ_{fluid} Introduced fluid density into control volume

ρ_i Intrusion density

ρ_{new} New density of control volume

$\rho_{original}$ Original density of control volume

ρ_p Particle density

ρ_{plume} Plume density

ρ_s Suspension density

σ Buoyancy frequency parameter

σ_c Critical buoyancy frequency parameter

σ_{ss} Buoyancy frequency parameter at steady state

θ Angular coordinates

Dimensionless Numbers

Fr Froude number

Gr Grashof number

Re Reynolds number

Ri Richardson number

We Weber number

Chapter 1

Introduction

Fluid flows driven by density differences, or buoyancy, appear everywhere in our daily lives. One example which we can all relate to is making your morning cup of coffee or tea. For many throughout the world, the first thing that they will do after getting out of bed in the morning is turn on their kettle. As the element heats the water, the local density of the liquid drops, inducing an upflow of warm water through a cooler, denser ambient. This process continues until the water boils, thus creating a vapour plume which rises from the kettle's spout. After pouring your drink, if so inclined, you add milk and create a convective instability due to adding a dense fluid atop a light one. You finally sit down and look out the window, and depending on the season, will likely either be greeted with wispy smoke plumes rising from chimneys or a convection-induced heat haze rising above warm sun-drenched roads.

When a continuous source of buoyancy exists at a point source, the turbulent flow created above it is called a plume. Named for the flow's similarity in appearance to that of a feather (of which early comparisons can be found in Tillard, 1832; and Caldcleugh, 1837), plumes are widely present across both industry and nature over an array of magnitudes ranging from millimetres in your coffee mug to kilometres in the world's ocean and atmosphere.

Plumes belong to a family of cone-shaped flows whose members also include jets, which develop above continuous point sources of momentum; forced plumes or buoyant jets, intermediate flows with both buoyancy and momentum at the source; and negatively buoyant jets known as fountains. The earliest mathematical attention specifically regarding the dynamics of buoyant plumes was by Yakov B. Zeldovich prior to the second world war (see Zeldovich, 1937), however qualitative descriptions of plumes date back to Ancient Roman times and the eruption of Mt. Vesuvius in 79 AD. In a letter to the historian Tacitus, who was interested in the circumstances leading to

(a) (b)

Fig. 1.1 (a) A smoke plume, taken from Hunt and Van den Bremer (2011). (b) A water jet, taken from Van Dyke (1982).

the death of author and philosopher Pliny the Elder, his nephew, Pliny the Younger described the events of the eruption which resulted not only in his uncle's death, but infamously destroyed the cities of Pompeii and Herculaneum. The translation of Pliny the Younger's description of the volcanic plume reads:

"*On the 24th of August, about one in the afternoon, my mother desired him* (Pliny the Elder) *to observe a cloud which appeared of a very unusual size and shape. He had just taken a turn in the sun and, after bathing himself in cold water and making a light luncheon, gone back to his books. He immediately arose and went out upon a rising ground from whence he might get a better sight of this very uncommon appearance. A cloud, from which mountain was uncertain, at this distance (but it was found afterwards to come from Mount Vesuvius), was ascending, the appearance of which I cannot give you a more exact description of than by likening it to that of a pine tree, for it shot up to a great height in the form of a very tall trunk, which spread itself out at the top into a sort of branches; occasioned, I imagine, either by a sudden gust of air that impelled it, the force of which decreased as it advanced upwards, or the cloud itself being pressed back again by its own weight, expanded in the manner I have mentioned. It appeared sometimes bright and sometimes dark and spotted, according as it was either more or less impregnated with earth and cinders.*"

This description of the volcanic plume rising from Mt. Vesuvius is not only among the first known descriptions of plumes, but also perhaps the first description of a multiphase plume, given that the flow was laden with both 'earth and cinders'. The behaviour of single-phase plumes has been investigated by many authors for nearly 85 years and is generally quite well understood. The addition of a second phase makes the plume dynamics significantly more complex and understanding the influence of the dispersed phase is vital to effectively model the many examples of multiphase plumes present in various industrial and natural processes.

For plumes laden with dense particles, including those associated with wastewater outfalls (Tate et al., 2019), industrial chimney stacks (Feng et al., 2020), hydrothermal vents on the seafloor (Fitzsimmons et al., 2017) and obviously explosive volcanic eruptions, interest lies with how particles are transported throughout the environment. To date, most attention has been given to the latter application due to the potential impact on human life, infrastructure, climate and the aviation industry (Budd et al., 2011; Durant et al., 2010).

In liquid environments, continuous localised releases of gas create multiphase plumes of bubbles and liquid, the behaviour of which is sometimes also of global interest. For example, in 2010, the blowout on BP's Deepwater Horizon rig in the Gulf of Mexico, and the subsequent oil plume driven by methane gas bubbles, drew worldwide attention due to its impact on the environment, local wildlife and public health (Beyer et al., 2016). Also within the last 15 years, large natural plumes of methane have been discovered rising from continental shelves around the world with some suggesting their development is associated with the melting of gas hydrate deposits due to anthropogenic climate change (Westbrook et al., 2009). Authors studying these plumes firsthand on the Eastern Siberian Artic Shelf have also postulated a 50 Gt release to the atmosphere over the next 50 years (Shakhova et al., 2010b), an event which would be catastrophic with the potential to lead to runaway climate change and an estimated $60 trillion worth of damage (Whiteman et al., 2013).

In this thesis, two key questions on multiphase plumes are addressed. Firstly, how do particle-laden plumes behave in a stratified environment; and secondly, how do bubble plumes, with multiple spreading events, transport dissolved species through the environment. To answer these questions, four experimental studies were conducted, with two focused on each question. Specifically, this thesis is structured as a series of four standalone papers, supported by a review of current literature, a summary of issues for further research and three appendices (see Appendix A, B and C) to provide more insight into experimental methods and analysis. A detailed review of the

(a)

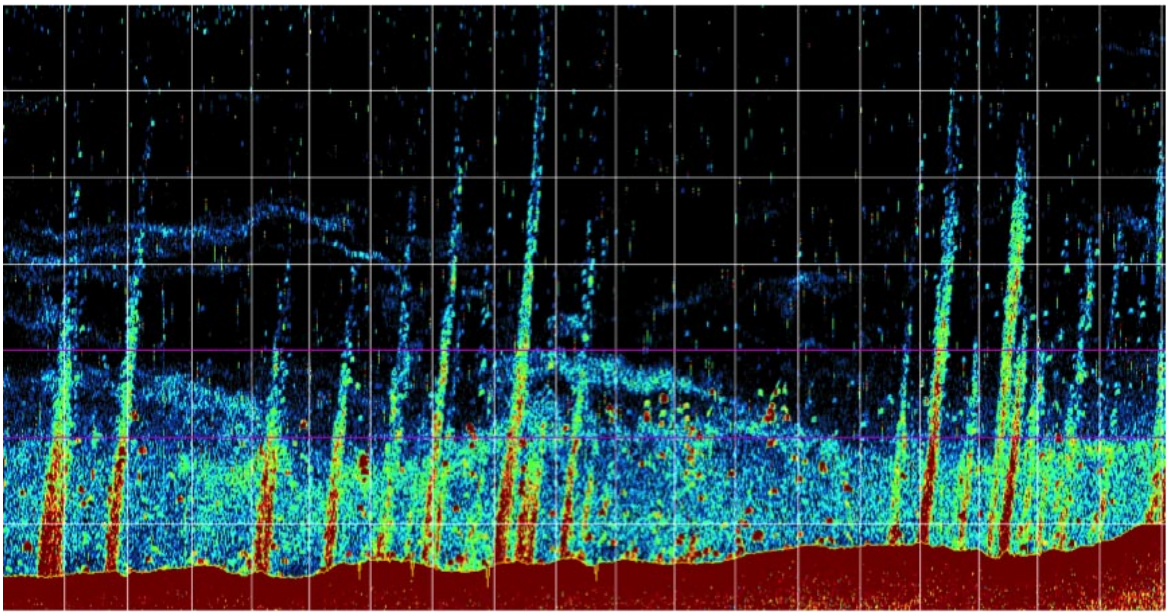

(b)

Fig. 1.2 (a) 2015 eruption of Calbuco, southern Chile (image from Marcelo Utreras) (b) Methane plumes rising from the seabed off West Spitsbergen (image from Natural Environment Research Council).

literature is provided in Chapter 2, introducing both single-phase plumes and simple plume theory. This is then followed by a review of previous research concerning the dynamics of multiphase plumes and submerged axisymmetric gravity currents. Chapter 3 is a paper published in the *Journal of Fluid Mechanics* detailing the steady-state behaviour of stratified particle-laden plumes. Five flow regimes, characterised by a criterion for the onset of ambient convection, are identified and physical parameters, including the plume rise heights, are reported. The work presented in Chapter 4 builds upon the previous chapter by focusing specifically on stratified particle-laden plumes rising through an ambient undergoing convection. Models to predict the radial extent of convection in the environment, the plume rise heights and other parameters of interest are developed and compared to experimental measurements. Chapter 5 presents a paper on the radial spread of submerged intrusions produced by bubble plumes written by myself, Ms. Arna Sigurðardóttir, Prof. Silvana Cardoso and other members of the Fluids and Environment group. This chapter is published in the Stokes 200 special edition of *Philosophical Transactions of the Royal Society A*. Also submitted to the *Journal of Fluid Mechanics*, Chapter 6 provides further insight into the radial mass transfer from bubble plumes to the environment and a simple diffusion model is presented. Finally, in Chapter 7, concluding remarks are presented, along with a discussion on issues for future work.

Chapter 2

Literature Review and Background

2.1 Buoyancy

A plume, by definition, is a turbulent convective flow driven by a localised source of buoyancy. Throughout the natural world, buoyancy is the driver of many flows and has continued to be a phenomenon of interest to many since, according to Vitruvius, Archimedes stepped into his bath over two millennia ago and watched the water rise (Morgan et al., 1914). Archimedes' principle is expressed explicitly as any body, totally or partially immersed in a fluid, is buoyed up by a force equal to the weight of the fluid displaced by the object. Mathematically, this upwards force exerted on the body by the fluid can be written as

$$F_b = \rho g V, \tag{2.1}$$

where F_b is the buoyancy force, ρ and V are the density and volume of the displaced fluid, and g is acceleration due to gravity.

Delving further into the idea of buoyancy force, consider a fluid parcel of density ρ within a quiescent ambient of some different density ρ_e. The difference in density between the fluid parcel and the environment will induce a resultant buoyancy force per parcel volume of

$$\frac{F_b}{V} = g(\rho_e - \rho), \tag{2.2}$$

which, if large enough to overcome the forces associated with the viscosity of the ambient, will cause the fluid parcel to accelerate vertically from rest, either rising or sinking depending on the relative magnitudes of ρ_e and ρ. The origin of this motion is

the direct result of an imbalance in pressure gradients, namely the hydrostatic pressure gradient in the environment $dp_e/dz = -g\rho_e$ and the local pressure gradient associated with the fluid parcel $dp/dz = -g\rho$. In work concerning flows arising due to natural convection, the convention is to present a scaled version of the buoyancy force in terms of some reference density, ρ_0. By doing so, the ambient may effectively be treated as weightless and the buoyancy-driven flow may be characterised as if it were being acted on by a reduced gravitational acceleration (Turner, 1979). This reduced gravity is defined as

$$g' = g\frac{\rho_e - \rho}{\rho_0}. \tag{2.3}$$

Here, it is important to note that, in the case of the work presented in this thesis, the reference density is taken as equivalent to the ambient density at the height of the plume source.

2.2 Boussinesq approximation

In many flows driven by natural convection, or simply the difference in density between the flow and the environment, density differences are generally small when compared to some reference density of interest. If one were to conduct an analysis on the conservation equations, taking into account these differences in density, the mathematics becomes very complicated such that some form of approximation becomes necessary to model the flow's behaviour (Tritton, 1977). As changes in density are small, an approximation that becomes worthwhile is to ignore any changes in fluid properties, other than changes in density giving rise to buoyancy forces.

This modification to the conservation equations, now well known as the Boussinesq approximation (Boussinesq, 1903), can be introduced simply by assessing the incompressible Euler equations of motion, written below using the pressure and density deviations from hydrostatic equilibrium (Turner, 1979),

$$\rho\frac{D\mathbf{u}}{dt} = -\nabla p' + \Delta\rho g, \tag{2.4}$$

with D/dt denoting differentiation following the flow's motion and $\mathbf{u} = (u, 0, \omega)$ as the velocity field comprised of vertical and radial components, ω and u. The terms on the right-hand side of (2.4), $p' = p_0 - p$ and $\Delta\rho = \rho_0 - \rho$, represent the deviations of

pressure and density from the state where $\nabla p_0 = \rho_0 g$. Using these definitions and then subsequently dividing by the reference density ρ_0, equation (2.4) may be rewritten as

$$\left(1+\frac{\Delta\rho}{\rho_0}\right)\frac{D\mathbf{u}}{dt} = -\frac{1}{\rho_0}\nabla p' + \frac{\Delta\rho}{\rho_0}g. \tag{2.5}$$

Here, it can be seen that $\Delta\rho/\rho_0$ appears on both the left and right-hand sides of the equation. However, in the case that $\Delta\rho \ll \rho_0$, the density ratio associated with the inertial term may be neglected and density differences are then only important in the buoyancy term, presented in equation (2.5) as the reduced gravity, $g' = g\,(\Delta\rho/\rho_0)$. Recent experiments have shown that the Boussinesq approximation remains reasonably accurate for scaled density differences of up to 15% (Ai et al., 2006; Mehaddi et al., 2015) and importantly, the plumes studied within this thesis fall well within this threshold. Note that near the source, density differences in bubble plumes exceed this threshold, however, due to entrainment of ambient fluid, the void fraction of weak bubble plumes soon becomes very low such that the Boussinesq approximation becomes applicable (Fabregat Tomàs et al., 2016; Socolofsky, 2001).

Although not strictly relevant to the work presented in the subsequent chapters, research has been conducted on non-Boussinesq plumes with notable contributions including that of Ricou and Spalding (1961) and Rooney and Linden (1996).

2.3 Turbulent entrainment

A defining characteristic of free turbulent flows is the mixing of external fluid into the flow through a process known as entrainment (Turner, 1979). Upon being released into an environment of greater density, the plume will begin to rise as an initially laminar flow however small perturbations quickly grow at the edge of the plume, causing it to become unstable and turbulent a short distance above the source. This transition is related to the plume's Reynolds number, defined as

$$Re = \frac{\omega L}{\nu}, \tag{2.6}$$

where ω and L represent a characteristic velocity and length, with ν as the kinematic viscosity of the surrounding fluid. Once Re exceeds a few thousand, the plume develops large eddies at its margins, creating a sharp boundary between the plume and the ambient, sometimes named the turbulent/non-turbulent interface (see Burridge et al., 2017). Across this interface, mixing occurs through multiple processes including the

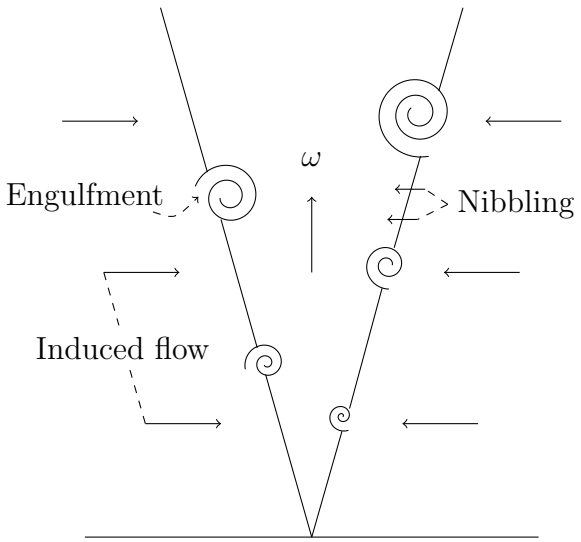

Fig. 2.1 Schematic of plume entrainment processes.

engulfment of ambient fluid into the plume by large eddies, induced inflow across the central core and smaller-scale processes, commonly referred to as 'nibbling' (Philip and Marusic, 2012; Turner, 1986).

The modelling of plume entrainment has historically taken one of two approaches, microscopic or macroscopic (Hunt and Van den Bremer, 2011). In the microscopic case, numerical modelling of plumes has been of interest in an attempt to further understand turbulence and turbulent entrainment (van Reeuwijk et al., 2016), along with gaining better insight into the relative contributions of the various entrainment processes (see Da Silva et al., 2014 and references therein). On the other hand, macroscopic modelling assumes that the timescale of the bulk flow is large compared to the eddy turnover time (Scase et al., 2006; Woods, 2010), such that the plume's dynamics may be represented using a simplistic integral approach, meanwhile also sufficiently capturing the complexities associated with turbulent entrainment.

Due to an interest in bulk flow behaviour rather than flow properties on a molecular level, the modelling presented from this point forwards takes the latter macroscopic approach towards understanding plume dynamics and the influence of turbulent entrainment.

2.4 Conservation equations

For a steady asymmetric flow of inviscid incompressible fluid, with a velocity field $\mathbf{u} = (u, 0, \omega)$, operating under the Boussinesq approximation and the assumption that mass diffusion is negligible, the equations of motion written in cylindrical co-ordinates (r, θ, z) are

$$\frac{1}{r}\frac{d}{dr}(ru) + \frac{d\omega}{dz} = 0, \tag{2.7a}$$

$$u\frac{d\omega}{dr} + \omega\frac{d\omega}{dz} = -\frac{1}{\rho_0}\frac{dp}{dz} - g\frac{\rho}{\rho_0}, \tag{2.7b}$$

$$u\frac{du}{dr} + \omega\frac{du}{dz} = -\frac{1}{\rho_0}\frac{dp}{dr}. \tag{2.7c}$$

When considering a plume or jet-like flow, the motion is confined to a defined radius b such that as $r \to b$, the vertical velocity $\omega \to 0$.

The dynamics of a turbulent plume depends on the magnitude and evolution of the fluxes of mass, momentum and buoyancy force, each of which can be presented in integral form as,

$$Q = 2\pi \int_0^\infty \omega r \, dr, \tag{2.8a}$$

$$M = 2\pi \int_0^\infty \omega^2 r \, dr, \tag{2.8b}$$

$$B = 2\pi \int_0^\infty \omega g' r \, dr. \tag{2.8c}$$

Due to the Boussinesq nature of these flows, changes in density are only important in regard to buoyancy and, as such, conservation of mass may be presented as conservation of volume.

These fluxes, along with the equations of motion presented above, may be utilised to determine the plume conservation equations with respect to height. Integrating (2.7a) between the radial limits of 0 and ∞ gives

$$\frac{d}{dz}\int_0^\infty \omega r \, dr \; = -(ru)|_0^\infty, \tag{2.9}$$

which, when considering the definition of volume flux and the fact that radial inflow from infinity is driven by turbulent entrainment into the plume, can also be written as

$$\frac{1}{2\pi}\frac{dQ}{dz} = -bu_e, \tag{2.10}$$

where u_e is the entrainment velocity at the edge of the plume.

Now consider the flow's conservation of momentum, described in (2.7b) with respect to the z-direction. In the environment outside of the plume, the vertical velocity component $\omega = 0$ and $\rho = \rho_e(z)$. This gives the hydrostatic relation,

$$\frac{dp}{dz} = -g\rho_e. \tag{2.11}$$

(2.11) can then be substituted into (2.7b) such that change in momentum within the plume is written as

$$u\frac{d\omega}{dr} + \omega\frac{d\omega}{dz} = g'. \tag{2.12}$$

Here, it can be seen that all changes in momentum are directly associated with the magnitude of the flow's reduced gravity.

The rate of change of momentum with respect to height in integral form is written as

$$\frac{1}{2\pi}\frac{dM}{dz} = \int_0^\infty \frac{d}{dz}\omega^2 r\,dr \;= 2\int_0^\infty \omega\frac{d\omega}{dz} r\,dr. \tag{2.13}$$

Using the continuity equation (2.7a), the momentum equation (2.12) and the mathematical identity,

$$\frac{d}{dr}(ru\omega) = ru\frac{d\omega}{dr} + \omega\frac{d}{dr}(ru), \tag{2.14}$$

(2.13) can be rewritten as

$$\frac{1}{2\pi}\frac{dM}{dz} = \int_0^\infty g' r\,dr - (ru\omega)|_0^\infty. \tag{2.15}$$

As $\omega|_\infty = 0$ and $(ru)|_0 = 0$, the final form of the rate of change of momentum with height can be presented as

$$\frac{1}{2\pi}\frac{dM}{dz} = \int_0^\infty g' r\,dr = \frac{1}{2}b^2 g'. \tag{2.16}$$

Finally, the rate of change in buoyancy with height is written as

$$\frac{1}{2\pi}\frac{dB}{dz} = \int_0^\infty \frac{d}{dz}(\omega g')r\,dr. \tag{2.17}$$

Using continuity (2.7a) and the definition of g' (2.3),

$$\frac{1}{2\pi}\frac{dB}{dz} = \int_0^\infty \omega\frac{g}{\rho_0}\frac{d\rho_e}{dz}r\,dr - \int_0^\infty \omega\frac{g}{\rho_0}\frac{d\rho}{dz}r\,dr\ - \int_0^\infty g'\frac{d}{dr}(ru)\,dr. \tag{2.18}$$

Also following continuity, conservation of mass in the system can be presented as

$$u\frac{d\rho}{dr} + \omega\frac{d\rho}{dz} = 0, \tag{2.19}$$

and utilised in (2.18) to give,

$$\frac{1}{2\pi}\frac{dB}{dz} = \int_0^\infty \omega\frac{g}{\rho_0}\frac{d\rho_e}{dz}r\,dr + \int_0^\infty u\frac{g}{\rho_0}\frac{d\rho}{dr}r\,dr\ - \int_0^\infty g'\frac{d}{dr}(ru)\,dr. \tag{2.20}$$

Here, it is important to note that

$$\frac{g}{\rho_0}\frac{d\rho}{dr} = \frac{dg'}{dr}, \tag{2.21}$$

and upon substitution, (2.20) may be presented as

$$\frac{1}{2\pi}\frac{dB}{dz} = \frac{g}{\rho_0}\frac{d\rho_e}{dz}\int_0^\infty \omega r\,dr - (rug')|_0^\infty. \tag{2.22}$$

The second term on the right-hand side of (2.22) is equivalent to zero as $g'|_\infty = 0$, along with $(ru)|_0 = 0$, producing the conservation equation for buoyancy flux in its final form,

$$\frac{1}{2\pi}\frac{dB}{dz} = \frac{g}{\rho_0}\frac{d\rho_e}{dz}\int_0^\infty \omega r\,dr. \tag{2.23}$$

Together, equations (2.10), (2.16) and (2.23) describe the vertical motion of a buoyant plume. In this form however, the equations cannot be solved due to the uncertainty surrounding the turbulent entrainment occurring at the edge of the plume, specifically the magnitude of u_e and its dependence on z. The following section will provide insight into how this problem was addressed by the authors originally confronted with this issue.

2.5 Plume theory

The term 'Plume theory' is generally associated with the work of Morton, Taylor and Turner (1956), who are widely credited for their research concerning the dynamics of free turbulent flows rising from point sources of buoyancy. In the following sections, the assumptions of Morton et al. (1956) and other authors prior (all of which are inherently built into the conservation equations derived previously) are discussed and the early solutions explaining the motion of plumes, including the approach for turbulence closure, are presented for flows rising through both uniform and stratified ambients.

2.5.1 Self-similarity and the entrainment assumption

Plumes are conical in shape and, in general, considered to be self-similar (Turner, 1979). Even in the earliest work of Zeldovich (1937) and Schmidt (1941), both authors assumed that the flow above a point source of heat would be geometrically similar at all heights. By making such an assumption, simple scaling may be utilised to determine bulk properties of the flow, namely the vertical velocity ω and the reduced gravity g'. In the case of turbulent plumes where molecular diffusion, heat conduction and viscosity are all negligible, these solutions may be presented as functions of only the source buoyancy flux B_0, the plume radius r and plume height z. Following Batchelor (1954), dimensional analysis suggests the scaling,

$$\omega(z,r) \sim B_0^{1/3} z^{-1/3} \exp\left(\frac{-r^2}{b_G^2}\right), \tag{2.24}$$

$$g'(z,r) \sim B_0^{2/3} z^{-5/3} \exp\left(\frac{-r^2}{b_G^2}\right), \tag{2.25}$$

$$b_G \sim z, \tag{2.26}$$

where the subscript G represents the values associated with Gaussian plume profiles, a topic which will be further touched on in the upcoming section 2.5.2. By extension, when considering (2.24) and (2.26), the scaling for the self-similar values of the plume volume and momentum fluxes may be written as,

$$Q \sim B_0^{1/3} z^{5/3}, \tag{2.27}$$

$$M \sim B_0^{2/3} z^{4/3}. \tag{2.28}$$

As specifically detailed by Batchelor (1954), upon the comparison of (2.27) with (2.10), the volume conservation equation specifying the rate of entrainment at the edge of the plume, it becomes clear that

$$u_e \sim z^{-1/3}, \tag{2.29}$$

which when considering the scaling proposed in equation (2.24) suggests

$$u_e = \alpha\omega, \tag{2.30}$$

where α is the entrainment coefficient. The use of this coefficient provides closure to the turbulence problem presented in section 2.4, and was first suggested by Sir Geoffrey I. Taylor in his work in 1945 concerning the dynamics of the hot gases produced following a large explosion (Taylor, 1945), before being heavily popularised later by Morton et al. (1956).

In the years that have followed, the use of the entrainment assumption has proven to be incredibly accurate at predicting plume properties, including the terminal height of plumes rising through stratified environments (see section 2.5.3) over a wide range of scales (Kaye, 2008; Turner, 1986). This suggests that the assumption of self-similarity is a reasonable one, at least for plumes rising large distances from the source (Carazzo et al., 2006), however some uncertainty remains surrounding the appropriate values for α. Experiments have shown values of entrainment coefficient varying between $0.065 < \alpha_j < 0.080$ for momentum-driven flows and $0.10 < \alpha_p < 0.16$ for flows driven by buoyancy (Carazzo et al., 2006; Fischer et al., 1979; Linden, 2000). Although measurement uncertainty may play some part in this variance, it has been proposed that the observed differences may be the result of the flow's initial conditions, with both buoyancy (Kaminski et al., 2005) and kinetic energy (van Reeuwijk and Craske, 2015) influencing the rate of entrainment, the latter being a key characteristic of the plume model developed by Priestley and Ball (1955). George (1989) has also argued that the differences in α are the result of the assumed self-similarity and in fact, a multiplicity of self-preserving states exist, each of which is a unique function of the flow's initial conditions. Irrespective of the origin of these differences, there is a consensus that the entrainment coefficient in momentum-driven jets is less than the value associated with plumes.

2.5.2 Gaussian and top-hat profiles

As shown in equations (2.24) and (2.25), a plume's velocity and buoyancy are both functions of height and radius. If one were to take a time-average across a plume, the radial profiles of these properties may both be represented using Gaussian curves (Turner, 1979). This radial profile was first proposed as a numerical solution by Schmidt (1941) and then later proven experimentally by Rouse et al. (1952).

Since this early work, the relative widths of the Gaussian profiles associated with the vertical velocity and buoyancy have been of interest. Taken as the radial distance where the property amplitude has decreased to $1/e$ of the value at the central axis, Papanicolaou and List (1988) determined that the width of the buoyancy profile exceeded that of the velocity profile, yet a few years later Shabbir and George (1994) found the opposite. This ratio of profile widths has previously appeared within the Gaussian forms of the conservation equations, however, as this value is very close to unity, it is generally ignored for simplicity.

To further simplify the approach, many other authors including Morton et al. (1956) have assumed that the plume properties have a 'top-hat' profile, where a single, radially-averaged value exists inside the plume and another value, usually equivalent to zero, exists outside it. The differences between the two approaches are shown visually in Figure 2.2 and presented mathematically as

$$\text{Gaussian:} \quad \omega = \omega_G \exp\left(\frac{-r^2}{b_G^2}\right),\ 0 < r < \infty \tag{2.31}$$

$$\text{Top-hat:} \quad \begin{cases} \bar{\omega} = \bar{\omega}, & r < b \\ \bar{\omega} = 0, & r > b \end{cases} \tag{2.32}$$

where ω_G represents the Gaussian centre line velocity. Note here that both the visual and mathematical representations of the differences are consistent for the reduced gravity.

As one might expect, differences also exist in the definition of the plume fluxes when utilising Gaussian profiles. Through substituting (2.31), and the equivalent reduced gravity definition, for their top-hat representations in equations (2.8a–c), the Gaussian centre line flux terms may be written as

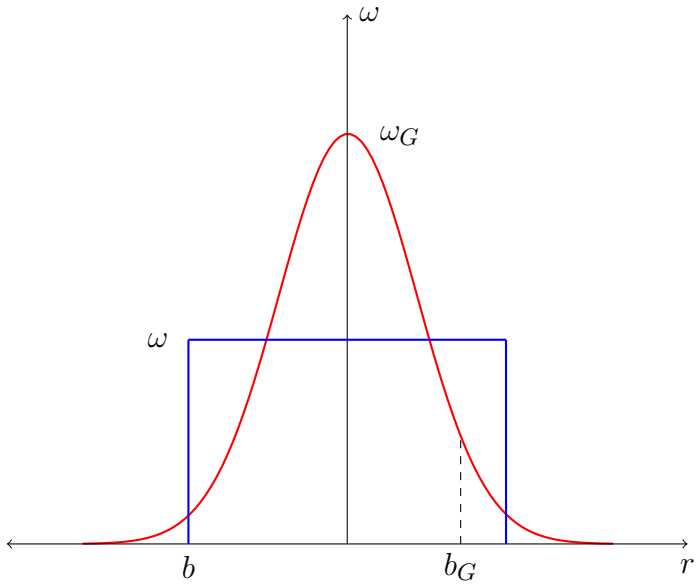

Fig. 2.2 Schematic of radial velocity profiles in a plume when considering both Gaussian (——) and 'top-hat' (——) assumptions.

$$Q = 2\pi \int_0^\infty \omega_G \exp\left(\frac{-r^2}{b_G^2}\right) r\, dr \;\; = \pi b_G^2 \omega_G, \tag{2.33a}$$

$$M = 2\pi \int_0^\infty \omega_G^2 \exp\left(\frac{-2r^2}{b_G^2}\right) r\, dr \;\; = \frac{1}{2}\pi b_G^2 \omega_G^2, \tag{2.33b}$$

$$B = 2\pi \int_0^\infty \omega_G g'_G \exp\left(\frac{-2r^2}{b_G^2}\right) r\, dr. \;\; = \frac{1}{2}\pi b_G^2 \omega_G g'_G. \tag{2.33c}$$

Evaluating the top-hat fluxes between $r = 0$ and $r = b$ gives

$$Q = \pi b^2 \bar{\omega}, \quad M = \pi b^2 \bar{\omega}^2, \quad B = \pi b^2 \bar{\omega} \bar{g}', \tag{2.34a-c}$$

which then, upon equating (2.34a-c) with equations (2.33a–c), allows the relationship between Gaussian and top-hat properties to be realised as

$$\bar{\omega} = \frac{1}{2}\omega_G, \quad \bar{g}' = \frac{1}{2} g'_G, \quad b = \sqrt{2} b_G. \tag{2.35a-c}$$

The entrainment coefficient also varies depending upon the shape of the plume profiles selected and from conservation of volume, the relationship is determined as

$$\alpha = \sqrt{2}\alpha_G. \tag{2.36}$$

From this point forward, unless directly specified, all plume properties and equations assume top-hat profiles.

2.5.3 Plume equations

Widely credited for being the pioneer of simple plume theory, Morton et al. (1956) utilised three core assumptions in their work, the ideas of which have been introduced in the previous subsections. Firstly, the rate of entrainment at the edge of the plume is proportional to some characteristic velocity at that height i.e. $\alpha = \bar{u_e}/\bar{\omega}$. Secondly, the top-hat profiles of velocity and buoyancy are self-similar at all heights above the source and finally, the flow is Boussinesq with the largest local variations in density being small compared to some reference density. Utilising these three assumptions, the conservation equations could be closed for turbulence, giving a result which today is generally known as the plume equations, written below in terms of the volume, momentum and buoyancy flux,

$$\frac{dQ}{dz} = 2\alpha(\pi M)^{1/2}, \tag{2.37a}$$

$$\frac{dM}{dz} = \frac{BQ}{M}, \tag{2.37b}$$

$$\frac{dB}{dz} = -N^2 Q. \tag{2.37c}$$

Along with the plume fluxes, an additional term known as the Brunt-Väisälä frequency or ambient buoyancy frequency appears in the equations. This frequency, defined as

$$N = \sqrt{-\frac{g}{\rho_0}\frac{d\rho_e}{dz}}, \tag{2.38}$$

dictates the rate at which a fluid parcel, displaced vertically from its height of neutral buoyancy, oscillates within a density stratified ambient.

In an unstratified environment, $N = 0$ and the plume buoyancy flux remains constant at all heights above the source. In this case, (2.37a) and (2.37b) may be combined to determine the constants associated with the similarity solutions specified in section 2.5.1 as,

$$\bar{\omega} = \frac{5}{6\alpha}\left(\frac{9\alpha}{10\pi}\right)^{1/3} B_0^{1/3} z^{-1/3}, \tag{2.39}$$

$$\bar{g}' = \frac{5}{6\pi\alpha}\left(\frac{9\alpha}{10\pi}\right)^{-1/3} B_0^{2/3} z^{-5/3}, \tag{2.40}$$

$$b = \frac{6\alpha}{5} z. \tag{2.41}$$

Although such a result is possible for plumes rising through uniform fluid, the same cannot be said for plumes in environments where $N > 0$. The key difference between stratified and unstratified plumes is the decay of buoyancy with height, a fact which is clearly identifiable from the buoyancy equation (2.37c). In a stably stratified environment, where density decreases with height, the plume will eventually become neutrally buoyant with its surroundings due to the entrainment of ambient fluid. As the density difference drives the change in vertical momentum, the momentum of the flow will also then decay to zero before the flow then falls back against itself and spreads radially at a height of neutral buoyancy. This behaviour is significantly more complex than its unstratified counterpart and obviously the same assumptions of self-similarity do not hold, especially above the height where buoyancy reduces to zero. Morton et al. (1956) identified this, but suggested that as entrainment is a function of the plume's vertical velocity, the level of entrainment at this height would be reasonably small and would only result in a small error in their model's ability to predict plume rise height. Through numerically integrating dimensionless forms of their equations with the initial conditions $Q_0 = M_0 = 0$ and $B_0 > 0$ at $z = 0$ (see Figure 2.3), they determined the following solutions for height and volume flux,

$$z = 2^{-5/8}\pi^{-1/4}\alpha^{-1/2} B_0^{1/4} N^{-3/4} \hat{z}, \tag{2.42}$$

$$Q = 2^{5/8}\pi^{1/4}\alpha^{1/2} B_0^{3/4} N^{-5/4} \hat{Q}, \tag{2.43}$$

where $\hat{z}$ and $\hat{Q}$ are numerical constants.

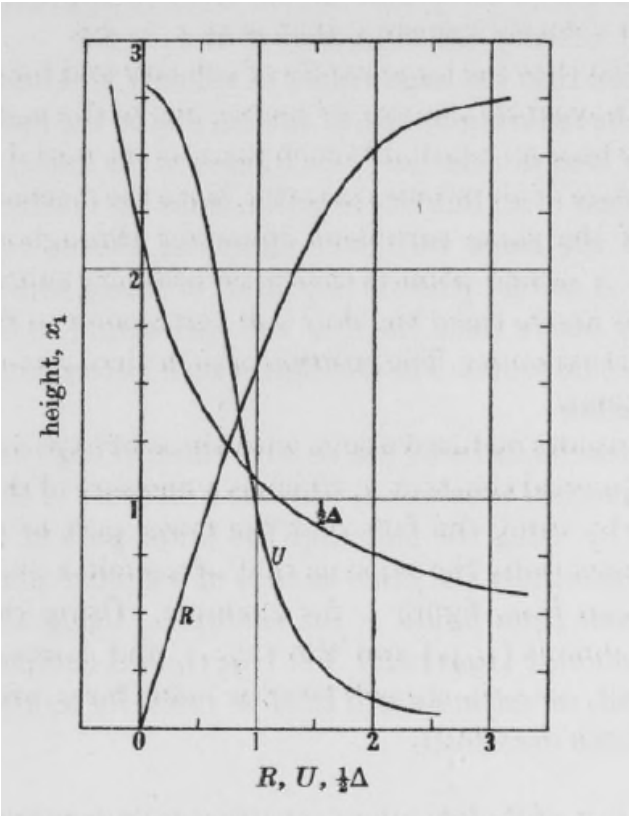

Fig. 2.3 The solution of the plume equations (2.37a–c) with respect to height as presented in Morton et al. (1956). The values of R, U and $\frac{1}{2}\Delta$ correspond to dimensionless values of plume radius, velocity and buoyancy.

With a value of $\hat{z}_m = 2.8$ for the height where velocity disappears, good agreement was found with laboratory experiments when using $\alpha = 0.118$. Equation (2.42) was later found to be suitable at also predicting the heights of large scale plumes including those associated with oil fires (Briggs, 1969) and explosive volcanic eruptions (Sparks, 1986). Since this initial approach, more complex models including large eddy simulations (LES) have been conducted and have found the value of $\hat{z}_m$ to vary between 2.72-2.82 using similar values of entrainment coefficient (Rooney and Devenish, 2014a). This alignment with the early solution of Morton et al. (1956) is quite extraordinary, especially considering (2.42) ignores a significant amount of the physics influencing the flow behaviour (Turner, 1986).

However, the same cannot be said for the spreading height and the final volume flux solutions as both are significantly influenced by any entrainment of lighter fluid into the plume between the neutral buoyancy height and the maximum plume height. In addition to this, there is potential for further entrainment into the descending fountain

at the top of the plume; a phenomenon which has been the focus of a number of studies including Cardoso and Woods (1993) and Debugne and Hunt (2016). The numerical constant for the neutral buoyancy height was determined to be $\hat{z_{B=0}} = 2.125$, with Morton et al. (1956) suggesting the spreading height would occur at some point between the neutral buoyancy and maximum heights. Theoretical work since has suggested a range of $2.22 < \hat{z}_s < 2.39$ for the spreading height (Briggs, 1982; Devenish et al., 2010) and this is supported by recent experimental measurements (Richards et al., 2014), once the appropriate virtual source corrections are applied (see section 2.5.4).

Finally, in the case of the volume flux, constant values in (2.43) range between $1.64 < \hat{Q}_s < 1.95$ (Rooney and Devenish, 2014a) which clearly is a much wider range than the constant associated with the maximum plume height. Previous authors have correlated the final volume flux to the terminal height of plumes in nature (see Bursik et al., 1992), however such a method may not be appropriate due to the range of $\hat{Q}_s$. In addition, (2.43) does not account for plume top entrainment, nor other complexities such as the influence of multiple phases or real, non-idealised sources (Woods, 1988).

2.5.4 Forced plumes

The dynamics of plumes described to this point have all been what one in the field would call pure, which simply refers to a plume rising from a virtual point source of buoyancy with zero volume or momentum flux. Such conditions allow the flow behaviour to be characterised only by the source buoyancy, however in both nature (see Woods, 1988) and the laboratory (Fan, 1967; Fox, 1970), plumes tend to rise from area sources where Q_0 and M_0 are non-zero (Hunt and Van den Bremer, 2011).

When considering a real plume source, the balance of natural and forced convection can be presented as the source Richardson number,

$$Ri_0 = \frac{b_0 \bar{g}'_0}{\bar{\omega_0}^2}, \tag{2.44}$$

which from inspection shows $Ri_0 \to \infty$ for a pure plume and $Ri_0 \to 0$ for a pure momentum-driven jet. Irrespective of the source conditions, plumes are expected to forget their initial conditions, tending towards self-similar behaviour after rising a certain distance from the source (Turner, 1986). This characteristic is revealed upon assessing the same balance of natural and forced convection at any height above the source of a pure plume. This local Richardson number is defined as

$$Ri(z) = \frac{b(z)\bar{g}'(z)}{\bar{\omega}(z)^2}, \tag{2.45}$$

and importantly, has been found to be constant at all heights in a pure plume rising from a virtual source with various studies arriving at a generally accepted far-field value of $Ri_p \approx 0.56$ (Fischer et al., 1979).

Taking advantage of this observation, the dynamics of plumes rising from non-idealised sources have been assessed by many authors in terms of a scaled Richardson number (Ezzamel et al., 2015; Hunt and Kaye, 2001; van Reeuwijk et al., 2016),

$$\Gamma_0 = \frac{Ri_0}{Ri_p} = \frac{5}{8\alpha\pi^{1/2}} \frac{{Q_0}^2 B_0}{{M_0}^{5/2}}, \tag{2.46}$$

where the real source fluxes are defined as $Q_0 = \pi b_0^2 \omega_0$, $M_0 = Q_0\omega_0$ and $B_0 = Q_0 g'$. This parameter was first utilised by Morton (1959), and later by Morton and Middleton (1973), extending his work on simple plume theory such that it could also be applied to real plume sources. Arguably, one of the most important takeaways from these two early works is the ability to classify the plume as pure ($\Gamma_0 = 1$), lazy ($\Gamma_0 > 1$) or forced ($\Gamma_0 < 1$); a result which subsequently enables the location of a real plume's virtual source to be predicted. Most recently worked on by Ciriello and Hunt (2020), the solution of Morton (1959), shown graphically in Morton and Middleton (1973) and provided explicitly by Hunt and Kaye (2001), is written as

$$-\frac{z_v + z_{avs}}{L_m} = \left(\frac{100}{16\alpha_p^2\pi}\right)^{1/4} \int_\gamma^1 v^3(v^5 - \gamma^5)^{-1/2}\, dv + \left(\frac{0.078}{\alpha_p^2\pi}\right)^{1/4} \gamma^{3/2}, \tag{2.47}$$

where z_v and z_{avs} correspond to the exact and asymptotic corrections, the latter only being appropriate at large distances from the source; and $\gamma = (1 - \Gamma_0)^5$. L_m is the momentum jet length scale and is defined as

$$L_m = \frac{M_0^{3/4}}{B_0^{1/2}}. \tag{2.48}$$

When considering plumes rising through stratified environments, an additional length scale associated with B_0 and N is present (Kaye, 2008), the scaling of which is given in (2.42). When combined with (2.48), the dimensionless parameter

$$\sigma = \left(\frac{M_0 N}{B_0}\right)^2, \tag{2.49}$$

may be written, detailing the relative magnitudes of jet length and plume rise height or alternatively, the timescale for the flow rise to $z = L_m$ with respect to the ambient stratification strength (Richards et al., 2014). Again introduced by Morton (1959) and utilised by others since (Bloomfield and Kerr, 2000; List, 1982), the buoyancy frequency parameter allows forced stratified plumes to be compared to those with zero momentum at the source. Specifically, when σ is small, buoyancy forces drive the flow's motion once the influence of stratification becomes important. Conversely, momentum forces dominate when σ is large, note however that the definition of large varies between $\sigma > 1$ (List, 1982) and $\sigma > 49$ (Richards et al., 2014). Irrespective of the transitional value, the rise height of the flow can be characterised as a function of σ with $z/L_m \sim \sigma^{-3/8}$ for $\sigma \ll 1$ and $z/L_m \sim \sigma^{-1/4}$ for $\sigma \gg 1$ (Fischer et al., 1979).

Together, Γ_0 and σ are important in understanding the behaviour of forced plumes with both values being used recently to model the rise height of forced plumes (Mehaddi et al., 2013), in addition to determining the appropriate transitional values of the entrainment coefficient (Papanicolaou et al., 2008; van Reeuwijk and Craske, 2015).

2.6 Multiphase plumes

The introduction of a secondary phase to the flow, whether that be particles or bubbles, has a significant influence on the plume's dynamics. The following sections provide an insight into the behaviour associated with both particle-laden plumes and bubble plumes.

2.6.1 Particle-laden plumes

A particle-laden plume is a flow which prominently consists of buoyant gas or liquid with a dispersed phase of dense, negatively buoyant particles. Due to their interest in understanding the dynamics of volcanic eruption columns, Carey, Sigurðsson and Sparks (1988) conducted the first experiments on particle-laden plumes and characterised the flow's buoyancy flux as a combination of the buoyancy contributed by the two phases,

$$B_0 = B_{0,f} + B_{0,p}, \tag{2.50}$$

where the individual fluid and particle buoyancy fluxes are defined as

$$B_{0,f} = Q_0 g \frac{(1-\phi_0)(\rho_0 - \rho_f)}{\rho_0}, \tag{2.51}$$

$$B_{0,p} = Q_0 g \frac{\phi_0(\rho_0 - \rho_p)}{\rho_0}, \tag{2.52}$$

with ϕ_0 representing the source particle volume fraction and ρ_p as the particle density.

Unlike particle or sediment plumes where dense particles are fed from a point source at a free surface to create a sinking plume (see Reingold, 1994), particle-laden plumes are produced within the ambient fluid and distinctly differ due to the physical interactions which occur between the plume and the particles. In a sinking sediment plume, once the plume reaches the floor or the height of neutral buoyancy, the particles do not interact with the plume flow. In the case of a particle-laden plume however, after spreading either at the free surface of a uniform environment or at the height of neutral buoyancy in a stratified ambient, the particles decouple from the radial flow and settle into the environment below effectively changing the bulk density of the fluid which the plume is rising through. From their experimental observations in a uniform environment, Carey et al. (1988) specifically described how the particles settling from the intrusion were pulled towards the plume, creating a veil of sedimenting particles around the convective flow. They also noted that the portion of particles settling close to the plume were re-entrained, whereas particles decoupling at greater radial distances simply settled onto the floor.

The authors believed the process of re-entrainment strongly impacted the plume dynamics and shortly after this initial work, released a subsequent paper modelling particle sedimentation from the lateral intrusion (Sparks et al., 1991). This work included two important derivations which have since shaped the approach to modelling particle-laden plumes. Firstly, the critical intrusion radius for particle re-entrainment,

$$r_c^2 = \frac{6}{5u_{st}} \left(\frac{9\alpha^4}{10\pi} \right)^{1/3} B_0^{1/3} z_s^{5/3}, \tag{2.53}$$

where u_{st} is the particle settling velocity; and secondly, the expected particle concentration profile along a well-mixed intrusion,

$$\phi(r) = \phi_s \exp\left[-\frac{\pi u_{st}}{Q_s} (r^2 - b_s^2) \right], \tag{2.54}$$

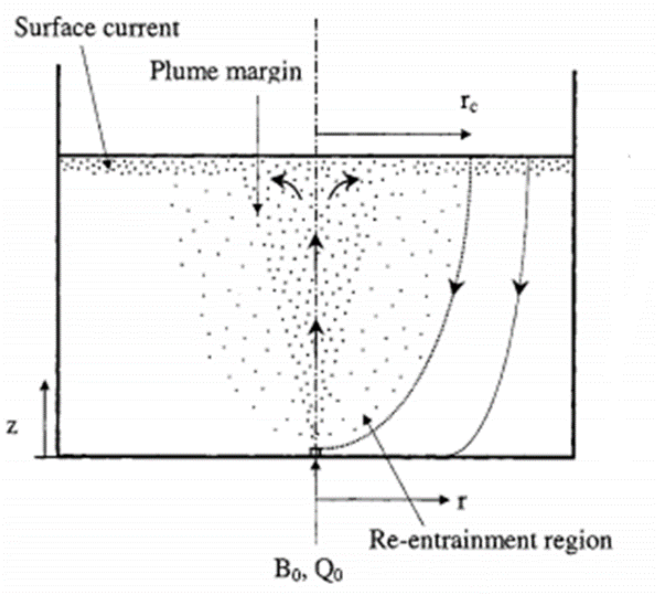

Fig. 2.4 Schematic of a particle-laden plume in a uniform environment, as shown by Zarrebini and Cardoso (2000)

where the subscript s denotes the value of these parameters at the plume spreading level.

The work of Carey et al. (1988) and Sparks et al. (1991) has led to a number of studies concerning sedimentation patterns of particle-laden plumes including work interested in mono (Zarrebini and Cardoso, 2000) and polydispersed (Cardoso and Zarrebini, 2001b) particles, particle fall-out from the plume margins (Ernst et al., 1996) and the non-intrusive measurement of sediment depth in a stratified ambient (Sutherland and Hong, 2016). Although useful, potentially of even more interest is the actual influence of particle re-entrainment on plume dynamics. Using similar forms of (2.53) and (2.54), combined with the assumption that the plume velocity significantly exceeds the particle settling velocity, the particle volume fraction at the spreading height may be written as

$$\phi_s = \frac{Q_0 \phi_0 e^1}{Q_s}. \tag{2.55}$$

This result, given by Veitch and Woods (2000), Zarrebini and Cardoso (2000) and Apsley and Lane-Serff (2019), shows that re-entrainment increases the spreading height concentration by a factor of e^1 compared to the case where no particles are re-entrained. Importantly, when the source concentration of a particle-laden plume is small, this e^1

factor has little influence on plume behaviour, however once some threshold source concentration is exceeded, the plume dynamics appear to change significantly. For plumes with a source concentration of less than $10\,\mathrm{gL}^{-1}$, Carey et al. (1988) described the plumes as dilute with similar dynamics to a single-phase plume. However, in their experiments with larger source concentrations, they observed the development of gravity flows at the edge of the plume and in some cases complete collapse of the umbrella region. Other experimental works investigated ambient convection in particle-laden plumes with Cardoso and Zarrebini (2001a) developing a criterion for the onset of convection at the edge of the plume after Veitch and Woods (2000) characterised the plume dynamics using the ratio of particle to fluid buoyancy flux at the source,

$$P = \frac{-B_{0,p}}{B_{0,f}} \approx \frac{\phi_0(\rho_p - \rho_0)}{(\rho_0 - \rho_f)}. \tag{2.56}$$

Using this ratio, Veitch and Woods (2000) found that convective downflows developed around the plume for $P > 0.2$ and once above $P \approx 0.6$, the plume tended to collapse and oscillate about the source.

Since the turn of the century, experiments have been conducted to better understand how plumes transport particles through a ventilated space (Mingotti and Woods, 2015), as well as their behaviour in stratified ambients. The first experimental work on particle-laden plumes in stratification was conducted by Guillaume Carazzo and Mark Jellinek, who published two studies investigating the dynamics and stability of intrusions produced by negatively buoyant particle-laden jets in a two-layer stratification (Carazzo and Jellinek, 2012, 2013). Although more representative of plumes in nature than experiments in a uniform environment, the absence of a linear density gradient inhibits dynamic behaviour which is likely to occur in particle-laden plumes rising through stratified environments, such as the ocean or the atmosphere. Examples of this behaviour includes the depression of the plume rise height and the development of secondary intrusions. As a particle-laden plume initially rises, the plume entrains particle-free ambient fluid, however, over time the particles settle from the intrusion and the environment at the edge of the plume also becomes laden with particles. This effective change in stratification strength ($dN/dt \neq 0$) causes the evolution of plume buoyancy with height to change, resulting in new lower maximum and neutral buoyancy heights being achieved.

In two of the first experimental works in linear stratification, Mirajkar et al. (2015) and Sutherland and Hong (2016) both observed this decrease in plume height and both proposed empirical equations to fit their results. Although the plume spreading heights

were presented, Mirajkar et al. (2015) only attempted to develop a prediction for the maximum steady-state height and using dimensional analysis, the authors proposed

$$z_m = \left[4.4 - 450\left(\frac{\phi_0 u_{st}}{(B_{0,f}N)^{1/4}}\right)\right] B_{0,f}^{1/4} N^{-3/4}, \tag{2.57}$$

with the value 4.4 determined from (2.42) using $\hat{z} = 2.8$ and $\alpha = 0.096$, and the value 450 to achieve an appropriate fit to their results. Notably, this equation ignores the negative buoyancy flux at the source by only utilising $B_{0,f}$ and also assumes some dependence on the particle settling velocity, yet u_{st} remained constant in their experiments.

Conversely, Sutherland and Hong (2016) only reported on the plume spreading height and due to their plumes having a large momentum flux at the source, presented their results as

$$\frac{z_s}{L_m} = 2.3(\pm 0.4)\sigma^{-0.45(\pm 0.07)}, \tag{2.58}$$

for $\sigma < 30$. The multiplier of 2.3 here is less than that associated with single-phase plumes (Richards et al., 2014) and the power of -0.45 is similar to the theory detailed in section 2.5.4, however, it is important to note that their experiments were only conducted over a period of 90 seconds and were potentially too short to achieve a steady state.

Since these initial works, Apsley and Lane-Serff (2019) developed a model detailing the decrease in height and potential collapse of a pure particle-laden plume. Using the theoretical particle trajectory between the intrusion and the edge of the plume, the steady-state height of the plume may be written as a function of the source buoyancy flux ratio,

$$\frac{z_\infty}{z_0} = \left(\frac{|j|}{1+|j|}\right)^{1/4}, \tag{2.59}$$

where $j = (1 - P_c/P)/(1 - P_c)$ with the critical ratio for pure plumes notably equivalent to the inverse of the re-entrainment coefficient presented in (2.55), $P_c = e^{-1}$. The parameters z_∞ and z_0 are the steady-state and initial plume heights, the latter determined using (2.42) with any given value of $\hat{z}$. This work has yet to be compared to any experiments and it is expected that its success will rely on the assumption of a quiescent environment. Importantly, in the event of any convective motion around the plume (as observed in the experiments of Carey et al., 1988; Veitch and Woods, 2000; and Cardoso and Zarrebini, 2001a), the particle trajectory will no longer follow

a defined path and thus, (2.59) would no longer be suitable to predict the plume steady-state height.

A second point of interest is the development of secondary intrusions, a phenomenon which has previously been observed in explosive volcanic eruptions (Sparks et al., 1986; Woods and Kienle, 1994). The first experimental interest in such behaviour was by Holasek et al. (1996), who conducted experiments simulating the separation of ash and gas in volcanic umbrella plumes. Their experiments involved the injection of particle-laden fluid into a stratified environment at the height of neutral buoyancy and over time, this current separated to form a 'particle-poor' intrusion above a 'particle-rich' intrusion. The authors stated that similar intrusions could be formed by particles settling from the umbrella cloud of a continuous particle-laden plume supplied from below. However, they also stated that the entrainment of ambient fluid back into the plume would significantly weaken the visual effect of multiple intrusions. Apsley and Lane-Serff (2019) also commented on the potential for the intrusion of a particle-laden plume to rise following the sedimentation of particles, however stated specifically that they did not expect such a rise to occur.

Contrary to the hypothesis proposed by Holasek et al. (1996), and later reiterated by Apsley and Lane-Serff (2019), the recent experimental work of Mingotti and Woods (2020) showed the development of multiple umbrella structures produced by a bottom supplied particle-laden plume rising through a stratified environment (see Figure 2.5a). These authors quantified the change in height between the particle-poor and particle-rich intrusions as

$$-\Delta z_s = 0.83\left(\frac{B_{0,p}}{B_0}\right) B_0^{1/4} N^{-3/4}, \tag{2.60}$$

by simply comparing the magnitude of particle and total buoyancy fluxes at the source. When compared to their experimental results, (2.60) generally underpredicted their observations, yet this was expected due to discounting particle re-entrainment effects.

As well as observing interesting behaviour above the primary intrusion, equally interesting dynamics unique to stratified particle-laden plumes are observed between the intrusion and the plume source. Beneath the primary intrusion, Mirajkar et al. (2015) described the presence of a parabolic cloud of dyed fluid and particles before, in a second paper, proposing a criterion for its collapse to the source as a function of the Richardson number (Balasubramanian et al., 2018). Arguably more noteworthy in both works was the development of a secondary intrusion between the primary intrusion and the source. Although a significant feature of their plumes (Figure 2.5b/c), in neither

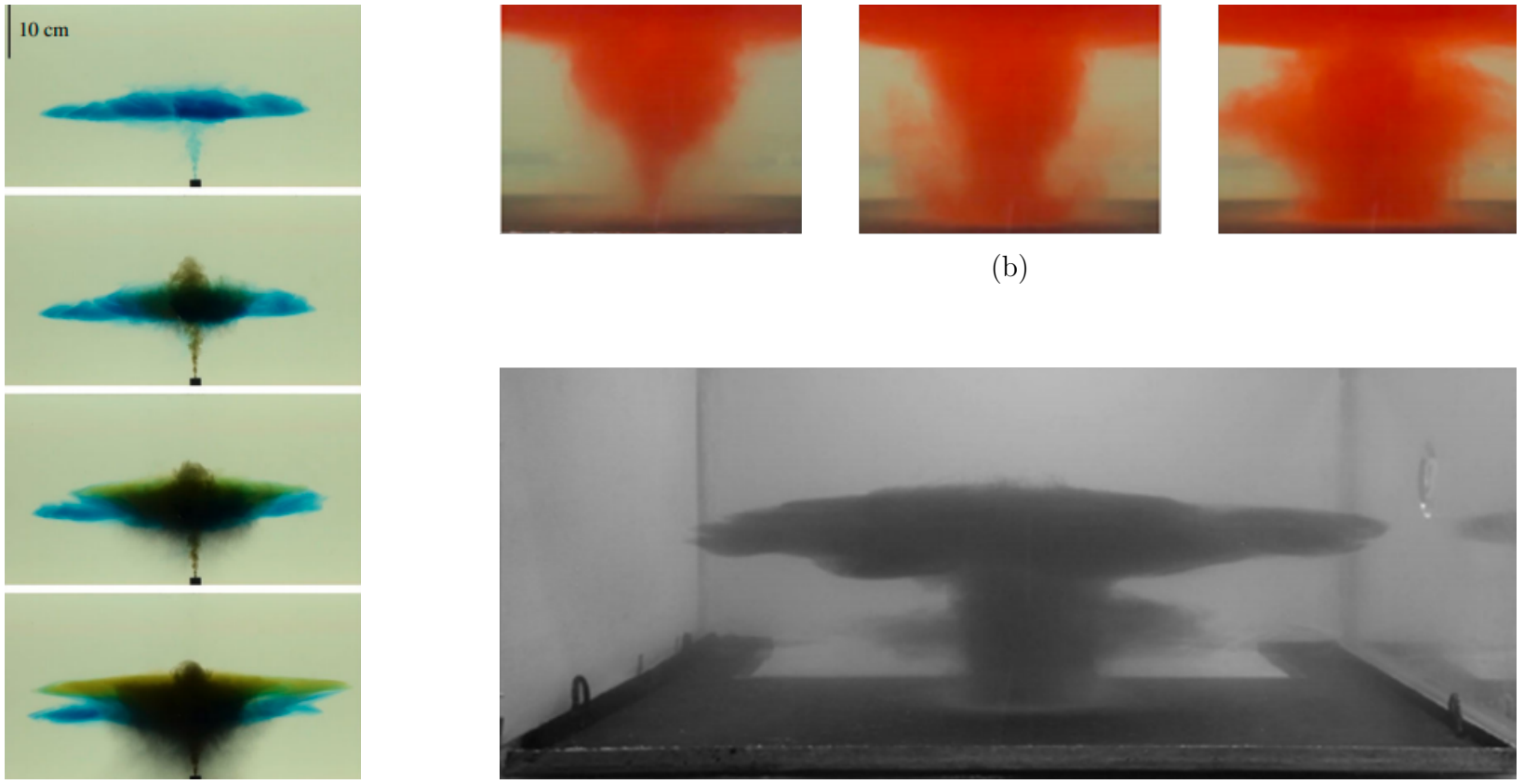

(a) (b) (c)

Fig. 2.5 (a) Series of photographs of an experiment $B_0 = 290\,\mathrm{cm^4 s^{-3}}$, $N = 0.73\,\mathrm{s^{-1}}$, $\sigma = 26.3$, $\phi_0 = 0.42\%$ performed by Mingotti and Woods (2020) (b) Series of photographs of an experiment $B_0 = 187\,\mathrm{cm^4 s^{-3}}$, $N = 0.67\,\mathrm{s^{-1}}$, $\sigma = 9.41$, $\phi_0 = 0.70\%$ performed by Balasubramanian et al. (2018) (c) A photograph of an experiment $B_0 = 333\,\mathrm{cm^4 s^{-3}}$, $N = 0.67\,\mathrm{s^{-1}}$, $\sigma = 2.99$, $\phi_0 = 0.70\%$ performed by Mirajkar et al. (2015)

case did the authors attempt to characterise the plume conditions required to develop such structures.

To conclude this section, it is important to mention that in all of the studies discussed above, with the exception of Ernst et al. (1996), the characteristic velocity of the plume, written as $(B_0^2/M_0)^{1/4}$ in a uniform environment and $(B_0 N)^{1/4}$ in a stratified environment, is much greater than the settling velocity of the dispersed particles. In the event that the plume velocity is less than the particle settling velocity, particles will likely fall out from the plume margins and there may even be the potential for a complete flow regime change as observed by Mingotti and Woods (2016) for particle-laden fountains. In the case of the particle-laden plume experiments presented in this thesis, all particles are expected to be transported to the plume maximum as $(B_0 N)^{1/4} \gg u_{st}$.

2.6.2 Bubble plumes

Multiphase bubble plumes develop above point source releases of gas in liquid environments and are characterised by a buoyancy flux,

$$B_0 = Q_b g \frac{(\rho_0 - \rho_b)}{\rho_0}, \tag{2.61}$$

where Q_b and ρ_b represent the bubble flowrate (or volume flux) and bubble density. Notably, as $\rho_0 \gg \rho_b$, the scaled density deficient tends towards a value of one and therefore,

$$B_0 \approx Q_b g. \tag{2.62}$$

Like other plumes, at a short distance above the source the rising bubbles create turbulent eddies which result in the entrainment of ambient liquid into the bubble core. In the early work of Sjöberg (1967) and Kobus (1969), both were specifically interested in experimentally measuring the rate of entrainment with respect to gas flowrate. These measurements were shortly followed by the derivation of the first bubble plume integral model by Cederwall and Ditmars (1970), who utilised the entrainment assumption to describe the flow behaviour. In this work, as well as in the two prior models, both a mean plume velocity and a bubble slip velocity entered the equations. Also despite the large density difference at the source, the flow was modelled under the Boussinesq approximation due to the significant dilution quickly achieved by liquid entrainment. A more comprehensive integral model was later presented by Milgram (1983) who,

through analysing an array of experimental data, determined that bubble plumes are not strictly self-similar and that both the plume entrainment coefficient and the momentum amplification factor (described as the ratio of the total momentum flux to the momentum flux carried by the mean flow) are functions of local plume properties.

Before Milgram (1983), the influence of ambient stratification on bubble plumes was explored both experimentally and theoretically by McDougall (1978). In his work, McDougall (1978) found that bubble plumes differ from single-phase plumes as the bubbles can rise faster than the liquid phase; and in a stratified environment, the gas continues to rise beyond the height at which simple plume theory predicts the plume will lose it's momentum. The same however is not the case for the liquid in the plume which peels away from the bubble core and spreads as a radial intrusion. To explain this complex behaviour, a double plume model was proposed with a central rising plume comprised of both liquid and bubbles and an outer descending plume which contributes only towards intrusion formation (Figure 2.6).

This model formulation was extend by Asaeda and Imberger (1993) to compare the intrusion heights in their experiments to the theory. Notably both McDougall (1978) and Asaeda and Imberger (1993) used similar non-dimensionalisation variables in their modelling approaches. Two of these key parameters, written following the nomenclature of Asaeda and Imberger (1993), are

$$P_N = \frac{N^3 H^4}{B_0}, \tag{2.63}$$

$$M_H = \frac{B_0}{4\pi\alpha^2 u_b^3 H}, \tag{2.64}$$

where u_b is the bubble slip velocity and H corresponds to the depth of the liquid reservoir. As well as being utilised in their modelling process, Asaeda and Imberger (1993) used (2.63) and (2.64) to characterise three bubble plume flow regimes (see Figure 2.7). First described by themselves a few years earlier (Asaeda and Imberger, 1989), they found that in the case of high gas flowrate and weak stratification (type 1), the flow created is reminiscent of a single-phase plume in a uniform environment where the liquid is carried by the bubbles up to the top of the reservoir, creating a liquid surface current. In type 2 plumes, those with moderate flowrates and stratification strengths, the plume creates a number of defined intrusions between the source and the surface; and for low flowrates and strong stratification (type 3), the plume emits multiple unsteady subsurface intrusions.

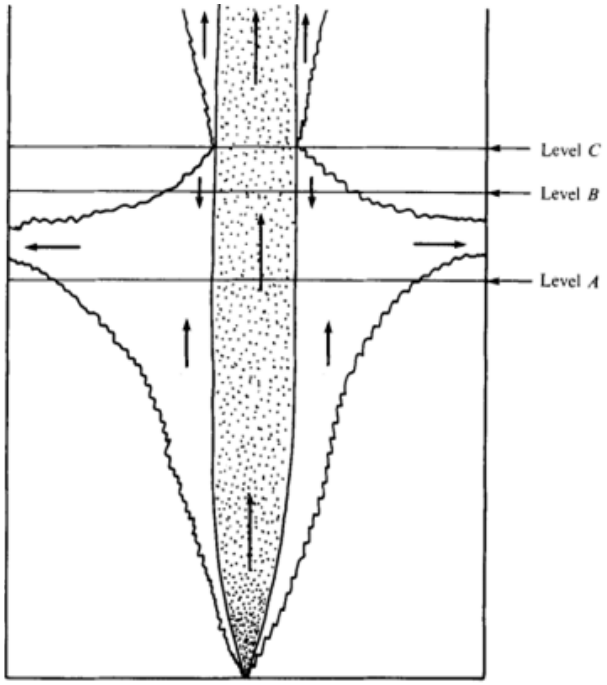

Fig. 2.6 Schematic of the double-plume structure proposed by McDougall (1978). The three horizontal lines correspond to points of interest in his model. Specifically, the vertical liquid velocity almost vanishes at level A; the upwards and downwards volume fluxes are equivalent at level B; and the double-plume model restarts at level C.

Although the transition between regimes could be determined using P_N and M_H, the transition was not well defined until the work of Scott Socolofsky in the early 2000s. First presented in his thesis (Socolofsky, 2001) and later in a set of papers co-authored with his thesis supervisor (Socolofsky and Adams, 2002, 2003, 2005), he showed that all bubble plume types could be well defined using the term U_N, which he coined the non-dimensional slip velocity. Using a combination of the previous parameters, U_N is defined as

$$U_N = \left(4\pi\alpha^2 M_H P_N^{1/4}\right)^{-1/3} = \frac{u_b}{(B_0 N)^{1/4}}, \tag{2.65}$$

where the denominator is simply the plume velocity scale. From his experiments and the data provided by Asaeda and Imberger (1993), type 1 plumes occur for $U_N < 1.5$; type 2 for $1.5 < U_N < 2.4$; and type 3 for $U_N > 2.4$ (Socolofsky and Adams, 2003).

Due to the large vertical extent of his experimental tank, Socolofsky (2001) also defined a fourth plume regime as type 1*, which simply refers to a type 1 plume

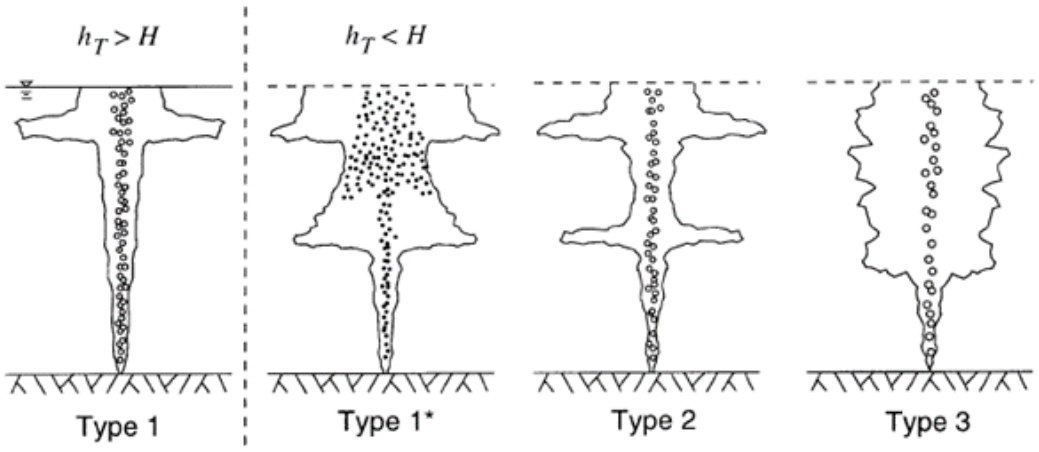

Fig. 2.7 Schematic of bubble plume regimes from Socolofsky (2001). Note that the trap height, h_T in his nomenclature, is equivalent to the spreading height z_s.

where the height of neutral buoyancy is less than the liquid height. The height of neutral buoyancy was initially likened to the height of the intrusion spreading from the plume and Socolofsky (2001) proposed the following empirical equation to predict this so called trap height (or spreading height) as a function of the non-dimensional slip velocity,

$$\frac{z_s}{(B_0/N^3)^{1/4}} = 2.8 - 0.27U_N, \tag{2.66}$$

with 2.8 being the equivalent neutral buoyancy height for a single-phase plume ($U_N = 0$). Along with heights of interest, Socolofsky (2001), and later in Socolofsky and Adams (2005), presented similar empirical predictions for the liquid volume fluxes associated with a bubble plume. Using these predictions, they also quantified the efficiency at which liquid peeled from the bubble core and found a decreasing efficiency with increasing slip velocity, aligning with their qualitative regime observations.

The bulk properties of bubble plumes, namely height and liquid volume fluxes, have continued to be of interest with several authors presenting different approaches to the problem since. Crounse et al. (2007) and Socolofsky et al. (2008) both adopted the double-plume integral approach initially proposed by McDougall (1978). However, in both cases, they focused their efforts on capturing the appropriate levels of entrainment occurring between the ambient and the inner and outer plumes such that the trap height and liquid volume fluxes could be predicted and compared to earlier experiments.

A new integral approach was taken by Chu and Prosperetti (2017), who formulated a single-plume integral model utilising a scaled Richardson number and buoyancy frequency parameter, similar to those discussed in section 2.5.4. Unlike previous studies, they recognised the distinct difference between the neutral buoyancy height in the plume and subsequent spreading height of the intrusion. Due to the advancement in computing, large eddy simulations (LES) of bubble plumes have been conducted and the impact of modelling the additional turbulent processes on predicting bulk quantities has been discussed (Yang et al., 2016; Zhou, 2020).

Although intrusion heights and liquid volume fluxes associated with bubble plumes have been of interest for over twenty years, another bulk quantity, the concentration of dissolved species, has been less studied despite the obvious mass transfer applications. Work has been conducted in regard to the effect of bubble dissolution on plume dynamics (Chu and Prosperetti, 2019; Domingos and Cardoso, 2013; Socolofsky and Bhaumik, 2008), however there has been little to no interest on how dissolved species is transported both vertically and radially throughout the water column.

In addition to the work conducted on bulk bubble plume properties in quiescent stratified environments, bubble plume research has spanned quite broadly with wide interest into areas including mixing processes (Baines and Leitch, 1989; Chen and Cardoso, 2000; Neto et al., 2016); plumes in cross-flow (Socolofsky, 2001) or rotating environments (Fabregat Tomàs et al., 2017); and detailed observations of velocity profiles (Seol et al., 2007) and turbulence (Lai and Socolofsky, 2019). For further details, see the recent bubble plume review of Boufadel et al. (2020).

2.7 Submerged axisymmetric intrusions

A common thread between all stratified plumes, irrespective of phase, is the development of lateral axisymmetric intrusions near the plume's height of neutral buoyancy. Assuming no additional entrainment of ambient fluid, the plume intrusion spreads with a flowrate,

$$Q_s = 2\pi R_i L_i u_i, \tag{2.67}$$

where R_i, L_i and u_i denote the radius, thickness and velocity of the intrusion. Many previous authors have investigated the spreading behaviour of submerged gravity currents in stratified fluid. Whether generated by turbulent plumes (Kotsovinos, 2000; Lemckert and Imberger, 1993a; Richards et al., 2014) or simple box withdrawal (Chen,

1980; Ivey and Blake, 1985; Zatsepin and Shapiro, 1982), such intrusions follow two key flow regimes. At small times (and small radial distances), inertial forces are important and the flow spreads according to a balance of the buoyancy and inertia forces. At large times, radial spread of the current is dictated by a balance of buoyancy and viscous forces. According to Ungarish (2009), the forces acting on a submerged intrusion are written as

$$F_B = \rho_i N^2 L_i^3 R_i, \tag{2.68}$$

$$F_I = \rho_i L_i R_i u_i^2, \tag{2.69}$$

$$F_V = \frac{\rho_i v R_i^2 u_i}{L_i}, \tag{2.70}$$

where F_B, F_I and F_V are the buoyancy, inertial and viscous forces acting on the current; and ρ_i is the intrusion density.

A comparison of F_B and F_I shows that the intrusion velocity in the inertia-buoyancy regime is dictated by a Froude number, $Fr = u_i/NL_i$, which when substituted into (2.67) gives

$$u_i = \frac{dR_i}{dt} = \left(\frac{FrQ_iN}{2\pi R_i}\right)^{1/2}. \tag{2.71}$$

Through integration, it is found that the intrusion radius in this regime may be written as a function of time t as

$$R_i = \left(\frac{9Fr}{8\pi}\right)^{1/3} (Q_iN)^{1/3} t^{2/3}. \tag{2.72}$$

Note here that the theoretical Froude number of an intrusion spreading in a stratified ambient is $Fr = 0.25$ (Bolster et al., 2008), resulting in a constant of proportionality of 0.45. This value is similar to experimental findings (Lemckert and Imberger, 1993a), yet significantly differs from the constant of 0.802 determined asymptotically by Chen (1980).

A few other authors, including those investigating intrusions emanating from particle-laden plumes, extended this analysis for constant intrusion buoyancy B_i using the relation $B_i \sim Q_s N^2 L_i$ (Kotsovinos, 2000; Mirajkar et al., 2015; Richards et al., 2014). This approach gives a different scaling of $t^{3/4}$ yet, as described by Rooney

and Devenish (2014a) and Johnson et al. (2015), requires assumptions to be made which do not hold in a stratified environment. Firstly, it assumes buoyancy flux is conserved across the intrusion, however, this is not true due to the flux of buoyancy between the upper and lower halves of the current to keep it well mixed. Taking a constant intrusion buoyancy flux also inherently utilises the assumption of Didden and Maxworthy (1982). They stated that stratification is unimportant in regard to the spread of a gravity current when the density difference between the current and the environment is large compared to the change in ambient density across the current depth. For an intrusion spreading at the height of neutral buoyancy in a stratified environment, this is simply not the case.

At greater times and radial distances, once viscous forces become important, the intrusion velocity reduces to

$$\frac{dR_i}{dt} = u_i = \frac{N^2 L_i^4}{\upsilon R_i} = \left(\frac{Q_s^4 N^2}{(2\pi)^4 \upsilon R_i^5} \right)^{1/5}. \tag{2.73}$$

The solution to (2.73) then gives the intrusion radius in the viscous-buoyancy regime as

$$R_i = \left(\frac{2}{\pi} \right)^{4/10} \left(\frac{Q_i^4 N^2}{\upsilon} \right)^{1/10} t^{1/2}. \tag{2.74}$$

There is general agreement across the literature that $R_i \sim t^{1/2}$ in this regime, however the constant of proportionality, along with the other scaling terms, appear to differ. As in the inertia-buoyancy regime, Kotsovinos (2000) took a constant buoyancy approach, however most other works suggest the scaling written in (2.74). The constant of proportionality simply determined through integration is 0.83, yet this is greater than that determined by Ungarish (2009) and much greater than those determined experimentally. Zatsepin and Shapiro (1982) and Ivey and Blake (1985) gave values of 0.53 and 0.45 respectively, and unlike in the inertia-buoyancy case, Chen (1980) gave a much more similar asymptotic value of 0.45.

It is worth noting that all of the studies discussed here were specifically interested in the spreading rate of a single intrusion in stratified fluid. As detailed in section 2.6.2, there is potential for multiple subsurface intrusions to be produced by bubble plumes and despite the fact that bubble plume intrusions have been studied (Lemckert and Imberger, 1993a), the influence of multiple spreading events is yet to be investigated.

Chapter 3

Steady-state dynamics of stratified particle-laden plumes

This chapter has been published as Barnard, J.M. (2021). On the dynamics of stratified particle-laden plumes. *Journal of Fluid Mechanics*, 925, A33.

3.1 Summary

An experimental study on stratified particle-laden plumes is presented and five steady-state flow regimes have been identified. The steady-state behaviour of the plume is directly related to the magnitude of the convective velocity associated with particle-induced instabilities, U_c, in relation to the terminal settling velocity of each individual particle, u_{st}. When $u_{st} > U_c$, the ratio of particle to fluid buoyancy flux at the source, P, becomes important. For $P < 0.2$, the plume dynamics appear very similar to a single-phase plume as particle recycling has minimal impact on the steady-state plume height. When $P > 0.2$, the plume height decreases significantly, creating an anvil-shaped intrusion similar to those associated with explosive volcanic eruptions. Importantly, the measured steady-state heights of plumes within this settling regime validate the collapse model of Apsley and Lane-Serff (2019). When $u_{st} \leq U_c$, particle re-entrainment behaviour changes significantly and plume dynamics become independent of P. When $u_{st} \approx U_c$, a trough of fluid becomes present in the sedimenting veil due to a significant flux of descending particles at the edge of the plume. Once $u_{st} < U_c$, the particles spreading in the intrusion become confined to a defined radius around the plume due to the significant ambient convection occurring beneath the current. For $u_{st} \ll U_c$, or in the case of these experiments, when $U_c \geq 1\,\mathrm{cms}^{-1}$, ambient convection becomes so strong that intrusion fluid is pulled down to the plume source, creating a

flow reminiscent of a stratified fountain with secondary intrusions developing between the original current and the tank floor. Through an extension of the work of Cardoso and Zarrebini (2001a), an analytical expression is developed to determine the onset of convection in the environment beyond the edge of the plume, which for a known particle settling velocity, can be used to characterise a plume's expected settling regime. In all plume regimes, the intrusion fluid is observed to rise in the environment following the sedimentation of particles and a simple model for the change in intrusion fluid height has been developed using the steady-state particle concentration at the spreading level.

3.2 Introduction

A particle-laden plume is a multiphase convective flow comprised of fluid and particles originating from a localised source of buoyancy. Such flows are ubiquitous in both industry and the environment. Industrial examples include smoke plumes generated by combustion processes and the release of wastewater effluent into marine outfalls. In nature, explosive volcanic eruptions propel dense particles and fine ash tens of kilometres into the atmosphere and in the deep ocean, black smokers and gas hydrate plumes disperse metallic and carbon-rich particles in the water column.

Attention was first given to the physical behaviour and properties of particle-laden plumes by Carey et al. (1988). In their unstratified plume experiments, they found that low concentration or 'dilute' particle-laden plumes behaved similarly to a single-phase plume with a reduced buoyancy flux. In the case of a single-phase plume, the buoyancy flux of the plume fluid, $B_{0,f}$, is produced due to the presence of a density deficit between the fluid in the environment and the fluid in the plume. This quantity drives the upwards motion of the flow and is defined as

$$B_{0,f} = Q_0 g \frac{(1-\phi_0)(\rho_0 - \rho_f)}{\rho_0}, \tag{3.1}$$

where Q_0 is the volume flux at the source; g is acceleration due to gravity; ϕ_0 is the source particle volume fraction (which is equal to zero in a single-phase plume); and ρ_f and ρ_0 are the density of the plume fluid and a reference density, generally taken as the density of the environment at the plume source. As observed by Carey et al. (1988), when dense particles are introduced into the flow at the source, an additional negative buoyancy flux is present and is defined as

$$B_{0,p} = Q_0 g \frac{\phi_0(\rho_0 - \rho_p)}{\rho_0}, \tag{3.2}$$

where ρ_p is the particle density. In their unstratified experiments, Carey et al. (1988) found that when the plume particle volume fraction was small (i.e. $B_{0,f} \gg -B_{0,p}$), the fine, dense particles were transported upwards with the plume before then subsequently spreading with the surface gravity current. The particles were observed to decouple from the radial flow and sediment into the ambient fluid below, creating a veil of particles around the plume. A portion of these particles in the sedimenting veil were re-entrained back into the main body of the plume; a process which the authors believed strongly impacted the plume dynamics.

Following this pioneering work, other experimental studies were conducted to gain a better understanding of the plume sedimentation behaviour (Cardoso and Zarrebini, 2001b; Ernst et al., 1996; Sparks et al., 1991; Zarrebini and Cardoso, 2000) and the influence of particle re-entrainment on plume dynamics (Cardoso and Zarrebini, 2001a; Veitch and Woods, 2000). Of the studies detailed above, all are associated with a plume rising in a uniform ambient with a gravity current spreading at the surface of an environment of finite vertical extent. Although a surface current can be compared to an intrusion of a stratified plume which spreads close to the height of neutral buoyancy, the absence of a linear density gradient inhibits dynamic behaviour which is likely to occur in particle-laden plumes rising through stratified environments.

The first linearly stratified particle-laden plume experiments were conducted by Mirajkar et al. (2015), who concentrated mostly on the maximum and spreading heights of the plume, as well as the spreading dynamics of the submerged plume intrusion. These authors shortly published a subsequent article, focusing their efforts on the parabolic cloud of fluid and particles which forms beneath the intrusion near the edge of the plume (Balasubramanian et al., 2018). Sutherland and Hong (2016) conducted stratified particle-laden plume experiments in an attempt to non-intrusively predict the particle sedimentation patterns using light attenuation techniques. Most recently, Mingotti and Woods (2020) completed a series of experiments with a primary focus of understanding the increase in intrusion interstitial fluid height following the sedimentation of particles from the plume's radially spreading gravity current.

Of the few authors to experimentally study stratified particle-laden plumes, all have noted that the maximum plume height was less than that of a single-phase plume due to particle re-entrainment. The maximum height of a single-phase plume was originally determined by Morton et al. (1956) as

$$z_m = 1.37\alpha^{-1/2}{B_0}^{1/4}N^{-3/4}, \tag{3.3}$$

where B_0 is the plume buoyancy flux at the source and α is the top hat entrainment coefficient. N is the ambient buoyancy frequency and is defined as

$$N = \sqrt{-\frac{g}{\rho_0}\frac{d\rho_e}{dz}}, \tag{3.4}$$

where $d\rho_e/dz$ is the ambient density gradient.

Mirajkar et al. (2015) utilised an empirical method to alter (3.3) through the use of additional constants to fit their experimental data. However, their B_0 terms excluded the negative buoyancy contributed by the particles in the plume at the source and they also considered the influence of particle settling velocity even though this remained constant throughout their experiments. Sutherland and Hong (2016) similarly fitted their results for intrusion height, z_s, empirically, however, due to having a relatively large momentum flux at the source, M_0, they classified their flows as forced plumes and presented their results as

$$\frac{z_s}{L_m} = f(\sigma), \tag{3.5}$$

where $\sigma = (M_0 N/B_0)^2$, a dimensionless parameter representing the balance between plume rise height ($z_m \sim (B_0/N^3)^{1/4}$) and momentum jet-length, $L_m = (M_0^3/B_0^2)^{1/4}$ (Kaye, 2008). Initially introduced by Morton (1959) and subsequently utilised by a number of authors including Fischer et al. (1979) and Bloomfield and Kerr (1998), σ allows forced flows to be compared to those with zero momentum at the source. Specifically, when σ is small, buoyancy forces drive the flow's motion once the influence of stratification becomes important. Conversely, momentum forces dominate when σ is large, note however that the definition of large varies between $\sigma > 1$ (Fischer et al., 1979) and $\sigma > 49$ (Richards et al., 2014).

A second important parameter to compare forced and pure plumes is the scaled source Richardson number,

$$\Gamma_0 = \frac{5}{8\alpha\pi^{1/2}}\frac{{Q_0}^2 B_0}{{M_0}^{5/2}}. \tag{3.6}$$

Having been utilised in various experimental and theoretical works concerning both single-phase and particle-laden plumes (Balasubramanian et al., 2018; Hunt and Kaye, 2001; Mehaddi et al., 2013), Γ_0 allows the plume to be classified as pure ($\Gamma_0 = 1$), lazy ($\Gamma > 1$) or forced ($\Gamma_0 < 1$), irrespective of the presence of an ambient density gradient.

In a recent theoretical study by Apsley and Lane-Serff (2019), a method of predicting the steady-state rise height of a pure particle-laden plume ($\sigma = 0, \Gamma = 1$) was proposed, along with an associated collapse criterion based upon the ratio of the particle and fluid buoyancy flux components present at the source,

$$P = \frac{-B_{0,p}}{B_{0,f}} \approx \frac{\phi_0(\rho_p - \rho_0)}{(\rho_0 - \rho_f)}. \tag{3.7}$$

This theory was developed assuming that the plume maintains a defined veil of particles and each individual particle follows a trajectory associated only with the particle settling velocity and the inward radial velocity produced by plume entrainment. Although a suitable assumption for dilute plumes, particle trajectory is expected to be influenced by convective instabilities in plumes with significant particle loading at the source.

Authors of a number of experimental studies considering the behaviour of unstratified particle-laden plumes (Cardoso and Zarrebini, 2001a; Carey et al., 1988; Veitch and Woods, 2000) found that flows with high particle concentrations at the source tended to be unstable, and in some cases produced downward currents in the environment. Specifically, Veitch and Woods (2000), the authors who introduced equation (3.7) into the literature, described the narrowing of the particle veil due to the presence of a counter-flowing collar of dense fluid around the plume for source buoyancy flux ratios greater than $P = 0.19$. This value is significantly less than the critical ratio of $P_c = e^{-1} (\approx 0.368)$ which Apsley and Lane-Serff (2019) proposed for the collapse (i.e. $z_m \approx 0$) of a pure particle-laden plume. Additionally, direct sampling of the particle concentration in the environment below a surface intrusion of a highly concentrated particle-laden plume showed that ambient convection was sufficient such that the environment became fully mixed with a particle concentration independent of height (Cardoso and Zarrebini, 2001a).

Similar observations have been made in stratified plumes. In both Mirajkar et al. (2015) and Balasubramanian et al. (2018), although not specifically stated by the authors, convection appears to be present in the environment surrounding the plume resulting in the production of a trough of plume fluid and particles below the intrusion, which under some conditions fully collapses to the base of the tank (see Figure 8, Mirajkar et al. (2015); and Figure 4, Balasubramanian et al. (2018)). Another interesting observation in both pieces of work is the development of a secondary intrusion between the original current and the source, yet in neither of their papers do the authors describe the physics leading to its development. In the concluding remarks of Mingotti and Woods (2020), the authors specifically state that further work

is required to understand the influence of convective sedimentation on the dynamics of a stratified particle-laden plume.

In this paper, an attempt to further this understanding has been made by determining the transition point of a stratified particle-laden plume from undergoing dilute behaviour to one influenced by the presence of ambient convection. A criterion for the onset of convection at the edge of the plume has been developed, which when combined with the source buoyancy flux ratio and the individual particle settling velocity, can be used to characterise a total of five steady-state flow regimes. The dynamics of each regime are qualitatively described and the respective plume heights are compared to models currently published within the literature.

3.3 Experimental methods

Particle-laden plume experiments were conducted in the laboratory through injecting a mixture of fresh water and particles into an acrylic tank with dimensions 69 cm x 69 cm x 50 cm. The tank was filled with aqueous saline solution to a height of 40 cm and a linear stratification was produced using the double-bucket method (Oster and Yamamoto, 1963). The strength of the density gradient created in each experiment is characterised using the ambient buoyancy frequency N.

The plume fluid was supplied to an upwards directed nozzle with an internal diameter of $d_n = 6$ mm. This nozzle was connected to a stirred vessel, placed at a height approximately 1 m above the nozzle, and was used to suspend the particles in fresh water. Acid Red 1 (Azophloxine) dye was added to the plume fluid to assist with plume visualisation, and an LED light sheet was placed outside the tank, directly behind the plume to provide an even distribution of light when viewing experiments.

Experimental conditions are provided in Table 3.1 and were designed so that plume dynamics could be observed for a range of source buoyancy flux ratios (P), whilst also varying source forcing and ambient stratification strength to give plume parameters between the values of $10^{-3} < \Gamma_0 < 10^{-1}$ and $0 < \sigma < 10$. Such parameter selection resulted in jet-length to plume rise height ratios between approximately $2 < z_m/L_m < 8$.

Particle-laden plumes, in theory, can be produced with P up to a value of 1 before becoming neutrally buoyant, however, in the case of these experiments, a range of $0 < P < 0.8$ was achieved. This experimental limitation was a result of attempting to limit $\sigma < 10$ with a source buoyancy flux which diminishes with increases in P, whilst also attempting to achieve an appropriate spreading height within the tank. In addition to this, the plume feed nozzle began to block for source particle

volume fractions exceeding 1.2%. Note that many of the experiments presented here have source conditions exceeding the critical buoyancy flux ratio for plume collapse $P_c = e^{-1}$, however this theoretical value refers to plumes rising from virtual point sources of buoyancy whereas the flows studied here are forced with non-zero volume and momentum fluxes.

A source flowrate between $Q_0 \approx 3-7\,\mathrm{cm^3 s^{-1}}$ was supplied to the nozzle using a peristaltic pump. The change in height of the stirred feed vessel over a known time was used to determine the exact flowrate and momentum flux ($M_0 = 4Q_0^2/\pi d_n^2$) for each individual experiment. The flow was observed to be turbulent no more than 2 cm above the plume nozzle with source Reynolds numbers between 700 and 1700. These values are of similar magnitude to previous turbulent plume studies (Carazzo et al., 2006). The source buoyancy flux, $B_0 = B_{0,f} + B_{0,p}$, was calculated using source values of volume flux (Q_0), particle volume fraction (ϕ_0) and a reference density, ρ_0, equivalent to the ambient density at the plume source. In all experiments, the positive buoyancy created by the density deficit between the fluid in the plume and the ambient fluid at the source ($B_{0,f}$) exceeded the negative buoyancy associated with the dense particles dispersed in the flow ($B_{0,p}$). Here, it is worth noting that the effective density of the particle-laden plumes in this study, defined as $\rho_{plume} = \phi_0\rho_p + (1-\phi_0)\rho_f$, were of a similar order of magnitude to the density of the environment, with the ratio of ρ_{plume}/ρ_0 exceeding 97.5% in all cases. As such, the resultant flow is Boussinesq with density effects being negligible except in the case of forces arising due to buoyancy.

Particle settling was assumed to follow Stokes law with the terminal particle velocity, u_{st}, defined as

$$u_{st} = \frac{g(\rho_p - \rho_0)d_p^2}{18\mu}, \tag{3.8}$$

where d_p is the particle diameter and $\mu = 8.9 \times 10^{-3}\,\mathrm{gcm^{-1}s^{-1}}$ is the dynamic viscosity of the ambient fluid. Three different types of monodisperse particles were used to achieve the range of settling speeds detailed in Table 3.1. The upper and lower velocities of $0.92\,\mathrm{cms^{-1}}$ and $0.45\,\mathrm{cms^{-1}}$ are associated with two sets of glass ballotini ($\rho_p = 2.5\,\mathrm{gcm^{-3}}$), each with average particle diameters of 100 μm and 70 μm. The third particle set, 70 μm silicon carbide particles ($\rho_p = 3.2\,\mathrm{gcm^{-3}}$), was used to achieve the intermediate velocity of $u_{st} \approx 0.64\,\mathrm{cms^{-1}}$. In all cases, the source buoyancy flux was sufficiently large such that the characteristic plume velocity, $(B_0 N)^{1/4}$, exceeded the particle settling velocity. This ensured all particles dispersed in the plume reached the maximum height, before spreading radially with the intrusion (Ernst et al., 1996).

Exp	u_{st} (cms^{-1})	Q_0 ($\mathrm{cm}^3\mathrm{s}^{-1}$)	M_0 ($\mathrm{cm}^4\mathrm{s}^{-2}$)	ϕ_0 (%)	B_0 ($\mathrm{cm}^4\mathrm{s}^{-3}$)	P (−)	Γ_0 ($-\times10^{-2}$)	N (s^{-1})	σ (−)
1	0.92	6.05	130	0.02	20.7	0.08	0.76	0.30	3.48
2	0.92	6.05	129	0.09	17.2	0.31	0.64	0.33	6.10
6	0.92	5.78	118	0.11	37.2	0.20	1.57	0.39	1.53
7	0.92	5.56	109	0.09	44.7	0.14	2.12	0.38	0.88
9	0.92	5.82	120	0.19	41.6	0.28	1.73	0.32	0.85
10	0.92	6.29	140	0.34	30.6	0.50	1.00	0.39	3.14
11	0.92	5.31	99.6	0.41	48.3	0.39	2.64	0.65	1.82
12	0.92	6.14	133	0.50	82.1	0.35	2.89	0.44	0.52
14	0.92	5.96	125	0.51	83.0	0.34	3.20	0.77	1.37
15	0.92	6.06	130	0.93	57.3	0.58	2.10	0.82	3.45
17	0.92	6.46	148	0.91	72.9	0.53	2.21	0.49	0.97
18	0.92	2.97	31.2	0.67	45.1	0.38	14.0	0.80	0.31
20	0.92	5.87	122	1.06	40.3	0.69	1.63	0.61	3.45
21	0.92	6.17	135	1.11	58.7	0.62	2.04	0.46	1.13
22	0.92	2.97	31.2	1.08	30.4	0.60	9.44	0.50	0.26
24	0.92	2.96	31.1	0.70	9.61	0.76	3.01	0.21	0.45
26	0.92	3.07	33.3	1.20	18.2	0.74	5.15	0.60	1.20
27	0.92	5.98	127	1.00	74.2	0.53	2.82	0.41	0.49
28	0.92	5.92	124	0.50	135	0.24	5.32	0.61	0.31
29	0.92	6.91	169	0.91	130	0.40	3.21	0.61	0.62
34	0.64	5.98	126	0.02	15.4	0.15	0.59	0.30	6.15
35	0.64	6.16	134	0.10	41.3	0.25	1.44	0.48	2.42
36	0.64	5.98	126	0.05	63.6	0.09	2.43	0.59	1.40
37	0.64	5.95	125	0.43	32.0	0.63	1.24	0.60	5.57
38	0.64	5.87	122	0.33	49.2	0.45	1.98	0.64	2.50
39	0.64	5.72	116	0.24	82.6	0.26	3.59	0.52	0.53
40	0.64	5.93	124	0.48	45.4	0.57	1.77	0.44	1.48
41	0.64	3.06	33.2	0.19	50.7	0.19	14.4	0.66	0.19
42	0.64	3.07	33.4	0.55	31.7	0.53	8.90	0.54	0.32
43	0.64	3.04	32.6	0.35	38.0	0.37	11.1	0.48	0.17
44	0.64	5.97	126	0.41	99.3	0.34	3.80	0.72	0.84
45	0.64	3.06	33.0	1.16	37.7	0.66	10.8	0.75	0.43
46	0.64	3.03	32.4	0.71	14.1	0.76	4.15	0.64	2.19
47	0.64	3.03	32.4	0.85	31.2	0.63	9.17	0.37	0.15
48	0.64	6.03	129	0.92	125	0.47	4.64	0.83	0.74
49	0.45	6.03	129	0.13	13.7	0.46	0.51	0.27	6.25
51	0.45	6.00	128	0.12	25.9	0.28	0.97	0.39	3.77
52	0.45	6.06	130	0.06	28.1	0.15	1.03	0.32	2.21
53	0.45	6.09	131	0.33	106	0.21	3.83	0.79	0.96
54	0.45	6.00	128	0.04	62.5	0.05	2.35	0.39	0.64
55	0.45	6.05	130	0.47	60.9	0.40	2.24	0.48	1.05
56	0.45	5.95	125	0.72	56.9	0.52	2.20	0.62	1.87
57	0.45	3.01	32.1	0.67	34.5	0.45	10.3	0.70	0.42
58	0.45	5.94	125	1.00	56.9	0.60	2.21	0.36	0.63
59	0.45	5.98	127	1.10	31.3	0.75	1.19	0.60	5.89
60	0.45	5.93	125	1.14	43.2	0.69	1.69	0.48	1.90
61	0.45	3.18	35.7	0.50	58.9	0.28	15.0	0.70	0.18
62	0.45	2.98	31.4	1.00	37.1	0.53	11.4	0.50	0.18
64	0.45	3.02	32.3	0.85	16.0	0.70	4.72	0.26	0.28
65	0.45	6.06	130	0.26	149	0.13	5.44	0.67	0.34

Table 3.1 List of experimental parameters

Experiments were captured using a Nikon D300s camera, fitted with an AF-S Micro NIKKOR 60 mm f/2.8G ED lens. For each experiment, the camera was placed on a 1.2 m high tripod approximately 2.5 m from the experimental tank. During the first 10 minutes of plume injection (the maximum time to achieve steady state), videos with a frame rate of 24 Hz were taken for post-experimental analysis. Such analysis was completed using MATLAB R2020B and included the determination of the maximum and spreading heights of each plume, as well as the plume volume flux at the spreading level, Q_s, by measuring the evolution of intrusion volume over time (Sigurðardóttir et al., 2020). After the 10-minute filming period, samples of plume fluid were taken near the top of the plume. The particles in these samples were washed and then dried to estimate the particle concentration at the plume spreading height. This method was determined to be accurate within $\pm 10\%$ by sampling a well-mixed tank with a known particle concentration.

All experimental measurements and other useful variables determined from image analysis are provided in the supplementary material (found at https://doi.org/10.17863/CAM.64736).

3.4 Qualitative experimental observations

In all experiments, the early behaviour of each plume was very similar. Upon initial release into the tank, each plume rose vertically from the nozzle and was observed to be turbulent and conical in shape. Within seconds, the plume reaches a maximum height before collapsing upon itself and spreading radially as a gravity current at the height of neutral buoyancy. The particles present within the plume initially spread with the current before decoupling from the radial flow and settling into the environment. After this initial stage of plume injection, the flow dynamics evolve due to the re-entrainment of particles. In some cases when viewing the plume, the dynamics remained very similar throughout the experiment with all the particles following a clear trajectory from the base of the intrusion to the edge of the plume. In other experiments, the environment around the plume appeared to be undergoing convection with particles moving erratically within a column of convecting fluid.

As shown visually in Figure 3.1, the steady-state behaviour of a particle-laden plume is observed to be very dependent upon whether the particles settle in the environment individually at their Stokes velocity u_{st}, or whether particle trajectory is dictated by an ambient convective velocity associated with particle-induced instabilities. In an unstratified environment, Cardoso and Zarrebini (2001a) determined a criterion for the

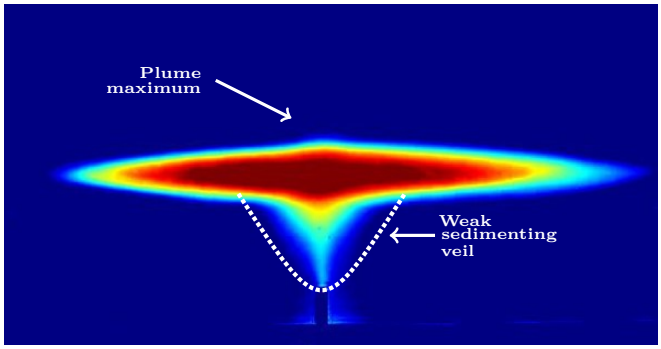

(a)

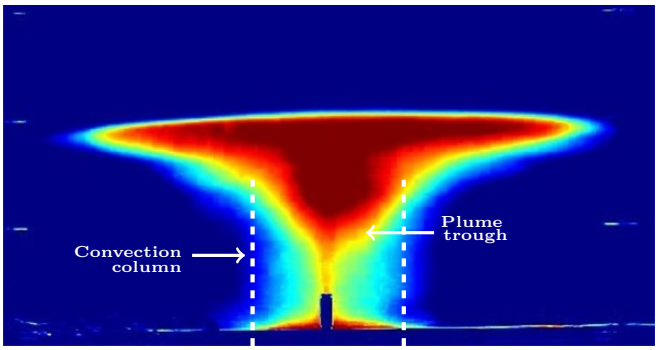

(b)

Fig. 3.1 False colour experimental images produced using MATLAB R2020B to aid in the identification of plume regimes. Images were time-averaged over 120 seconds once steady state was achieved. Navy and maroon represent maximum and minimum values of light intensity. (a) Experiment 11, quiescent at steady state. Weak sedimenting veil and plume maximum visible. (b) Experiment 55, undergoing convection at steady state. Both the convection column and the plume trough are clearly visible.

onset of convection based upon the ambient convective velocity, U_c. They determined this velocity to be a function of the particle concentration gradient present beneath the plume's surface current, represented by $d\phi/dz$, and proposed the scaling,

$$U_c \sim \left(\rho_p \frac{d\phi}{dz}\right)^{1/4}. \tag{3.9}$$

In an attempt to characterise these qualitative observations into defined flow regimes, it is assumed that when the environment around the plume is still and the particles are settling at a terminal velocity, $u_{st} > U_c$. Conversely, when the environment is undergoing convection and the particle trajectory is controlled by fluid motion, $u_{st} < U_c$. Using this *a priori* assumption, along with the buoyancy flux ratio P (for

consistency with previous work qualitatively evaluating the dynamics of particle-laden plumes, specifically Veitch and Woods, 2000), five flow regimes are characterised. These regimes include Type 1 and 1* plumes, where individual particles settle in the environment at a terminal sedimentation velocity ($U_c/u_{st} < 1$); transitional Type 2 plumes, where both individual particle settling and ambient convection appear to be present ($U_c/u_{st} \approx 1$); and Type 3 plumes, where particle settling is driven by ambient convection ($U_c/u_{st} > 1$), which in some cases, leads to the development of secondary intrusions (Type 3*, $U_c/u_{st} \gg 1$). Descriptions of the specific dynamics unique to each regime, along with illustrations and photographs of each plume type, are presented in the subsequent paragraphs.

3.4.1 Type 1 plumes: $U_c/u_{st} < 1$ and $P > 0.2$

In a Type 1 plume, the terminal settling velocity of the particles exceeds the ambient convective velocity associated with particle-induced instabilities. As predicted by Apsley and Lane-Serff (2019), the buoyancy flux ratio has a significant impact upon the steady-state height of plumes where $u_{st} > U_c$. When particle buoyancy at the source is very small compared to the buoyancy of the fluid, the plume silhouette at steady state is representative of a stratified single-phase plume. A defined plume maximum remains present above the spreading intrusion and the particles flow radially in the gravity current before settling into the ambient fluid below.

At steady state, the flux of particles in the intrusion beyond the critical re-entrainment radius (Sparks et al., 1991) is equivalent to the particle flux at the source. Any particles settling from the intrusion within this critical radius are re-entrained into the plume, and from both experimental measurements (see Figure 3.3) and previous theoretical predictions (Veitch and Woods, 2000; Zarrebini and Cardoso, 2000), this results in a particle concentration at the spreading level e^1 times greater than if there was no re-entrainment. Even with this multiplier, the concentration of particles in plumes within this regime is so small that re-entrainment has very little influence on the steady-state plume maximum.

3.4.2 Type 1* plumes: $U_c/u_{st} < 1$ and $P > 0.2$ when $\sigma \ll 1$

Type 1* is very similar to its predecessor, however, particle recycling results in a significant decrease in maximum height until a steady state is achieved either within

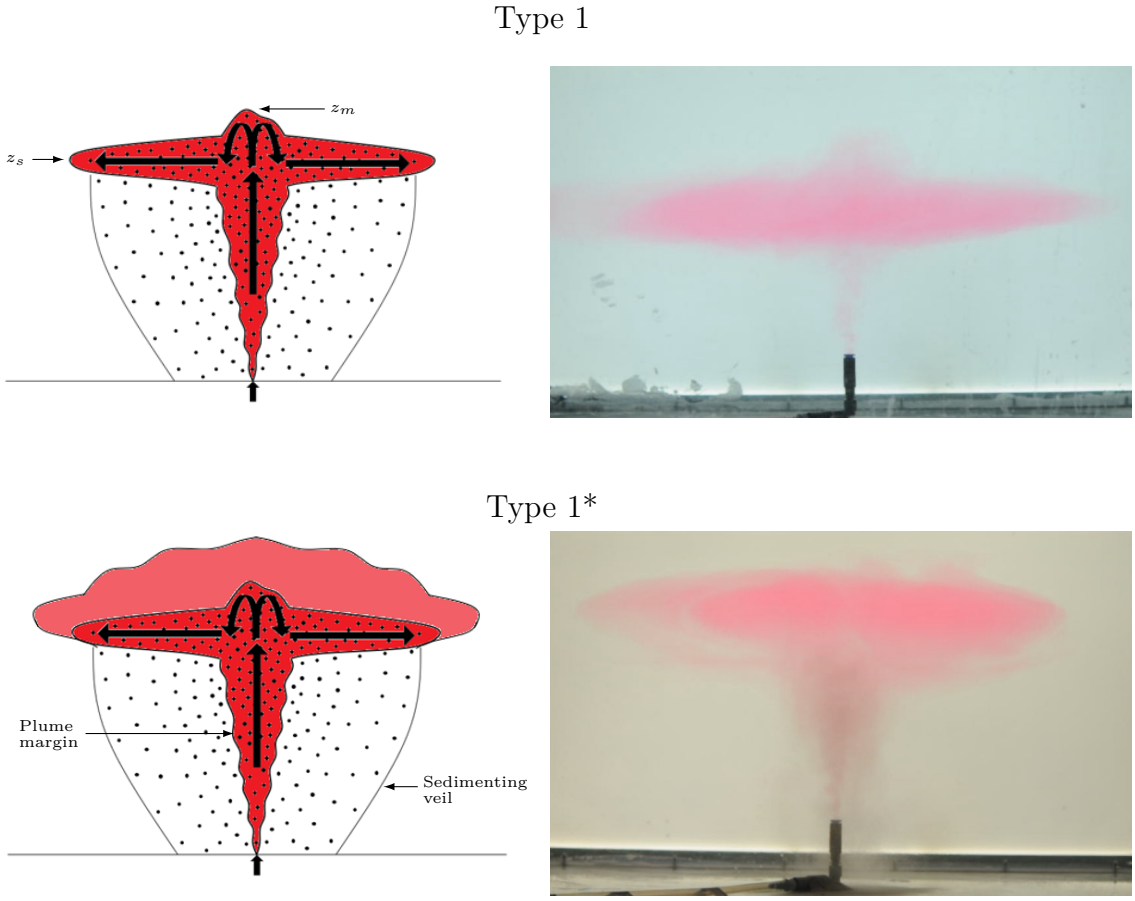

Fig. 3.2 Illustrations and photographs (taken at ≈ 300 s) of Type 1/1* plumes. Photographs shown are experiment 54 (Type 1); and experiment 12 (Type 1*).

or below the original intrusion. The 'single-phase' silhouette described for Type 1 begins to disappear for source buoyancy flux ratios of $P > 0.2$ for plumes with negligible momentum at the source (i.e. $\sigma \ll 1$). Although suitable for pure plumes, the transitional value of $P > 0.2$ is very dependent upon the level of forcing at the source as non-zero volume and momentum fluxes will increase this value due to the additional entrainment of ambient fluid both at the plume margins and in the descending fountain at the plume maximum (see Figure 10 in Apsley and Lane-Serff, 2019). To fully characterise this regime for plumes rising from non-idealised sources, a forced plume equivalent of the model derived by Apsley and Lane-Serff (2019) would need to be developed and this is outside of the scope of this current study.

Although the plume height decreases, the general behaviour of the plume remains consistent. The intrusion spreads below the plume maximum and a sedimenting veil can be observed around the plume. Notably, the measurements presented in Figure

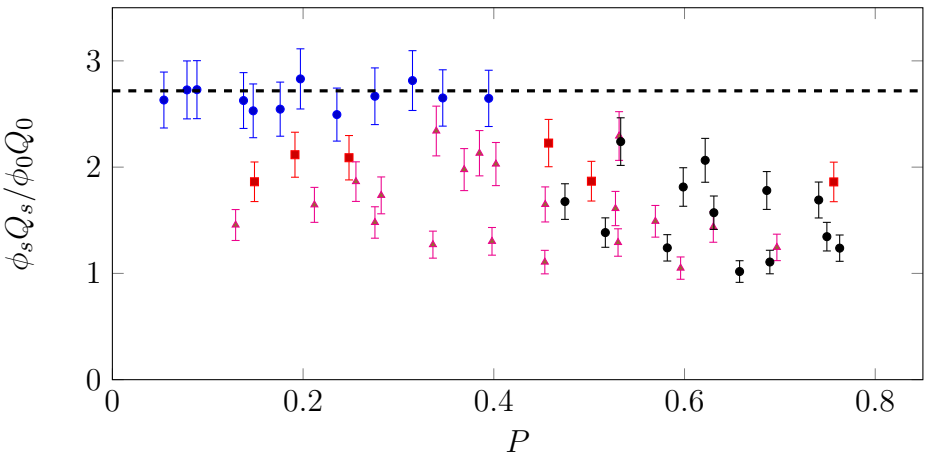

Fig. 3.3 The ratio of the particle flux at the spreading level to the plume source against the buoyancy flux ratio, P. The y axis presents the coefficient associated with the re-entrainment of particles into the plume at steady state which, when no ambient convection is present, is expected to be equivalent to e^1 (presented as the dotted line). The particle concentration at the spreading height of Type 1/1* (•) plumes aligns with the predicted value, however all plumes (Type 2 ▪, Type 3 ▲, and Type 3* •) where convection is present appear to re-entrain less particles.

3.3 for both regimes with plumes rising through quiescent environments (Type 1/1*) suggest that the intrusions are well mixed with a particle concentration which decays exponentially with radius (Sparks et al., 1991).

Over time, the trajectory of the particles in the environment remains relatively unchanged, however the position of fluid in the intrusion does not. Due to the changing plume height, a defined intrusion, like one would observe in a single-phase plume, is not present as the spreading height decreases until reaching a new steady state. Also, in some instances after the particles have settled into the environment below, the fluid in the intrusion rises to a new height of neutral buoyancy, as observed by Mingotti and Woods (2020). This phenomenon was particularly evident in weakly stratified experiments with a large flux of particles at the source i.e. large $Q_0\phi_0$ and small N.

3.4.3 Type 2 plumes: $U_c/u_{st} \approx 1$, independent of P

Within this regime, the convective velocity in the environment below the plume intrusion is assumed to be approximately equivalent to the settling velocity of each individual particle. The particles remain dispersed in the plume intrusion before settling into the environment below. A sedimenting veil is present and the majority of the particles

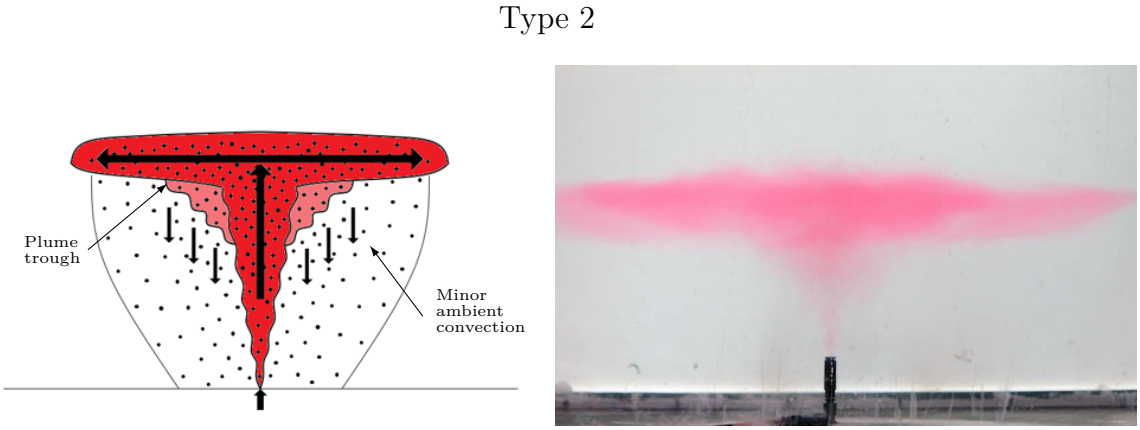

Fig. 3.4 Illustrations and photographs (taken at ≈ 300 s) of a Type 2 plume. Photograph shown is experiment 10.

appear to settle according to their terminal velocity. However, in some portions of the veil, minor convection can be seen as well as the presence of a small parabolic cloud of dyed fluid directly below the intrusion. Previous authors referred to this phenomenon as the plume trough (Balasubramanian et al., 2018; Mirajkar et al., 2015). The plume trough appears close to the plume edge and is created by the large, localised flux of sedimenting particles dragging the lighter interstitial plume fluid from the intrusion into the ambient fluid below.

An assessment of Figure 3.3 shows a reduction in particle re-entrainment compared to Type 1/1* plumes for not only Type 2 flows, but all those rising in the presence of ambient convection. This suggests either a change in the intrusion's distribution of particles or more likely, a change in the particle trajectory from the intrusion to the plume margin. Unlike in particle-laden plumes rising through unstratified environments (see Veitch and Woods, 2000), the lack of trend in Figure 3.3 shows that the buoyancy flux ratio at the source has little to no influence on the development of the plume trough or any other convective instabilities occurring within the sedimenting veil.

3.4.4 Type 3 plumes: $U_c/u_{st} > 1$, independent of P

Once ambient convection overcomes the settling of individual particles, an obvious transition in dynamics occurs. After a period of re-entrainment similar to the previous regimes, the particle concentration at the top of the plume reaches some threshold which subsequently causes the particles dispersed in the gravity current to decouple from the intrusion fluid close to the edge of the plume. This decoupling is followed by

packets of highly concentrated particle-laden ambient fluid settling towards the base of the tank at speeds significantly greater than the individual particle's Stokes velocity.

This localised settling creates a column of convecting ambient fluid around the plume between the intrusion and the tank floor, similar to the annulus of fluid and particles observed for plumes with source loading exceeding $P \approx 0.20$ in a uniform environment (Veitch and Woods, 2000). Although a specific value for transition was noted in the unstratified case, as previously noted for Type 2 plumes, no specific threshold of buoyancy flux ratio was observed to achieve $u_{st} < U_c$ across the three different settling speeds presented in this study. Upon reaching the tank base, the particles in the convection column deposit onto the floor and the once particle-laden fluid slightly rises back up in the stratified environment. In the convection zone, the plume trough remains present below the intrusion and very small portions of dyed fluid are dragged down into the convection column.

The steady-state plume heights are less than what would be observed in a single-phase plume, yet due to the change in particle trajectory associated with the transition from sedimenting veil to convection column, the model assumptions of Apsley and Lane-Serff (2019) no longer hold. The decoupling of the solid and fluid phases also more obviously shows the light interstitial fluid in the intrusion rising and spreading at a new neutral buoyancy height above the original current.

3.4.5 Type 3* plumes: $U_c/u_{st} \gg 1$, independent of P

When the particle concentration at the spreading level is very large, convection at the edge of the plume becomes so great that dyed plume fluid is dragged down from the maximum plume height to the base of the tank, mixing with the ambient fluid below to create a flow reminiscent of a stratified single-phase fountain (Bloomfield and Kerr, 1998). Although no association to a fountain was made, Balasubramanian et al. (2018) also observed that particles in the intrusion of plumes with high source concentrations drag down plume fluid from the intrusion to the plume source. These authors compare the radius of the trough to an altered version of the critical re-entrainment radius; however such a comparison is not suitable as the particle trajectory is governed by the fluid motion instead of the individual particle settling speed.

As the downflow reaches the base of the tank, a particle-laden gravity current can be seen spreading radially away from the nozzle. As in previous particle-laden current experiments (Woods and Bursik, 1994), the gravity current becomes buoyant following the deposition of the particles onto the tank floor and can then be seen to rise into the stratified environment. This dyed fluid reaches a neutrally buoyant

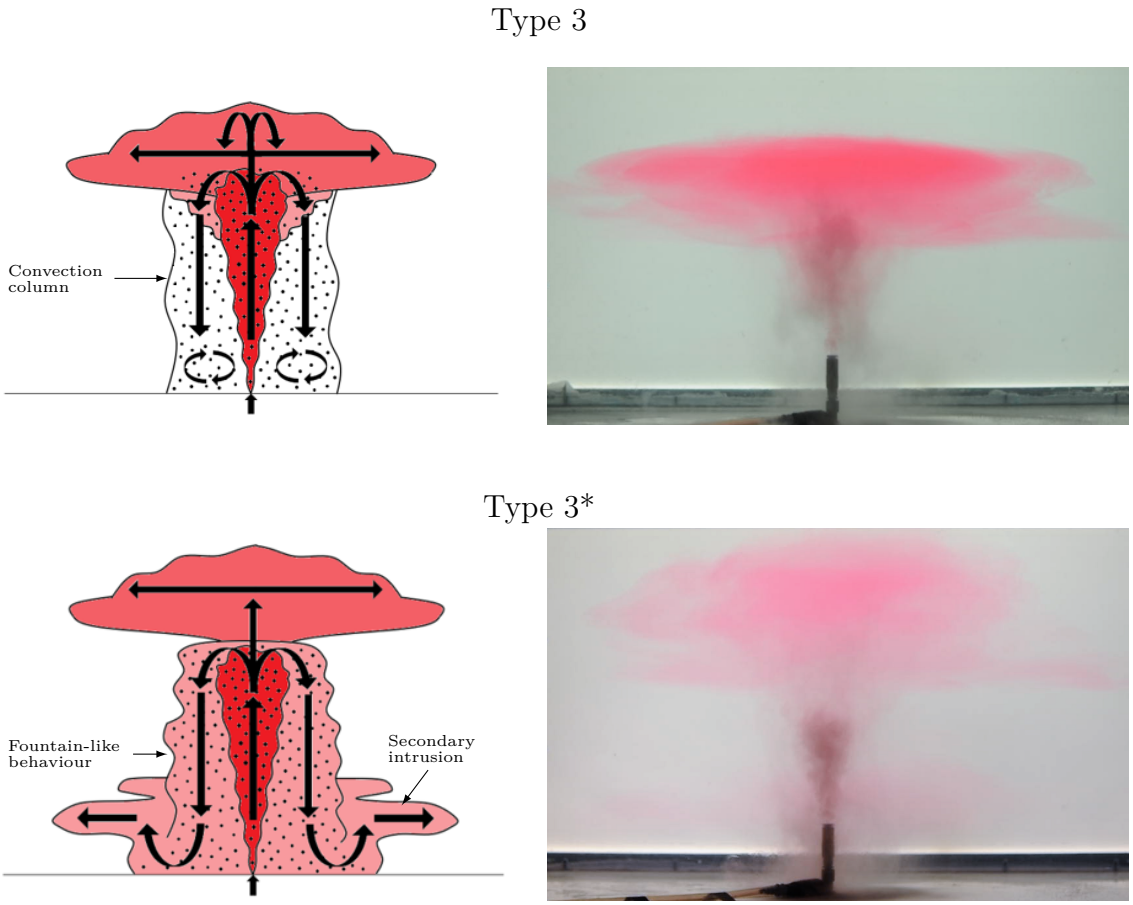

Fig. 3.5 Illustrations and photographs (taken at ≈ 300 s) of Type 3/3* plumes. Photographs shown are experiment 29 (Type 3); and experiment 21 (Type 3*).

height and then spreads between the main current and the base of the tank as a secondary intrusion, as observed previously in other stratified particle-laden plume experiments (Balasubramanian et al., 2018; Mirajkar et al., 2015). In addition to observing fountain-like flow behaviour, buoyant fluid can be seen to rise from the main intrusion to spread as a new intrusion above the original current (as has been observed in other regimes).

At this qualitative stage of the study, the transition from Type 3 to 3* behaviour is somewhat ambiguous other than expecting larger convective velocities to be present in the environment around Type 3* plumes. In an attempt to address this, quantitative detail on this flow transition is presented and discussed in section 3.5.1.

3.5 Criterion for the onset of ambient convection

Experimental observations show that within the environment near the edge of a Type 3 (and 3*) plume, parcels of particle-laden fluid can be seen settling around the plume at speeds much greater than the settling velocity of each individual particle. This convection is confined to a defined radius around the plume, suggesting that the unstable stratification produced by the presence of particles in the environment below the gravity current is directly associated with the intrusion particle concentration; a concentration which decays exponentially away from the edge of the plume (Sparks et al., 1991).

Given that the convection observed is a result of a Rayleigh-Taylor instability, created by a denser fluid-particle suspension lying above lighter particle-free fluid, it is likely that the velocity of the convective front will change in time, firstly accelerating downwards before decelerating due to the ambient stratification (Lawrie and Dalziel, 2011). Rather than capturing these time and position dependent complexities, it is of more interest to simply determine the plume conditions required for the onset of ambient convection such that the steady-state flow regime may be predicted.

In their study on particle-laden plumes in a uniform environment, Cardoso and Zarrebini (2001a) utilised a scaling approach to estimate the magnitude of the ambient convective velocity, the scaling of which is presented in (3.9). The full equation they derived is written as

$$U_c \approx \left(\frac{Gr_c g \nu^2}{\rho_0}\right)^{1/4} \left(\rho_p \frac{d\phi}{dz}\right)^{1/4}, \tag{3.10}$$

where ν is the kinematic viscosity of the fluid-particle suspension; and Gr_c is the critical Grashof number, a dimensionless parameter analogous to the Reynolds number for natural convection; defined as

$$Gr_c = \frac{g'_s L_c^3}{\nu^2} = \frac{g \rho_p L_c^4}{\rho_0 \nu^2} \frac{d\phi}{dz}, \tag{3.11}$$

where $g'_s = g\Delta\rho_s/\rho_0$ is the reduced gravity of the fluid-particle suspension with $\Delta\rho_s$ representing the density difference between the suspension and the ambient; and L_c as the convection length scale.

Cardoso and Zarrebini (2001a) determined $d\phi/dz$ numerically through solving a set of differential equations, however, a simple extension to their analysis allows the gradient to be determined analytically. Here, it is proposed that the density gradient

resulting in ambient convection is solely due to the presence of particles in the gravity current, and that the gradient can be determined through the combination of the radial change of intrusion particle concentration, $d\phi/dr$, and the expected trajectory of particles in the environment prior to the onset of convection, dr/dz, both of which are well defined within the literature. Sparks et al. (1991) determined the change in gravity current particle concentration with radial position as

$$\frac{d\phi}{dr} = \left(\frac{2\phi_s \pi u_{st} r}{Q_s}\right) \exp\left[\frac{-\pi u_{st}(r^2 - {b_s}^2)}{Q_s}\right], \tag{3.12}$$

where r is the radial position along the intrusion and ϕ_s, b_s and Q_s are the particle volume fraction, plume radius and volume flux at the spreading height. Equation (3.12) assumes that the intrusion is well mixed and based upon experimental measurements of particle re-entrainment in quiescent plumes (see Figure 3.3) and also the successful comparison of these experiments to the theory of Apsley and Lane-Serff (2019) (see Figure 3.9), the utilisation of this model here is reasonable.

Particle trajectory in the environment around the plume can be written as (Apsley and Lane-Serff, 2019; Zarrebini and Cardoso, 2000)

$$\frac{dr}{dz} = \frac{-u_e}{u_{st}} = \frac{b\alpha\omega}{u_{st} r}, \tag{3.13}$$

where u_e is the entrainment velocity and ω is the plume velocity. Using (3.12), (3.13) and the fact that $Q_s = \pi {b_s}^2 \omega$, the analytical expression for the particle concentration gradient present below the plume intrusion may be written as

$$\frac{d\phi}{dz} = \frac{d\phi}{dr}\frac{dr}{dz} = \left(\frac{2\alpha\phi_s}{b_s}\right) \exp\left[\frac{-\pi u_{st}(r^2 - {b_s}^2)}{Q_s}\right]. \tag{3.14}$$

As interest lies in determining the transition of plume regime between individual particle settling ($u_{st} > U_c$) and convective settling ($u_{st} < U_c$) in the environment at the edge of the plume, the intrusion radius is set as $r = b_s$ before substituting (3.14) into (3.10) to give

$$U_c \approx \left(\frac{G r_c g \nu^2}{\rho_0}\right)^{1/4} \left(\frac{2\alpha\rho_p\phi_s}{b_s}\right)^{1/4}. \tag{3.15}$$

In this form, equation (3.15) is suitable to determine the convective velocity in the environment at the edge of the plume and, for a known particle settling velocity,

can be used as the criterion for determining the transition of settling behaviour in particle-laden plumes. Although a distant similarity can been seen between (3.15) and (3.10), it is worthwhile utilising the definition of Gr_c to recast equation (3.15) such that any inferred dependence on ν may be eliminated. Upon substituting (3.11) into (3.15), after some rearrangement, a dimensionless form of U_c may be presented as

$$\frac{U_c}{\left(\dfrac{gL_c^4N_s^2}{b_s}\right)^{1/4}} \approx \left(\frac{2\alpha\rho_p\phi_s}{\rho_0}\right)^{1/4}, \tag{3.16}$$

where $N_s = (g\rho_p d\phi/\rho_0 dz)^{1/2}$ is the buoyancy frequency associated with the particle concentration gradient below the intrusion.

3.5.1 Regime diagram

Experimental measurements of α (determined using the bulk parameter method; see section 3.6 and Appendix C.1) and b_s were input into equation (3.15), the criterion for the onset of convection at the edge of the plume (see Table 3.2 for associated values). It is important to note that the values of b_s presented were estimated from image analysis in the early stages of plume injection, at the height associated with the steady-state plume intrusion (see Appendix B). The reasoning for this is because the development of the sedimenting veil and plume trough tended to obscure the view of the plume at this height, making exact measurements of this radius at steady state particularly difficult. Due to the approach taken, the plume radius presented is likely not the exact radius of the plume at this steady-state height as there will likely be some evolution between these initial stages and the final steady-state value. Importantly though, the ambient convective velocity and plume radius scales as $U_c \sim b_s^{-1/4}$, thus even a 25% difference between the radius estimates and actual radius will only result in a 6% difference between the predicted values of U_c. In regard to the particle concentration at the spreading level, for consistency across all experiments, a Type 1/1* spreading level particle concentration of $\phi_s = Q_0\phi_0 e^1/Q_s$ was assumed and used in (3.15). In Figure 3.6, u_{st} is plotted against U_c and shows that the regimes can be suitably separated when using a critical Grashof number of $Gr_c = 2.2 \times 10^4 \pm 1 \times 10^4$, for $\rho_0 = 1\,\mathrm{gcm}^{-3}$ and $\nu = 8.9 \times 10^{-3}\,\mathrm{cm}^2\mathrm{s}^{-1}$. For the experiments plotted, this empirically determined value of Gr_c results in $U_c/u_{st} < 0.90$ for quiescent plumes; $U_c/u_{st} > 1.05$ for plumes undergoing ambient convection; and a range of $0.93 < U_c/u_{st} < 1.11$ for transitional Type 2 plumes.

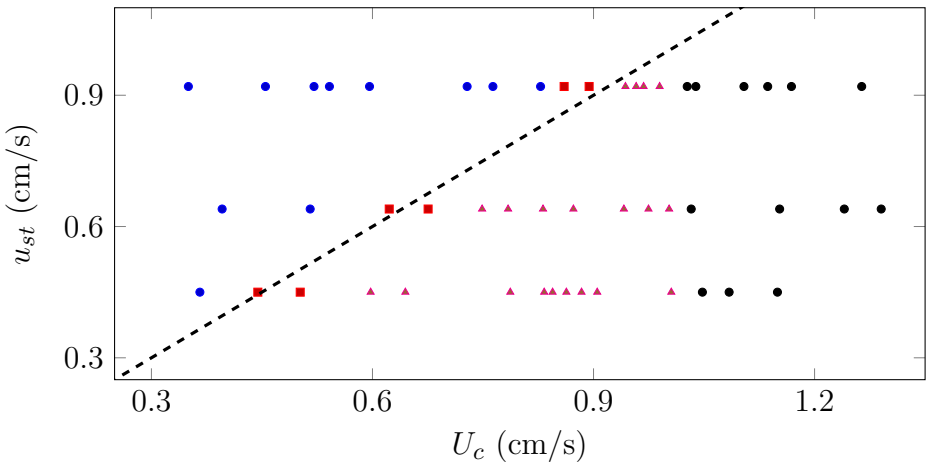

Fig. 3.6 Plume regime diagram plotting the individual particle settling velocity, u_{st}, against the ambient convective velocity, U_c. The dashed line corresponds to a critical Grashof number of $Gr_c = 2.2 \times 10^4$. Type 1/1* (•) plumes appear on the left of the plot, Type 3 (▲) and 3* (•) on the right and Type 2 (■) approximately on the dashed line.

From an assessment of (3.15), it can be seen that high dilution of the particles at the spreading level (i.e. large Q_s), along with a large plume rise height (as $z_s \sim b_s/\alpha$; Morton et al., 1956), will both strongly mitigate the development of ambient convection. Therefore, the parameters which appear to be of most importance in defining the settling regime are the particle flux at the source; the magnitude of the flow's driving force (that being B_0 for pure plumes or a combination of B_0, Q_0 and M_0 for forced plumes); and the strength of the ambient stratification N, given that both the plume spreading height and the volume flux associated with it are functions of these source and stratification parameters. Particle density ρ_p, is less significant in defining the settling regime as any increases in convective velocity owing to increases in particle density will be immediately mitigated by increases in individual particle settling speed.

An interesting observation is that the regimes can be determined from the particle-induced density gradient alone, and that the fluid density gradient appears to have no influence on the convective velocity achieved, even in cases where $d\rho_e/dz$ is large enough to result in a negative (stable) density gradient when added to the value calculated using equation (3.14). This suggests that either the local density gradient present in the ambient fluid is not important; or due to the presence of the plume trough, over the course of the experiment, the fluid directly below the intrusion may become well mixed, allowing the suspension of particles to create an unstable stratification.

Exp	b_s (cm)	Q_s (cm^3s^{-1})	α (−)	u_{st} (cms^{-1})	U_c (cms^{-1})	***Type*** (−)
1	2.2	66.9	0.080	0.92	0.34	1
2	2.3	59.1	0.064	0.92	0.51	1*
6	2.1	63.0	0.084	0.92	0.53	1
7	3.0	63.7	0.090	0.92	0.44	1
9	2.1	82.9	0.100	0.92	0.58	1
10	1.3	69.2	0.063	0.92	0.84	2
11	2.2	43.7	0.079	0.92	0.80	1*
12	3.0	100.6	0.105	0.92	0.71	1*
14	1.6	42.0	0.072	0.92	0.93	3
15	2.0	40.2	0.081	0.92	1.07	3*
17	1.7	75.9	0.093	0.92	1.00	3*
18	2.3	31.8	0.120	0.92	0.94	3
20	1.5	49.3	0.082	0.92	1.14	3*
21	1.8	74.9	0.088	0.92	1.01	3*
22	1.8	27.8	0.116	0.92	1.10	3*
24	2.0	58.4	0.118	0.92	0.87	2
26	1.3	20.4	0.070	0.92	1.23	3*
27	1.9	88.1	0.110	0.92	0.92	3
28	2.3	84.3	0.124	0.92	0.74	1*
29	1.7	78.1	0.113	0.92	0.96	3
34	2.0	60.5	0.063	0.64	0.38	1
35	1.8	57.5	0.084	0.64	0.60	2
36	1.8	54.6	0.096	0.64	0.50	1
37	1.4	42.4	0.068	0.64	0.97	3
38	2.2	44.5	0.078	0.64	0.81	3
39	1.8	71.6	0.106	0.64	0.73	3
40	2.0	56.8	0.086	0.64	0.85	3
41	2.5	41.0	0.115	0.64	0.66	2
42	1.8	34.1	0.102	0.64	0.95	3
43	2.4	42.7	0.109	0.64	0.76	3
44	1.5	50.2	0.094	0.64	0.91	3
45	1.5	24.7	0.091	0.64	1.25	3*
46	1.3	16.6	0.064	0.64	1.20	3*
47	1.5	57.2	0.125	0.64	1.00	3*
48	1.8	50.8	0.110	0.64	1.12	3*
49	3.5	65.5	0.069	0.45	0.49	2
51	1.9	53.6	0.084	0.45	0.58	3
52	2.3	69.9	0.071	0.45	0.43	2
53	2.0	48.4	0.091	0.45	0.76	3
54	3.5	88.9	0.097	0.45	0.36	1
55	1.4	66.9	0.095	0.45	0.84	3
56	1.2	47.7	0.074	0.45	1.05	3*
57	2.0	23.3	0.095	0.45	0.98	3
58	3.0	82.4	0.098	0.45	0.86	3
59	1.4	49.1	0.083	0.45	1.12	3*
60	2.0	52.0	0.063	0.45	1.02	3*
61	2.5	37.5	0.121	0.45	0.81	3
62	3.0	42.6	0.117	0.45	0.88	3
64	2.7	50.1	0.109	0.45	0.82	3
65	3.1	92.0	0.120	0.45	0.63	3

Table 3.2 List of measured and calculated parameters

Alternatively, the localised and continuous sedimentation of particles could also impact the fluid stratification as previously shown by Blanchette (2013). Using simulations, they showed that a single pass of particles settling at their Stokes velocity through a stratified environment can result in the short-term disturbance of the ambient density gradient (with regeneration occurring over a multiple of N^{-1} seconds), or in some extreme cases, can lead to the complete destruction of the fluid stratification. This work considered only isolated settling events, whereas particle settling in this study's experiments occurs continuously between the intrusion and the tank floor. Therefore, it is not unreasonable to expect that a similar disruption to the fluid density gradient could occur in the environment immediately below the intrusion over the length scale of interest.

In Figure 3.6, the transition from Type 3 to 3* plumes is observed to occur when $U_c \geq 1\ \mathrm{cms}^{-1}$, irrespective of particle settling speed. This suggests that the transition is a direct result of sufficiently strong convection pulling intrusion fluid to the plume source and one would expect that this would occur for a consistent ambient velocity, especially in the case of these experiments where the intrusion heights above the source are reasonably small. However, it is not expected that this transition will necessarily be the same in plumes with much greater intrusion heights, such as those present in nature.

The critical Grashof number determined here is an order of magnitude larger than previously suggested for convection in unstratified particle-laden plumes, however, it is important to note that the value of $Gr_c = 10^3$ used by Cardoso and Zarrebini (2001a) was adopted from Hoyal et al. (1999), who investigated the development of particle-rich fingers across a density interface in a step stratified fluid. Hoyal et al. (1999) considered the convection length scale to be equivalent to the finger thickness, yet the critical Grashof number determined here is expected to be associated with a length scale in the z-direction. Thus, the critical value used by both Hoyal et al. (1999) and Cardoso and Zarrebini (2001a) is not directly comparable to the result determined here.

Carazzo and Jellinek (2012) studied negatively buoyant particle-laden jets in a two-layer stratification which produced umbrella cloud Grashof numbers between $10^2 \sim 10^7$ using a length scale of $L_c = z_m - z_s$. A value of $Gr_c \approx 2.2 \times 10^4$, along with the particle-induced ambient density gradients determined for each experiment, suggests convection length scales in this study between 2 cm and 4 cm. These values are certainly of the order of magnitude of the differences observed between the experimental plume maximum and spreading heights.

In their work, Carazzo and Jellinek (2012) noted that some of their experiments developed ambient convection below the intrusion yet did not state the critical umbrella cloud Grashof number for convection to occur. The authors instead conducted a similar approach to Hoyal et al. (1999) using $Gr_c = 10^3$ and a smaller length scale associated with the intrusion's particle-bearing boundary layer. Rather than considering the influence of natural convection, Carazzo and Jellinek (2012) suggested the transition of flow regime from buoyant plume to collapsing fountain is a function of the source Richardson number (i.e. Γ_0). This approach was extended to linearly stratified plumes by Balasubramanian et al. (2018), yet from the results in this study, neither the scaled source Richardson number, nor σ, are capable of independently defining the regime transition in initially buoyant, linearly stratified particle-laden plumes. The influence of these two parameters is discussed further in the next section.

3.5.2 Influence of a real plume source

For a plume where Q_0 and M_0 are sufficiently small, the flow can be considered to be driven only by buoyancy and will act as a pure plume. In this instance, the onset of convection can be predicted using the solution of Morton et al. (1956) for the maximum flowrate in a plume, $Q_s \approx 3.5\alpha^{1/2} B_0^{3/4} N^{-5/4}$, and the radius at the spreading level can be estimated using the equivalent radius of a plume rising in a uniform environment, $b_s = 6\alpha z_{B=0}/5$, where $z_{B=0}$ corresponds to the stratified plume's height of neutral buoyancy. Such an approximation is reasonable considering that the differences in plume radius between an unstratified and stratified plume up to the height of neutral buoyancy are small and, as stated above, the differences present are almost eliminated due to the fact that $U_c \sim b_s^{-1/4}$.

In the case of forced plumes, such as those in this study, the approach described above cannot be taken as both volume flux and radius are dependent upon Γ_0 and σ. Mehaddi et al. (2013), who theoretically studied the evolution of stratified single-phase plumes with respect to these parameters, determined that

$$\frac{Q_s}{Q_0} = \frac{(\sigma+1)^{3/8}}{\Gamma_0^{1/2}\sigma^{5/8}} \left[\frac{5}{2}\beta\left[\frac{1}{2},\frac{5}{4}\right] - I(\sigma) + \frac{\Gamma_0\sigma^{5/4}}{(\sigma+1)^{3/4}}\right]^{1/2}, \tag{3.17}$$

and

$$\frac{b_s}{b_0} = \frac{(\sigma+1)^{1/8}}{\Gamma_0^{1/2}\sigma^{3/8}} \left[\frac{5}{4}\beta\left[\frac{1}{2},\frac{5}{4}\right] - I(\sigma) + \frac{\Gamma_0\sigma^{5/4}}{(\sigma+1)^{3/4}}\right]^{1/2}, \tag{3.18}$$

where $I(\sigma) = (5/4)\int_0^\sigma [t^{1/4}/(t+1)^{7/4}]dt$ is an incomplete beta function and the beta function $\beta[1/2, 5/4] = 1.748$.

An analysis of (3.17) and (3.18) using the source conditions of this study's experiments suggests that $Q_s b_s / Q_0 b_0 \approx 2.5(1+\sigma)^{1/2}/\sigma\Gamma_0$. By substituting this expression into (3.16), along with the definitions of Γ_0, σ and $b_0 = Q_0/(\pi M_0)^{1/2}$, the theoretical convective velocity may be written as

$$\frac{U_c}{(g'_s L_c^3 N^2)^{1/4}} \approx \left(\frac{e^1}{2}\right)^{1/4} \left[\frac{\rho_p \phi_0}{(\rho_0 - \rho_{plume})(\sigma+1)^{1/2}}\right]^{1/4}, \tag{3.19}$$

where $g'_s L^3 N^2$ is a velocity scale, which despite appearing to contain unknown values, is simply a rewritten form of the critical Grashof number and is equivalent to $Gr_c \nu^2 N^2$.

Out of interest, (3.19) may also be written in terms of P as

$$\frac{U_c}{(g'_s L^3 N^2)^{1/4}} \approx \left(\frac{e^1}{2}\right)^{1/4} \left[\frac{P}{1-P}\frac{1+\rho_0/(\rho_p - \rho_0)}{(\sigma+1)^{1/2}}\right]^{1/4}. \tag{3.20}$$

Here, it is clear that P, an alternative definition of particle loading at the source, does have some influence over the magnitude of U_c. However, as per equation (3.15), source parameters and ambient stratification strength are also important and therefore, unlike unstratified particle-laden plumes (see Veitch and Woods, 2000) and as observed in section 3.4, the value of P alone cannot dictate the steady-state plume dynamics.

Now, having derived equation (3.19), the convective velocity in the environment at the edge of the plume can now be estimated using a number of source parameters and the strength of the ambient density gradient. To determine this method's suitability, it must be compared to the approach using experimental measurements taken at the plume spreading height. By equating (3.19) with (3.16), and accounting for that fact that the two velocity scales in each equation are simply rearrangements of Gr_c, dimensionless scaling may be presented as

$$\frac{(g'_s L^3 N^2)}{\left(\dfrac{g L_c^4 N_s^2}{b_s}\right)} = \frac{N^2 b_s}{g} \approx 4\left[\frac{\alpha B_0 (\sigma+1)^{1/2}}{Q_s g}\right]. \tag{3.21}$$

A plot of (3.21) (see Figure 3.7) shows that the two prediction methods do in fact scale together, however instead of being equivalent, the method utilising source parameters tends to result in convective velocity predictions $5-10\%$ larger than those

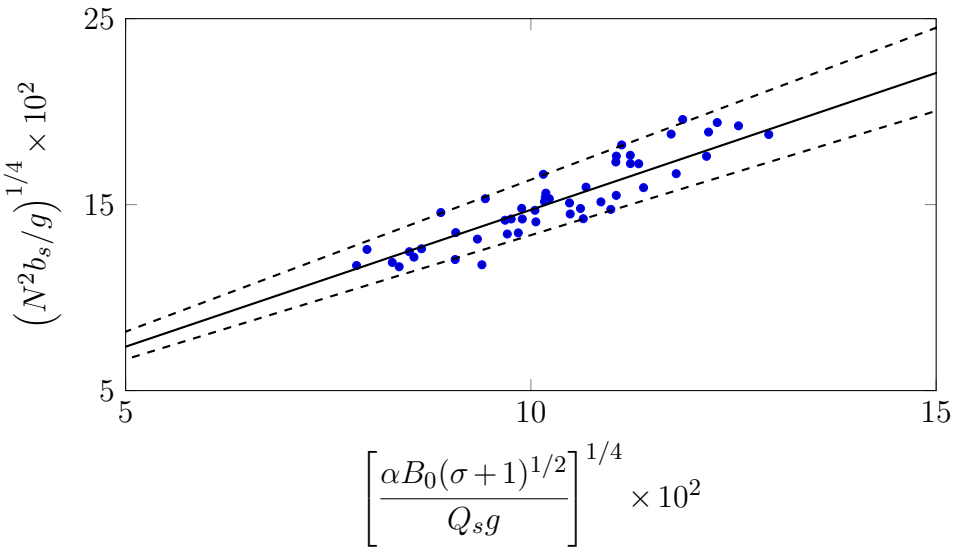

Fig. 3.7 Comparison of the dimensionless velocity predictions using the scaling presented in (3.21), raised to the $1/4^{\text{th}}$ power. The solid line represents a gradient of 1.50 with the dashed lines showing a gradient range of 1.35 - 1.67.

predicted using experimental measurements. The difference observed is expected to be due to an underprediction of both the plume volume flux and plume radius at the spreading level. In terms of volume flux, the theoretical prediction is associated with entrainment into the plume up to its maximum height and does not account for any additional entrainment into the descending fountain at the top of the plume - a phenomenon which has been observed previously in similar experimental studies (Cardoso and Woods, 1993; Hunt and Burridge, 2015). Similarly, the value of plume radius calculated by Mehaddi et al. (2013) is at the height of neutral buoyancy (which moves closer to the source for increasing σ and decreasing Γ_0), whereas the experimental measurements are of the plume radius at the spreading level, which occurs at some height between $z_{B=0}$ and z_m. Even with these limitations, Figure 3.7 shows that an additional coefficient of $4^{1/4}/1.5 \approx 0.95$ on the right-hand side of equation (3.19) can predict the convective velocity below the gravity current, and hence the expected settling regime for a given particle settling velocity, within approximately 10% of that determined from experimental measurements.

To further confirm this approach, comparisons can also be made to other studies where convective behaviour has been observed in particle-laden plumes. Due to only changing the source particle concentration, the experiments of Mirajkar et al. (2015) allow for the most straight-forward application of equation (3.19). Their source

conditions were $Q_0 \approx 33\ \mathrm{cm^3 s^{-1}}$, $M_0 \approx 860\ \mathrm{cm^4 s^{-2}}$ and $B_0 \approx 333 - 661\ \mathrm{cm^4 s^{-3}}$ for source particle concentrations of $\phi_0 = 0.7\%$ and $\phi_0 = 0\%$ respectively. The stratification strength of $N = 0.67\ \mathrm{s^{-1}}$ remained constant across all their experiments and resulted in forced plumes with $\sigma \approx 0.76 - 2.99$. The ballotini ($\rho_p \approx 2.5\ \mathrm{gcm^{-3}}$) used in all their plumes had a settling velocity of $u_{st} \approx 0.8\ \mathrm{cms^{-1}}$ and from equation (3.19), the settling regime change is expected to occur for $\phi_0 \approx 0.35\%$. This value aligns with their observations as upon assessment of their figures (see their Figure 8), clear Type 2 behaviour can be seen in their 0.35% experiment, followed by Type 3/3* behaviour when $\phi_0 > 0.35\%$. It is also worth noting that their Type 3* plume has a predicted convective velocity of $U_c \approx 0.96\ \mathrm{cms^{-1}} \pm 0.1\ \mathrm{cms^{-1}}$, a value similar to this study's observation for Type 3* plumes developing once $U_c \geq 1\ \mathrm{cms^{-1}}$.

3.6 Steady-state plume heights

As observed by previous authors experimentally studying stratified particle-laden plumes, a significant reduction in plume height is seen due to the re-entrainment of particles. The theoretical model of Apsley and Lane-Serff (2019) assumes a re-entrainment model where particle trajectory between the intrusion and the plume margins is associated only with the particle settling velocity and the radial velocity in the environment due to plume entrainment. With steady-state height measurements extracted from experimental analysis (see Appendix B for methodology), an opportunity exists to verify the model's suitability to predict both the maximum rise and spreading heights of Type 1/1* plumes (where $u_{st} > U_c$).

The key equations of their model include the steady-state height of the plume as a function of P,

$$z_\infty = z_0 \left(\frac{|j|}{1 + |j|} \right)^{1/4}, \tag{3.22}$$

where z_∞ and z_0 are the steady-state and initial plume heights, with j defined as

$$j = \frac{1 - P_c/P}{1 - P_c}. \tag{3.23}$$

Here, P_c is the critical buoyancy ratio for plume collapse, which Apsley and Lane-Serff (2019) determined to be equivalent to $P_c = e^{-1}$ for pure plumes. Their second equation of interest is the change in plume height with time, t, as

$$z = z_0 - \left(1 - (1 - P_c)^{1/4}\right) u_{st} t. \tag{3.24}$$

In the case of both (3.22) and (3.24), the values of z, z_∞ and z_0 refer to the spreading height of the plume, which Apsley and Lane-Serff (2019) assumed to be the height of neutral buoyancy for plumes with no additional entrainment in the descending fountain at the top of the plume. Under this particular condition, one would expect that the model can be expanded simply to also predict the maximum height of the plume by utilising the Morton et al. (1956) constant for the dimensionless height where momentum in the plume goes to zero. Apsley and Lane-Serff (2019) non-dimensionalised their height predictions using the scale $l_p = \alpha^{-1/2} B_0^{1/4} N^{-3/4}$, such that the steady-state heights of a plume where $P = 0$ (single-phase) are $z_s/l_p = 1.04$ and $z_m/l_p = 1.37$.

To allow a direct comparison of the experimental results to their theory, appropriate values for α must be estimated. Kaye (2008) states that the two basic approaches for determining α in stratified plumes experimentally is through either measuring the radial growth rate of the plume near the source and using $\alpha = 5b/6z$ or through measuring a bulk property such as z_m and then subsequently inferring α from equation (3.3). In this study, the latter approach has been utilised (see Appendix C.1). Obviously, due to the presence of particles in the plume, additional complexities are present when considering the value of z_m compared to a single-phase plume as the maximum height of a particle-laden plume decays over time due to particle re-entrainment. To avoid this problem, α was estimated using the value of z_m prior to any particle recycling, such that the plume rise height would be equivalent to that of a single-phase plume with the same source buoyancy flux.

Also, due to using a real source, an adjustment to account for the source momentum and volume fluxes must be applied such that $z_m = z_{max} - z_v$, where z_{max} is the plume height above the nozzle and z_v is the virtual source. Virtual sources were estimated for each experiment and were found to vary between -0.6 cm and -3.2 cm using the method for forced plumes described initially by Morton (1959) and later by Hunt and Kaye (2001) (see Appendix C.2). Using the approach described above, the experimental plumes had top hat entrainment coefficients varying between that of a pure plume ($\alpha_p = 0.118$) when $\sigma = 0$ and a pure jet ($\alpha_j = 0.076$) for $\sigma \geq 1$ (Carazzo et al., 2006). Unlike in unstratified plumes, the entrainment coefficient appeared independent of Γ_0, aligning with observations from previous experimental work on plumes in a stratified environment (Konstantinidou and Papanicolaou, 2003).

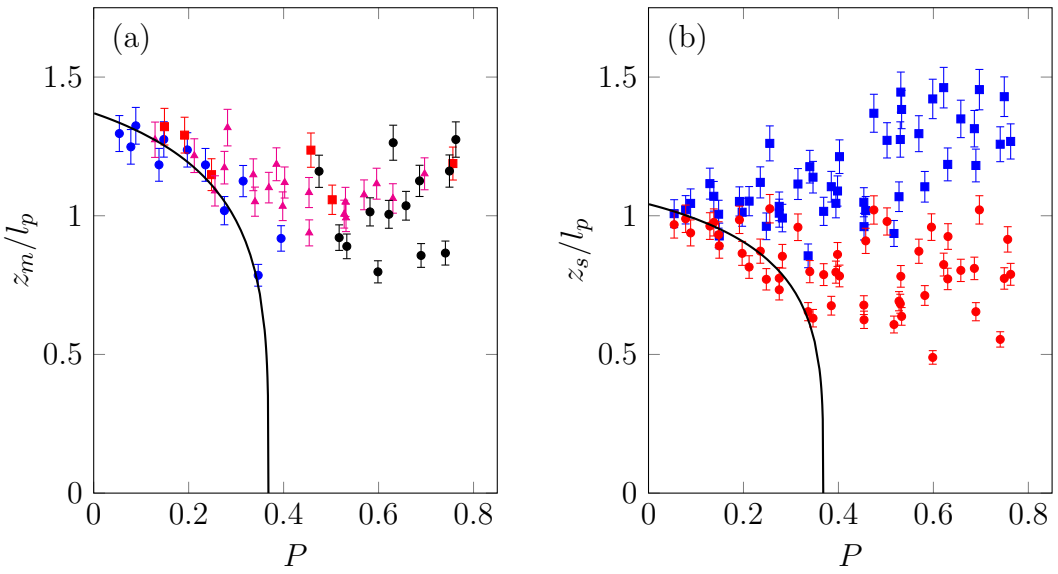

Fig. 3.8 Various plume heights as a function of P where (a) shows the dimensionless steady-state maximum heights categorised by each plume type: 1/1* (•), 2 (▪), 3 (▲), and 3* (•); and (b) the dimensionless steady-state heights of the particle-laden intrusion (•) and the height of neutral buoyancy of the intrusion fluid following the sedimentation of particles (▪). In both figures, the solid lines represent the Apsley and Lane-Serff (2019) collapse model with the parameters $P_c = e^{-1}$ and $\epsilon = 0$.

Having determined appropriate values for α, the heights associated with each plume were non-dimensionalised and are presented in Figure 3.8 against the source buoyancy flux ratio, P. Figure 3.8b details the steady-state spreading height of the plume intrusion, consisting of both fluid and particles, and also the final height of the buoyant interstitial fluid which rises from the main current following the sedimentation of the once dispersed particles into the environment below. Further discussion on the change in intrusion fluid height is presented in section 3.6.1.

The steady-state maximum height of the plume above the virtual source, along with the flow regime observed, is detailed in Figure 3.8a. Interestingly, all plumes where $P < 0.2$ follow the Apsley and Lane-Serff (2019) prediction, irrespective of flow regime. However, for $P > 0.2$, the point at which significant height decay occurs, only a number of Type 1* measurements continue to follow the theory, with the majority of other plumes remaining significantly above the predictions. For plumes where $u_{st} < U_c$, diversion from the theory is expected due to the significant difference in ambient particle motion, whereas the steady-state heights achieved by plumes where $u_{st} > U_c$, it is expected that the differences observed is due to real source effects, particularly

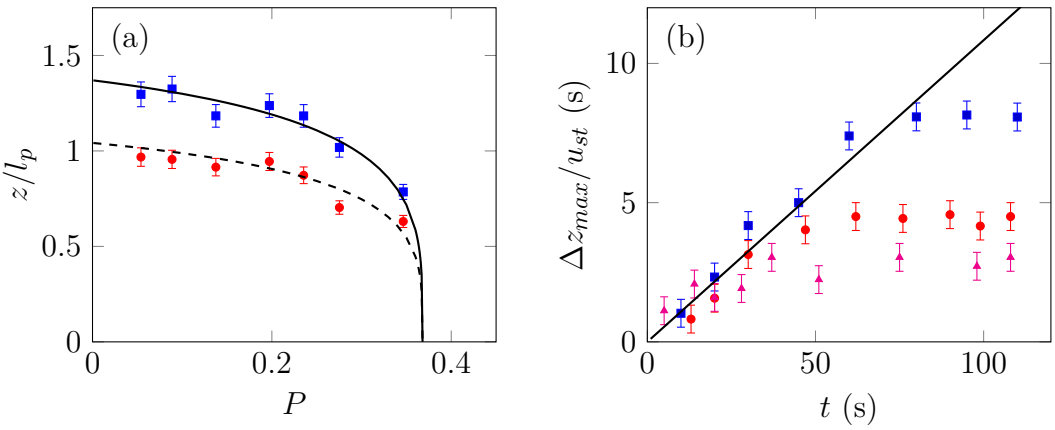

Fig. 3.9 (a) Comparison of the rise (▪) and spreading (•) height of Type 1/1* plumes with the collapse model of Apsley and Lane-Serff (2019). The plumes included have small jet length scales ensuring $z_{max}/L_m > 3$. The average entrainment coefficient of the plumes is $\alpha = 0.1 \pm 0.01$. (b) Change in plume height as a function of time. The points plotted are from experiments 6 (•), 12 (▪) and 54 (▲). The black line has a gradient of 0.108, associated with a buoyancy flux ratio of $P_c = e^{-1}$.

differences in entrainment behaviour both at the plume margins and in the descending fountain at the plume maximum.

To confirm this, an additional plot of dimensionless height against P has been produced and only Type 1/1* plumes with a jet-length, L_m, less than 30% of the steady-state maximum have been included. From Figure 3.9a, it can be said that by excluding plumes with large momentum fluxes at the source, the height prediction of Apsley and Lane-Serff (2019) is within the uncertainty of the experimental measurements. This model verification is further supported by analysing the change in plume height with time. A number of maximum height measurements were taken at various times for three Type 1/1* experiments with small values of L_m. In Figure 3.9b, the change in plume height over the particle settling velocity, $\Delta z_{max}/u_{st}$, is plotted against time t and the gradient predicted by equation (3.24), $(1-(1-P_c)^{1/4}) \approx 0.108$, is found to provide reasonable height estimates prior to the experimental measurements tailing off due to reaching a steady state.

Given the accuracy achieved by the model for plumes with small values of L_m, it is expected that this pure plume model could also predict the expected steady-state height of forced particle-laden plumes if appropriate alterations were made. Apsley and Lane-Serff (2019) proposed an additional term, $\epsilon = Q_s/Q_t - 1$ (with Q_t as the plume volume flux at the theoretical neutral buoyancy height), to account for any additional entrainment into the plume's descending fountain and found that $\epsilon > 0$ produced

larger values of P_c and as a result, greater steady-state plume heights. Although this term accounts for one source of the additional volume present in a forced plume, it is expected that the addition of other parameters accounting for the volume entering at the source and the differences in entrainment at the plume margins would need to be utilised to accurately predict the plume height.

3.6.1 Change in intrusion height

In both this study and the work of Mingotti and Woods (2020), the interstitial fluid in the plume intrusion appears to separate from the main current following the sedimentation of particles. This fluid spreads at a new height of neutral buoyancy, above the original current, and creates an anvil shaped intrusion reminiscent of particle-laden plumes in nature (Sparks et al., 1986; Woods and Kienle, 1994). Notably in their theoretical work, Apsley and Lane-Serff (2019) commented on the potential for the intrusion fluid to increase in height following particle sedimentation, however specifically stated that they did not expect such a rise to occur.

Following their experimental observations, Mingotti and Woods (2020) produced a very simple model to estimate the change in fluid height with respect to the particle and fluid density deficits present at the plume source. Such an approach neglects the influence of particle re-entrainment on the particle concentration at the spreading level, however, reasonable agreement was achieved with their measurements taken at early stages of plume evolution. At steady state however, an approach ignoring re-entrainment cannot be used as both measurements in this study (Figure 3.3) and previous theoretical works (Zarrebini and Cardoso, 2000) have shown that re-entrainment significantly increases the particle concentration at the spreading level, and thus will have a significant impact on the magnitude of negative buoyancy present in the plume intrusion. To take advantage of the measurements of the spreading level particle concentration collected during each experiment, a simple theory which accounts for the re-entrainment of particles can be developed. Using the definition of N, the density of the fluid at any height in the environment away from the reference height (taken as the height of the source) can be determined as

$$\rho = \rho_0 \left(1 - \frac{N^2 z}{g}\right). \tag{3.25}$$

Now consider the difference between the density of the intrusion of fluid and particles and the density of the interstitial fluid only, with corresponding steady-state heights of z_s and z_f respectively, using (3.25),

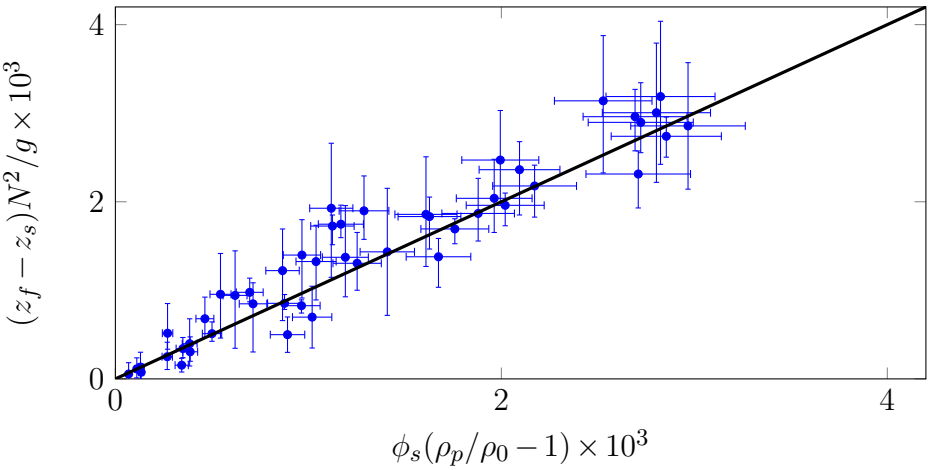

Fig. 3.10 Change in intrusion fluid height following the sedimentation of particles from the two-phase intrusion. The solid line has a gradient of 1.

$$\rho_i - \rho_f = \frac{\rho_0 N^2}{g}(z_f - z_s). \tag{3.26}$$

As the density of the intrusion is defined as $\rho_i \approx \rho_f + \phi_s \rho_p$, (3.26) can be rearranged to

$$z_f - z_s \approx \frac{\phi_s g}{N^2}\left(\frac{\rho_p}{\rho_0} - 1\right), \tag{3.27}$$

given that $\rho_f/\rho_0 \approx 1$.

In Figure 3.10, the experimental results for the change in intrusion fluid height are presented. When estimating the height difference using the leading edges of both the multiphase intrusion below the plume maximum and the new fluid-only intrusion present higher in the environment (heights of which are presented visually in Figure 3.8b), good agreement is found with equation (3.27). Note that some scatter does exist and, in some cases, the uncertainties are quite large and this is expected to be an outcome of how the respective heights of the particle-rich and particle-poor intrusions were estimated (a detailed description of this methodology is provided in Appendix B). Nevertheless, with this finding, the expected change in intrusion fluid height associated with particle fallout in a Type 1/1* plume can be readily determined using a re-entrainment coefficient of e^1 as long as the particle flux at the source and the intrusion volume flux are known. However, this is not the case for plumes rising in the presence of ambient convection as the re-entrainment behaviour in these plumes is not yet understood and is outside of the scope of this particular study.

3.7 Conclusion

From this work, five different flow regimes in stratified particle-laden plumes have been identified. Although a number of parameters are important in defining the different plume types, what must be known in all cases is whether the particles are settling in the environment with some terminal settling velocity or whether the particle's downwards motion is dictated by ambient convection.

When no convection is present, the particle motion in the environment can be easily predicted and experiments have shown that the steady-state heights associated with these plumes can be determined by the model of Apsley and Lane-Serff (2019). However, when ambient convection becomes important (i.e. $u_{st} < U_c$), the particle trajectory, and therefore particle re-entrainment, can no longer be predicted using the models currently present within the literature.

Because of this, further investigations into particle-laden plumes rising in the presence of ambient convection must be conducted such that additional insight can be gained into these complex flows. Examples of this include gaining a better understanding of the radial extent of convection in the environment and whether this has any influence on the transition between Type 3 and 3* behaviour, and also the development of methods to predict important flow characteristics such as the maximum plume height and the heights of the primary and secondary intrusions.

Chapter 4

Multiphase plumes rising through particle-induced convection

4.1 Summary

Stratified multiphase plumes consisting of fluid and particles are unique flows with dynamic behaviour of great interest. In these plumes, buoyant fluid transports dense particles high into the environment until reaching a height of neutral buoyancy and spreading as an intrusion. The particles dispersed in the intrusion sediment into the quiescent environment below and some particles are re-entrained into the main plume whilst others settle onto the floor. This re-entrainment behaviour can significantly alter the plume dynamics and in some cases, result in the transition of particle settling regime from simple Stokes settling to convective settling driven by particle-induced instabilities. In this study, stratified multiphase plumes rising in the presence of particle-induced convection are experimentally investigated. From samples taken within the convection column surrounding the plume, it has been determined that the ambient particle concentration, ϕ_e, is independent of height. Also, a change in ambient density exists at the edge of the plume, $\Delta\rho_e$, yet the fluid density gradient remains approximately equivalent to the initial gradient present prior to plume injection. These two key findings are utilised to determine the steady-state rise height of these plumes through numerically integrating the plume equations of Morton et al. (1956). Methods are presented to determine other important characteristics including the secondary intrusion height; the radial extent of ambient convection; and the particle concentration within the convection column and at the plume's spreading height. Further discussion is also provided surrounding the conditions leading to the onset of ambient convection and potential mechanisms are considered for the observed ambient density change.

4.2 Introduction

Particle-laden plumes are flows of great interest to engineers and geologists alike due to their strong presence in both nature and a wide variety of industries. Various authors have experimentally studied these complex flows in an attempt to understand their dynamics (Balasubramanian et al., 2018; Carey et al., 1988; Ernst et al., 1996; Mingotti and Woods, 2020; Mirajkar et al., 2015; Sparks et al., 1991; Sutherland and Hong, 2016; Veitch and Woods, 2000; Zarrebini and Cardoso, 2000). Originating from a localised source of buoyancy, a multiphase plume of fluid and particles propels itself upwards in the environment, entraining ambient fluid at its margins. The driving force of the plume, the source buoyancy flux, is defined as

$$B_0 = Q_0 g \left[1 - \left(\frac{(1-\phi_0)\rho_f + \phi_0 \rho_p}{\rho_0} \right) \right], \tag{4.1}$$

where Q_0 is the volume flux at the source, g is acceleration due to gravity, ϕ_0 is the source particle volume fraction, and ρ_f, ρ_p and ρ_0 are the density of the plume fluid; the density of the particles; and some reference density, generally taken as the density of the environment at the plume source.

In a uniform environment of finite vertical extent, the plume rises until reaching the surface and spreads as a multiphase gravity current. In a stratified environment, such as the ocean or the atmosphere, the plume reaches a height where its effective density is equivalent to the environment, causing the flow to lose its upwards momentum, leading to the development of a radial intrusion at the height of neutral buoyancy. In either case, the particles in the current immediately begin to decouple from the radial flow and sediment into the environment below, creating a veil of particles around the plume. Within this veil, particles are settling individually at their Stokes velocity and are pulled towards the plume margins as a result of entrainment. This inwards particle trajectory causes particles settling from the current at small distances from the plume margins to be re-entrained into the main flow whilst particles sedimenting at greater radial distances settle directly onto the floor. The re-entrainment of particles settling through a quiescent environment increases the plume's volume fraction at the spreading level by a factor of e^1, significantly affecting the plume dynamics (see Apsley and Lane-Serff, 2019).

Although the impact of this process is observed in plumes rising through uniform environments (Carey et al., 1988; Veitch and Woods, 2000; Zarrebini and Cardoso, 2000), its effect is most evident in stratified plumes, as the maximum rise height is very

dependent upon the effective density of the fluid entrained into the plume from the environment. Morton et al. (1956) determined the maximum height of a single-phase plume as

$$z_m = 1.37\alpha^{-1/2} B_0^{1/4} N^{-3/4}, \tag{4.2}$$

where α is the entrainment coefficient and N is the ambient buoyancy frequency. Without making virtual source adjustments, equation (4.2) is only applicable to pure plumes, where the source momentum flux, M_0, is zero. For flows with non-zero volume and momentum fluxes at the source (known as forced plumes or buoyant jets), the plume height can be written as a function of the buoyancy frequency parameter, $\sigma = (M_0 N/B_0)^2$ (Fischer et al., 1979), as

$$\frac{z_m}{L_m} = f(\sigma), \tag{4.3}$$

where $L_m = (M_0^3/B_0^2)^{1/4}$ is the length scale above the source where buoyancy effects begin to dominate the motion of the flow. Note here that when $\sigma \ll 1$, buoyancy forces at the source dominate and $z/L_m \sim \sigma^{-3/8}$, giving the same result as in (4.2). Conversely, when $\sigma \gg 1$, $z/L_m \sim \sigma^{-1/4}$.

In both cases, the strength of the ambient density gradient negates the extent of the plume rise, and the presence of particles in the environment only magnifies this effect. Apsley and Lane-Serff (2019) showed theoretically that the presence of particles in the environment around a plume does not only lead to a significant depression in the steady-state rise height, but also in some cases can lead to full plume collapse. Considering the evolution of particle concentration within the plume after n recycling events, Apsley and Lane-Serff (2019) determined the steady-state rise height of a stratified particle-laden plume as

$$\frac{z_\infty}{z_0} = \left(\frac{|j|}{1+|j|}\right)^{1/4}, \tag{4.4}$$

where z_∞ and z_0 are the steady-state and initial plume heights, and j is defined as

$$j = \frac{1 - P_c/P}{1 - P_c}, \tag{4.5}$$

with $P = \phi_0(\rho_p - \rho_0)/(\rho_0 - \rho_f)$ and $P_c = e^{-1}$ for pure plumes.

From their work, the influence of re-entrainment on particle-laden plumes rising through still stratified environments is well understood. This is due to the fact that the

steady-state particle concentration at the edge of the plume can be readily determined from the expected particle trajectory between the radial current and the plume margins. This, however, is no longer the case once convective instabilities become present within the sedimenting veil. The earliest experiments concerning these multiphase flows showed the potential for the presence of particle-induced convection in the environment. For unstratified plumes with source concentrations exceeding $10\,\mathrm{gL}^{-1}$, Carey et al. (1988) observed ambient convection ranging from dilute gravity flows at the plume edge to total collapse of the umbrella cloud region. This variety of ambient convection, as well as its absence, was later characterised by Veitch and Woods (2000) using P, the ratio of particle to fluid buoyancy at the source. The transition of a plume rising through a quiescent environment to one undergoing convection was determined by Cardoso and Zarrebini (2001a) through numerically solving for the particle-induced density gradient present below the surface current, $\rho_p(d\phi/dz)$. In addition to this, the authors derived a convection criterion associated with the Grashof number, a dimensionless parameter analogous to the Reynolds number for natural convection which can be defined as

$$Gr = \frac{g\Delta\rho_s L_c^3}{\rho_0 \nu^2} = \frac{g\rho_p L_c^4}{\rho_0 \nu^2}\frac{d\phi}{dz}, \tag{4.6}$$

where $\Delta\rho_s$ is the density difference between the suspension at the base of the gravity current and the ambient, L_c is the convection length scale, and ν is the kinematic viscosity of the suspension.

In Chapter 3, this work was extended by analytically determining $d\phi/dz$ and subsequently applied to stratified plumes. The specific regimes unique to stratified particle-laden plumes were also characterised by comparing the respective magnitudes of the individual particle settling velocity, u_{st}, to the ambient velocity associated with particle-induced convection, U_c. When $u_{st} > U_c$, plumes with Type 1/1* behaviour rise through quiescent environments and their steady-state heights can be predicted using equation (4.4). Transitional Type 2 behaviour is observed when $u_{st} \approx U_c$, whilst Type 3/3* plumes become present when $u_{st} < U_c$. The behaviour of Type 3/3* plumes includes previously observed ambient convection related dynamics such as the separation of interstitial fluid at the top of the plume (Mingotti and Woods, 2020) and the development of secondary intrusions (Balasubramanian et al., 2018; Mirajkar et al., 2015). A key observation from each of the studies where ambient convection is discussed is that once convection has begun, the particles in the environment no longer travel along a predictable path, but instead behave as passive tracers with all

motion dictated by the background fluid flow. Such erratic particle motion in the environment means current models for particle re-entrainment are not suitable for use when determining flow characteristics, one example being the steady-state plume rise height.

In this paper, an experimental study is presented focusing on gaining further understanding of the dynamics of Type 3/3* plumes. Motivated by experimental observations, a method is proposed to predict both the steady-state rise height and the secondary intrusion height of these plumes. Further discussion is also provided on the ambient convection surrounding the plume including a prediction of the convection column radius, along with an assessment concerning the convection length scale.

4.3 Methods

4.3.1 Experimental

Particle-laden plume experiments were conducted in the laboratory through injecting a mixture of fresh water and particles into an acrylic tank with dimensions 69 cm x 69 cm x 50 cm. The tank was filled with aqueous saline solution to a height of 40 cm and a linear stratification was produced using the double-bucket method (Oster and Yamamoto, 1963). The strength of the density gradient created in each experiment is characterised using the ambient buoyancy frequency,

$$N = \sqrt{-\frac{g}{\rho_0}\frac{d\rho_e}{dz}}, \tag{4.7}$$

where $d\rho_e/dz$ is the ambient density gradient.

The plume fluid was supplied to an upwards directed nozzle with an internal diameter of $d_n = 6$ mm. This nozzle was connected to a stirred vessel, placed at a height approximately 1 m above the nozzle, and was used to suspend the particles in fresh water. Acid Red 1 (Azophloxine) dye was added to the plume fluid to assist with plume visualisation, and an LED light sheet was placed outside the tank, directly behind the plume to provide an even distribution of light when viewing experiments.

Photographs of typical experiments and experimental conditions are presented in Figure 4.1 and Table 4.1 respectively. Each experiment was designed such that ambient convection would be present within the environment around the plume. In addition to this condition, the different fluxes at the source, along with the strength of the ambient density gradient, were carefully selected to ensure that each plume achieved

an appropriate initial spreading height within the tank. Source volume fluxes between $Q_0 \approx 3-7\text{cms}^{-1}$ were supplied to the nozzle using a peristaltic pump. The change in height of the stirred feed vessel over a known time was used to determine the exact flow rate and momentum flux ($M_0 = 4Q_0^2/\pi d_n^2$) for each individual experiment. The degree of forcing at the source was varied such that $0 < \sigma < 10$ and $10^{-3} < \Gamma_0 < 10^{-1}$, where $\Gamma_0 = 5Q_0^2 B_0/8\alpha\pi^{1/2}M_0^{5/2}$ is the scaled source Richardson number with values of $\Gamma_0 = 0$ and $\Gamma_0 = 1$ corresponding to pure jet flow and pure plume flow, respectively.

The plume was observed to be turbulent no more than 2 cm above the nozzle with source Reynolds numbers between 700 and 1700. These values are of similar magnitude to previous turbulent plume studies (Carazzo et al., 2006). In all experiments, the positive buoyancy created by the density deficit between the fluid in the plume and the ambient fluid at the source exceeded the negative buoyancy associated with the dense particles dispersed in the flow. It is also worth noting that the effective density of the particle-laden plumes in this study, defined as $\rho_{plume} = \phi_0\rho_p + (1-\phi_0)\rho_f$, were of a similar order of magnitude to the density of the environment, with the ratio of ρ_{plume}/ρ_0 exceeding 97.5% in all cases. As such, the resultant flow is Boussinesq with density effects being negligible except in the case of forces arising due to buoyancy.

In order for convection to be present in the environment around the plume at steady state, the magnitude of the ambient convective velocity below the intrusion, U_c, must exceed the terminal settling velocity of each individual particle, u_{st}. A method to estimate U_c below the intrusions of particle-laden plumes rising through stratified salt water was presented in Chapter 3 and may be written in terms of the source buoyancy and volume flux as

$$U_c \approx 6.6\left(\frac{\rho_p\phi_0}{(1+\sigma)^{1/2}}\frac{Q_0N^2}{B_0}\right)^{1/4}. \tag{4.8}$$

This prediction method was found to be accurate within 10% of the speeds calculated from experimental measurements and whilst some of the experiments in Table 4.1 do fall within the lower margin of error of (4.8) (suggesting that $u_{st} > U_c$), all experiments presented show signs of ambient convection at steady state.

Particle settling prior to the onset of convection was assumed to follow Stokes law with a terminal particle velocity of

$$u_{st} = \frac{g(\rho_p - \rho_0)d_p^2}{18\mu}, \tag{4.9}$$

where d_p is the particle diameter and $\mu = 8.9\times10^{-3}\,\text{gcm}^{-1}s^{-1}$ is the dynamic viscosity of the ambient fluid. Three different types of monodisperse particles were used

Exp	$\boldsymbol{u_{st}}$ ($\mathrm{cms^{-1}}$)	$\boldsymbol{Q_0}$ ($\mathrm{cm^3s^{-1}}$)	$\boldsymbol{M_0}$ ($\mathrm{cm^4s^{-2}}$)	$\boldsymbol{\phi_0}$ (%)	$\boldsymbol{B_0}$ ($\mathrm{cm^4s^{-3}}$)	$\boldsymbol{\Gamma_0}$ ($-\times 10^{-2}$)	$\boldsymbol{N}$ ($\mathrm{s^{-1}}$)	$\boldsymbol{\sigma}$ (-)	***Type*** (-)
13	0.92	5.80	119	0.70	69.4	2.86	0.70	1.44	3
14	0.92	5.96	125	0.51	83.0	3.17	0.77	1.37	3
15	0.92	6.06	130	0.93	57.3	2.08	0.82	3.45	3*
17	0.92	6.46	148	0.91	72.9	2.18	0.49	0.97	3*
18	0.92	2.97	31.2	0.67	45.1	13.9	0.80	0.31	3
20	0.92	5.87	122	1.06	40.3	1.61	0.61	3.45	3*
21	0.92	6.17	135	1.11	58.7	2.01	0.46	1.13	3*
22	0.92	2.97	31.2	1.08	30.4	9.34	0.50	0.26	3*
25	0.92	6.22	137	1.08	60.6	2.03	0.63	2.02	3*
26	0.92	3.07	33.3	1.20	18.2	5.09	0.60	1.20	3*
27	0.92	5.98	127	1.00	74.2	2.79	0.41	0.49	3
29	0.92	6.91	169	0.91	130	3.18	0.61	0.62	3
30	0.92	5.82	120	0.70	127	5.20	0.60	0.32	3
31	0.92	5.75	117	1.13	111	4.69	0.48	0.26	3*
37	0.64	5.95	125	0.43	32.0	1.22	0.60	5.57	3
38	0.64	5.87	122	0.33	49.2	1.96	0.64	2.50	3
39	0.64	5.72	116	0.24	82.6	3.55	0.52	0.53	3
40	0.64	5.93	124	0.48	45.4	1.75	0.44	1.48	3
42	0.64	3.07	33.4	0.55	31.7	8.80	0.54	0.32	3
43	0.64	3.04	32.6	0.35	38.0	10.9	0.48	0.17	3
44	0.64	5.97	126	0.41	99.3	3.76	0.72	0.84	3
45	0.64	3.06	33.1	1.16	37.7	10.6	0.75	0.43	3*
46	0.64	3.03	32.4	0.71	14.1	4.10	0.64	2.19	3*
47	0.64	3.03	32.4	0.85	31.2	9.07	0.37	0.15	3*
48	0.64	6.03	129	0.92	125	4.58	0.83	0.74	3*
50	0.45	5.97	126	0.24	40.1	1.52	0.52	2.65	3
51	0.45	6.00	128	0.12	25.9	0.96	0.39	3.77	3
53	0.45	6.09	131	0.33	106	3.79	0.79	0.96	3
55	0.45	6.05	130	0.47	60.9	2.21	0.48	1.05	3
56	0.45	5.95	125	0.72	56.9	2.18	0.62	1.87	3*
57	0.45	3.01	32.1	0.67	34.5	10.2	0.70	0.42	3
58	0.45	5.94	125	1.00	56.9	2.19	0.36	0.63	3
59	0.45	5.98	127	1.10	31.3	1.18	0.60	5.89	3*
60	0.45	5.93	125	1.14	43.2	1.67	0.48	1.90	3*
61	0.45	3.18	35.7	0.50	58.9	14.8	0.70	0.18	3
62	0.45	2.98	31.4	1.00	37.1	11.3	0.50	0.18	3
63	0.45	3.01	32.1	0.60	11.7	3.43	0.31	0.71	3
64	0.45	3.02	32.3	0.85	16.0	4.67	0.26	0.28	3
65	0.45	6.06	130	0.26	149	5.38	0.67	0.34	3

Table 4.1 List of experimental parameters

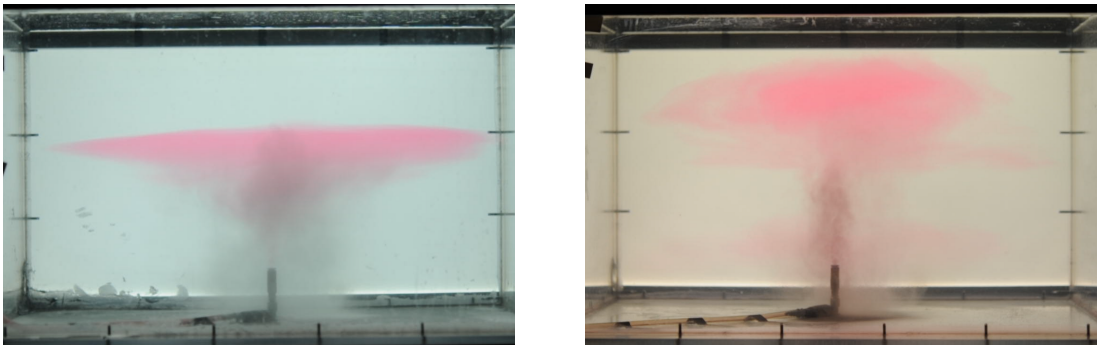

(a) (b)

Fig. 4.1 Photographs of typical experiments after 300 seconds. (a) Experiment 55, Type 3; (b) Experiment 21, Type 3*.

to achieve the range of settling speeds detailed in Table 1. The upper and lower velocities of $0.92\,\mathrm{cms}^{-1}$ and $0.45\,\mathrm{cms}^{-1}$ are associated with two sets of glass ballotini ($\rho_p = 2.5\,\mathrm{gcm}^{-3}$), each with average particle diameters of 100 μm and 70 μm. The third particle set, 70 μm silicon carbide particles ($\rho_p = 3.2\,\mathrm{gcm}^{-3}$), was used to achieve the intermediate velocity of $u_{st} \approx 0.64\,\mathrm{cms}^{-1}$. In all cases, the source buoyancy flux was sufficiently large such that the characteristic plume velocity, $(B_0 N)^{1/4}$, exceeded the particle settling velocity. This ensured all particles dispersed in the plume reached the maximum height, before spreading radially with the intrusion (Ernst et al., 1996).

Experiments were captured using a Nikon D300s camera, fitted with an AF-S Micro NIKKOR 60 mm f/2.8G ED lens. For each experiment, the camera was placed on a 1.2 m high tripod approximately 2.5 m from the experimental tank. During the first 10 minutes of plume injection (the maximum time to achieve steady state), videos with a frame rate of 24 Hz were taken for post-experimental analysis. After the end of the filming period, samples were taken within the plume at the spreading level and at 2 cm increments within the convection column between the intrusion and the source. The fluid density of the samples was recorded using an Anton Paar DMA35n density meter. The particles in the samples were washed and then dried to estimate the particle volume fraction. This method was determined to be accurate within $\pm 10\%$ by sampling a well-mixed tank with a known particle concentration.

Note that in all experiments, the timescale to achieve a filling box like flow (Cardoso and Woods, 1993) was large compared to the length of the experiment and any major changes to the ambient stratification were the result of particle-induced convection rather than filling box effects.

4.3.2 Image Analysis

Image analysis was completed by assessing the level of light intensity captured by the camera using MATLAB R2020B. Individual images were extracted from the video footage at a rate of one image per second. Prior to further analysis, a base image, taken before plume injection, was subtracted from each experimental image to remove any inconsistencies in light intensity associated with the light sheet. Due to the opaque nature of the particles dispersed in the plume, less light is captured by the camera in areas of the tank where particles are present. Due to this, the particles, in a sense, could be tracked to determine a number of important flow characteristics.

As the particles dispersed in the plume are expected to be carried upwards in the environment until momentum is no longer present, the evolution of the maximum plume height over time could be determined. Similarly, following the transition from Stokes settling to convective settling, all the particles spreading from the plume become confined to a defined radius associated with the convection column. As this column is rich with particles, the intensity of light captured in this area is low allowing the radius of convection to be estimated. Figure 4.2 shows examples of the image analysis conducted to determine the maximum plume height and the convection column radius.

Image analysis was also used to determine the volume flux of the plume at the spreading level, Q_s, by measuring the evolution of intrusion volume over time as described by Sigurðardóttir et al. (2020).

4.4 Results

In all experiments, plume behaviour was consistent with previous experimental studies. Upon initial injection of the fluid and particles, the plume rose upwards and was observed to be turbulent and conical in shape. Due to the entrainment of dense, stratified fluid, the plume quickly became neutrally buoyant after an initial period of acceleration. Each plume continued to rise until upwards inertia had decayed to zero at a height of $z_m \approx 1.37\alpha^{-1/2}B_0^{1/4}N^{-3/4}$ above the virtual source (Morton et al., 1956). The fluid and particles descended from this maximum height, creating a fountain at the top of the plume before spreading as an intrusion between the plume's height of neutral buoyancy and maximum height. The particles initially spread with the current, however, eventually sedimented from the base of the intrusion at their Stokes velocity into the environment below. Any particles settling into the environment close to the plume margins were re-entrained into the upwards flow, whereas particles settling from

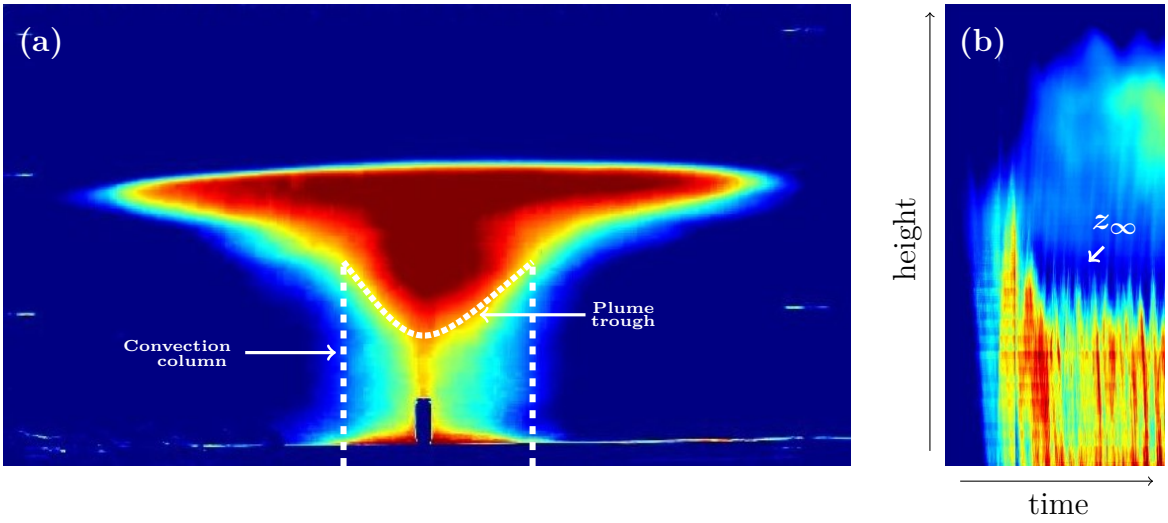

Fig. 4.2 False colour images produced using MATLAB R2020B where navy and maroon represent maximum and minimum values of light intensity. (a) Experiment 55, time-averaged over 120 seconds once steady state was achieved. Both the convection column and the plume trough are clearly visible. (b) A 300 second time series of experiment 21. The red/yellow colour shows the evolution of the terminal rise height as the solid particles dispersed in the flow reduces the intensity of light captured by the camera. The light blue/green near the top right of the figure shows the spreading height of the buoyant fluid which rises from the current following the sedimentation of particles.

the intrusion at greater radial distances were not re-entrained and sedimented onto the tank floor.

As described in Chapter 3, after a series of particle recycling events, the concentration of particles at the plume's spreading level reaches a threshold where the ambient convective velocity associated with particle-induced instabilities exceeded the terminal settling velocity of each individual particle. This transition in settling regime caused a significant change in flow dynamics where the veil of sedimenting particles around the plume evolved into a column of convecting ambient fluid. Within the convection column, a trough of dyed intrusion fluid was present and under some circumstances, the convection in the environment became so great that dyed fluid in the trough was actually dragged to the base of the tank, before rising again as a secondary intrusion between the original current and the tank floor.

In-situ fluid measurements at various heights in the convection column have provided previously unknown details regarding the ambient conditions at the edge of a Type 3/3* plume. Significantly, these measurements provide crucial information to further understand the re-entrainment of particles into the plume which subsequently can

be used to predict flow dynamics such as the terminal rise height. The key findings are a) the particle concentration within the convection column, ϕ_e, is independent of height; and b) the ambient density in the convection column remains stratified with approximately the same density gradient prior to plume injection ($dN/dt \approx 0$), however, a constant change in fluid density, $\Delta\rho_e$, is observed between the plume spreading height and the base of the tank. A constant ambient particle concentration has been previously observed in unstratified particle-laden plumes undergoing ambient convection, however, Cardoso and Zarrebini (2001a) found this concentration was consistent across the entire width of the tank, whereas observations in this work are confined within much smaller radii. The latter observation regarding the change in ambient density is unique to this study as it appears that no prior experimental measurements have been taken within the environment of a stratified particle-laden plume.

Figure 4.3 details an example of these measurements taken within a plume's convection column and Table 4.2 provides the specific values of ϕ_e and $\Delta\rho_e$ for each experiment. Other tabulated parameters include the steady-state plume height above the nozzle, z_{max}; the secondary intrusion height above the tank floor, z_{si}; the particle concentration ϕ_s, and plume radius b_s, at the spreading height; the convection column radius, R_c; and depth of the plume trough, L_t. Further discussion on each of these parameters is provided in the following subsections.

4.4.1 Plume heights

Maximum height

The evolution of volume, momentum and buoyancy flux of a single-phase plume with height can be determined from the following conservation equations,

$$\frac{dQ}{dz} = 2\alpha(\pi M)^{1/2}, \tag{4.10a}$$

$$\frac{dM}{dz} = \frac{BQ}{M}, \tag{4.10b}$$

$$\frac{dB}{dz} = -N^2 Q. \tag{4.10c}$$

Morton et al. (1956) famously derived these equations and numerically determined the neutral buoyancy and maximum heights of a plume rising through a stratified environment. Veitch and Woods (2000) and Apsley and Lane-Serff (2019) both built

Exp	z_{max} (cm)	R_c (cm)	b_s (cm)	Q_s (cm^3s^{-1})	ϕ_s (%)	ϕ_e (%)	$\Delta\rho_e$ ($gcm^{-3} \times 10^{-3}$)	L_t (cm)	z_{si} (cm)
13	13.5	3.5	2.5	48.5	0.19	0.11	-3.3	5.2	-
14	13.0	3.3	1.6	43.0	0.17	0.10	-7.3	4.4	-
15	9.8	4.4	2.0	38.4	0.38	0.10	-5.8	-	6.8
17	13.1	4.6	1.7	67.5	0.19	0.08	-3.2	-	10.6
18	9.9	3.0	2.3	30.7	0.14	0.06	-2.3	3.2	-
20	12.5	3.6	1.5	46.0	0.26	0.15	-2.8	-	7.1
21	15.1	4.1	1.8	68.7	0.19	0.15	-3.3	-	12.6
22	8.6	3.2	1.8	29.2	0.18	0.09	-2.0	-	7.5
25	12.6	5.1	2.5	48.3	0.32	0.10	-4.8	-	10.3
26	8.9	3.3	1.3	20.9	0.28	0.11	-2.5	-	6.9
27	15.8	4.7	1.9	96.1	0.14	0.09	-3.2	5.1	-
29	15.0	4.9	1.7	81.6	0.15	0.08	-4.3	5.8	-
30	16.3	4.6	1.9	90.9	0.11	0.06	-2.8	4.1	-
31	17.1	5.5	1.7	104.1	0.12	0.09	-3.2	-	9.2
37	12.1	6.7	1.4	43.4	0.10	0.03	-2.5	-	-
38	10.9	5.7	2.2	45.6	0.07	0.04	-2.5	-	-
39	15.3	6.3	1.8	75.8	0.03	0.02	-1.3	-	-
40	15.8	6.1	2.0	58.1	0.08	0.03	-2.0	-	-
42	11.2	5.6	1.8	35.8	0.06	0.03	-2.6	-	-
43	13.7	5.1	2.4	43.7	0.05	0.02	-1.4	-	-
44	13.6	6.6	1.5	51.4	0.06	0.03	-3.9	-	-
45	9.9	6.0	1.5	26.2	0.14	0.04	-3.8	-	6.3
46	12.5	4.5	1.3	17.0	0.17	0.05	-2.7	-	7.7
47	17.0	7.7	1.5	57.9	0.08	0.02	-1.2	-	12.3
48	12.4	8.1	1.8	47.4	0.19	0.04	-6.0	-	7.8
50	16.1	8.1	3.1	53.0	0.05	0.02	-1.0	4.7	-
51	18.3	5.6	1.9	54.8	0.02	0.02	-0.6	4.3	-
53	14.3	9.9	2.0	49.6	0.08	0.02	-2.0	4.8	-
55	14.7	10.8	1.4	68.4	0.05	0.01	-0.8	5.4	-
56	11.8	10.8	1.2	48.8	0.13	0.03	-2.0	-	5.3
57	10.4	7.9	2.0	24.7	0.09	0.03	-1.8	5.0	-
58	19.5	11.9	3.0	73.0	0.08	0.03	-1.4	6.5	-
59	11.9	10.2	1.4	50.2	0.19	0.05	-2.9	-	8.6
60	13.4	11.9	2.0	53.2	0.19	0.03	-2.4	-	10.9
61	11.6	9.3	2.5	38.5	0.06	0.02	-1.5	6.4	-
62	12.1	9.9	3.0	43.6	0.09	0.02	-0.9	7.2	-
63	15.8	9.5	1.2	41.4	0.07	0.01	-0.3	6.8	-
64	18.0	9.3	2.7	52.1	0.06	0.02	-0.5	6.1	-
65	16.4	10.1	3.1	88.0	0.03	0.01	-1.0	6.6	-

Table 4.2 List of experimental measurements. The values of ϕ_e and $\Delta\rho_e$ presented are averages of the measurements taken through the convection column. Note that only plume trough depths, L_t, for Type 3 ballotini experiments were measured as the silicon carbide particles inhibited the trough view and the trough depth of Type 3* plumes was equivalent to the plume spreading height as dyed fluid is dragged to the tank floor.

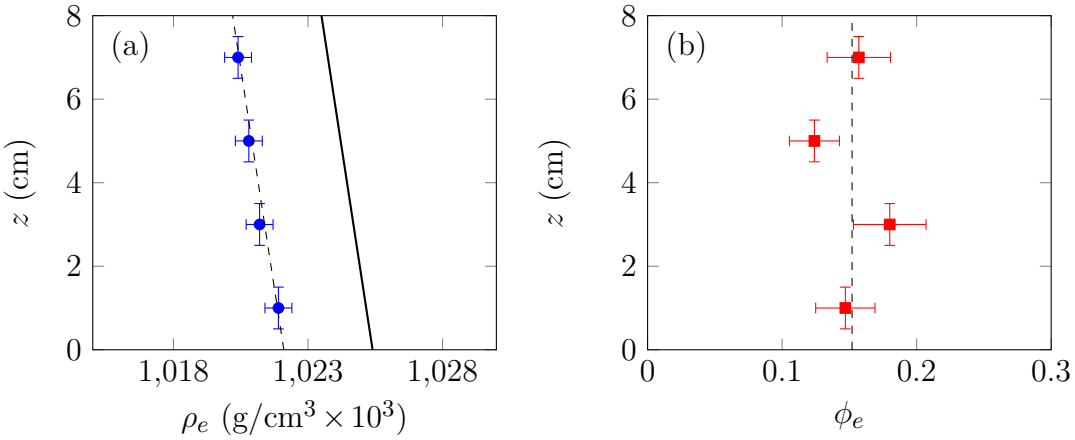

Fig. 4.3 Example measurements within the convection column of experiment 21. (a) Ambient density measurements, showing the initial (——) and steady-state (•) ambient density at various heights. Note that the solid and dashed lines have the same gradient; and (b) the particle volume fraction, where the dashed line represents the average of the four measurements.

upon these equations for application to particle-laden plumes, through either adding new terms or new equations, to account for the increased decay in buoyancy when compared to a single-phase plume due to particle re-entrainment.

Although these extensions are necessary to determine the heights of Type 1/1* plumes, where the particle concentration in the environment increases with height, the same is not expected to be required for Type 3/3* plumes where measurements have shown that the ambient concentration of particles is independent of height. Thus, instead of utilising additional terms or equations, the steady-state height of a Type 3/3* plume will likely be determined using the same set of equations. However, appropriate alterations must be made to the definition of the initial buoyancy flux B_0, and also to the entrainment coefficient as entrainment into the plume is a function of the ratio of momentum and buoyancy fluxes at the source (Fischer et al., 1979; Konstantinidou and Papanicolaou, 2003).

The initial buoyancy flux of the plume at $t = 0$ is determined with the source volume flux and the plume's reduced gravity $g' = g(\rho_0 - \rho_{plume})/\rho_0$, a function of the plume density and the density of the environment at the source. This ambient density, taken here as the reference density ρ_0, will remain constant whilst the environment is quiescent, however, following the onset of ambient convection around the plume, the density within the convection column decreases. When accounting for the presence of

particles in the environment, the steady-state density of the environment at the source is equivalent to

$$\rho_{0,ss} = \rho_0 + \Delta\rho_e + \phi_e\rho_p. \tag{4.11}$$

By substituting ρ_0 with $\rho_{0,ss}$ in the definition of buoyancy flux, the magnitude of the initial ($t = 0$) and steady-state buoyancy flux and buoyancy frequency parameter values can be directly compared as

$$B_{0,ss} = B_0\left(1 + \frac{\Delta\rho_e + \phi_e\rho_p}{\rho_0 - \rho_{plume}}\right), \tag{4.12}$$

and,

$$\sigma_{ss} = \sigma\left(1 + \frac{\Delta\rho_e + \phi_e\rho_p}{\rho_0 - \rho_{plume}}\right)^{-2}. \tag{4.13}$$

Upon assessment of (4.12) and (4.13), in the absence of particles and ambient convection, as one would expect, the initial and steady-state values become equivalent. In the case of these experiments, $-\Delta\rho_e \gg \phi_e\rho_p$, and therefore, $B_{0,ss} < B_0$. As $z_{max} \sim B_0^{1/4}$, a decrease in buoyancy at the source suggests a decrease in plume height, however, this drop in height has the potential to be mitigated as a result of decreased entrainment ($z_{max} \sim \alpha^{-1/2}$) due to the fact that $\alpha = f(\sigma)$ and $\sigma \sim B_0^{-2}$.

Previous experimental work in a stratified ambient (Konstantinidou and Papanicolaou, 2003) suggests that the entrainment coefficient, α, can be determined using the empirical equation,

$$\alpha = \alpha_p \exp\left[\ln\left(\frac{\alpha_j}{\alpha_p}\right)\left(\frac{\sigma}{\sigma_c}\right)^2\right], \tag{4.14}$$

where α_p and α_j represent the extreme entrainment coefficients for a pure plume and a pure jet; and σ_c is the critical buoyancy frequency parameter where momentum begins to dominate the flow behaviour. Although (4.14) suggests a decrease in entrainment coefficient is likely to be observed due to a drop in source buoyancy, this is only the case in initially weakly forced plumes ($\sigma \ll \sigma_c$). Previous experiments conducted within the same experimental apparatus with similar source and ambient conditions suggest a minimum entrainment coefficient of $\alpha_j = 0.074$ once jet-like behaviour is achieved ($\sigma_c \approx 1$) (see Appendix C.1). A similarly traditional value of $\alpha_p = 0.118$ was deemed suitable to predict the bulk entrainment coefficient of these plumes and thus, this value will also be used in this work.

Now with the appropriate methods to determine the steady-state source buoyancy flux and entrainment coefficient of each plume, equations (4.10a–c) can be solved to determine the maximum Type 3/3* plume height, specifically by predicting the height where vertical momentum in the plume decays to zero. As mentioned previously, other authors studying forced plumes have shown that $z/L_m = f(\sigma)$ (Fischer et al., 1979; Richards et al., 2014). This scaling is not directly evident upon numerically solving equations (4.10a–c) in their dimensional form, thus, to observe this scaling, and to allow direct comparison of each experiment to the solution, the equations are non-dimensionalised such that the maximum plume height can be presented against σ. Using the dimensional scales of B_0, M_0 and N, along with the dimensionless entrainment coefficient, α, for consistency with recent literature (Apsley and Lane-Serff, 2019), equations (4.10a–c) become

$$\frac{d\hat{Q}}{d\hat{z}} = 2(\pi\hat{M})^{1/2}, \tag{4.15a}$$

$$\frac{d\hat{M}}{d\hat{z}} = \frac{\hat{B}\hat{Q}}{\hat{M}}, \tag{4.15b}$$

$$\frac{d\hat{B}}{d\hat{z}} = -\hat{Q}, \tag{4.15c}$$

where

$$Q = \sigma^{1/2}\alpha^{1/2}(M_0^5/B_0^2)^{1/4}\hat{Q}, \quad M = \sigma M_0\hat{M}, \tag{4.16a-d}$$

$$B = \sigma M_0 N\hat{B}, \quad z = \alpha^{-1/2}(M_0^3/B_0^2)^{1/4}\hat{z}.$$

These dimensionless equations were then solved numerically for σ between 0.1 and 50, using incremental steps of 1×10^{-3}. Note here that to achieve the scaling in (4.16d), the non-dimensionalisation process did not include Q_0, a value which in the experiments presented is non-zero and not insignificant enough to have a negligible influence on plume rise height. As a result, dimensional initial conditions of $Q_0 = 3$ cm^{3}s^{-1} and $Q_0 = 6$ cm^{3}s^{-1} were used to create two separate curves to reflect the spread of volume flux in the experiments. Also note that the dimensionless value, $\hat{Q}_0 = (\pi^3 d_n^6 N^2/64 Q_0^2 \alpha^2 \sigma^3)^{1/4}$, is dependent upon α and N. Therefore, to give the greatest spread in predicted heights, the pure plume and pure jet entrainment coefficients were utilised, along with the experimental range of stratification strengths, $0.2s^{-1} < N < 0.8s^{-1}$.

To solve equations (4.15a–c), the dimensionless initial conditions of momentum flux and buoyancy flux are $\hat{M}_0 = \sigma^{-1}$ and $\hat{B}_0 = \sigma^{-3/2}$. The two numerical solutions for maximum plume height (taken as $\hat{z}$ at $\hat{M} = 1 \times 10^{-5}$) are plotted in Figure 4.4, along with the experimental measurements of the maximum plume height above the nozzle, non-dimensionalised using the terms associated with steady-state source conditions. The solutions presented here represent the relationship of plume height and σ for the maximum and minimum values of $\hat{Q}_0$ across the experiments. Upon assessment, it is found that greater than 85% of the measurements fall within the two predictions when considering the experimental uncertainty, suggesting that the described method is appropriate for determining the steady-state rise height of a Type 3/3* plume.

Although only two extreme curves have been plotted here to allow for model comparison across all the experiments, in practice, it is expected that a more accurate prediction for the maximum plume height will be achieved by integrating equations (4.15a–c) with $\hat{Q}_0$ determined from real experimental/field conditions, as opposed to using the extreme values of α and N as done here.

Secondary intrusion height

Secondary intrusions are a phenomenon previously observed in a number of experimental studies (Balasubramanian et al., 2018; Mirajkar et al., 2015) and are unique to particle-laden plumes rising in stratified environments. The key difference between plumes undergoing ambient convection with secondary intrusions (Type 3*) against those plumes without multiple intrusions (Type 3) is the strength of the ambient convection present directly beneath the intrusion.

In Chapter 3, some discussion was presented stating that in addition to the strength of the ambient convection, the radial extent of convection may be a factor in the development of multiple intrusions. Yet, as shown in section 4.4.2, secondary intrusion development appears to be independent of the convection radius (see Figure 4.6). The empirical transition to Type 3* behaviour, as observed in both these experiments and those of Mirajkar et al. (2015), is that the convective velocity below the intrusion has to exceed $U_c > 1\ \mathrm{cms}^{-1}$. Once this velocity is exceeded, both dyed plume fluid and ambient fluid below the intrusion is dragged down to the base of the tank. Turbulent convection then ceases once the particles have settled onto the tank floor and the buoyant dyed fluid rises in the environment until reaching a neutrally buoyant height.

To estimate this height, one of two approaches can be taken. Either a numerical model, similar to that proposed by Bloomfield and Kerr (1998) for stratified fountains, could be developed and utilised to determine the evolution of fluid density in the

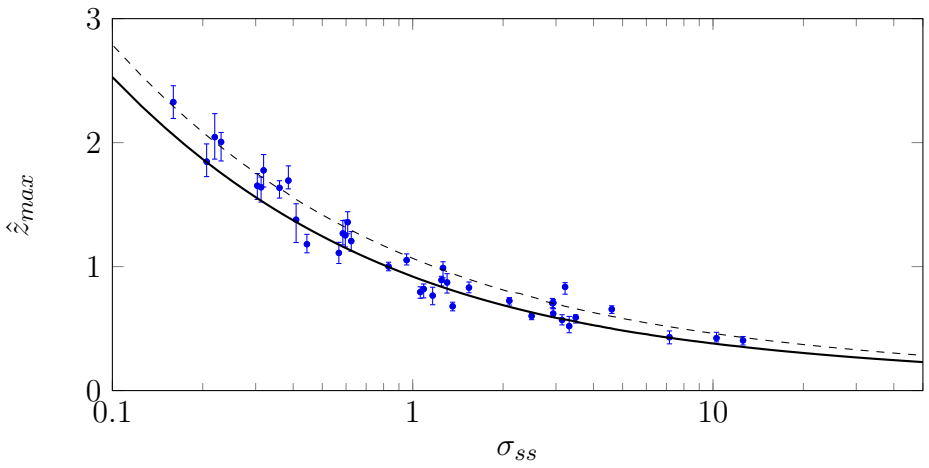

Fig. 4.4 Dimensionless maximum plume heights, $\hat{z}_{max}$, against σ_{ss}. Experimental measurements were taken above the nozzle at steady state and were non-dimensionalised using the steady-state values of buoyancy flux, $B_{0,ss}$, and entrainment coefficient, α. The dashed and solid lines represent the numerical solution for minimum and maximum initial values of dimensionless volume flux, $\hat{Q}_0 \approx 0.2\sigma^{-3/4}$ and $\hat{Q}_0 \approx 0.8\sigma^{-3/4}$.

fountain-like downflow; or a much simpler approach, reminiscent of Mingotti and Woods (2020), could be taken by utilising experimental measurements of convection column fluid density and particle volume fraction. Taking the latter approach, the change in height of a fluid parcel in a stratified environment Δz, can be written as a function of the density deficit between the fluid parcel and the environment $\Delta\rho$, as

$$\Delta z = \frac{g}{N^2\rho_0}\Delta\rho. \tag{4.17}$$

Assuming no additional entrainment into the current once it has reached the base of the tank, the total density deficit equals the sum of the change in density in the convection column as a result of dragging light fluid to the tank base and the density associated with the volume fraction of particles which deposit onto the tank floor,

$$\Delta\rho = -\Delta\rho_e + \phi_e\rho_p. \tag{4.18}$$

By considering $\Delta z = z_{si} - z_b$, with z_b as the height of the base of the tank, combined with the fact that $-\Delta\rho_e \gg \phi_e\rho_p$, the height of the secondary intrusion above the tank base can be written as

$$z_{si} \approx -\frac{g}{N^2\rho_0}\Delta\rho_e, \tag{4.19}$$

as $z_b = 0$.

In Figure 4.5, experimental results for the secondary intrusion height of the Type 3* plumes are presented. It is found that the experimental heights, which relate to the leading edge of the major intrusion observed between the tank floor and the primary intrusion, fit well against the theory. However, in all cases the secondary intrusions tended to be relatively thick, regardless of the ambient stratification strength. This suggests that along with the largest secondary intrusion, where the majority of dyed fluid came to rest, other smaller spreading events occurred between the tank base and the predicted height of neutral buoyancy. These minor events are likely associated with smaller volumes of fluid escaping the convection column prior to reaching the tank floor.

4.4.2 Ambient convection

Convection column radius

Cardoso and Zarrebini (2001a) determined that the magnitude of the convective velocity below a surface current produced by a particle-laden plume is a function of the particle-induced density gradient present at the base of the intrusion. This ambient velocity associated with particle-induced instabilities can be written as

$$U_c \approx \left(\frac{Gr_c \nu^2 g}{\rho_0}\right)^{1/4} \left(\rho_p \frac{d\phi}{dz}\right)^{1/4}, \tag{4.20}$$

where Gr_c is the critical Grashof number leading to the onset of ambient convection. This work was extended in Chapter 3, allowing the particle gradient to be determined analytically as

$$\frac{d\phi}{dz} = \left(\frac{2\alpha\phi_s}{b_s}\right) \exp\left[\frac{-\pi u_{st}(r^2 - {b_s}^2)}{Q_s}\right], \tag{4.21}$$

where r represents the intrusion radius.

Equation (4.21) shows that the particle gradient at the base of the intrusion decays exponentially with r^2, suggesting that some critical intrusion radius, R_c, exists where convection in the environment ceases due to the ambient velocity becoming equivalent to the individual particle settling velocity (as observed in both current and previous experiments). Upon substituting (4.21) into (4.20) and setting $U_c = u_{st}$ and $r = R_c$, after some rearrangement,

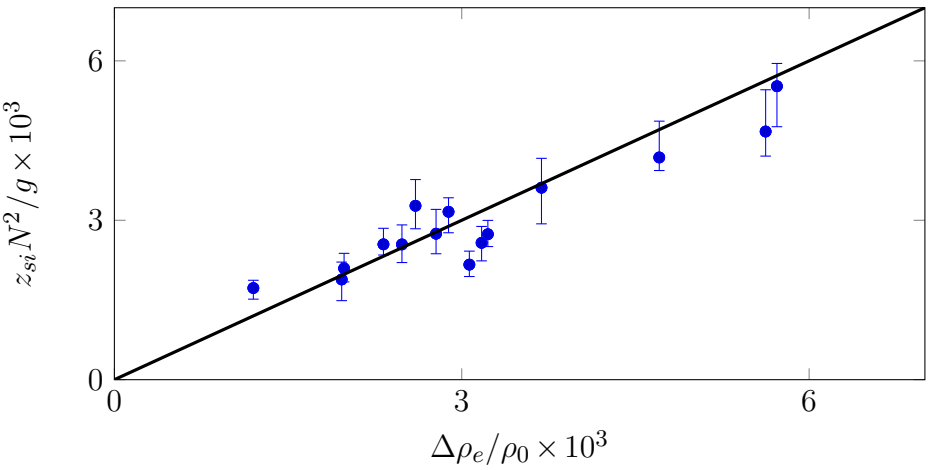

Fig. 4.5 Dimensionless secondary intrusion height above the tank floor against the scaled change in density within the convection column.

$$\frac{\pi(R_c^2 - b_s^2)u_{st}}{4Q_s} \approx \ln\left[\frac{(Gr_c\nu^2 g)^{1/4}}{b_s^{1/4}u_{st}}\left(\frac{2\alpha\rho_p\phi_s}{\rho_0}\right)^{1/4}\right]. \tag{4.22}$$

The left and right-hand sides of (4.22) are plotted using experimental data in Figure 4.6. As expected, the plotted points show a linear relationship and pass through the origin when utilising a critical Grashof number of $Gr_c = 4.6 \times 10^4 \pm 1.6 \times 10^4$ with $\rho_0 = 1\,\mathrm{gcm}^{-3}$ and $\nu = 8.9 \times 10^{-3}\,\mathrm{cm}^2\mathrm{s}^{-1}$. Notably, when accounting for experimental uncertainty, an overlap is present between the range of Gr_c found here and the range determined for the settling regime transition in Chapter 3. Upon inspection of Figure 4.6, it can also be noted that the range of convection column radii is similar for both Type 3 and 3* plumes, suggesting that no radial length scale exists which leads to the development of secondary intrusions between the primary current and the tank floor.

Another point of interest is that, as per the settling regime transition, the density gradient used to determine the radial extent of convection does not account for the ambient density gradient, $d\rho_e/dz$. Further discussion concerning this oddity is presented later in this section.

A note on the critical Grashof number

The critical Grashof number used to predict the radius of convection in the experiments is very similar to the expected value for settling regime transition in stratified particle-laden plumes, however, it significantly differs from previous work conducted in an

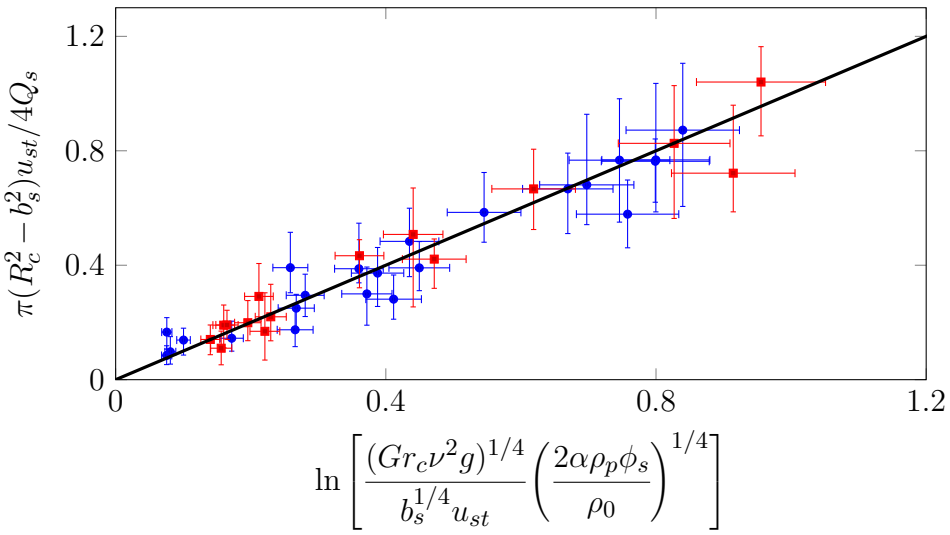

Fig. 4.6 The scaled convection column radius against the dimensionless particle loading at the plume spreading height. For the experimental data to pass through the origin as plotted, $Gr_c = 4.6 \times 10^4$. Data points are split into Type 3 (•) and 3* (▪) plumes.

environment where no ambient density gradient was present. Authors who studied particle-laden currents, either at the surface of an unstratified environment or at the density interface of a two-layer stratification, have suggested a critical value of $Gr = 10^3$ for convective sedimentation (Carazzo and Jellinek, 2012; Cardoso and Zarrebini, 2001a; Hoyal et al., 1999).

From the definition of the Grashof number, the likely driver for this significant difference lies with the convection length scale, as $Gr \sim L_c^4$ when calculated using the particle-induced density gradient below the plume intrusion. If no other parameters influence the observed differences in the critical Grashof number, this scaling suggests that the convection length scale in the stratified case is approximately 3 times greater than in the unstratified case. Previous suggestions in the literature regarding the length scale associated with convective sedimentation from a particle-laden current include the thickness of the particle-bearing layer at the base of the intrusion (Cardoso and Zarrebini, 2001a), and for currents which have been produced by stratified particle-laden plumes or jets, the difference in the spreading and maximum plume heights (Carazzo and Jellinek, 2012). Due to an interest in convection below the intrusion, the former approach is expected to be more suitable than the latter.

In a fluid of uniform density, a particle-rich interface with a thickness of less than 2 cm is sufficient to achieve turbulent ambient convection below intrusions with similar particle concentration gradients as those in this study (Carazzo and Jellinek, 2012;

Cardoso and Zarrebini, 2001a; Hoyal et al., 1999). This small interface is not consistent with the experiments presented here and in fact, turbulent convection between the intrusion and the plume source is only realised following the development of a particle-rich trough of dyed fluid below the intrusion. The reasoning for this is likely because the sedimentation in previous studies occurs within a fluid of uniform density where there are no barriers to inhibit the descent of dense particle-rich fingers from the current to the base of the tank. This however is not the case in linearly stratified experiments where the density of the environment increases when moving from the fluid surface towards the tank floor. This gradient creates the potential for the particle-rich fluid associated with convective sedimentation to decelerate and become neutrally buoyant at a height above the base of the tank. In the case of such an event, the light fluid will rise back up in the environment, whilst the heavy particles will continue to settle, but at a velocity independent of ambient convection. This process is observed in transitional Type 2 plumes, where both Stokes settling and convective settling are present below the intrusion.

Therefore, it is expected that the convection length scale in these intrusions is associated with the depth of the plume trough, or alternatively, the depth dyed fluid is pulled down from the intrusion into the environment. For trough depths less than the critical length scale, the buoyancy forces driving the downwards convection quickly decay to zero and any perturbations are sufficiently damped by viscous forces. Conversely, beyond this critical depth, buoyancy forces in the trough are large enough such that turbulent convection continues to the base of the tank. For those experiments where the plume trough is clearly visible, the trough depths (both time-averaged and spatially averaged across the width of the convection column) are plotted on Figure 4.7 against the critical convection length scale,

$$L_c = \left(\frac{\rho_0 Gr_c \nu^2}{g\rho_p} \left(\frac{d\phi}{dz} \right)_{R_c}^{-1} \right)^{1/4}, \tag{4.23}$$

where $Gr_c = 4.6 \times 10^4$.

In all cases, it is found that the average trough depth across the convection column exceeds the critical length scale leading to the onset of convection. It is important to note that the plume trough is parabolic in shape with the greatest depth present at the edge of the plume. This, combined with the fact that $d\phi/dz$ decays exponentially away from the plume edge, suggests the maximum Gr below the intrusion develops at a radius of $r = b_s$, before decaying to the critical value, Gr_c, at $r = R_c$. Although the

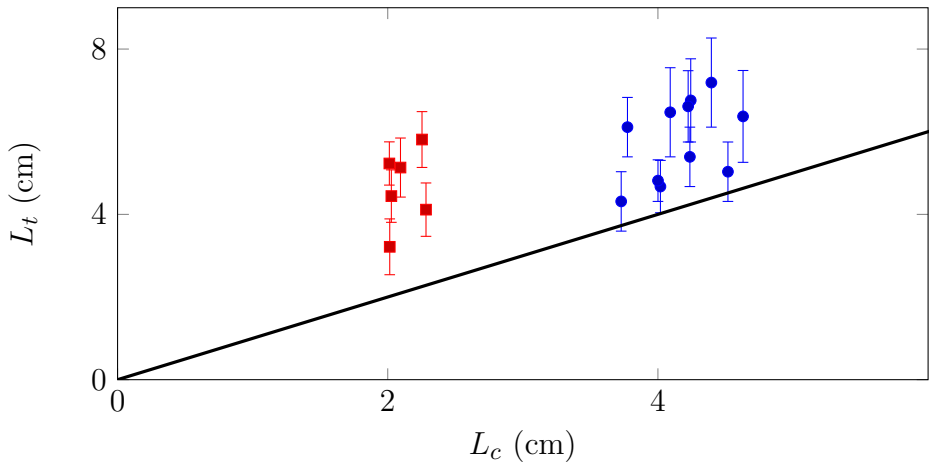

Fig. 4.7 Plume trough depth against the convection length scale at R_c. The solid line details the critical length scale and the data points relate to depth of the plume trough, averaged across space and time, for 70 μm (●) and 100 μm (■) ballotini experiments.

flow transition at the edge of the plume was determined in Chapter 3 using Gr_c, the particle gradient below the intrusion calculated then assumed a particle re-entrainment coefficient of $Q_s\phi_s/Q_0\phi_0 = e^1$. Despite being necessary at that stage to understand steady-state plume behaviour using source and ambient parameters, concentration sampling at the top of the plume showed that this level of re-entrainment was not achieved when convection was present in the environment (see section 4.4.3 for further details). Therefore, in order to obtain an ambient velocity sufficient to overcome the terminal velocity of each individual particle, the Grashof number at the edge of the plume must be larger than Gr_c. Here, it is expected that this large Gr is mostly a result of the large convection length scale present at short radial distances from the plume. It is also expected that the ratio $Gr(d\phi/dz)^{-1}$ is inversely proportional to r due to the observed change in trough depth when moving away from the edge of the plume.

Mechanism for the change in ambient density

In section 4.4, $\Delta\rho_e$, the term associated with the measured density difference at all heights in the convection column compared to the original stratification, was introduced. This value is of vital importance when determining both the terminal steady-state rise height of the plume and the height of the secondary intrusion above the tank floor. As such, the physical origin of this term must be understood. Inspection of Tables 4.1 and 4.2 appears to show that the magnitude of the density change is proportional to the

ambient stratification strength, suggesting that light fluid, high in the tank, is mixing with the heavier fluid present at lower levels. The only potential mechanism which could drive this mixing is if, whilst settling, the particles present in the environment drag down a portion of lighter fluid from above to mix with the denser fluid below - a phenomenon previously observed in simulations concerning particles settling through a stratified ambient (Blanchette, 2013).

Now, consider the potential for each particle settling from the intrusion to drag down some volume of intrusion fluid (or ambient fluid at that height), resulting in a reduction in the density of the fluid in the convection column. The maximum required volume of fluid per particle to achieve a certain change in ambient density can be determined by conducting a simple mass balance for the extreme case of mixing between fluid in the intrusion and the environmental fluid directly below. The balance is written as

$$V_p\rho_p + [V_t - (V_p + V_f)]\rho_{original} + V_f\rho_{fluid} = (V_t - V_p)\rho_{new} + V_p\rho_p, \tag{4.24}$$

where V_t is the total volume of the control volume; V_f and V_p are the respective volumes of the newly introduced fluid and particle components; $\rho_{original}$ is the original density of the fluid in the control volume; ρ_{fluid} is the density of the fluid introduced into the control volume; and ρ_{new} is the new density of the fluid in the control volume after mixing. As $V_t \gg V_p$, (4.24) can be simplified to

$$[V_t - (V_p + V_f)]\rho_{original} + V_f\rho_{fluid} \approx V_t\rho_{new}. \tag{4.25}$$

If $\rho_{original} = \rho_0$, following some rearrangement, (4.25) may be rewritten as

$$-\frac{1}{\phi_e}\frac{\Delta\rho_e}{\rho_0} \approx 1 + \frac{V_f}{V_p}\left(1 - \frac{\rho_{fluid}}{\rho_0}\right), \tag{4.26}$$

where $\Delta\rho_e = \rho_{new} - \rho_0$ and $\phi_e = V_p/V_t$. For simplicity, ρ_{fluid} is assumed to be associated with the fluid at the height of the intrusion and using the definition $\rho_{fluid} = \rho_0(1 - N^2 z_s/g)$, (4.26) can be simplified to

$$-\frac{1}{\phi_e}\frac{\Delta\rho_e}{\rho_0} \approx 1 + \frac{V_f}{V_p}\left(\frac{N^2 z_s}{g}\right). \tag{4.27}$$

Previous forced plume studies have suggested $z_s \sim \alpha^{-1/2}(B_0/N^3)^{1/4}$ for $\sigma < 49$ (Richards et al., 2014; Sutherland and Hong, 2016). With this scaling, along with

$V_p = \pi d_p^3/6$, (4.27) may be written in terms of both source and stratification parameters as

$$-\frac{1}{\phi_e}\frac{\Delta\rho_e}{\rho_0} \approx 1 + \frac{6V_f}{\pi d_p^3}\left(\frac{B_0^{1/4}N^{5/4}}{\alpha^{1/2}g}\right). \tag{4.28}$$

Upon plotting the left and right-hand sides of equation (4.28) on Figure 4.8, it is found that the experimental measurements follow the appropriate scaling when V_f is constant, irrespective of particle diameter, and equivalent to 2.25×10^{-4} cm^3. This suggests that each particle drags $\approx 10^3$ times its volume of fluid down into the environment. Such a volume does not seem unreasonable given the experimental observations concerning the radial extent of ambient convection seen in plumes with relatively dilute currents. It is also noteworthy that the radial extent of ambient convection, which directly relates to the downwards movement of fluid in the environment, is dependent upon the particle settling velocity rather than the particle diameter alone. Some scatter is observed in Figure 4.8, however this is likely due to ignoring the presence of momentum at the plume source (instead of differences in α), along with any small measurement errors associated with $\Delta\rho_e$ and ϕ_e.

As the intrusion continues to spread (see Figure 4.9), it can be said that the majority of the intrusion fluid does not mix with the ambient fluid in the convection column below and that most of the lighter fluid originates from lower levels in the tank. However, this does not mean that fluid from the intrusion is not initially dragged down into the environment, as is the case with the plume trough, prior to then rising again once the fluid has separated from the particles. Although $\Delta\rho_e$ is not necessarily the result of intrusion fluid being mixed throughout the entire convection column, it is expected that the particles settling through the column promotes the mixing of light ambient fluid with the heavier fluid below (Blanchette, 2013). As the particle settling in the convection column is continuous, the ambient stratification will be unable to restore itself to its original state, resulting in a lower ambient density near the source.

This mixing would cause one to expect that the ambient stratification would be destroyed, however, the stratified fluid external to the convection column becomes entrained. This is due to the radial inflow of fluid into both the central plume and the down-flowing convection column (see Figure 4.9a), where predicted velocities are of the same order of magnitude as those in fountains with similar absolute source values of M_0 and B_0 (Bloomfield and Kerr, 2000; Mingotti and Woods, 2016). It is this entrainment behaviour which is expected to cause the ambient stratification within the

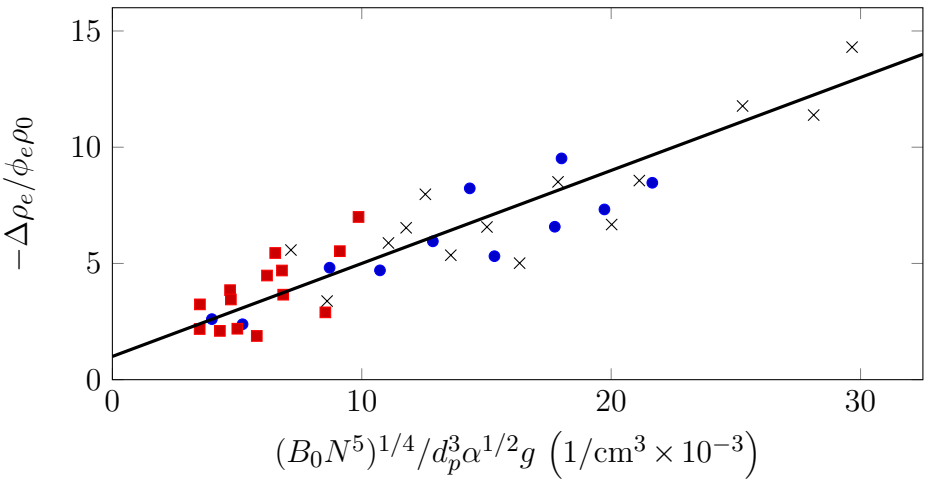

Fig. 4.8 The change in ambient density within the convection zone against the scale $(B_0N^5)^{1/4}/d_p^3\alpha^{1/2}g$. The points plotted represent results from 70μm (•) and 100μm (▪) ballotini and 70μm silicon carbide (×) experiments. The solid line has a coefficient of $6V_f/\pi = 4.3\times10^{-4}$ cm^3 and as per equation (4.28), an intercept of $y = 1$ when $x = 0$.

convection column to remain similar to its initial value and thus, results in a $\Delta\rho_e$ term constant with height.

Note however, to achieve this change in density below the intrusion whilst also observing little change in the ambient density gradient, the stratification in a portion of the environment must be destroyed such that the density jump can be achieved. Although not captured by discrete measurements, this density jump likely occurs immediately below the intrusion and is potentially associated with the plume trough (see Figure 4.9b). It is also expected that this density jump is likely the reason why the fluid density gradient plays no role in determining the radial extent of ambient convection, nor in the transition of particle settling regime.

4.4.3 Particle concentrations

The concentration of particles, both in the environment at the edge of the plume and in the plume at the spreading level, are key parameters in determining points of interest which have been discussed in previous sections, notably the plume rise height and the radial extent of ambient convection. Experimental measurements have suggested that the particle concentration within the convection column is constant and to predict this concentration, the work of Martin and Nokes (1988) is utilised. These authors considered crystal settling in a convecting magma chamber and stated that the velocity

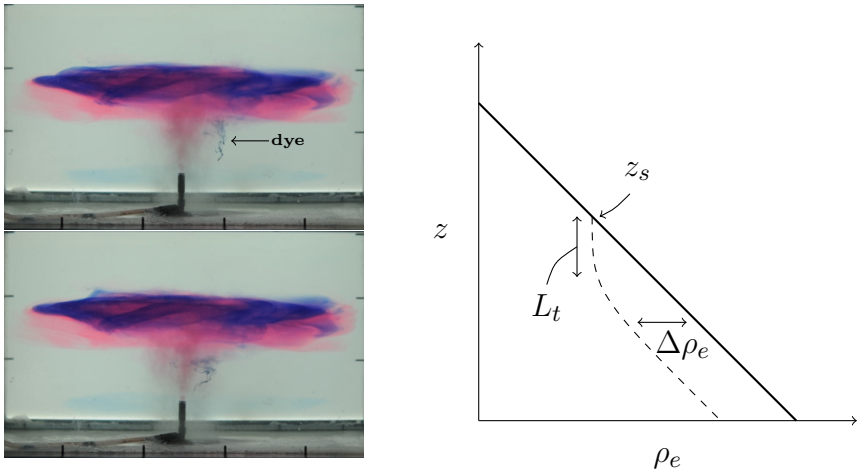

(a) (b)

Fig. 4.9 (a) Two subsequent frames of experiment 30 taken at steady state. Blue dye of the appropriate density was injected into the environment outside the convection column and the images show the lateral entrainment of ambient fluid. Convective instabilities appear to have negligible influence on the radial flow and allows the density gradient to be maintained. Blue dye was also injected near the source to observe spreading of the intrusion post-convection. Note the presence of a secondary intrusion near the source which is only visible in this Type 3 plume due to the injection of additional dye; (b) A schematic of the proposed density jump within the convection column to achieve $\Delta\rho_e$ and $dN/dt \approx 0$ between the source and the plume trough.

of the fluid must decrease to zero at the chamber boundaries, thus any particles in suspension must settle onto the base with their Stokes velocity. With this in mind, a steady-state balance may be written to give the ambient particle volume fraction as,

$$\phi_e = \frac{Q_0\phi_0}{\pi R_c^2 u_{st}}. \tag{4.29}$$

Here, a similarity to the work of Cardoso and Zarrebini (2001a) can be seen, note however their ambient particle concentration prediction for an unstratified plume was across the entire radius of the tank, whereas the prediction presented here is confined to the convection column radius around the plume. Due to the well-mixed ambient particle concentration, a second simple balance can be written to give the plume spreading level particle volume fraction as,

$$\phi_s = \frac{Q_0\phi_0 + (Q_s - Q_0)\phi_e}{Q_s}, \tag{4.30}$$

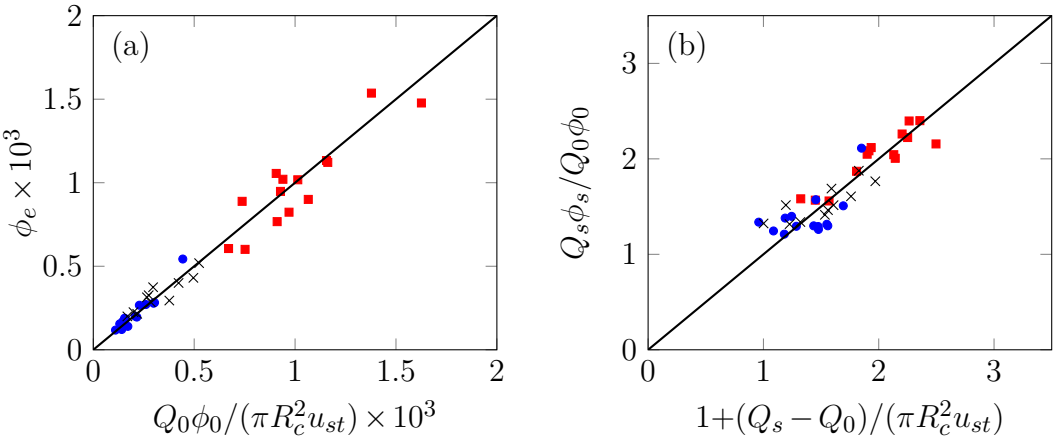

Fig. 4.10 Experimental measurements of (a) the convection column particle volume fraction, and (b) the plume re-entrainment coefficient, $Q_s\phi_s/Q_0\phi_0$, against the well-mixed theory. The points plotted represent results from 70 μm (•) and 100 μm (▪) ballotini and 70 μm silicon carbide (×) experiments.

which, once (4.29) is substituted into (4.30), becomes

$$\phi_s = \frac{Q_0\phi_0}{Q_s}\left[1+\frac{(Q_s-Q_0)}{\pi R_c^2 u_{st}}\right]. \tag{4.31}$$

Equations (4.29) and (4.31) are compared to experimental measurements in Figure 4.10 and it is found that both suitably predict the ambient and spreading particle volume fractions within the experimental uncertainty. Due to the success of these simple models, it's also worth noting that upon comparison of equation (4.31) with equation (4.22), the re-entrainment coefficient ($= Q_s\phi_s/Q_0\phi_0$) can be alternatively written in the form, $1+0.25/\ln[(Gr_c\nu^2 g/b_s)^{1/4}(2\alpha\rho_p\phi_s/\rho_0)^{1/4}u_{st}^{-1}]$, assuming that $Q_s \gg Q_0$ and $R_c \gg b_s$.

In Figure 4.10b, it is found that this coefficient in plumes rising in the presence of ambient convection can be as small as one, indicating that little to no particle re-entrainment occurs. The majority of values plotted are significantly less than the re-entrainment coefficient associated with plumes rising through quiescent environments ($= e^1$) and it is expected that this reduction in re-entrainment is a key factor in mitigating plume collapse.

4.5 Conclusion

Discrete measurements inside the convection column of stratified particle-laden plumes have provided great insight into not only particle re-entrainment behaviour, but also the condition of the fluid stratification surrounding the plume following the onset of particle-induced convection.

These insights have allowed many parameters in Type 3/3* plumes to be accurately predicted. Among those parameters is the steady-state rise height which can be determined by utilising a simple initial condition modification when integrating the well-known plume equations. In addition to this, it is found that the radial extent of convection in the environment can be predicted using approximately the same Grashof number as that to determine the particle settling regime. However, no relationship has been determined between this radius and the development of secondary intrusions between the primary intrusion and the tank floor.

Instead, it is expected that observing a fountain-like downflow is associated with one of two things. Either the depth of the plume trough, which is also the length scale associated with the onset of convection, is responsible for the transition; or alternatively, Type 3 and 3* plumes may in fact be one and the same. This hypothesis is suggested as actually observing the fountain between the primary intrusion and the base of the tank is fully dependent upon a sufficient concentration of dye being present within the dragged down fluid. This may not be the case if the source fluid becomes very dilute through entrainment and notably, secondary intrusions do becomes visible in Type 3 plumes when dye is added to the convection column (see Figure 4.9a). This suggests that a fountain-like downflow may be visible in these plumes given a greater source dye concentration.

Irrespective of whether a physical difference between Type 3 and 3* plumes does indeed exist, neither the experimental measurements in this study, nor the previous convective velocity estimates, provide a clear picture on this regime transition. It is therefore suggested that future authors first identify whether this observation is simply the result of insufficient dye by conducting a number of experiments with varying dye concentration in the source fluid. If this is determined not to be the case, it would be best to focus their efforts specifically on gaining an array of direct velocity and density measurements within the trough region below the plume intrusion.

Chapter 5

Radial spreading of turbulent bubble plumes

This chapter has been published as Sigurðardóttir, A., Barnard, J.M., Bullamore, D., McCormick, A., Cartwright, J., and Cardoso, SSS. (2020). Radial spreading of turbulent bubble plumes. *Philosophical Transactions of the Royal Society A*, 378(2179):20190513. The manuscript was prepared by Ms. Arna Sigurðardóttir, myself and Prof. Silvana Cardoso following the Stokes 200 conference. Most experiments and analysis presented were conducted by Ms. Sigurðardóttir and myself. Some experiments were also conducted by Part IIB students, Ms. Danielle Bullamore and Ms. Amy McCormick.

5.1 Summary

Weak bubble plumes carry liquid from the environment upwards and release it at multiple intermediate levels in the form of radial intrusive currents. In this study, laboratory experiments are performed to explore the spreading of turbulent axisymmetric bubble plumes in a liquid with linear density stratification. The thickness, volumetric flowrate, and spreading rates of multiple radial intrusions of plume fluid were measured by tracking the movement of dye injected at the source of bubbles. The experimental results are compared with scaling predictions. Our findings suggest that the presence of multiple intrusions reduces their spreading rate in the viscous-buoyancy regime compared to that of a single intrusion. This work is of relevance to the spreading of methane plumes issuing from the seabed in the Arctic Ocean, above methane-hydrate deposits. The slower, multiple spreading favours the presence of methane-rich seawater close to the plume, which may reduce the dissolution of methane in the bubbles, and thus promote the direct transport of methane to the atmosphere.

5.2 Introduction

In 1851, Stokes derived an expression for the drag on a spherical pendulum bob moving in a viscous fluid (Stokes, 1851). This expression, by a modification of the boundary conditions, can describe the drag on a spherical bubble, and a further reshaping can also approximate the drag on a non-spherical bubble. Many such bubbles together constitute either a bubble cloud or a bubble plume. Bubble plumes are formed above a continuous source of gas bubbles in a liquid environment. The bubbles rise owing to buoyancy and carry ambient fluid upwards forming a plume of two phases (Asaeda and Imberger, 1993; Milgram, 1983; Schladow, 1992; Wüest et al., 1992). The bubbles originate either from point sources that form axisymmetric plumes, or line sources that give rise to two-dimensional plumes. In weak bubble plumes, a double structure develops: the bubbles are concentrated in a central region, around which liquid rises (McDougall, 1978; Socolofsky and Adams, 2003, 2005). The outer liquid plume rises more slowly than the inner plume and entrains ambient liquid. Liquid between the inner and outer plumes is exchanged by turbulent eddies. In a linear density stratification, the bubbles carry the negatively buoyant liquid upwards over only a relatively short distance, subsequently releasing it to the environment. This liquid from the outer plume then descends to a level of neutral buoyancy where it spreads horizontally. The liquid peeling occurs periodically throughout the vertical extent of the plume. The horizontal plume-liquid currents spreading in the environment are called intrusions. Similar mechanisms of intrusion formation have been described for gravity currents (Hogg et al., 2017) and single-phase plumes (Gladstone and Woods, 2014) in stratified environments.

Intrusive gravity currents, formed from direct injection of fluid or by a single-phase plume in a stratified environment, have been of interest to many researchers (Chen, 1980; Ivey and Blake, 1985; Kotsovinos, 2000; Ungarish, 2009; Zatsepin and Shapiro, 1982). Intrusion behaviour is characterised in terms of two spreading regimes when buoyancy is driving the flow. The initial spreading is determined by a balance of the inertial retarding force and the buoyancy force, leading to the spreading relation (Lemckert and Imberger, 1993a),

$$R_i = c_I (Q_i N)^{1/3} t^{2/3}, \tag{5.1}$$

where R_i is the radial position of the tip of the intrusion, N is the ambient buoyancy frequency, Q_i is the intrusion volumetric flowrate, and t is time. This balance corresponds to an intrusion Froude number $Fr = 8\pi c_I^3/9$ (Rooney and Devenish, 2014b;

Woods, 2010). At later times, the intrusion flow is slower, so that viscous forces become important. Once the viscous-buoyancy regime is established, the tip of the intrusion moves according to (Lemckert and Imberger, 1993a),

$$R_i = c_V \left(\frac{Q_i^4 N^2}{\nu} \right)^{1/10} t^{1/2}, \tag{5.2}$$

where ν is the kinematic viscosity. Lemckert and Imberger (1993a) proposed a time-scale for the change of regime, from the time taken for the inertia-buoyancy current thickness to collapse to the viscous-buoyancy one, as

$$t_r \sim GN^{-1} = \left(\frac{Q_i^2 N}{\nu^3} \right)^{1/5} N^{-1}. \tag{5.3}$$

Previous experimental and theoretical work suggests the ranges $c_I = 0.40 - 0.80$ and $c_V = 0.45 - 0.52$ (Chen, 1980; Ivey and Blake, 1985; Lemckert and Imberger, 1993a; Maxworthy et al., 2002; Zatsepin and Shapiro, 1982).

The initial vertical thickness of the intrusion formed from plume spreading is generally agreed to follow the scaling,

$$L_i \sim \ L_p = (B_0/N^3)^{1/4}, \tag{5.4}$$

where B_0 is the buoyancy flux at the source of the plume (Asaeda and Imberger, 1993; Chen, 2001). The exact value of the coefficient depends on the relative speeds of the bubbles and the plume. The typical range is $0.7 < L_i/L_p < 4.5$, the higher values being observed for higher plume speeds (Asaeda and Imberger, 1993; Chen, 2001).

In contrast to the above work on single intrusions, weak bubble plumes spread forming multiple intrusions, between which ambient fluid is entrained into the plume. This periodic spreading pattern has not been studied quantitatively before. In this work, laboratory experiments are performed to explore the spreading of weak axisymmetric bubble plumes in a liquid with linear density stratification. The thickness, volumetric flowrate, and spreading rates of the multiple radial intrusions were measured by tracking the movement of dye injected at the source of bubbles. This preliminary study helps the understanding of the structure and spreading of methane bubble plumes in the Arctic sea. Numerous such plumes (where $B_0 \approx 10^3 \sim 10^4\ \mathrm{cm^4 s^{-3}}$) transport the methane from depth to shallower regions in the seawater, and possibly to the atmosphere (Shakhova et al., 2019, 2010a, 2015).

5.3 Experimental methods

Laboratory experiments were carried out using the equipment shown schematically in Figure 5.1a. Tank T1 was made of acrylic and had inner dimensions of 69 cm x 69 cm x 50 cm. A double bucket system (B1 and B2) was used to create a linear density profile (Oster and Yamamoto, 1963). The density profile in tank T1 was measured using an Anton Paar DMA35n density meter. Nitrogen gas was supplied into tank T1 at a height 2.5 cm above the tank base using a stainless steel tube with a diameter of 1 mm (with the exception of three experiments where a 0.5 mm tube was used, marked with * in Table 5.1), forming a stream of bubbles. The flowrate of nitrogen was measured with a rotameter and controlled with a needle valve. Pressure in the nitrogen supply line was kept constant at 2 bara. The bubbles formed were ellipsoidal, with diameters in the range 2-12 mm. The bubble size can be assumed constant owing to negligible breakup, coalescence and expansion over the small height of the tank (Clift et al., 1978). Dye was fed into the tank at the same height as the gas using a syringe pump via a silicone tube of 1 mm diameter. The dye was a 5 gL^{-1} mixture of Acid Red 1 (Azophloxine) in water and was delivered at a rate of 5 $\mathrm{cm}^3\mathrm{min}^{-1}$.

A Nikon D300s DSLR camera with an AF-S Micro NIKKOR 60 mm f/2.8G ED lens was used to capture the experiments at 24 Hz and the images were processed using the MATLAB R2020B image processing toolbox. To ensure consistent lighting of the videos for image processing, an LED light sheet was placed behind the tank and all other light was eliminated by turning off ceiling lights and using two sets of blinds on the windows. From tracking the movement of the dye, the radius and thickness of each intrusion, as well as the total volume within it could be determined (Figure 5.1b). Further detail of the image processing is given in Bullamore (2019); McCormick (2019); and Sigurðardóttir (2019).

The experiments conducted in this project are given in Table 5.1 (complete raw data may be found at https://doi.org/10.17863/CAM.51658). The slip velocity of the bubbles u_b is presented in non-dimensional form,

$$U_N = \frac{u_b}{(B_0 N)^{1/4}}. \tag{5.5}$$

For most of the range of U_N studied, the bubble plumes have distinct and steady sub-surface intrusions (Asaeda and Imberger, 1993; Socolofsky and Adams, 2003).

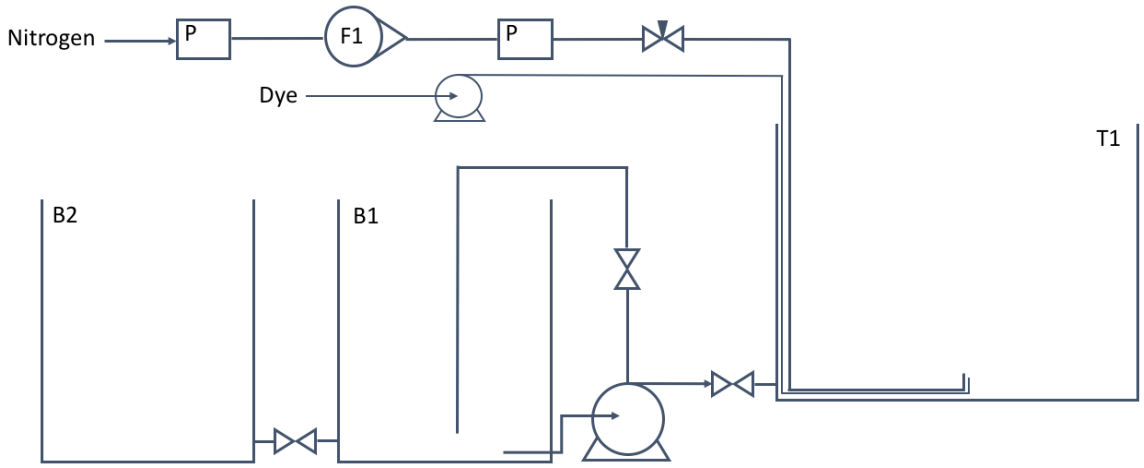

(a)

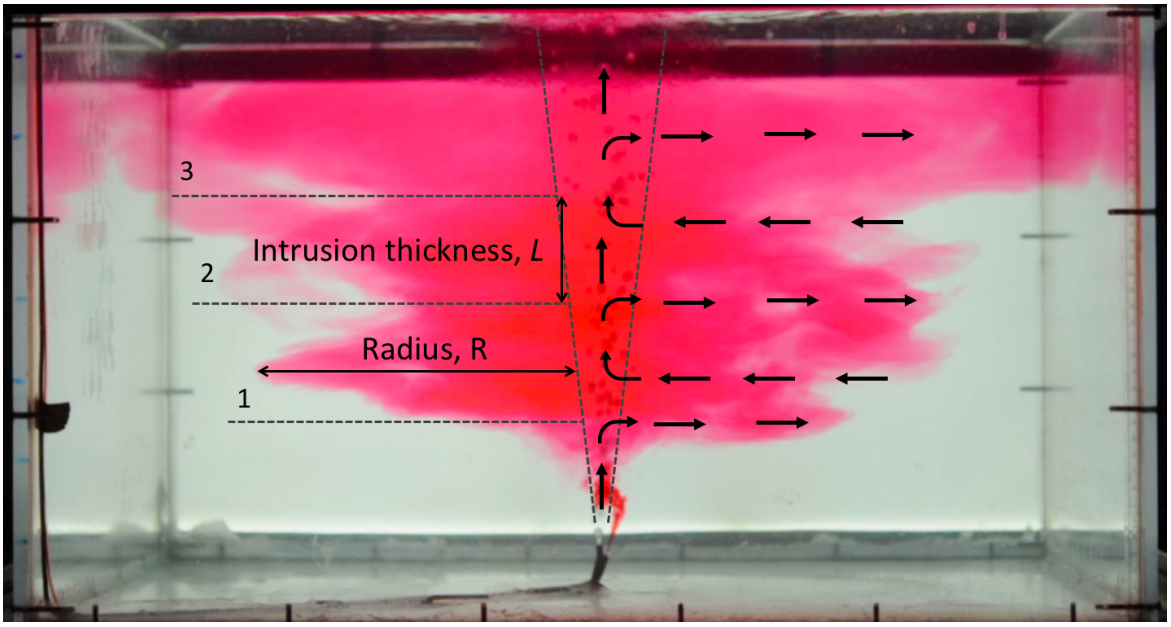

(b)

Fig. 5.1 (a) Schematic of the experimental setup. (b) General pattern of plume spreading. For each intrusion, the radius R_i and thickness at the edge of the plume L_i were measured. The edge of the plume is taken to be the radius of the bubble core, indicated by the dotted lines. Black arrows illustrate the flow of liquid. Intrusions are numbered from the bottom as shown.

Exp	$\boldsymbol{Q_b}$ ($\mathrm{cm^3 s^{-1}}$)	$\boldsymbol{B_0}$ ($\mathrm{cm^4 s^{-3}}$)	$\boldsymbol{N}$ ($\mathrm{s^{-1}}$)	**Intrusions** (-)	$\boldsymbol{U_N}$ (-)
1*	20	19620	1.10	2	2.00
2*	20	19620	1.45	3	1.87
3	18	17658	0.79	1	2.25
4	18	17658	1.03	2	2.10
5	18	17658	1.12	2	2.06
6	18	17658	1.25	2	2.00
7	15	14715	0.82	2	2.32
8	15	14715	0.93	2	2.25
9	15	14715	1.22	2	2.10
10*	15	14715	1.35	3	2.05
11	10	9810	0.97	3	2.46
12	10	9810	1.02	3	2.43
13	10	9810	1.11	3	2.38
14a	10	9810	1.23	4	2.31
14b	10	9810	1.23	4	2.31
15	10	9810	1.45	4	2.23
16	5	4905	1.04	3	2.88
17a	5	4905	0.92	3	2.97
17b	5	4905	0.92	3	2.97
17c	5	4905	0.92	3	2.97
17d	5	4905	0.92	3	2.97
17e	5	4905	0.92	3	2.97
17f	5	4905	0.92	3	2.97

Table 5.1 List of experimental parameters. Note here that the source buoyancy flux is defined as $B_0 \approx Q_b g$.

5.4 Results and Discussion

Figure 5.2 shows the typical evolution of the spreading of the bubble plumes. The injected red dye is quickly diluted within the plume and carried upwards. At early times, multiple intrusions develop, which gradually spread radially. The entrainment of ambient fluid into the plume occurs in the non-dyed fluid region below and between the intrusions. Once the intrusions reach the wall of the tank, the dyed fluid is re-entrained into the plume and eventually fills the entire tank.

The intrusion thickness, measured at the edge of the plume, is approximately independent of time and proportional to the Ozmidov Length, L_p (Asaeda and Imberger, 1993), as shown in Figure 5.3. The results are separated by intrusion number and can be seen to follow the expected scaling of (5.4) with a coefficient $L_i/L_p = 0.83 \pm 0.14$.

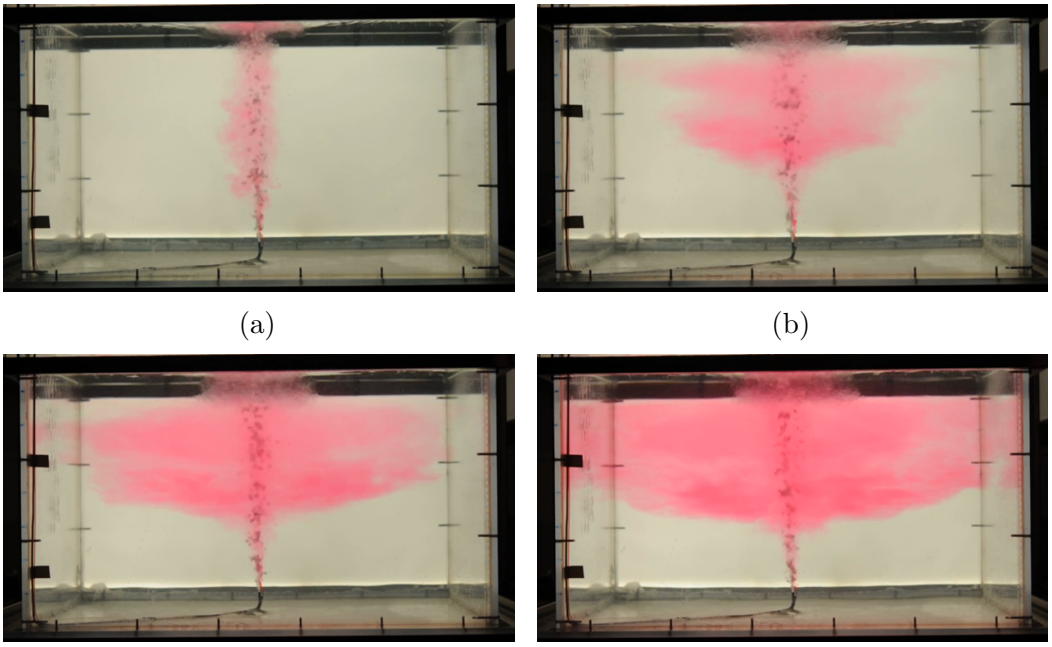

Fig. 5.2 Spreading of a bubble plume with gas flowrate 18 cm^3s^{-1}, in stratification with $N = 1.25$ s^{-1} (experiment 6). Photographs were taken after (a) 1 s, (b) 30 s, (c) 60 s, and (d) 90 s.

The measurements presented are instantaneous ones; the typical time evolution is shown in Figure 5.3b for intrusions 1 and 2 in experiment 17d. The scatter of the data in the time evolution is consistent with that in the scaling. The difficulty in measuring the intrusion thickness using image processing, owing to the local mixing produced by the bubble core, precluded the use of a time-averaged thickness for all intrusions.

The intrusion flowrates, Q_i, were determined from the slope of the straight line fit for the intrusion volume as a function of time (Figure 5.4). The intrusion volume was calculated by measuring the intrusion thickness as a function of radius at a given time, from the two-dimensional image view from the front of the tank, and then integrating assuming axisymmetry. However, discrepancies were observed to occur between the right and left sides of each current, as seen in Figure 5.4, partly owing to this axisymmetric assumption. The initial behaviour, while the plume is established, was neglected in the calculation of the flowrate. The large-time behaviour, with an apparent constant volume, is an image-processing artefact and was also neglected. Indeed, as an intrusion approaches the tank wall, it spreads vertically; this spreading was neglected in the calculation of the intrusion volume flux owing to the utilisation of an image-analysis control volume of set height. The set control volume height results

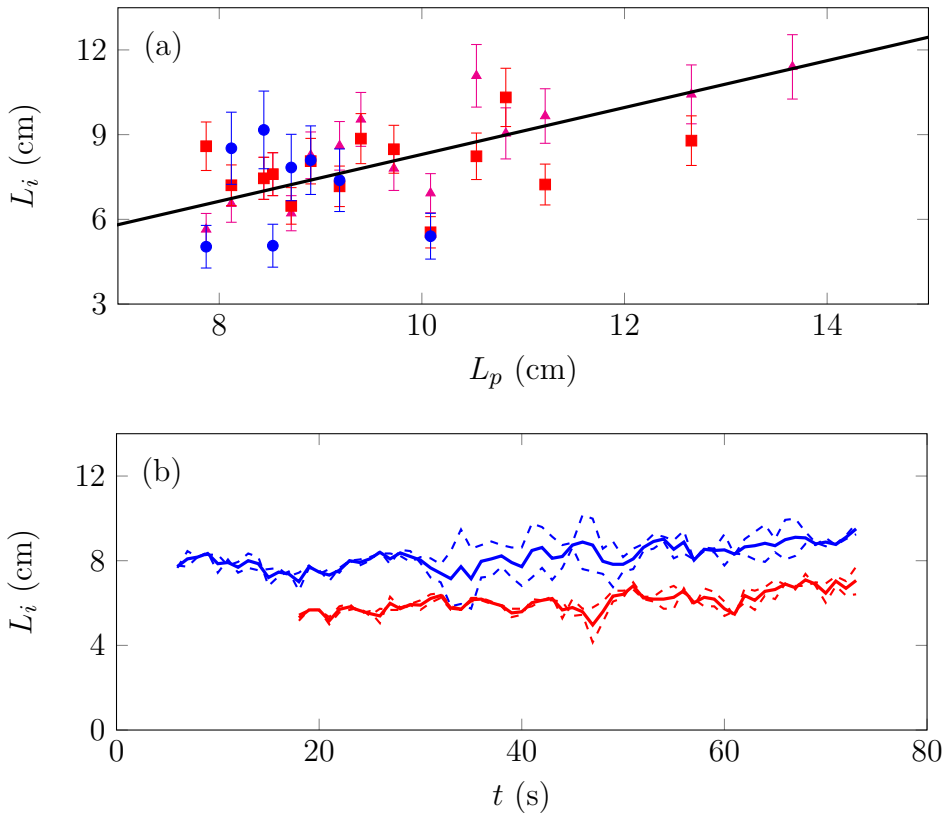

Fig. 5.3 (a) Instantaneous intrusion thickness against the Ozmidov length, where the points correspond to intrusion numbers 1 (●); 2 (■); and 3 (▲) counted from below. The scaling is constrained to intersect the origin. The error bars represent the standard deviation of results from repeated experiments. (b) Evolution of the thickness of intrusions 1 (——) and 2 (——) for experiment 17b. Dashed lines show variations between results from the left and right-side of the plume images.

in the flattening of the volume curves, as shown in Figure 5.4, and allows the intrusion volume flux to be determined from the curve using the largest time interval with an approximately constant slope prior to any intrusion interaction with the wall.

Figure 5.5 shows the intrusion flowrate plotted against the scaling group, $(B_0^3/N^5)^{1/4}$. The flowrate is larger for the top intrusion owing to the release of the liquid carried with the bubbles in the central part of the plume, in addition to the liquid dragged in the outer plume. For the lower intrusions, 1 and 2, the flowrate follows the expected scaling with a coefficient $Q_i/(B_0^3/N^5)^{1/4} = 0.13 \pm 0.06$. This flux is much lower than that reported by Socolofsky and Adams (2003) for sediment plumes in the same range of U_N (their Figure 8), possibly owing to the much weaker plumes studied here. The relatively large experimental error is a result of the deviation of the plume spreading

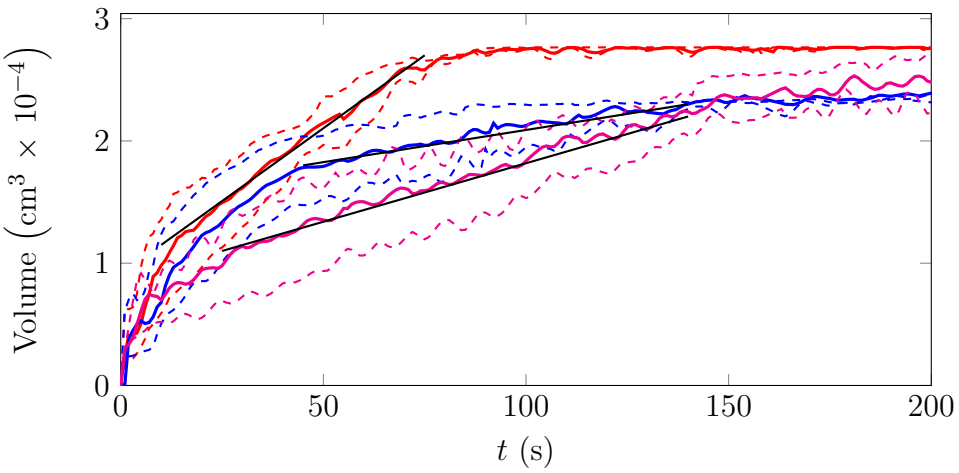

Fig. 5.4 Intrusion volume with respect to time for Experiment 17f. Coloured lines correspond to the volume of intrusion 1 (—); 2 (—); and 3 (—). Coloured dashed lines show variations between results from the left and right-side of the plume images. The slope of the best line through the data is the volumetric flowrate of the intrusion, Q_i.

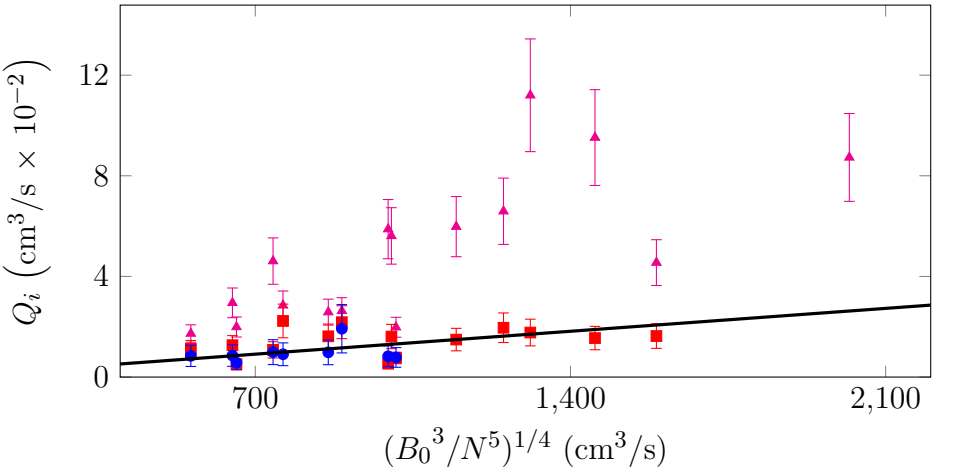

Fig. 5.5 Intrusion flowrate against $({B_0}^3/N^5)^{1/4}$. Points correspond to intrusion numbers 1 (•); 2 (■); and 3 (▲). The scaling is constrained to intersect the origin. The error bars represent the standard deviations of results from repeated experiments.

from the exact axisymmetric one and is consistent with the magnitude of the difference between the left and right-hand side results presented in Figure 5.4.

Figure 5.6 presents the radial spreading of several intrusions as a function of time. The inertia-buoyancy and viscous-buoyancy regimes were identified, from the changing slopes, from $t^{2/3}$ in the inertia-buoyancy regime to $t^{1/2}$ in the viscous-buoyancy regime,

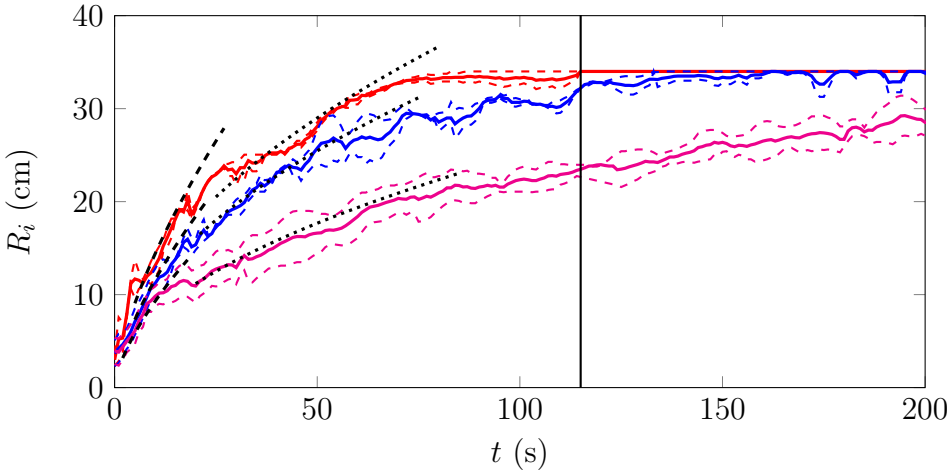

Fig. 5.6 Intrusion radius with respect to time for experiment 17b. Solid lines correspond to average radius for intrusion 1 (—); 2 (—); and 3 (—). Coloured dashed lines show variations between results from the left and right-side of the plume images. Predicted inertia-buoyancy ($R_i \sim t^{2/3}$) and viscous-buoyancy ($R_i \sim t^{1/2}$) regimes are shown by black dashed lines and black dotted lines, respectively. The vertical line signals the time at which the surface intrusion reaches the wall of the tank.

as shown. In the experiments presented here, the transition time between the inertia-buoyancy and viscous-buoyancy regimes, from (5.3) is expected to be about 100 s. The results indicate on average a lower transition time of around 20 s, which may be explained by the counterflow present in the multiple intrusions studied here. In each experiment, the top intrusion reached the wall of the tank after approximately 100 s.

The results from all the experiments are presented in Figures 5.7 and 5.8 for the inertia-buoyancy and viscous-buoyancy regimes, respectively. Multiple experiments with the same flowrate were conducted, therefore these figures do present a number of different intrusion paths associated with the same flowrate. The reference time, t_r, and reference radius, R_r, are taken to be the time and radius at which the transition to the viscous regime occurs. In the inertia-buoyancy regime, the inner plume radius, b_i, is used as a reference. Note that this radius was estimated at early times due to the inner plume being experimentally indistinguishable from the down-flowing outer plume shortly after plume injection (see Appendix B for details).

The spreading relationship determined for the inertia-buoyancy regime is $R_i = 0.39\,(Q_i N)^{1/3} t^{2/3}$, corresponding to an average Froude number of $Fr = 0.17$. The coefficient has a standard deviation of 0.08, corresponding to a Froude number range of $0.09 < \mathrm{Fr} < 0.31$. For the viscous-buoyancy regime, we obtained $R_i = 0.15\,(Q_i^4 N^{24}/\nu)^{1/10} t^{1/2}$,

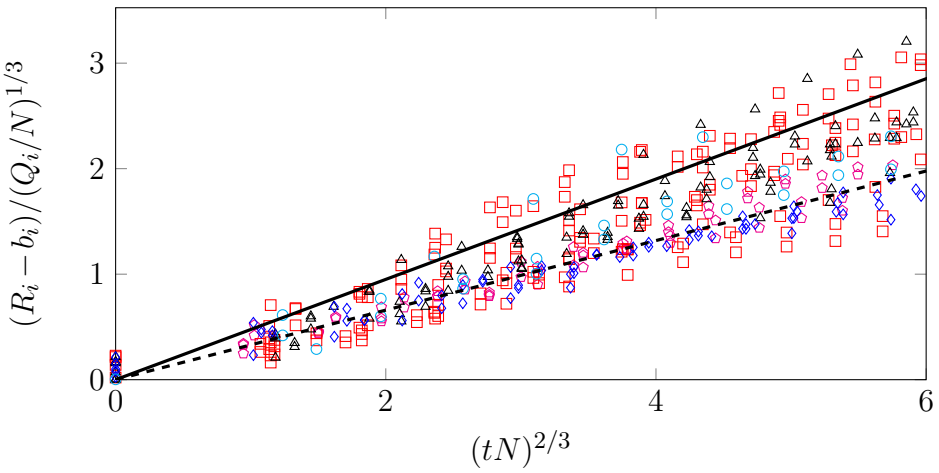

Fig. 5.7 Dimensionless intrusion radius with respect to dimensionless time in the inertia-buoyancy regime. Points correspond to bubble flowrates of $Q_b = 5$ cm^{3}s^{-1} (⬠); 10 cm^{3}s^{-1} (□); 15 cm^{3}s^{-1} (△); 18 cm^{3}s^{-1} (◇); and 20 cm^{3}s^{-1} (○). The black line and dashed line represent a Froude number of 0.3 and 0.1 respectively.

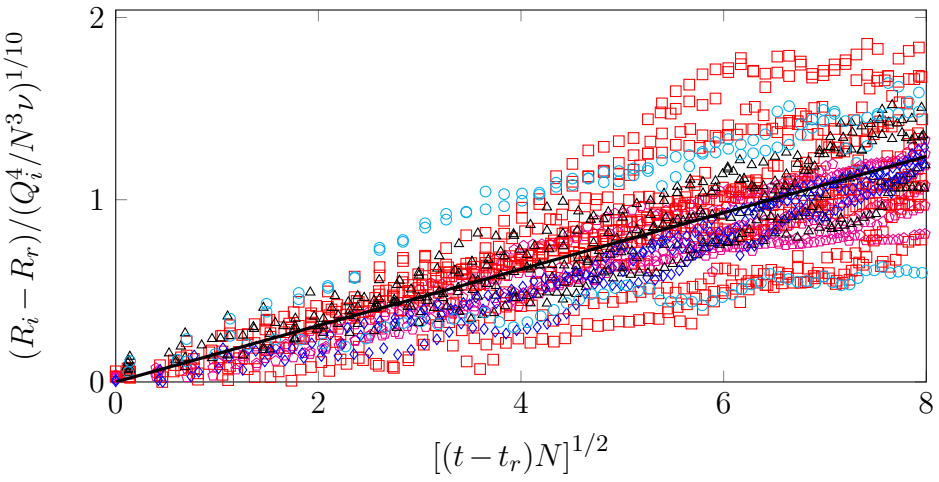

Fig. 5.8 Dimensionless intrusion radius with respect to dimensionless time in the viscous-buoyancy regime. Points correspond to bubble flowrates of $Q_b = 5$ cm^{3}s^{-1} (⬠); 10 cm^{3}s^{-1} (□); 15 cm^{3}s^{-1} (△); 18 cm^{3}s^{-1} (◇); and 20 cm^{3}s^{-1} (○). The black line represents the average scaling.

where the coefficient has a standard deviation of 0.02. The presence of the tank wall slows the spreading rate of the intrusion at large times in this regime, as noted in previous work (Ivey and Blake, 1985). The intrusion radius beyond which the presence of the wall became important varied for each experiment. To prevent wall effects from influencing the calculation of the intrusion spreading rate, we neglected all radial measurements

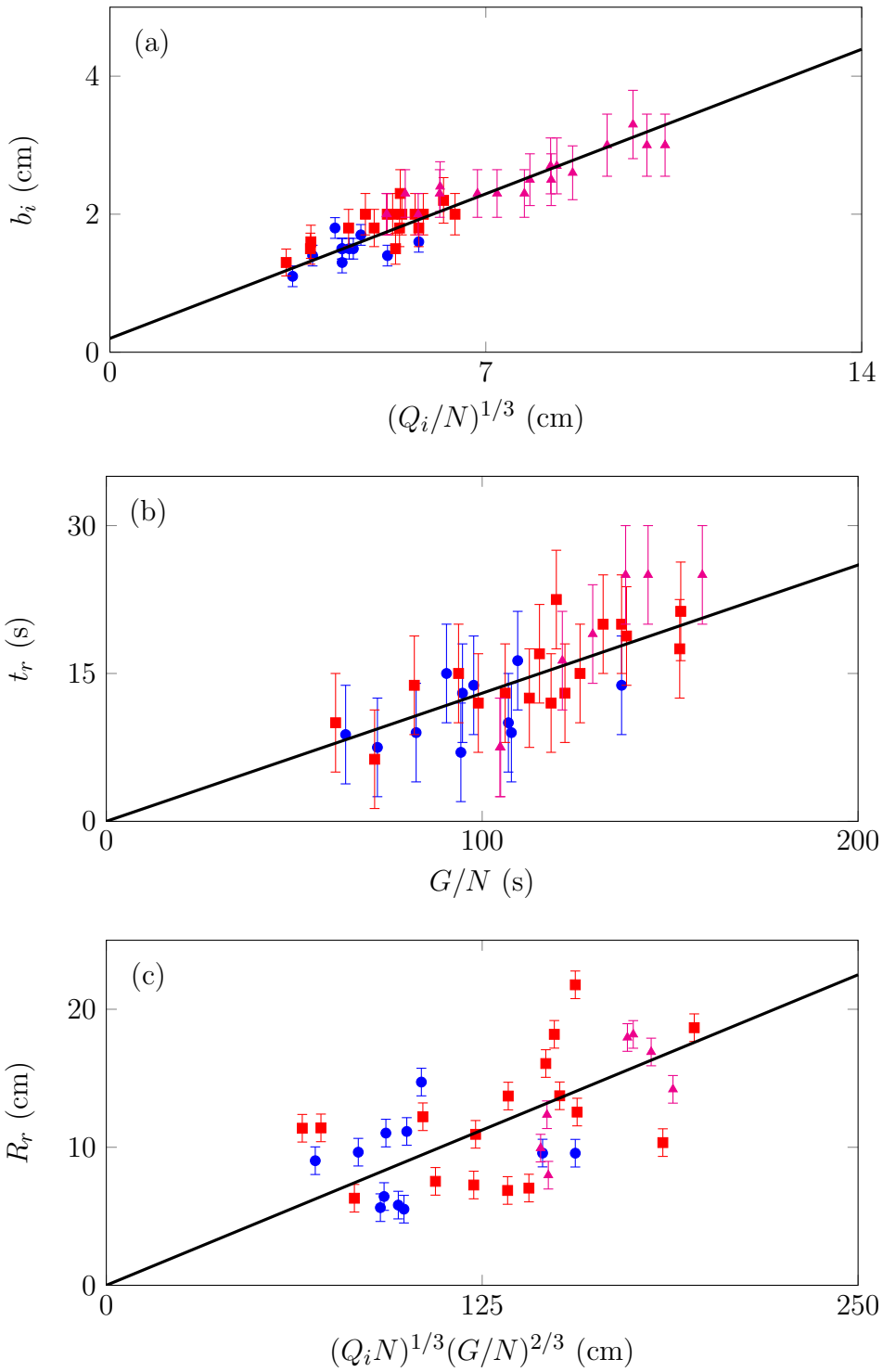

Fig. 5.9 The points correspond to intrusion numbers 1 (●); 2 (■); and 3 (▲) counted from below. (a) Plume radius b_i against $(Q_i/N)^{1/3}$. The line of best fit has a coefficient of 0.33 ± 0.07. (b) Reference time t_r against G/N as predicted by the scaling (5.3). The line of best fit has a coefficient of 0.13 ± 0.05. (c) Reference radius R_r against the length scale predicted by (5.3) and (5.1). The line of best fit has a coefficient of 0.09 ± 0.03.

Study	c_I	c_V	**Type of flow**
Chen (1980)	0.802	0.45	Asymptotic solutions for submerged spreading.
Zatsepin & Shapiro (1982)	Not studied	0.52	Laboratory experiments: Constant discharge at level of neutral buoyancy.
Ivey & Blake (1985)	Not studied	0.45	Laboratory experiments: Constant discharge at level of neutral buoyancy.
Lemckert & Imberger (1993a)	0.40 ± 0.13	Not studied	Field experiments: Intrusions generated by deep-set point-source bubble plume systems.
Current results	0.39 ± 0.08	0.15 ± 0.02	Laboratory experiments: Intrusions of point-source bubble-plumes.

Table 5.2 Comparison of spreading coefficients for the inertia-buoyancy and viscous-buoyancy regimes for radial intrusions in linear stratification.

beyond which there was an obvious gradient reduction without subsequent recovery back to the original gradient. The offsets b_i, R_r and t_r used in Figures 5.7 and 5.8 are presented in Figure 5.9 as a function of the experimental parameters. The offset of 0.20 from the origin in Figure 5.9b is associated with the plume originating from a real source. Assuming a plume spread similar to that of a single-phase plume in an unstratified environment, the average virtual source is 2.6 cm below the real source for an average plume entrainment coefficient $\alpha = 0.063$, aligning with previous measurements for weak bubble plumes (Milgram, 1983). The scatter in Figure 5.9c reflects the difficulty in setting the transition between the inertia and viscous regimes and partly explains the spread of data in Figure 5.8.

Table 5.2 compares these results to previous work in linear density stratification, with either direct injection of fluid into an intrusion or a plume intrusion. Although we do not present the results of Kotsovinos (2000) for a jet intrusion, owing to the different scaling used in that study, it is worth noting that his results (see his Figures 14 and 15) are in quantitative agreement with those of Zatsepin and Shapiro (1982) and Lemckert and Imberger (1993a). For the inertia-buoyancy regime, our finding of $c_I = 0.39$ is consistent with the measurement of Lemckert and Imberger (1993a) for a single intrusion formed from a bubble plume. The theoretical result of Chen (1980) is

much larger at $c_I = 0.802$. The speed of the intrusion in this regime is largely set by the energy dissipation at its nose (Ungarish, 2009), so the consistency of the coefficients for single and multiple spreadings suggests that the periodic counterflow of ambient fluid in the latter does not affect the energy balance. For the viscous-buoyancy regime, the theoretical results of Chen (1980), and the experimental results of Ivey and Blake (1985) and Zatsepin and Shapiro (1982), for direct injection of fluid, are in the narrow range of $c_V = 0.45 - 0.52$. The coefficient found in our work for multiple bubble-plume intrusions is significantly smaller. The slower spreading in our study may be explained by the counter flow of the environmental fluid between the multiple intrusions as it is entrained into the plume. Although this counter flow does not seem to affect the dissipation of energy at the nose of the intrusion in the inertia-buoyancy regime, a higher viscous friction is expected at lower speeds.

Our findings suggest that dissolved methane may be retained relatively close to rising methane bubble plumes in the Arctic sea, thus reducing the dissolution of methane and promoting the direct transport of methane to the atmosphere. However, given the implications, especially when considering the potential application described here, a caveat must be added to these results as the intrusions studied in this work were confined with a maximum spreading radius of approximately 30 cm. This means that the individual spreading regimes in a given intrusion may only cover a distance of 15 cm or less and this made it particularly difficult to both apply power laws and determine the point of regime transition. Also, despite our best efforts to eliminate wall effects, confinement may continue to influence the spreading rate of the intrusions, especially in the viscous-buoyancy regime, where the significant reduction in spreading rate compared to typical intrusions is observed.

5.5 Conclusion

Laboratory experiments were performed to quantify the spreading of turbulent axisymmetric bubble plumes in a linear density stratification. Weak bubble plumes characterised by multiple, periodic radial intrusions were considered. It was found that the spreading in the inertia-buoyancy regime was slower than theoretical results for single intrusions but consistent with experimental observations of bubble plume systems forming single intrusions. This consistency of the intrusion speed for single and multiple spreadings suggests that the periodic counterflow of ambient fluid in the latter does not affect the energy balance at the nose of an intrusion. Spreading in the viscous-buoyancy regime was significantly slower than that reported from both

theoretical and experimental results for single intrusions formed by direct injection of fluid. This slower spreading may be explained by the higher viscous friction caused by the counter flow of the environmental fluid between multiple intrusions, as it is entrained into the plume. This finding is of relevance to the spreading of dissolved methane by bubble plumes in the Arctic Sea. It would be of interest to extend this work to either unconfined bubble plume intrusions or alternatively, to intrusions spreading over a greater spacial range than the somewhat limited results presented here.

Chapter 6

Diffusion of dissolved species from ellipsoidal bubble plumes

This chapter has been submitted to the *Journal of Fluid Mechanics* as Barnard, J.M.; Harris, M.; Sigurðardóttir, A.; and Spry, M. (2021). *Diffusion of dissolved species from stratified ellipsoidal bubble plumes*. The text and analysis was all completed myself, expanding upon the work presented in Ms. Arna Sigurðardóttir's MPhil thesis (see Sigurðardóttir, 2019). Experiments were conducted by myself and Part IIB students, Mr. Matthew Harris and Mr. Matthew Spry.

6.1 Summary

The continuous release of bubbles from a point source into a liquid environment results in the development of a multiphase bubble plume, a flow of great interest in both industry and nature. As the bubbles rise, liquid becomes entrained into the bubble core and is carried to greater heights in the environment. When rising through a stratified ambient such as the ocean, dense liquid tends to peel away from the buoyant bubble core, creating multiple submerged intrusions capable of transporting any dissolved species radially away from the plume at various heights throughout the water column. In this study, plumes of ellipsoidal bubbles rising through stratified fluid were experimentally investigated in an attempt to understand the radial mass transfer of dissolved species from these plumes to the environment. Using dye as a representation for dissolved species, discrete measurements were taken radially along the plumes' submerged intrusions to show the presence of two distinct regions. Close to the bubble core, dye concentration decays from a maximum value at the centre of the plume to a lesser value at some defined radius. The intrusion dye concentration then

remains unchanged for increasing radial distances, suggesting that the plume bubble core induces significant near-field mixing and results in the re-entrainment of dissolved species from the environment back into the plume. Motivated by these observations, we develop a simple diffusion model characterised by a mixing radius R_m, an effective diffusion coefficient δ, and a constant dependent upon the plume's non-dimensional slip velocity, $U_N = u_b/(B_0 N)^{1/4}$. The results presented provide insight into not only how dissolved species is transported radially away from the plume, but also how mass is carried to greater heights in the environment due to the recirculation of fluid close to the edge of the plume.

6.2 Introduction

Bubble plumes are complex multiphase flows widely present in many industrial and environmental processes. For many years, bubble plumes have been utilised to destratify lakes and reservoirs (McDougall, 1978; McGinnis et al., 2004; Schladow, 1992), and more recently, have been observed rising through the ocean's water column due to the release of gaseous hydrocarbons from either natural seeps (Leifer et al., 2006; Skarke et al., 2014), or from industrial accidents such as Deepwater Horizon (Socolofsky et al., 2011).

Upon the release of a continuous stream of bubbles into a liquid environment, buoyancy forces drive the bubbles upwards, creating turbulence which subsequently results in the entrainment of ambient liquid into the bubble core. The magnitude of this driving force is characterised by a source buoyancy flux,

$$B_0 = Q_b g \frac{\rho_0 - \rho_b}{\rho_0}, \tag{6.1}$$

where Q_b is the bubble volume flux; g is acceleration due to gravity; and ρ_b and ρ_0 represent the density of the gas phase, and some reference density, generally taken as the density of the environment at the plume source. Importantly, due to gas compressibility, Q_b and ρ_b are both functions of height and the values utilised in (6.1) are also associated with the depth of the plume source.

Initially detailed by McDougall (1978) in his work on bubble plumes in quiescent linear stratification, bubble plumes differ from single-phase plumes because of two key aspects. Firstly, there is potential for the gas and liquid phases within the plume to have different rise velocities and secondly, in the case of a plume produced in a stratified environment, the bubble phase will continue to rise past the terminal height

predicted by simple plume theory (see Morton et al., 1956) and will create additional plume structures at greater heights above the source. Each additional plume structure, or peeling event, tends to follow a similar pattern where the bubbles force the fluid up in the environment until reaching a height where the density deficit between the interstitial fluid in the plume and the stratified ambient results in the detrainment, or peeling, of liquid from the bubble core. This peeling creates a counter flowing outer plume which traps at the height of neutral buoyancy, before spreading in the environment as a radial intrusion. To model this complex behaviour, McDougall (1978) proposed a plume model comprised of a rising inner plume of liquid and bubbles and a outer plume with regions of both ascending and descending liquid.

Since, this pioneering work, many authors have studied linearly stratified bubble plumes, both experimentally (Asaeda and Imberger, 1993; Sato and Sato, 2001; Seol et al., 2009; Sigurðardóttir et al., 2020; Socolofsky and Adams, 2003, 2005) and theoretically (Chu and Prosperetti, 2017; Crounse et al., 2007; Fabregat Tomàs et al., 2016; Socolofsky et al., 2008; Yang et al., 2016; Zhou, 2020). An important finding consistent across both experimental and theoretical works is the importance of the relative magnitude of the bubble slip velocity, u_b, to the plume velocity. Asaeda and Imberger (1993) characterised three stratified bubble plume regimes, each with distinctly different dynamics, as a function of two parameters associated with the plume buoyancy flux, the bubble slip velocity and the strength of ambient density gradient. Socolofsky (2001) expanded upon their analysis by considering an infinitely deep reservoir and subsequently re-defined the regimes as a function of a single parameter, the non-dimensional slip velocity,

$$U_N = \frac{u_b}{(B_0 N)^{1/4}}, \tag{6.2}$$

where N is the ambient buoyancy frequency.

U_N has since been shown to have a significant impact on the level of entrainment into both the inner and outer plumes, subsequently influencing both the plume trap height and the magnitude of the various liquid volume fluxes associated with each peeling event. Socolofsky and Adams (2003) identified the liquid fluxes for the n^{th} peeling event of a bubble plume (see Figure 6.1) as the inner plume flowrate at the trap height, Q_n, and the peeling height, Q_{n+1}; the entrainment volume flux into the inner, Q_r, and outer plume, Q_e; the detrainment or peeling flux, Q_p; and finally, the volume flux of the intrusion spreading in the environment, Q_i. Using these fluxes,

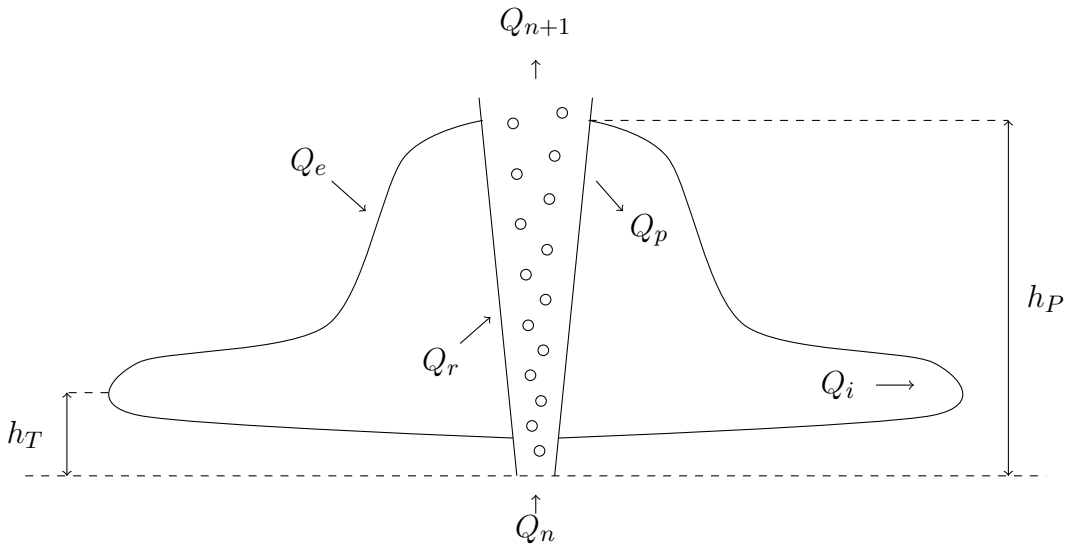

Fig. 6.1 A schematic of the n^{th} peeling event above the plume source. h_P and h_T denote the plume peel and trap heights.

the transfer of liquid between the inner and outer plumes can be described with the following balances,

$$Q_n + Q_r = Q_{n+1} + Q_p, \tag{6.3a}$$

$$Q_e + Q_p = Q_i + Q_r, \tag{6.3b}$$

$$Q_n + Q_e = Q_{n+1} + Q_i. \tag{6.3c}$$

A particular point of interest here is to extend equations (6.3a–c) to account for a dissolved species in the plume, present due to either bubble dissolution, chemical reaction or the entrainment of pollutants from the environment (Chu and Prosperetti, 2019; Domingos and Cardoso, 2013; Socolofsky and Bhaumik, 2008). In certain industrial or environmental settings, estimating the mass flux of dissolved species spreading with an intrusion is an important assessment tool in understanding the mass transfer from the plume to the environment. One such example is the transfer of hydrocarbons to the environment from deep ocean plumes associated with well blowouts (Socolofsky et al., 2011).

Localised mixing associated with the recirculation of fluid into the bubble core has the potential to reduce the concentration of dissolved species in the intrusion spreading radially from the plume and could promote the transport of mass to greater heights in the environment, potentially all the way to the liquid surface. The effect of localised

mixing in the intrusion close to the bubble core can be realised by considering the simple mass balance,

$$Q_e c_e + Q_n c_n = Q_i c_i + Q_{n+1} c_{n+1}, \tag{6.4}$$

where c_n and c_{n+1} represent the concentration of the dissolved species in the plume entering and leaving the n^{th} intrusion; c_i is the concentration in the intrusion; and c_e is the concentration in the environment. Now consider the mathematical identity associated with a well-mixed peeling event where the concentration of dissolved species in the inner and outer plume is assumed to be equivalent,

$$Q_e c_e + Q_n c_n = Q_i c_n + Q_{n+1} c_n. \tag{6.5}$$

Upon subtracting equation (6.4) from (6.5), the subsequent expression presents the difference between a discharge of dissolved species from a plume with localised mixing in the intrusion around the bubble core against the well-mixed case,

$$Q_i(c_n - c_i) = Q_n(c_{n+1} - c_n). \tag{6.6}$$

Here, it can be seen that the recirculation of fluid back into the plume bubble core results in a decreased discharge of dissolved species to the environment. Until present, no experimental measurements have been taken along the intrusion of a bubble plume to inform on the influence of localised mixing on dissolved species concentration, nor on the presence of the subsequent radial concentration profile associated with it. Socolofsky (2001) alluded to a radial concentration profile in the intrusions produced by their plumes due to waiting at least an hour after each experiment to allow for horizontal mixing of the dye before taking fluorescence measurements at a single radial location in their tank. The simulations of Yang et al. (2016) and Zhou (2020) also show an intrusion concentration profile, with dissolved species concentration decreasing for increasing radial distances away from the bubble core.

In this study, we show through experimental measurements that the concentration of dissolved species in a bubble plume intrusion of constant flowrate and density is, in fact, a function of intrusion radius, with two distinct concentration regimes present in the intrusion. Close to the edge of the plume is a mixing zone, where the concentration of dissolved species decays from a maximum value at the centre of the plume to some lesser concentration at a defined radius. Beyond the mixing zone, the concentration remains constant as the intrusion continues to spread radially. Motivated by these

experimental observations, we present a diffusion model to predict the concentration profile in a submerged intrusion spreading from a plume of ellipsoidal bubbles capable of comparison to both direct measurements and experimental or field images. We also discuss the relative magnitudes of the inner and outer plume radii and comment on the potential influence of mixing on the intrusion spreading rate.

6.3 Experimental methods

Bubble plume experiments were conducted in the laboratory through supplying nitrogen gas at the base of an acrylic tank with dimensions 69 cm x 69 cm x 50 cm. The tank was filled with aqueous sodium chloride solution to a height of 40 cm and a linear stratification was produced using the double-bucket method (Oster and Yamamoto, 1963). The strength of the density gradient created in each experiment is characterised using the ambient buoyancy frequency,

$$N = \sqrt{-\frac{g}{\rho_0}\frac{d\rho_e}{dz}}, \tag{6.7}$$

where $d\rho_e/dz$ is the ambient density gradient. This gradient was determined by measuring the density of the fluid in the mixed feed bucket with an Anton Paar DMA35n density meter whilst filling the tank. Measurements were taken at every 5 cm increment between the experimental tank being empty up to the maximum water level of 40 cm. To prevent any mixing with the less dense fluid present at higher levels in the tank, the inflow from the double-bucket system was kept sufficiently small to ensure laminar flow across the experimental tank base.

The gas was supplied to an upwards directed straight orifice, positioned in the centre of the tank using stainless steel tubing. Both the orifice and tubing had an internal diameter of $d_n = 1$ mm. A rotameter and needle valve were used to measure and control the nitrogen flowrate. The gas was delivered at a pressure of 2 bara, with pressure gauges positioned either side of the rotameter to ensure negligible pressure drop through the system. $5\,\mathrm{gL}^{-1}$ Acid Red 1 (Azophloxine) dye was fed into the tank via 1 mm diameter silicone tubing with an outlet at the same height as the bubble nozzle to assist with plume visualisation. The dye was delivered using a syringe pump at a rate of $5\,\mathrm{cm}^3\mathrm{min}^{-1}$. To ensure consistent lighting, a LED light sheet was placed outside the tank, directly behind the plume to provide an even distribution of light when viewing experiments.

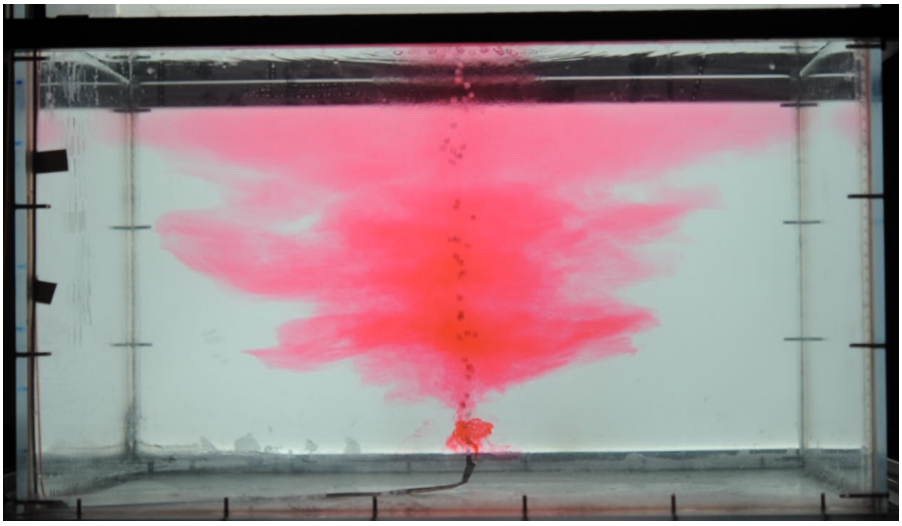

Fig. 6.2 A photograph of experiment 17 after 140 seconds. Two submerged intrusions ($n = 2$), along with the surface current, are clearly visible.

A photograph of a typical experiment and experimental conditions are presented in Figure 6.2 and Table 6.1 respectively. Each experiment was designed such that the bubble plumes produced would have distinct and steady sub-surface intrusions (Asaeda and Imberger, 1993; Socolofsky and Adams, 2005). The bubbles formed were ellipsoidal, with diameters in the range of $d_b = 0.2 - 1.2$ cm and an approximately constant rise velocity of $u_b \approx 24\,\mathrm{cms}^{-1}$ (Clift et al., 1978). Due to negligible breakup, coalescence and expansion over the small height of the tank, the bubble size was assumed to be constant, resulting in Weber and Reynolds numbers of $We = \rho_0 u_b^2 d_b / T = 1 - 10$ and $Re = u_b d_b / v = 550 - 3300$, where $T = 72\,\mathrm{gs}^{-2}$ is the surface tension between nitrogen and water and $\nu = 8.9 \times 10^{-3}\,\mathrm{cm}^2\mathrm{s}^{-1}$ is the kinematic viscosity of water. Source volume fluxes between $Q_b \approx 2.5 - 18.5\,\mathrm{cm}^3\mathrm{s}^{-1}$ (measured at a pressure of 2 bara) were supplied to the bubble nozzle, and with ambient stratification strengths between $N \approx 0.4 - 1.4\,s^{-1}$, the non-dimensional slip velocity of the plumes varied between $U_N \approx 1.9 - 4.4$. This range was constrained by the experimental apparatus as flow rates less than $2.5\,\mathrm{cm}^3\mathrm{s}^{-1}$ could not be reliably measured and only surface intrusions were produced when either $Q_b > 18.5\,\mathrm{cm}^3 s^{-1}$ or $N < 0.4\,s^{-1}$.

Experiments were captured at 24Hz using a Nikon D300s camera, fitted with an AF-S Micro NIKKOR 60mm f/2.8G ED lens. For each experiment, the camera was placed on a 1.2 m high tripod approximately 2.5 m from the experimental tank. Experimental images were processed using MATLAB R2020B. After the end of the filming period, prior to the submerged intrusions impacting the wall, samples were taken from the lowest intrusion in 5 cm increments from the centre of the plume to

Exp	$\boldsymbol{Q_b}$ ($\mathrm{cm}^3 s^{-1}$)	$\boldsymbol{B_0}$ ($\mathrm{cm}^4\mathrm{s}^{-3}$)	$\boldsymbol{N}$ (s^{-1})	$\boldsymbol{U_N}$ (-)	$\boldsymbol{n}$ (-)	$\boldsymbol{b_i}$ (cm)	$\boldsymbol{Q_s}$ ($\mathrm{cm}^3\mathrm{s}^{-1}$)
2	10	9810	1.11	2.39	2	2.3	175.9
4	5	4905	0.92	2.98	2	2.4	148.4
5	8	7850	0.97	2.61	2	3.7	247.8
6	15	14715	1.41	2.03	2	4.3	139.4
7	10	9810	1.00	2.45	2	4.2	241.0
9	17.5	17170	1.17	2.05	1	6.4	210.3
10	5	4905	1.21	2.78	2	2.9	122.9
11	12.5	12260	1.16	2.23	2	4.9	170.7
12	9	8830	1.35	2.34	2	4.2	142.3
13	18.5	18150	1.27	1.98	1	3.7	172.1
14	2.5	2450	0.52	4.09	1	3.2	215.6
15	5	4905	0.63	3.28	1	2.6	291.1
16	2.5	2450	0.41	4.32	1	2.8	374.7
17	2.5	2450	0.76	3.72	2	3.0	163.7

Table 6.1 List of experimental parameters. Here, n is the number of submerged intrusions; b_i is the inner plume radius; and Q_s is the volume flux of the surface intrusion, determined using the method described by Sigurðardóttir et al. (2020) (for details concerning the estimation of the inner plume radius and the intrusion volume flux, see Appendix B). Note that these authors, using the same experimental apparatus as in this study, determined the volume flux of submerged intrusions as $Q_i \approx 0.13(B_0^3/N^5)^{1/4}$.

the tip of the intrusion. Note that during the sampling procedure, the gas supply was turned off to prevent any further intrusion spread such that samples could be taken from both the left and right-hand sides of the intrusion. The fluid density of the samples was recorded using an Anton Paar DMA35n density meter. The concentration of dye within each sample was determined using a Thermo Scientific Evolution 201 UV-Visible spectrophotometer.

Note that in all experiments, the time to achieve a filling box like flow (Baines and Leitch, 1992) was large compared to the length of the experiment and any major changes to the local concentration/density were the result of isolated mixing events rather than filling box effects.

6.4 Theory

Measurements taken from within the submerged intrusions show the concentration of dye decreases radially away from the edge of the plume until reaching some steady value at large distances. This is a very interesting result, especially due to the fact

that both the flowrate and density appear to remain independent of intrusion radius. In this section, we develop a model for the transport of dissolved species in a bubble plume and consider two distinct regions which are depicted in Figure 6.3. Firstly, a mixing region close to the bubble core where the intrusion concentration decays radially, followed by a non-mixing region at large radial distances where the concentration of dissolved species is constant.

In a bubble plume spreading event, at the peel height, the majority of fluid (and any dissolved species) will peel from the plume bubble core and will subsequently begin to spread radially with the intrusion. Importantly, entrainment into both the inner and outer plumes results in significant mixing which can cause a portion of the dissolved species to recirculate back into the plume, with the potential of being carried to greater levels in the environment. To simplify this complex behaviour within the mixing region, we propose the use of a diffusion coefficient D to model the mass transfer of dissolved species from the intrusion into the entrainment region between the multiple spreading currents as this is where re-circulation is most likely to occur. This simplification is shown visually in Figure 6.3, where a peeling event of thickness L_i is split into two equally thick horizontal regions, one associated with the spreading intrusion and the other with the entrainment of ambient fluid.

By considering the constant intrusion volume flux Q_i and the length scale $L_i/2$, we write a mass balance accounting for the diffusion of dissolved species from the intrusion into the entrainment region above as

$$Q_i c_{ir} = Q_i c_{ir+dr} + D\frac{(c_{ir} - c_{er})}{L_i/2} 2\pi r dr, \tag{6.8}$$

where c_{ir} and c_{er} are the respective concentrations of dissolved species in the intrusion and entrainment region at some radius, r. This balance may be re-arranged such that the change in intrusion concentration with radius can be written as

$$\frac{dc_i}{dr} = -\frac{4D\pi r}{Q_i L_i}(c_{ir} - c_{er}). \tag{6.9}$$

If considering the mass transfer from the perspective of the entrainment region, we have

$$\frac{dc_e}{dr} = -\frac{4D\pi r}{Q_e L_i}(c_{ir} - c_{er}), \tag{6.10}$$

which can then be utilised with (6.9) to give

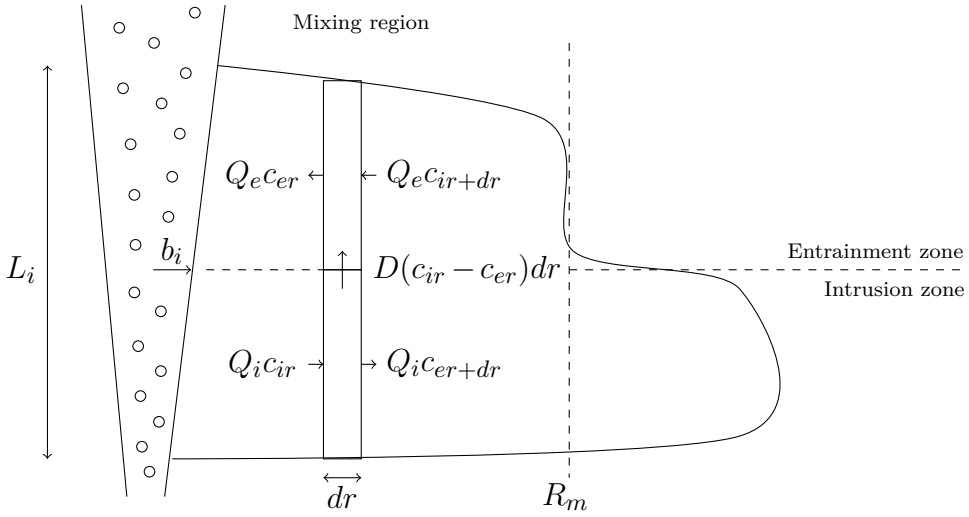

Fig. 6.3 A submerged peeling event schematic showing intrusion and entrainment zones. Q is volume flux; c is concentration of dissolved species; and the subscripts i and e refer to the respective values within the intrusion and entrainment regions. b_i is the radius of the inner plume, R_m is the radius of the mixing region; and D is the diffusion coefficient.

$$\frac{dc_i}{dr} = \frac{Q_e}{Q_i}\frac{dc_e}{dr}. \tag{6.11}$$

Following the integration of equation (6.11) between the intrusion radius r and the plume radius b_i, after some rearrangement, the concentration in the entrainment region can be determined as

$$c_e = \frac{Q_i}{Q_e}\left(c_i - c_{i0} + \frac{Q_e}{Q_i}c_{e0}\right), \tag{6.12}$$

where c_{i0} and c_{e0} represent the concentration in the intrusion and the entrainment region at $r = b_i$. Upon substituting (6.12) into (6.9),

$$\frac{dc_i}{dr} = -\frac{4D\pi r}{Q_i L_i}\left[c_i\left(1 - \frac{Q_i}{Q_e}\right) - \frac{Q_i}{Q_e}\left(c_{i0} + \frac{Q_e}{Q_i}c_{e0}\right)\right]. \tag{6.13}$$

This gives the first order ordinary differential equation,

$$\frac{dc_i}{dr} + \frac{4D\pi r}{Q_i L_i}(a \cdot c_i + m) = 0, \tag{6.14}$$

where $a = (1 - \frac{Q_i}{Q_e})$, with an expected value between 0 and 1; and $m = \frac{Q_i}{Q_e}\left(c_{i0} + \frac{Q_e}{Q_i}c_{e0}\right)$. With the boundary condition $c_i = c_{i0}$ when $r = b_i$, the solution to (6.14) is

$$c_i = -\frac{m}{a} + \left(c_{i0} + \frac{m}{a}\right)\exp\left[-\frac{2aD\pi}{Q_i L_i}(r^2 - b_i^2)\right], \tag{6.15}$$

or

$$\frac{c_i}{c_{i0}} = -\frac{1-a}{a} + \left(1 + \frac{1-a}{a}\right)\exp\left[-\frac{2aD\pi}{Q_i L_i}(r^2 - b_i^2)\right], \tag{6.16}$$

when c_{e0} is assumed to be negligible. The model can be further simplified by assuming $Q_i = Q_e$, which then following the integration of equation (6.14), gives the quadratic decay equation,

$$\frac{c_i}{c_{i0}} = 1 - \frac{2D\pi}{Q_i L_i}(r^2 - b_i^2). \tag{6.17}$$

Although significantly simpler than (6.16), the assumptions built into equation (6.17) requires that all fluid entrained into the bubble core of the plume peels into the intrusion for each spreading event. Such behaviour has been observed in previous studies considering surface or Type 1 intrusions, however, peeling efficiencies of less than one are expected for submerged intrusions produced by Type 2 and Type 3 plumes (Socolofsky and Adams, 2005). In either case, irrespective of whether $a > 0$ or $a = 0$, the concentration within the mixing zone is expected to decay linearly with r^2 until reaching the critical radius, R_m, associated with the end of the mixing region. Beyond this critical radius, the concentration is expected to remain constant.

Here, it can also be noted that the simpler derivation, equation (6.17), may be re-cast easily in terms of the non-mixing region concentration, c_∞/c_{i0}, and the mixing radius, R_m, as

$$\frac{c_i}{c_{i0}} = 1 - \left(1 - \frac{c_\infty}{c_{i0}}\right)\frac{1 - j(r^2 - b_i^2)}{1 - j(R_m^2 - b_i^2)} \tag{6.18}$$

where $j = 2D\pi/Q_i L_i$ and c_∞/c_{i0} is simply calculated from (6.17) with $r = R_m$.

6.4.1 Model extension to experimental images

The model derived above is suitable for direct comparison to intrusion concentration samples taken at known radial positions from the axis of a bubble plume. Although useful in settings where intrusion sampling and any subsequent analysis is straight

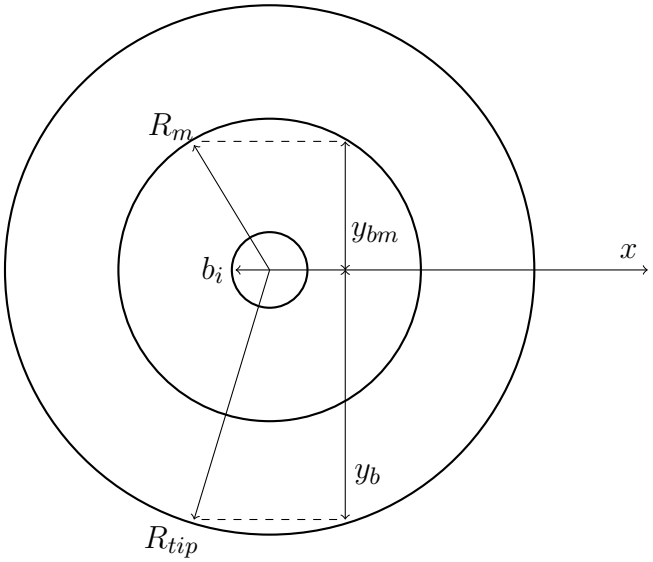

Fig. 6.4 A schematic of an axisymmetric bubble plume intrusion from above.

forward, equations (6.16) and (6.17) are not necessarily useful for application to studies where sampling and analysis may prove difficult. Therefore, we extend our approach such that the models can be applied to front-on images of bubble plume intrusions through the utilisation of the Beer-Lambert Law (Beer, 1852; Lambert, 1760), of which the modern derivation reads

$$A = \epsilon l c_a, \tag{6.19}$$

where A is absorbance, ϵ is the molar absorptivity, l is the optical distance and c_a is the concentration of the attenuating species. This law enables the intensity of light captured in the image to be converted into an average dye concentration across the depth of the intrusion.

If we consider an axisymmetric intrusion viewed from above (Figure 6.4), images would be captured in an experiment by a camera positioned directly in line with the plume, at $x = 0$, with the lens pointing down the y-axis. Due to the circular nature of the intrusion, the total light path decreases with x and is equivalent to $2y_b$, which is equivalent to $2(R_{tip}^2 - x^2)^{1/2}$. With the presence of the mixed region, the concentration across the intrusion cannot be determined by y_b alone. Using y_b, along with the associated light path of the mixed region, $2y_{bm} = 2(R_m^2 - x^2)^{1/2}$, the average concentration across the intrusion, c_i, can be written with respect to x as

$$\frac{\bar{c}_i}{c_{i0}} = \frac{1}{2y_b}\left[\frac{\bar{c}_{im}}{c_{i0}}2y_{bm} + \frac{\bar{c}_\infty}{c_{i0}}2(y_b - y_{bm})\right], \tag{6.20}$$

where $\bar{c}_{im}$ and $\bar{c}_\infty$ are the average dye concentration inside and outside of the mixed region. As concentration is constant outside the mixed region, $\bar{c}_\infty/c_{i0}$ can simply be calculated from equation (6.16) or (6.17), depending upon the chosen value of a, with $r = R_m$. Comparatively, to determine the average dye concentration in the mixed region with respect to x, equations (6.16) and (6.17) must be integrated. By initially converting from a one-dimensional coordinate system into Cartesian coordinates using $r^2 = x^2 + y^2$, the resulting equations, after some rearrangement, were integrated between the limits of y_{bm} and $-y_{bm}$ for a fixed value of x to give

$$\frac{\bar{c}_{im}}{c_{i0}} = \begin{cases} 1 - \dfrac{j}{2y_{bm}}\left[(x^2 - b_i^2)2y_{bm} + \dfrac{2}{3}y_{bm}^3\right], & a = 0, \\ 1 - \dfrac{\left(1 - \frac{\bar{c}_\infty}{c_{i0}}\right)}{\left(1 - e^{-ja(R_m^2 - b_i^2)}\right)}\left[1 - \dfrac{\mathrm{erf}(y_{bm}(ja)^{1/2})\pi^{1/2}e^{-ja(x^2-b_i^2)}}{2y_{bm}(ja)^{1/2}}\right], & a > 0, \end{cases} \tag{6.21}$$

where erf is the error function.

In its current form, equation (6.20) cannot be directly compared to the image intensity of an intrusion as c_{i0} can only be determined from directly sampling the centre of the plume. To remedy this, the average concentration across the intrusion can be presented in terms of image intensity, $\bar{c}_i 2y_b$. In this case, the equivalent for $\bar{c}_{i0}$ is the maximum image intensity, $c_{max}2R_{tip}$. The ratio of the sample and image maxima can be written as

$$\frac{c_{max}2R_{tip}}{c_{i0}} = 2b_i + \frac{\bar{c}_{im}}{c_{i0}}2(R_m - b_i) + \frac{\bar{c}_\infty}{c_{i0}}2(R_{tip} - R_m). \tag{6.22}$$

After dividing (6.20) by the left-hand side of (6.22), the outcome is an equation suitable for direct comparison to experimental images of submerged intrusions spreading from a bubble plume,

$$\frac{\bar{c}_i 2y_b}{c_{max}2R_{tip}} = \frac{\bar{c}_{im}2y_{bm}}{c_{max}2R_{tip}} + \frac{\bar{c}_\infty 2(y_b - y_{bm})}{c_{max}2R_{tip}}. \tag{6.23}$$

6.4.2 Definition of a

In order for the $a > 0$ model to be useful, the coefficient a must be predictable, however, in the form,

$$a = 1 - \frac{Q_i}{Q_e}, \tag{6.24}$$

this is not possible as there is no reliable way to determine the level of entrainment into the outer plume experimentally. Therefore, (6.24) must be manipulated such that a becomes a function of known parameters and is thus predictable. Consider the mass balance presented in (6.3b) yet normalised by the entrainment flux into the outer plume, Q_e. This gives

$$1 + \frac{Q_p}{Q_e} = \frac{Q_i}{Q_e} + \frac{Q_r}{Q_e}, \tag{6.25}$$

or

$$a = \frac{Q_r - Q_p}{Q_e}. \tag{6.26}$$

Here it can be readily identified that a is a function of the volume of fluid both being entrained and detrained from the inner plume during a peeling event. A number of methods exist to estimate entrainment and detrainment from the bubble core including continuous peeling models proposed by Crounse et al. (2007) and Yang et al. (2016), however, the most suitable approach here is to utilise the peeling efficiency (Socolofsky, 2001),

$$f = \frac{Q_p}{Q_n + Q_r}, \tag{6.27}$$

which is a known function of U_N. When considering the 1st peeling event ($n = 1$), entrainment between the source and the trap height is expected to be small and in this case, we may substitute (6.27) into (6.26) to give

$$a \approx \frac{Q_r}{Q_e}(1 - f). \tag{6.28}$$

This substitution deems to be very useful as Socolofsky (2001) determined Q_r/Q_e to be a constant statistically independent of U_N and thus, a must scale simply with the peeling efficiency as

$$a \sim (1-f). \tag{6.29}$$

The peeling efficiency in the past has been presented a linear function of U_N (Socolofsky and Adams, 2003), however we propose an alternative approach to determine f, and subsequently a, from experimental liquid flowrate measurements.

If we consider (6.3c) and (6.24), their combination gives

$$Q_{n+1} = Q_n + naQ_e, \tag{6.30}$$

where n is the number of submerged intrusions. If entrainment between the source and the first peeling event is negligible ($Q_1 \approx 0$) and entrainment into the outer plume remains consistent for all peeling events, the volume flux of the surface intrusion can be written as

$$Q_s = Q_e\,(1+na)\,. \tag{6.31}$$

Upon dividing (6.31) by Q_i, the subsequent result, following some rearrangement, allows a to be determined as

$$a = \frac{(Q_s/Q_i - 1)}{(Q_s/Q_i + n)}, \tag{6.32}$$

along with the expected scaling of

$$f \sim 1 - \frac{(Q_s/Q_i - 1)}{(Q_s/Q_i + n)}. \tag{6.33}$$

6.5 Results

Of the experiments conducted, all were consistent with previous experimental bubble plume studies. Once released into the environment, the bubbles rise upwards due to buoyancy and burst once reaching the liquid surface. Close to the bubble source, ambient liquid becomes entrained into the bubble core, carrying liquid to greater heights in the environment, before peeling away from the rising bubbles and descending in the environment as an outer plume. Due to the stratified nature of the environment, a portion of fluid in the outer plume spreads as a submerged lateral intrusion, whilst some is also re-entrained into the bubble core as demonstrated by the presence of dye in each of the peeling events present throughout the tank. The following subsections

detail our observations and provide experimental validation of the model derived in section 6.4.

6.5.1 Concentration of dissolved species

Figure 6.5 details the experimental measurements of concentration of dissolved species, normalised by the concentration at $r = b_i$, against the intrusion radius. Two clear regimes are seen to be present, with a significant decrease in concentration occurring at radial distances close to the bubble core. With intrusion radius non-dimensionalised, the radial extent of the mixing region clearly appears to be a function of the length scale, $L_p = (B_0/N^3)^{1/4}$. Values of mixing radius were determined first by fitting equation (6.17) (with $2D\pi/Q_iL_i$ set to a constant) to the experimental concentration measurements and setting R_m equivalent to the radius where the first instance of $c_i = c_{\text{inf}}$ occurred. The mixing radius values which gave the best fit to the experimental data followed $R_m/L_p = 1.34 \pm 0.05$ (see Figure 6.6a). Notably, Lemckert and Imberger (1993b) determined a similar coefficient for the outer plume radius of their plumes, $b_o/L_p = 0.97 \pm 0.28$, suggesting R_m is approximately equivalent to the outer plume radius. An observation also of interest is that Type 2 plumes ($1.6 < U_N < 2.4$) appear to decay to a lesser value of c_∞/c_{i0} than their Type 3 ($U_N > 2.4$) counterparts. This, however, is expected given that the coefficient a increases with non-dimensional slip velocity.

To apply our diffusion model, parameters including the diffusion coefficient D, the intrusion flowrate Q_i, the height of the peeling event L_i, and the value of a must be defined. Previous experimental work suggests that $Q_i \sim (B_0^3/N^5)^{1/4}$ and $L_i \sim L_p$, however the coefficient associated with each scaling term varies greatly across different studies with $Q_i/(B_0^3/N^5)^{1/4} = 0.13 - 0.90$ (Sigurðardóttir et al., 2020; Socolofsky and Adams, 2003) and $L_i/L_p = 0.70 - 4.50$ (Chen, 2001). In order to prevent the use of a combination of coefficients being used from different studies, we propose an effective diffusion coefficient in the form $\delta = D/Q_iL_i$. As we expect the diffusion coefficient to scale as $D \sim (B_0/N)^{1/2}$, it is also expected that $\delta \sim L_p^{-2}$. Prior to evaluating the value of δ/L_p^{-2}, a value of a must be selected to determine the appropriate equation to compare to the experimental data. Note that in all our experiments, the surface intrusion volume flux exceeds that of the submerged currents, suggesting that $a > 0$ in all cases, however both $a = 0$ and $a > 0$ models are compared to the experimental data in order to determine the suitability of each.

When $a = 0$, a best fit value of $\delta/L_p^{-2} = 0.053 \pm 0.004$ is determined, providing a reasonable fit to the experimental measurements within the mixing region (see Figure

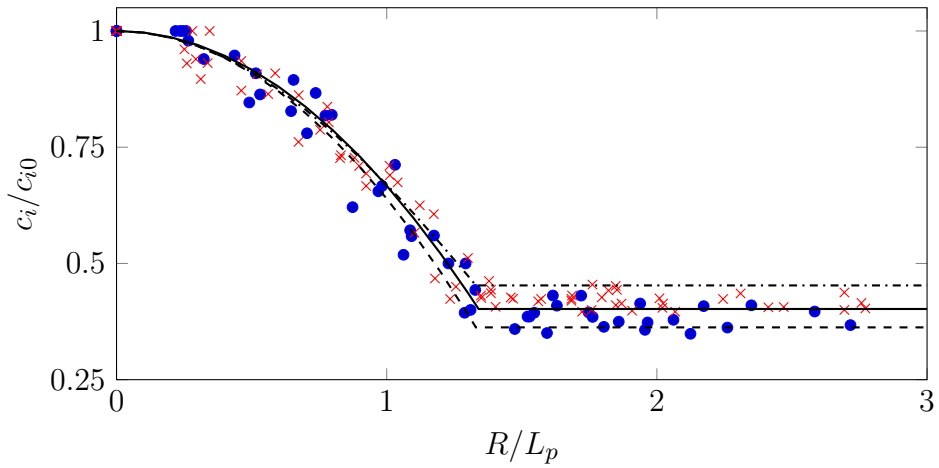

Fig. 6.5 Normalised intrusion concentration, c_i/c_{i0}, against dimensionless intrusion radius. Experiments are separated into Type 2 (•) and Type 3 (×) plumes. The solid, dashed and dotted lines correspond to the diffusion models: $a = 0$ (——) and $a > 0$ with values of $a = 0.01$ (- - -) and $a = 0.50$ (-·-·-). Note that the line associated with $a = 0$ falls within the two $a > 0$ curves because the $a = 0$ model can only predict a single, best fit value of c_{inf} for a given value of δ. In comparison, the $a > 0$ model can predict a range of c_{inf} for a given value of δ and a given range of a.

6.6b). Beyond the mixing region however, the single value of $(c_\infty/c_{i0})_{a=0} = 0.40$ leads to a 10% error between the model and the experimental measurements. In the case of $a > 0$, a for each experiment was estimated using equation (6.33), resulting in $\delta/L_p^{-2} = 0.058 \pm 0.002$). Unlike the quadratic decay case, here c_∞/c_{i0} is not a set value and is determined by the magnitude of a. When considering (6.29), a is equivalent to a constant multiplied by a function of U_N, with the constant representing the ratio of entrainment fluxes into the inner and outer plumes. The approach by Socolofsky and Adams (2003) suggests $Q_r/Q_e \approx 1.07$ and with this estimate, a simply reduces to

$$a = 1 - f, \tag{6.34}$$

which subsequently allows the peeling efficiency to be directly computed from surface and submerged intrusion volume fluxes, resulting in similar values to those determined by Socolofsky (2001) and Yang et al. (2016) (see Figure 6.7a). Previously, the peeling efficiency has been predicted using $f = 1 - 0.07U_N^{1.2}$ (Socolofsky, 2001); however, in this form, $f = 0$ when $U_N \approx 9.2$. In nature, it is unlikely that liquid peeling from bubble plumes will become 100% inefficient for $U_N > 9.2$, instead we expect that f will approach zero asymptotically and thus, suggest

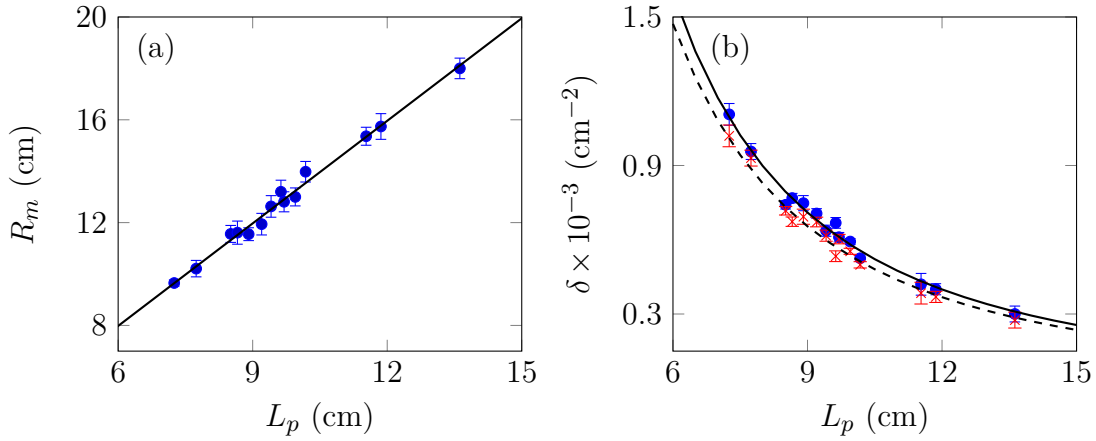

Fig. 6.6 Experimental measurements of (a) the mixing radius R_m with the solid line representing the scaling $R_m/L_p = 1.34$, and (b) the effective diffusion coefficient δ for $a > 0$ (•) and $a = 0$ (×) with the solid and dashed lines representing the scaling $\delta_{a>0}/L_p^{-2} = 0.058$ (——) and $\delta_{a=0}/L_p^{-2} = 0.053$ (- - -).

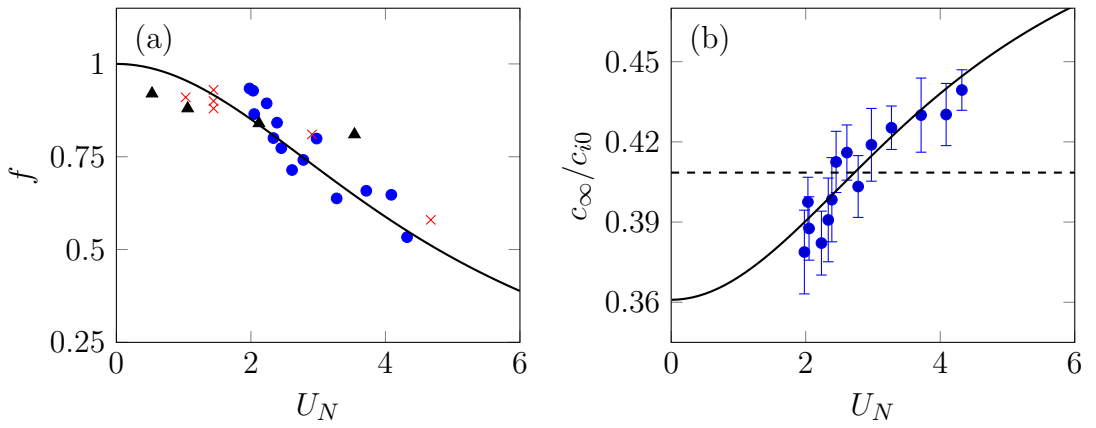

Fig. 6.7 (a) The plume peeling efficiency f against U_N. Results from this work (•) are compared with Socolofsky and Adams (2005) (×) and Yang et al. (2016) (▲). The solid line represents equation (6.35). (b) c_∞/c_{i0} against U_N. The solid and dashed lines correspond to the model with $a > 0$ (——) and $a = 0$ (- - -) respectively.

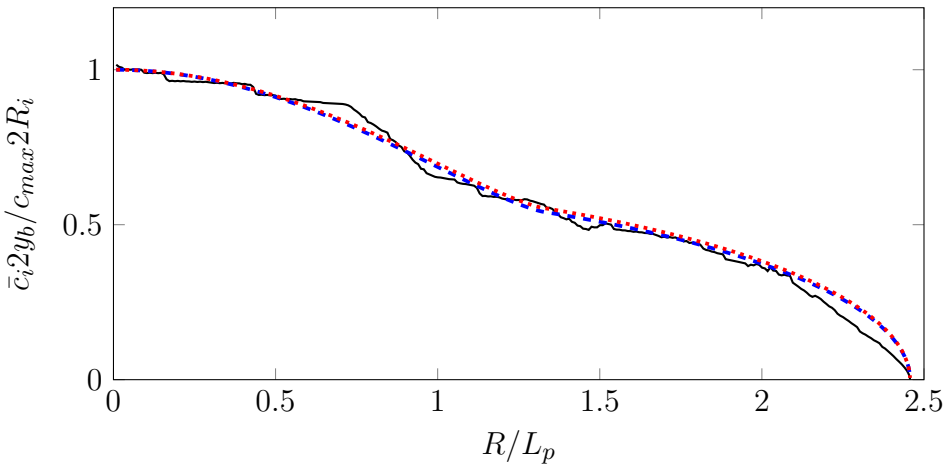

Fig. 6.8 Comparison of the model extension to the concentration profile of the first submerged intrusion above the source in Experiment 9. The solid line denotes the intrusion concentration profile gained through image analysis; and the dashed and dotted lines correspond to the diffusion models with $a = 0.16$ (- - -) and $a = 0$ (·····). Model inputs here include $R_i = 25$ cm and $c_{max}2R_i/c_{i0} = 30.3$ cm.

$$f = 1 - \frac{0.07U_N^2}{1.6 + 0.07U_N^2}. \tag{6.35}$$

Through a combination of (6.34) and (6.35), the $a > 0$ model can be compared to the experimental data to show a good fit across both the mixing and non-mixing regions (see Figure 6.7b).

A similar result is found for the model extension, with equation (6.23), using both zero and non-zero values of a, providing a reasonable fit to the concentration profiles determined from image analysis in all experiments. An example of this fit is shown in Figure 6.8. Interestingly, when considering the entire radial extent of the intrusion, the difference between the two models is negligible with an average value of $\bar{c}_{i,a>0}/\bar{c}_{i,a=0} = 0.99 \pm 0.01$ across all experiments. Note however this ratio increases to a maximum of $\bar{c}_{i,a>0}/\bar{c}_{i,a=0} = 1.08$ in the non-mixing region of intrusions where $c_\infty/c_{i0} \not\approx (c_\infty/c_{i0})_{a=0}$. This suggests that the $a > 0$ extension to determine the diffusion of dissolved species from the plume using intrusion images is superior to the simpler $a = 0$ approach, especially for intrusions where $R_{tip} \gg R_m$. However, it is also worth noting that if the user of this model is interested in utilising the methodology described to determine the magnitude of the plume mixing radius, to then subsequently estimate

source values of B_0, the simpler method is expected to also provide a reasonable estimate.

As a final comment regarding the fit of the model to the experimental images, the derivation in section 6.4.1 is based upon the assumption of symmetry around the plume axis, and as shown in Figure 6.2, the intrusions created initially do show some asymmetry. However, upon turning off the central plume, disturbances in the tank tend to settle, creating defined horizontal intrusions. Although some concentration variances may be present across the thickness of the intrusion in the theta direction, by taking an average of the light intensity captured by the camera across the depth of the intrusion, these differences are captured and distributed evenly, allowing for direct comparison to the model. Also, in all of the experiments conducted in this study, the difference in radius of the left- and right-hand sides of the lowest intrusion were less than 10%.

6.5.2 Potential influence of mixing on radial spreading

Although not strictly relevant to the diffusion of dissolved species from a bubble plume, however important in the overall scheme of mass transfer from the plume to the environment, an interesting comparison can be made between the mixing radius identified in this study and the expected transitional radius between intrusion spreading regimes. The recent study of Sigurðardóttir et al. (2020) identified that multiple intrusions emanating from Type 2 & 3 bubble plumes tended to spread three times slower than individual intrusions produced either by plumes or through the direct injection of fluid into a stratified environment when viscous forces were dominant (see Ivey and Blake, 1985). Sigurðardóttir et al. (2020) suggested this potential reduction in spreading rate was due to the counter-flow present between the multiple intrusions associated with entrainment into the plume, and our findings here tend to support this hypothesis.

Sigurðardóttir et al. (2020) determined the following equation for the transition radius between spreading regimes in their bubble plume intrusions as

$$R_r \approx 0.09(Q_i N)^{1/3}(G/N)^{2/3}, \tag{6.36}$$

where $G = (Q_i^2 N/\nu^3)^{1/5}$. If combined with their estimate, $Q_i \approx 0.13(B_0^3/N^5)^{1/4}$, (6.36) may be recast as

$$R_r \approx 0.0265\nu^{2/5}(B_0^9/N^{19})^{1/20}. \tag{6.37}$$

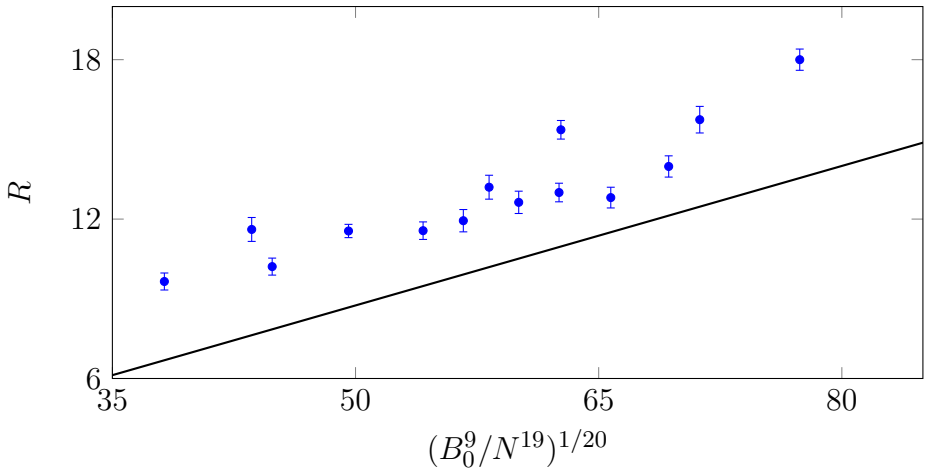

Fig. 6.9 Intrusion radius against the scale $(B_0^9/N^{19})^{1/20}$. The points (•) denote the intrusion mixing radius and the solid line (——) with the gradient $0.0265v^{-2/5}$, where $v = 8.9 \times 10^{-3}\,\mathrm{cm^2 s^{-1}}$, is the predicted radius where the spreading regime transition occurs (Sigurðardóttir et al., 2020).

The comparison of this scaling with R_m in Figure 6.9 shows that the significant reduction in spreading rate occurs shortly before exiting the mixing region, which we have found is approximately equivalent to the edge of the downwards flowing outer plume. At this point in the environment, both vertical and inwards radial mixing will be strong and could have the potential to accentuate the deceleration of an already slowing current. Importantly, this level of mixing is not present at such large radial extents in either single-phase plumes or in simple asymmetric spreading currents and is therefore the likely culprit for the decreased rate of spread in the viscous-buoyancy regime of submerged bubble plume intrusions.

6.6 Conclusion

Our ellipsoidal bubble plume experiments in stratified fluid have shown the presence of a defined mixing region at small radial distances along the submerged intrusions spreading from the plume. In this region of the intrusion, the concentration of dissolved species decays from a maximum value at the centre of the plume to some constant concentration, which after the development of a simple diffusion model, is determined to be inversely proportional to the efficiency at which entrained liquid peels from the bubble core.

The models developed for comparison to both direct measurements and experimental images show reasonable fit to the experimental data. It is worth noting however that the range of plume slip velocities studied was between $2 \gtrsim U_N \gtrsim 4.5$. This is reasonable considering laboratory size constraints, however does not extend to the range of non-dimensional slip velocities associated with bubble plumes in nature where the environment is very weakly stratified. Therefore, it would be of interest for future experiments to be conducted to explore whether the mixing behaviour remains consistent for $U_N > 5$.

Although limited to a somewhat restrictive range of U_N, these findings are not only useful in understanding how mass is transported radially away from a bubble plume, but also provides insight into how localised mixing promotes the transport of dissolved species to greater heights above the plume source. High concentrations of dissolved species close to the edge of the plume has the potential to influence the rate of bubble dissolution, a process expected to scale as $dc_b/dt \sim (1 - c_i/c_{i0})$. Importantly, the combination of such a model with the work which we have presented here could be utilised to estimate the mass transfer associated with multiple submerged spreading events, in addition to potentially predicting the flux of gas, if any, escaping from a liquid environment of finite vertical extent. Note that the model presented in this work does not account for bubble dissolution and it may be of interest to future authors to extend the analysis to capture more of the physics associated with these complex multiphase flows.

Chapter 7

Conclusion and future work

In this thesis, the dynamics of stratified multiphase plumes, consisting of both liquid and particles and liquid and bubbles, have been investigated. Related, yet unique in their own right, particle-laden plumes and bubble plumes were created within the laboratory with the intent of further exploring their behaviour within stratified ambients. Motivated by the qualitative observations made during these experiments of both the plume itself and the resultant intrusion which spreads radially at the height of neutral buoyancy, mathematical models were successfully developed to describe the flow behaviour. These models will prove useful to those interested in understanding the dynamics of similar flows present within industry and the natural world. In this final chapter, a summary of the work presented in the previous chapters is provided and appropriate conclusions are drawn. This is then followed by a short discussion on the issues for future research.

7.1 Concluding remarks

In Chapter 3, stratified particle-laden plume experiments were conducted and five different flow regimes were identified and qualitatively described. A key dividing characteristic of these regimes was the development of particle-induced convection in the environment around the plume. Building upon the work of Cardoso and Zarrebini (2001a), a criterion for the onset of ambient convection was developed and a critical Grashof number was determined to separate the plume regimes. The maximum steady-state height of the plume, along with the particle-rich and particle-poor intrusion heights, were also presented. These heights were compared to the model of Apsley and Lane-Serff (2019), showing its suitability for plumes rising within a quiescent

environment. A model was also developed to predict the change in intrusion interstitial fluid height and was found to be accurate when compared to all experimental results.

Following on from the previous chapter, Chapter 4 put the spotlight on particle-laden plumes rising through ambient convection. Direct measurements within the convection column between the intrusion and the source showed that particle concentration is independent of height and that the ambient density decreases to a lesser value, yet remains stratified with a density gradient consistent with the quiescent surroundings. Using this observation, a simple extension to the plume theory developed by Morton et al. (1956), accounting for the steady-state conditions at the source, allows the maximum steady-state plume height to be predicted with reasonable accuracy. The change in ambient density within the convection column also provides a reasonable estimate for the neutral buoyancy height of the secondary intrusion which develops between the primary intrusion and the source in Type 3* plumes. Finally, an extension of the analytical convection criterion, developed in Chapter 3, allows the radius of convection to be estimated and in turn enables both the ambient and spreading level particle concentration to be determined.

Chapter 5 is the first to concentrate solely on stratified bubble plumes and presents a collaborative work specifically interested in the spreading rate of multiple submerged intrusions. From our observations and subsequent analysis of the intrusion spreading rates, we found that the initial spread at early times within the inertia-buoyancy regime is consistent with previous experimental studies investigating the spread of a single plume intrusion. This, however, was not the case at large times and radial distances once viscous forces became important. Upon eliminating any wall effects, the multiple intrusions appeared to spread around three times slower than an isolated intrusion, suggesting the potential for a higher viscous friction as a result of the counter flow produced between the intrusions as ambient fluid becomes entrained into the central plume.

Continuing an interest in the intrusion of a bubble plume, this time from the viewpoint of mass transfer to the environment, Chapter 6 explores the transport of dissolved species from the plume to the water column. Liquid samples taken from the centre of the plume along the radial intrusion show the decay of dissolved species from a maximum value at the bubble core to some lesser concentration which remains constant beyond a defined radius. In an attempt to predict the concentration of dissolved species in a bubble plume intrusion, we developed a simple diffusion model with a mixing and non-mixing region. This model was developed so that it could be compared to both discrete measurements and front-on images with both proving to be successful in

predicting the change in dissolved species concentration with radius. Model parameters including the diffusion coefficient, the intrusion mixing radius, and the ratio of detrainment to entrainment were determined using experimental measurements and were found to be functions of both source values and stratification strength. An interesting observation was that the mixing radius was almost equivalent to the spreading regime transitional radius, providing further evidence that the slower spreading rate observed in Chapter 5 is due to the entrainment and mixing of fluid occurring between the multiple intrusions.

7.2 Future research

Chapters 3 and 4, along with the work of Apsley and Lane-Serff (2019), provides a complete road map to the dynamics of stratified particle-laden plumes, detailing the heights and particle concentrations of interest for plumes rising in both quiescent and convecting environments. There does however remain some points of interest for further research. As shown within this thesis, the work of Apsley and Lane-Serff (2019) successfully predicts the height of pure Type 1/1* plumes, yet the current model does not account for the changes to the flow behaviour associated with non-zero volume and momentum fluxes. Although in their analysis they have provided an additional term to account for any plume-top entrainment, it would be of interest to extend the model further to account for real plume sources. Secondly, despite my best efforts, the transition from a Type 3 to 3* plume remains unclear. In Chapter 3, it was shown using both current and previous experiments that secondary intrusions appear to develop once $U_c > 1$ cms^{-1}, however this will likely break down for particles with settling velocities exceeding this value. In Chapter 4, it was concluded that the transition to a fountain-like downflow is likely either associated with the depth of the plume trough or the observed difference in regimes is simply a characteristic associated with the concentration of dye in the source feed. Therefore, it is suggested that future authors focus their efforts specifically on firstly confirming whether concentration of dye influences the observed regime transition before attempting to gain direct velocity and density measurements within the trough region below the plume intrusion.

In regard to bubble plumes, the work presented here focuses mainly on the dynamics of the intrusions rather than the plume itself and how dissolved species is transported throughout the water column. Many of the plumes in nature (where it would be of interest to apply this work) exist within very weakly stratified environments. Such

an environment leads to plumes with large non-dimensional slip velocities which, in most cases, exceed those of the experiments presented here. The experimental range began at the lowest end of where multiple spreading events become present ($U_N \approx 1.5$), however reached a maximum around $U_N \approx 4.5$ due to laboratory size constraints. For comparison, $U_N \approx 10$ for Artic methane plumes rising in the Laptev Sea on the Eastern Siberian Artic Shelf ($Q_b \approx 5\,\mathrm{cm^3 s^{-1}}$ and $N \approx 0.01\,\mathrm{s^{-1}}$, Shakhova et al., 2014). Therefore, to allow the model presented in Chapter 6 to be compared with confidence to either these plumes or other examples, it would be worthwhile to conduct additional experiments with larger values of U_N. Also, as noted in Chapter 5, it would be of interest to study the spreading of bubble plume intrusions in a larger radial space to eliminate any concerns associated with confinement or limited intrusion spread.

Finally, the third area of future research with both industrial and natural applications is the development of particle-laden plumes or bubble plumes through chemical reaction. Recent work in the Fluids and Environment group (see Mingotti and Cardoso, 2019) investigated single-phase plumes with internal changes in buoyancy due to chemical reaction. It would be of interest to build upon both this work and the work presented in this thesis by investigating the dynamics of particle-laden plumes created through precipitation reactions or bubble plumes created through solid-gas reactions.

References

Ai, J., Law, A. W. K., and Yu, S. C. M. (2006). On Boussinesq and non-Boussinesq starting forced plumes. *Journal of Fluid Mechanics*, 558:357.

Apsley, D. D. and Lane-Serff, G. F. (2019). Collapse of particle-laden buoyant plumes. *Journal of Fluid Mechanics*, 865:904–927.

Asaeda, T. and Imberger, J. (1989). Behaviours of bubble plumes in a linear stratification. *Doboku Gakkai Ronbunshu*, 1989(411):55–62.

Asaeda, T. and Imberger, J. (1993). Structure of bubble plumes in linearly stratified environments. *Journal of Fluid Mechanics*, 249:35–57.

Baines, W. D. and Leitch, A. M. (1989). Destruction of stratification by bubble plume. *J. Hydraul. Eng. ASCE*, 118(4):559–577.

Baines, W. D. and Leitch, A. M. (1992). Destruction of stratification by bubble plume. *Journal of Hydraulic Engineering*, 118(4):559–577.

Balasubramanian, S., Mirajkar, H. N., and Banerjee, A. K. (2018). Role of dispersed particles on the dynamics of an umbrella cloud of a forced plume in a linearly stratified environment. *Environmental Fluid Mechanics*, 18(4):985–1006.

Batchelor, G. K. (1954). Heat convection and buoyancy effects in fluids. *Quarterly journal of the royal meteorological society*, 80(345):339–358.

Beer, A. (1852). Bestimmung der absorption des rothen lichts in farbigen flussigkeiten. *Ann. Physik*, 162:78–88.

Beyer, J., Trannum, H. C., Bakke, T., Hodson, P. V., and Collier, T. K. (2016). Environmental effects of the Deepwater Horizon oil spill: a review. *Marine pollution bulletin*, 110(1):28–51.

Blanchette, F. (2013). Mixing and convection driven by particles settling in temperature-stratified ambients. *International Journal of Heat and Mass Transfer*, 56(1-2):732–740.

Bloomfield, L. J. and Kerr, R. C. (1998). Turbulent fountains in a stratified fluid. *Journal of Fluid Mechanics*, 358:335–356.

Bloomfield, L. J. and Kerr, R. C. (2000). A theoretical model of a turbulent fountain. *Journal of Fluid Mechanics*, 424:197–216.

Bolster, D., Hang, A., and Linden, P. F. (2008). The front speed of intrusions into a continuously stratified medium. *Journal of Fluid Mechanics*, 594:369–377.

Boufadel, M. C., Socolofsky, S. A., Katz, J., Yang, D., Daskiran, C., and Dewar, W. (2020). A review on multiphase underwater jets and plumes: Droplets, hydrodynamics, and chemistry. *Reviews of Geophysics*, 58(3):e2020RG000703.

Boussinesq, J. (1903). *Théorie analytique de la chaleur mise en harmonic avec la thermodynamique et avec la théorie mécanique de la lumière: Tome I-II*. Gauthier-Villars.

Briggs, G. A. (1969). Plume rise: A critical survey. Technical report, Air Resources Atmospheric Turbulence and Diffusion Lab., Oak Ridge, Tenn.

Briggs, G. A. (1982). Plume rise predictions. In *Lectures on air pollution and environmental impact analyses*, pages 59–111. Springer.

Budd, L., Griggs, S., Howarth, D., and Ison, S. (2011). A fiasco of volcanic proportions? eyjafjallajökull and the closure of european airspace. *Mobilities*, 6(1):31–40.

Bullamore, D. (2019). *Methane Plumes in the Arctic*. CET IIB Thesis, Department of Chemical Engineering and Biotechnology, University of Cambridge, UK.

Burridge, H. C., Parker, D. A., Kruger, E. S., Partridge, J. L., and Linden, P. F. (2017). Conditional sampling of a high Péclet number turbulent plume and the implications for entrainment. *Journal of Fluid Mechanics*, 823:26–56.

Bursik, M. I., Sparks, R. S. J., Gilbert, J. S., and Carey, S. N. (1992). Sedimentation of tephra by volcanic plumes: I. theory and its comparison with a study of the Fogo A plinian deposit, Sao Miguel (Azores). *Bulletin of Volcanology*, 54(4):329–344.

Caldcleugh, A. (1837). Some account of the volcanic eruption of Cosiguina in the Bay of Fonseca, commonly called the Coast of Conchagua, on the western coast of Central America. In *Abstracts of the Papers Printed in the Philosophical Transactions of the Royal Society of London*, number 3, pages 363–364. The Royal Society London.

Carazzo, G. and Jellinek, A. M. (2012). A new view of the dynamics, stability and longevity of volcanic clouds. *Earth and Planetary Science Letters*, 325:39–51.

Carazzo, G. and Jellinek, A. M. (2013). Particle sedimentation and diffusive convection in volcanic ash-clouds. *Journal of Geophysical Research: Solid Earth*, 118(4):1420–1437.

Carazzo, G., Kaminski, E., and Tait, S. (2006). The route to self-similarity in turbulent jets and plumes. *Journal of Fluid Mechanics*, 547:137.

Cardoso, S. S. S. and Woods, A. W. (1993). Mixing by a turbulent plume in a confined stratified region. *Journal of Fluid Mechanics*, 250:277–305.

Cardoso, S. S. S. and Zarrebini, M. (2001a). Convection driven by particle settling surrounding a turbulent plume. *Chemical engineering science*, 56(11):3365–3375.

Cardoso, S. S. S. and Zarrebini, M. (2001b). Sedimentation of polydispersed particles from a turbulent plume. *Chemical engineering science*, 56(16):4725–4736.

Carey, S. N., Sigurðsson, H., and Sparks, R. S. J. (1988). Experimental studies of particle-laden plumes. *Journal of Geophysical Research: Solid Earth*, 93(B12):15314–15328.

Cederwall, K. and Ditmars, J. D. (1970). *Analysis of air-bubble plumes*. California Institute of Technology.

Chen, J. C. (1980). *Studies on gravitational spreading currents*. PhD thesis, California Institute of Technology.

Chen, M. H. (2001). *Bubble plumes*. PhD Thesis, Department of Chemical Engineering, University of Cambridge, UK.

Chen, M. H. and Cardoso, S. S. S. (2000). The mixing of liquids by a plume of low-reynolds number bubbles. *Chemical Engineering Science*, 55:2585–2594.

Chu, S. and Prosperetti, A. (2017). Bubble plumes in a stratified environment: Source parameters, scaling, intrusion height, and neutral height. *Physical review fluids*, 2(10):104503.

Chu, S. and Prosperetti, A. (2019). Multiphase buoyant plumes with soluble drops or bubbles. *Physical review fluids*, 4(8):084306.

Ciriello, F. and Hunt, G. R. (2020). Analytical solutions and virtual origin corrections for forced, pure and lazy turbulent plumes based on a universal entrainment function. *Journal of Fluid Mechanics*, 893.

Clift, R., Grace, J. R., and Weber, M. E. (1978). Bubbles, drops, and particles: Mineola.

Crounse, B. C., Wannamaker, E. J., and Adams, E. E. (2007). Integral model of a multiphase plume in quiescent stratification. *Journal of hydraulic engineering*, 133(1):70–76.

Da Silva, C. B., Taveira, R. R., and Borrell, G. (2014). Characteristics of the turbulent/nonturbulent interface in boundary layers, jets and shear-free turbulence. In *Journal of Physics: Conference Series*, volume 506, page 012015. IOP Publishing.

Debugne, A. L. R. and Hunt, G. R. (2016). A phenomenological model for fountain-top entrainment. *Journal of Fluid Mechanics*, 796:195–210.

Devenish, B. J., Rooney, G. G., and Thomson, D. J. (2010). Large-eddy simulation of a buoyant plume in uniform and stably stratified environments. *Journal of Fluid Mechanics*, 652:75.

Didden, N. and Maxworthy, T. (1982). The viscous spreading of plane and axisymmetric gravity currents. *Journal of Fluid Mechanics*, 121:27–42.

Domingos, M. G. and Cardoso, S. S. S. (2013). Turbulent two-phase plumes with bubble-size reduction owing to dissolution or chemical reaction. *Journal of Fluid Mechanics*, 716:120–136.

Durant, A. J., Bonadonna, C., and Horwell, C. J. (2010). Atmospheric and environmental impacts of volcanic particulates. *Elements*, 6(4):235–240.

Ernst, G. G. J., Sparks, R. S. J., Carey, S. N., and Bursik, M. I. (1996). Sedimentation from turbulent jets and plumes. *Journal of Geophysical Research: Solid Earth*, 101(B3):5575–5589.

Ezzamel, A., Salizzoni, P., and Hunt, G. R. (2015). Dynamical variability of axisymmetric buoyant plumes. *J. Fluid Mech*, 765:576–611.

Fabregat Tomàs, A., Poje, A. C., Özgökmen, T. M., and Dewar, W. K. (2016). Dynamics of multiphase turbulent plumes with hybrid buoyancy sources in stratified environments. *Physics of Fluids*, 28(9):095109.

Fabregat Tomàs, A., Poje, A. C., Özgökmen, T. M., and Dewar, W. K. (2017). Numerical simulations of rotating bubble plumes in stratified environments. *Journal of Geophysical Research: Oceans*, 122(8):6795–6813.

Fan, L.-N. (1967). *Turbulent buoyant jets into stratified or flowing ambient fluids*. California Institute of Technology.

Feng, L., Yang, T., Wang, D., Wang, Z., Pan, Y., Matsui, I., Chen, Y., Xin, J., and Huang, H. (2020). Identify the contribution of elevated industrial plume to ground air quality by optical and machine learning methods. *Environmental Research Communications*, 2(2):021005.

Fischer, H. B., List, E. J., Koh, C. R., Imberger, J., and Brooks, N. H. (1979). *Mixing in inland and coastal waters*. Academic Press New York.

Fitzsimmons, J. N., John, S. G., Marsay, C. M., Hoffman, C. L., Nicholas, S. L., Toner, B. M., German, C. R., and Sherrell, R. M. (2017). Iron persistence in a distal hydrothermal plume supported by dissolved–particulate exchange. *Nature Geoscience*, 10(3):195–201.

Fox, D. G. (1970). Forced plume in a stratified fluid. *Journal of Geophysical Research*, 75(33):6818–6835.

George, W. K. (1989). The self-preservation of turbulent flows and its relation to initial conditions and coherent structures. *Advances in turbulence*, 3973.

Gladstone, C. and Woods, A. W. (2014). Detrainment from a turbulent plume produced by a vertical line source of buoyancy in a confined, ventilated space. *Journal of Fluid Mechanics*, 742:35–49.

Hogg, C., Dalziel, S., Huppert, H., and Imberger, J. (2017). Inclined gravity currents filling basins: The impact of peeling detrainment on transport and vertical structure. *Journal of Fluid Mechanics*, 820:400–423.

Holasek, R. E., Woods, A. W., and Self, S. (1996). Experiments on gas-ash separation processes in volcanic umbrella plumes. *Journal of volcanology and geothermal research*, 70(3-4):169–181.

Hoyal, D. C. J. D., Bursik, M. I., and Atkinson, J. F. (1999). Settling-driven convection: A mechanism of sedimentation from stratified fluids. *Journal of Geophysical Research: Oceans*, 104(C4):7953–7966.

Hunt, G. R. and Burridge, H. C. (2015). Fountains in industry and nature. *Annual Review of Fluid Mechanics*, 47:195–220.

Hunt, G. R. and Kaye, N. G. (2001). Virtual origin correction for lazy turbulent plumes. *Journal of Fluid Mechanics*, 435:377–396.

Hunt, G. R. and Van den Bremer, T. S. (2011). Classical plume theory: 1937–2010 and beyond. *IMA journal of applied mathematics*, 76(3):424–448.

Ivey, G. N. and Blake, S. (1985). Axisymmetric withdrawal and inflow in a density-stratified container. *Journal of Fluid Mechanics*, 161:115–137.

Johnson, C. G., Hogg, A. J., Huppert, H. E., Sparks, R. S. J., Phillips, J. C., Slim, A. C., and Woodhouse, M. J. (2015). Modelling intrusions through quiescent and moving ambients. *Journal of Fluid Mechanics*, 771:370.

Kaminski, E., Tait, S., and Carazzo, G. (2005). Turbulent entrainment in jets with arbitrary buoyancy. *Journal of Fluid Mechanics*, 526:361.

Kaye, N. B. (2008). Turbulent plumes in stratified environments: A review of recent work. *Atmosphere-ocean*, 46(4):433–441.

Kobus, H. E. (1969). Analysis of the flow induced by air-bubble systems. In *Coastal Engineering*, pages 1016–1031.

Konstantinidou, K. and Papanicolaou, P. N. (2003). Vertical round and orthogonal buoyant jets in a linear density-stratified fluid. In *Proc. 30th IAHR Congress on Water Engineering and Research in a Learning Society: Modern Developments and Traditional Concepts*, pages 293–300.

Kotsovinos, N. E. (2000). Axisymmetric submerged intrusion in stratified fluid. *J. Hydraul. Eng. ASCE*, 126(6):446–456.

Lai, C. C. K. and Socolofsky, S. A. (2019). The turbulent kinetic energy budget in a bubble plume. *Journal of Fluid Mechanics*, 865:993–1041.

Lambert, J. H. (1760). *Photometria sive de mensura et gradibus luminis, colorum et umbrae*. sumptibus vidvae E. Klett, typis CP Detleffsen.

Lawrie, A. G. W. and Dalziel, S. B. (2011). Rayleigh-Taylor mixing in an otherwise stable stratification. *Journal of fluid mechanics*, 688:507.

Leifer, I., Luyendyk, B. P., Boles, J., and Clark, J. F. (2006). Natural marine seepage blowout: Contribution to atmospheric methane. *Global Biogeochemical Cycles*, 20(3).

Lemckert, C. J. and Imberger, J. (1993a). Axisymmetric intrusive gravity currents in linearly stratified fluids. *Journal of Hydraulic Engineering*, 119(6):662–679.

Lemckert, C. J. and Imberger, J. (1993b). Energetic bubble plumes in arbitrary stratification. *J. Hydraul. Eng. ASCE*, 119:680–703.

Linden, P. (2000). Convection in the environment. In Worster, M. G., Moffatt, H. K., and Batchelor, G. K., editors, *Perspectives in Fluid Dynamics: A Collective Introduction to Current Research*, chapter 6, pages 289–345. Cambridge University Press, Cambridge, England.

List, E. J. (1982). Mechanics of turbulent buoyant jets and plumes. In *Turbulent buoyant jets and plumes*, pages 1–68. Elsevier.

Martin, D. and Nokes, R. (1988). Crystal settling in a vigorously convecting magma chamber. *Nature*, 332(6164):534–536.

Maxworthy, T., Leilich, J., Simpson, J. E., and Meiburg, E. H. (2002). The propagation of a gravity current into a linearly stratified fluid. *Journal of Fluid Mechanics*, 453:371–394.

McCormick, A. (2019). *Methane Bubble Plumes in the Arctic*. CET IIB Thesis, Department of Chemical Engineering and Biotechnology, University of Cambridge, UK.

McDougall, T. J. (1978). Bubble plumes in stratified environments. *Journal of Fluid Mechanics*, 85(4):655–672.

McGinnis, D. F., Lorke, A., Wüest, A., Stöckli, A., and Little, J. C. (2004). Interaction between a bubble plume and the near field in a stratified lake. *Water Resour. Res.*, 40(W10206).

Mehaddi, R., Candelier, F., and Vauquelin, O. (2013). Naturally bounded plumes. *Journal of Fluid Mechanics*, 717:472.

Mehaddi, R., Vauquelin, O., and Candelier, F. (2015). Experimental non-Boussinesq fountains. *Journal of Fluid Mechanics*, 784.

Milgram, J. H. (1983). Mean flow in round bubble plumes. *Journal of Fluid Mechanics*, 133:345–376.

Mingotti, N. and Cardoso, S. S. S. (2019). Mixing and reaction in turbulent plumes: the limits of slow and instantaneous chemical kinetics. *Journal of Fluid Mechanics*, 861:1–28.

Mingotti, N. and Woods, A. W. (2015). On the transport of heavy particles through an upward displacement-ventilated space. *Journal of Fluid Mechanics*, 772:478–507.

Mingotti, N. and Woods, A. W. (2016). On turbulent particle fountains. *Journal of Fluid Mechanics*, 793:R1.

Mingotti, N. and Woods, A. W. (2020). Stokes settling and particle-laden plumes: implications for deep-sea mining and volcanic eruption plumes. *Philosophical Transactions of the Royal Society A*, 378(2179):20190532.

Mirajkar, H. N., Tirodkar, S., and Balasubramanian, S. (2015). Experimental study on growth and spread of dispersed particle-laden plume in a linearly stratified environment. *Environmental Fluid Mechanics*, 15(6):1241–1262.

Morgan, M., Warren, H. L., et al. (1914). *Vitruvius: the ten books on architecture.*

Morton, B. R. (1959). Forced plumes. *Journal of Fluid mechanics*, 5(1):151–163.

Morton, B. R. and Middleton, J. (1973). Scale diagrams for forced plumes. *Journal of Fluid Mechanics*, 58(1):165–176.

Morton, B. R., Taylor, G. I., and Turner, J. S. (1956). Turbulent gravitational convection from maintained and instantaneous sources. *Proceedings of the Royal Society of London. Series A. Mathematical and Physical Sciences*, 234(1196):1–23.

Neto, I. E., Cardoso, S. S. S., and Woods, A. W. (2016). On mixing a density interface by a bubble plume. *Journal of Fluid Mechanics*, 802:R3.

Oster, G. and Yamamoto, M. (1963). Density gradient techniques. *Chemical Reviews*, 63(3):257–268.

Papanicolaou, P. N. and List, E. J. (1988). Investigations of round vertical turbulent buoyant jets. *Journal of Fluid Mechanics*, 195:341–391.

Papanicolaou, P. N., Papakonstantis, I. G., and Christodoulou, G. C. (2008). On the entrainment coefficient in negatively buoyant jets. *Journal of Fluid Mechanics*, 614:447.

Philip, J. and Marusic, I. (2012). Large-scale eddies and their role in entrainment in turbulent jets and wakes. *Physics of Fluids*, 24(5):055108.

Priestley, C. H. B. and Ball, F. K. (1955). Continuous convection from an isolated source of heat. *Quarterly Journal of the Royal Meteorological Society*, 81(348):144–157.

Reingold, L. S. (1994). An experimental comparison of bubble and sediment plumes in stratified environments. *Master's thesis, Massachusetts Institute of Technology, Cambridge, MA*.

Richards, T. S., Aubourg, Q., and Sutherland, B. R. (2014). Radial intrusions from turbulent plumes in uniform stratification. *Physics of Fluids*, 26(3):036602.

Ricou, F. P. and Spalding, D. B. (1961). Measurements of entrainment by axisymmetrical turbulent jets. *Journal of fluid mechanics*, 11(1):21–32.

Rooney, G. G. and Devenish, B. J. (2014a). Plume rise and spread in a linearly stratified environment. *Geophysical & Astrophysical Fluid Dynamics*, 108(2):168–190.

Rooney, G. G. and Devenish, B. J. (2014b). Plume rise and spread in a linearly stratified environment. *Geophysical & Astrophysical Fluid Dynamics*, 108(2):168–190.

Rooney, G. G. and Linden, P. F. (1996). Similarity considerations for non-Boussinesq plumes in an unstratified environment. *Journal of fluid mechanics*, 318:237–250.

Rouse, H., Yih, C. S., and Humphreys, H. W. (1952). Gravitational convection from a boundary source. *Tellus*, 4(3):201–210.

Sato, K. and Sato, T. (2001). A study on bubble plume behavior in stratified water. *Journal of marine science and technology*, 6(2):59–69.

Scase, M. M., Caulfield, C. P., Dalziel, S. B., and Hunt, J. C. R. (2006). Time-dependent plumes and jets with decreasing source strengths. *Journal of Fluid Mechanics*, 563:443.

Schladow, S. G. (1992). Bubble plume dynamics in a stratified medium and the implications for water quality amelioration in lakes. *Water Resources Research*, 28(2):313–321.

Schmidt, W. (1941). Turbulente ausbreitung eines stromes erhitzter luft. *ZAMM-Journal of Applied Mathematics and Mechanics/Zeitschrift für Angewandte Mathematik und Mechanik*, 21(5):265–278.

Seol, D. G., Bhaumik, T., Bergmann, C., and Socolofsky, S. A. (2007). Particle image velocimetry measurements of the mean flow characteristics in a bubble plume. *Journal of engineering mechanics*, 133(6):665–676.

Seol, D. G., Bryant, D. B., and Socolofsky, S. A. (2009). Measurement of behavioral properties of entrained ambient water in a stratified bubble plume. *Journal of hydraulic engineering*, 135(11):983–988.

Shabbir, A. and George, W. K. (1994). Experiments on a round turbulent buoyant plume. *Journal of Fluid Mechanics*, 275:1–32.

Shakhova, N., Semiletov, I., and Chuvilin, E. (2019). Understanding the permafrost–hydrate system and associated methane releases in the East Siberian Arctic Shelf. *Geosciences*, 9(251).

Shakhova, N., Semiletov, I., Leifer, I., et al. (2014). Ebullition and storm-induced methane release from the East Siberian Arctic Shelf. *Nature Geosci*, 7:64–70.

Shakhova, N., Semiletov, I., Salyuk, A., Yusupov, V., Kosmach, D., and Gustafsson, Ö. (2010a). Extensive methane venting to the atmosphere from sediments of the East Siberian Arctic Shelf. *Science*, 327(5970):1246–1250.

Shakhova, N., Semiletov, I., Sergienko, V., Lobkovsky, L., Yusupov, V., Salyuk, A., Salomatin, A., Chernykh, D., Kosmach, D., Panteleev, G., Nicolsky, D., Samarkin, V., Joye, S., Charkin, A., Dudarev, O., Meluzov, A., and Gustafsson, O. (2015). The East Siberian Arctic Shelf: towards further assessment of permafrost-related methane fluxes and role of sea ice. *Philosophical Transactions of the Royal Society A: Mathematical, Physical and Engineering Sciences*, 373(2052):20140451.

Shakhova, N. E., Alekseev, V. A., and Semiletov, I. P. (2010b). Predicted methane emission on the East Siberian shelf. *Doklady Earth Sciences*, 430(2):190–193.

Sigurðardóttir, A., Barnard, J. M., Bullamore, D., McCormick, A., Cartwright, J., and Cardoso, S. S. S. (2020). Radial spreading of turbulent bubble plumes. *Philosophical Transactions of the Royal Society A*, 378(2179):20190513.

Sigurðardóttir, A. (2019). *Mixing Induced by Bubble Plumes*. MPhil Thesis, Department of Chemical Engineering and Biotechnology, University of Cambridge, UK.

Sjöberg, A. (1967). *Strömningshastigheter kring luft-bubbelridåt äthetshomogent och stillastående vatten.* Report No. 39, Chalmers Institute of Technology, Hydraulics Division.

Skarke, A., Ruppel, C., Kodis, M., Brothers, D., and Lobecker, E. (2014). Widespread methane leakage from the sea floor on the northern US Atlantic margin. *Nature Geosience*, 7:657–661.

Socolofsky, S. A. (2001). *Laboratory Experiments of Multi-phase Plumes in Stratification and Crossflow*. PhD thesis, Massachusetts Institute of Technology, USA.

Socolofsky, S. A. and Adams, E. E. (2002). Multi-phase plumes in uniform and stratified crossflow. *J. Hydraul. Eng. ASCE*, 40(6):661–672.

Socolofsky, S. A. and Adams, E. E. (2003). Liquid volume fluxes in stratified multiphase plumes. *J. Hydraul. Eng. ASCE*, 129:905–914.

Socolofsky, S. A. and Adams, E. E. (2005). Role of slip velocity in the behavior of stratified multiphase plumes. *J. Hydraul. Eng. ASCE*, 131:273–282.

Socolofsky, S. A., Adams, E. E., and Sherwood, C. R. (2011). Formation dynamics of subsurface hydrocarbon intrusions following the Deepwater Horizon blowout. *Geophysical Research Letters*, 38(9).

Socolofsky, S. A. and Bhaumik, T. (2008). Dissolution of direct ocean carbon sequestration plumes using an integral model approach. *Journal of Hydraulic Engineering*, 134(11):1570–1578.

Socolofsky, S. A., Bhaumik, T., and Seol, D. G. (2008). Double-plume integral models for near-field mixing in multiphase plumes. *Journal of Hydraulic Engineering*, 134(6):772–783.

Sparks, R. S. J. (1986). The dimensions and dynamics of volcanic eruption columns. *Bulletin of Volcanology*, 48(1):3–15.

Sparks, R. S. J., Carey, S. N., and Sigurðsson, H. (1991). Sedimentation from gravity currents generated by turbulent plumes. *Sedimentology*, 38(5):839–856.

Sparks, R. S. J., Moore, J. G., and Rice, C. J. (1986). The initial giant umbrella cloud of the May 18th, 1980, explosive eruption of Mount St. Helens. *Journal of Volcanology and Geothermal Research*, 28(3-4):257–274.

Stokes, G. G. (1851). On the effect of internal friction of fluids on the motion of pendulums. *Transactions of the Cambridge Philosophical Society*, 9(ii):8–106.

Sutherland, B. R. and Hong, Y. (2016). Sedimentation from particle-bearing plumes in a stratified ambient. *Physical Review Fluids*, 1(7):074302.

Tate, P. M., Holden, C. J., and Tate, D. J. (2019). Influence of plume advection and particle settling on wastewater dispersion and distribution. *Marine pollution bulletin*, 145:678–690.

Taylor, G. I. (1945). Dynamics of a mass of hot gas rising in air. us atomic energy commission, mddc 919. *LADC 276*.

Tillard, S. (1832). A narrative of the eruption of a volcano in the sea off the Island of St. Michael. In *Abstracts of the Papers Printed in the Philosophical Transactions of the Royal Society of London*, number 1, pages 422–423. The Royal Society London.

Tritton, D. J. (1977). *Physical fluid dynamics*. Van Nostrand Reinhold.

Turner, J. S. (1979). *Buoyancy effects in fluids*. Cambridge University Press.

Turner, J. S. (1986). Turbulent entrainment: the development of the entrainment assumption, and its application to geophysical flows. *Journal of Fluid Mechanics*, 173:431–471.

Ungarish, M. (2009). *An Introduction to Gravity Currents and Intrusions.* Chapman and Hall/CRC, New York.

Van Dyke, M. (1982). *An album of fluid motion.* The Parabolic Press, Stanford, CA.

van Reeuwijk, M. and Craske, J. (2015). Energy-consistent entrainment relations for jets and plumes. *Journal of Fluid Mechanics*, 782:333–355.

van Reeuwijk, M., Salizzoni, P., Hunt, G. R., and Craske, J. (2016). Turbulent transport and entrainment in jets and plumes: a dns study. *Physical Review Fluids*, 1(7):074301.

Veitch, G. and Woods, A. W. (2000). Particle recycling and oscillations of volcanic eruption columns. *Journal of Geophysical Research: Solid Earth*, 105(B2):2829–2842.

Westbrook, G. K., Thatcher, K. E., Rohling, E. J., Piotrowski, A. M., Pälike, H., Osborne, A. H., Nisbet, E. G., Minshull, T. A., Lanoisellé, M., James, R. H., et al. (2009). Escape of methane gas from the seabed along the West Spitsbergen continental margin. *Geophysical Research Letters*, 36(15).

Whiteman, G., Hope, C., and Wadhams, P. (2013). Vast costs of Arctic change. *Nature*, 499(7459):401–403.

Woods, A. W. (1988). The fluid dynamics and thermodynamics of eruption columns. *Bulletin of Volcanology*, 50(3):169–193.

Woods, A. W. (2010). Turbulent plumes in nature. *Annual Review of Fluid Mechanics*, 42(1):391–412.

Woods, A. W. and Bursik, M. I. (1994). A laboratory study of ash flows. *Journal of Geophysical Research: Solid Earth*, 99(B3):4375–4394.

Woods, A. W. and Kienle, J. (1994). The dynamics and thermodynamics of volcanic clouds: theory and observations from the April 15 and April 21, 1990 eruptions of Redoubt Volcano, Alaska. *Journal of Volcanology and Geothermal Research*, 62(1-4):273–299.

Wüest, A., Brooks, N. H., and Imboden, D. M. (1992). Bubble plume modeling for lake restoration. *Water Resources Research*, 28(12):3235–3250.

Yang, D., Chen, B., Socolofsky, S. A., Chamecki, M., and Meneveau, C. (2016). Large-eddy simulation and parameterization of buoyant plume dynamics in stratified flow. *Journal of Fluid Mechanics*, 794:798.

Zarrebini, M. and Cardoso, S. S. S. (2000). Patterns of sedimentation from surface currents generated by turbulent plumes. *AIChE journal*, 46(10):1947–1956.

Zatsepin, A. G. and Shapiro, G. I. (1982). A study of axisymmetric intrusions in a stratified fluid. *Izvestiya Akademii Nauk SSSR, Fizika Atmosfery i Okeana*, 18:77–80.

Zeldovich, Y. B. (1937). The asymptotic laws of freely-ascending convective flows. *Zhurnal eksperimental'noy i teoreticheskoy fiziki*, 7(12):1463–1465.

Zhou, G. (2020). Computational study of the source-area effect for bubble plumes in stratified environments. *Journal of Hydraulic Engineering*, 146(6):04020039.

Appendix A

Additional experimental details

A.1 Apparatus

Annotated photographs of the experimental apparatus are shown in Figure A.1.

A.1.1 Double bucket system

The double bucket system used for all experiments consisted of two 118 L buckets connected at the base, one of which was also connected to a Stuart Turner CH 4-30 multistage pump (see Figure A.2). Unlike more traditional configurations where the bucket directly feeding the experimental tank is mechanically agitated, a recycle was utilised instead. The relative magnitude of the recycle and tank flowrates were controlled with manual valves. The recycle was the larger of the two to ensure that the bucket was well mixed. The flowrate into the experimental tank was small to ensure laminar flow across the tank base. This ensured that the stratification being produced would not be disturbed by the inflow. An example of the ambient stratification within the experimental tank is shown in Figure A.3.

A.1.2 Agitated tank

The agitator used to disperse particles throughout the feed for the particle-laden plume experiments was a six-blade turbine configuration with 50 mm long blades and a 340 mm long shaft. The agitator motor used was a SciQuip Basic20 Digital Overhead Stirrer and was generally set at a rate of 400 RPM. The agitated tank had four evenly spaced rectangular baffles, each with a depth of 30 mm.

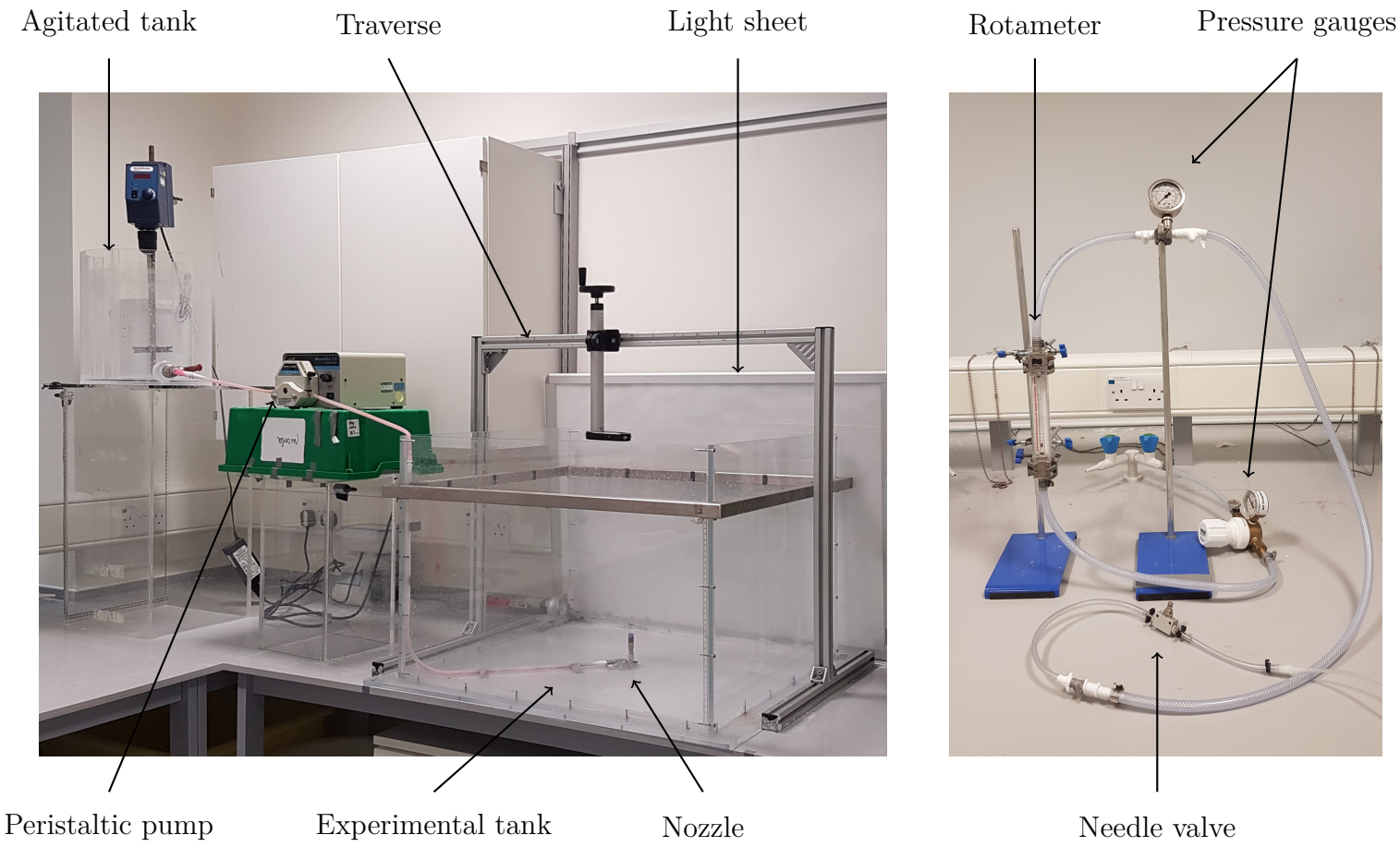

Fig. A.1 Experimental apparatus. The left-hand figure shows the configuration for particle-laden plumes. The right-hand figure shows the extension to produce bubble plumes.

Fig. A.2 Double bucket system

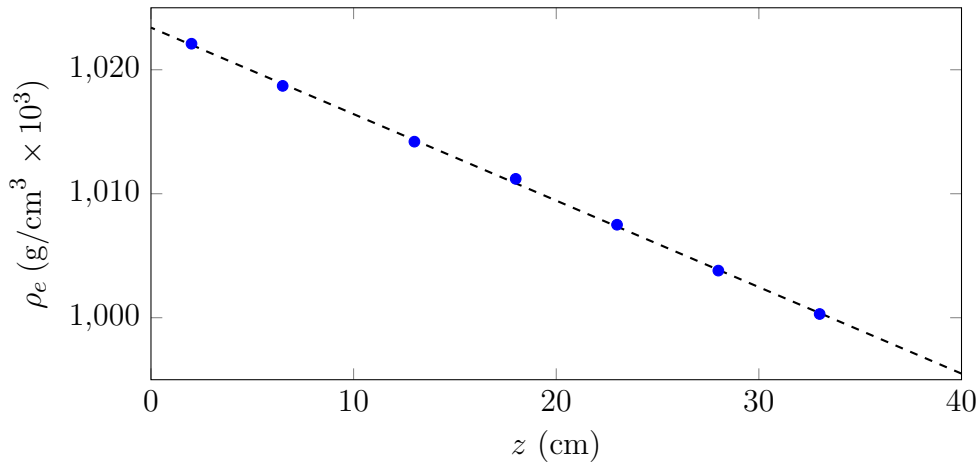

Fig. A.3 An example of the density gradient built in the tank. The points correspond to density measurements taken from within the mixed bucket for a known tank liquid level above the plume nozzle. Here, $d\rho_e/dz = -0.7 \times 10^3\,\mathrm{gcm}^{-4}$ and $\rho_0 = 1.024\,\mathrm{gcm}^{-3}$ giving a stratification strength of $N = 0.82$.

A.1.3 Sampling traverse

In order to take accurate samples within the experimental tank without disrupting the stratification, a custom traverse system was built. The traverse used was a 300 mm long Type 30 RK LightUnit, purchased from Rose + Krieger and capable of 220 mm travel. This unit was mounted to a custom apparatus above the tank such that it could be moved horizontally across the tank width. A 20 ml syringe could be attached to the traverse and a custom 400 mm long needle was used to take samples. The needles used were approximately 16 gauge (1.2 mm internal diameter) as this was suitable to sample particle-rich fluid without the needle blocking. The traverse system in visible in Figure A.1.

A.2 Particle size

The ballotini used in the particle-laden plume experiments were purchased from Sigmund Lindner GmbH (through VMR International) and are marketed as SiLibeads®. The products purchased had size ranges of 40-70 μm and 70-110 μm respectively. The silicon carbide particles were purchased from Washington Mills and had a size distribution between 25-114 μm (Carborex® F180). All particles were sieved prior to use to further narrow the size distribution. The larger ballotini was sieved between 90 μm and 106 μm sieves, whereas the smaller ballotini and silicon carbide was sieved using 63 μm and 75 μm sieves. This sieving lead to average particle sizes of 69 $\mu\text{m} \pm 2$ μm and 98 $\mu\text{m} \pm 2.5$ μm.

A.3 Bubble size

Bubble size is dependent on many factors including upstream pressure and flowrate, salinity and interface tension. Due to our interest in developing ellipsoidal bubbles, where rise velocity is essentially constant irrespective of bubble size, controlling bubble size was not important provided the diameters ranged between 1-20 mm. Using 1 mm diameter stainless steel tubing, bubble diameters ranged between 2-12 mm for $Q_b < 20\ \text{cm}^3\text{s}^{-1}$. A smaller 0.5 mm tube was trialled for a few larger flowrate experiments, but little to no difference was found when compared to the 1 mm tubing.

Appendix B

Measurement and data analysis

B.1 Heights of interest

B.1.1 Maximum plume height

The maximum height of particle-laden plumes were measured both at early stages before the re-entrainment of particles, and at steady state after the significant reduction in height occurred. Note that the method of measuring these heights, as described below, was consistent in both cases.

After filming an experiment, every 24^{th} frame (resulting in a single image per second) of the video was extracted using MATLAB R2020B and the images were subsequently subtracted from a base image taken prior to plume injection, eliminating any inconsistencies in the light sheet. Each of these frames were then cropped such that the nozzle was positioned at the base of the image. These cropped images were then averaged across the width of the tank, creating a vector to represent the distribution of light intensity through the vertical extent of the tank for each given second. These vectors could then be combined to create a time series showing the plume height over time (see Figure B.1). In this time series, the navy and maroon colours represent the two extremes of light intensity, those being the maximum and minimum light captured by the camera. On the left-hand side of the figure, shortly after plume injection, particle concentration in the plume is low thus the light captured by the camera is high. However, this light intensity decreases over time as particles become re-entrained. In-order to effectively measure the height of the plume, a threshold of light intensity needed to be determined for both the initial maximum height and the steady-state height by comparing the false colour time series to a number of full-colour experimental photographs. Once a threshold was determined, the time series was further cropped to

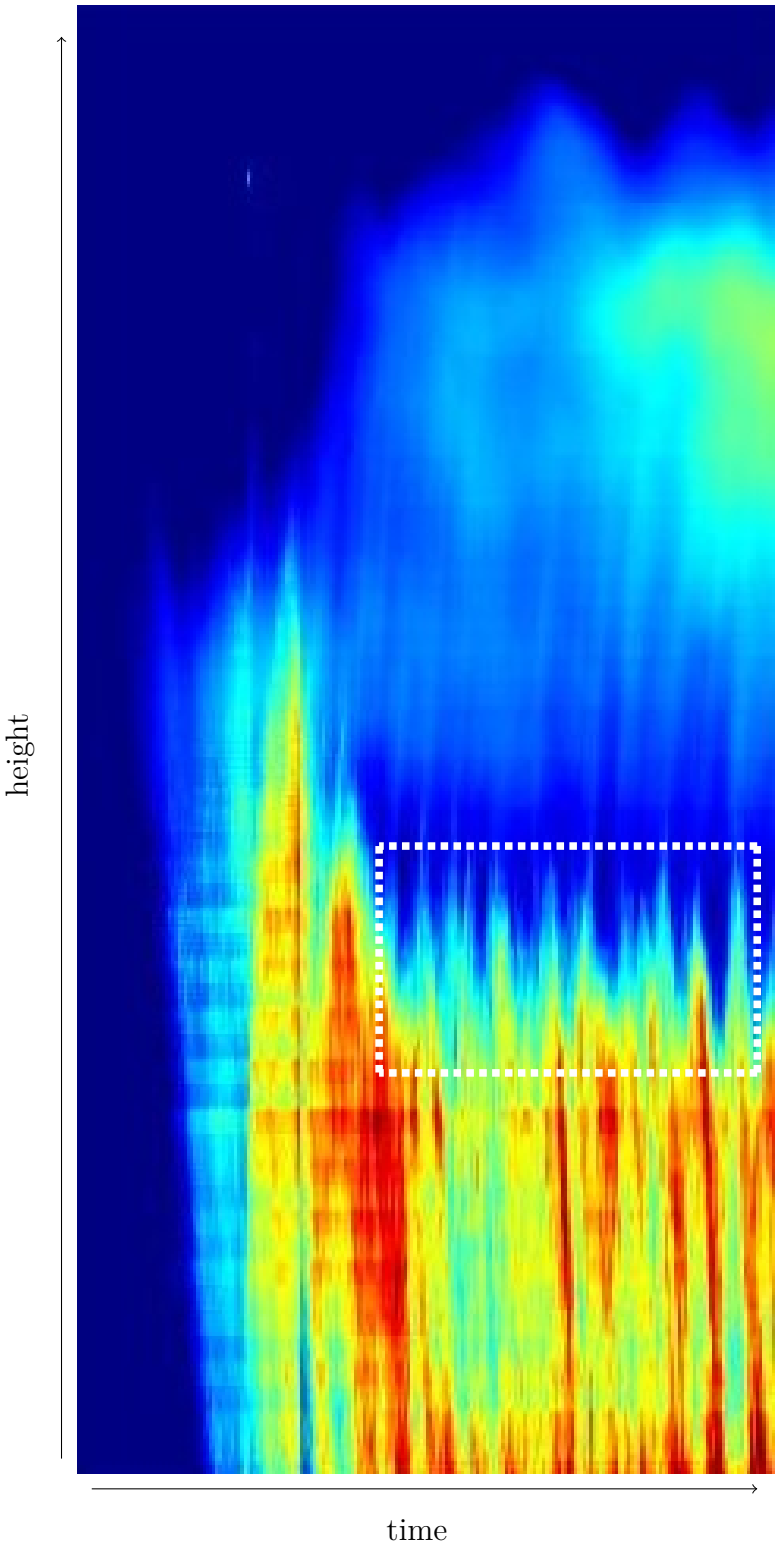

Fig. B.1 A time series of particle-laden plume experiment 21 where navy and maroon represent maximum and minimum values of light intensity. The area highlighted by white dashed lines is an example focus area for further image analysis to determine the steady-state plume height.

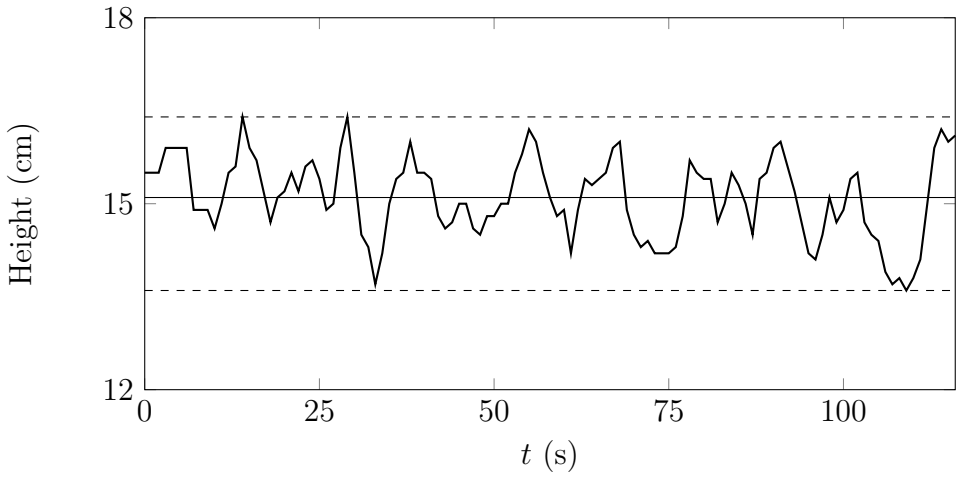

Fig. B.2 A plot of steady-state plume height over time. It can be seen that even at steady state, the plume height oscillates around a central average represented by the straight black line. The dashed lines represent the upper and lower height limits.

fit either the initial experimental period prior to any significant height decay or the period following the decay until the plume appears reach a steady-state value. Finally, the number of pixels exceeding the threshold could be counted for each given time period to determine the average plume height and the upper and lower height limits (see Figure B.2).

B.1.2 Primary intrusion heights

Measuring the primary intrusion heights of a particle-laden plume, those being the particle-rich intrusion and the particle-poor intrusion, at steady state was somewhat complex due to each experiment falling under a different flow regime and having a differing stratification strength in the environment. For example, in a Type 1 plume, low particle concentration in the flow results in minimal separation of the fluid, making differentiating the particle-rich and particle-poor intrusions a challenge, even in weakly stratified ambients. Conversely, for plumes undergoing convection, the leading edge of the particle-poor intrusion is easily visible above the plume maximum, however, the fluid in the particle-rich intrusion immediately rises, posing an issue that either image analysis removes the very dilute intrusion from processed images or a defined leading edge may not exist independently of the particle-poor intrusion above.

Due to these reasons, these heights could not necessarily be determined from a single image created through image analysis alone, but though different visual approaches including viewing multiple stills, along with video footage, to understand where the

radial spreading was occurring. This agile approach allowed the best height estimates to be made. The following paragraphs provide descriptions and visual detail of the approach taken in an attempt to show how the challenges described in attempting to measure these heights were overcome.

A photograph and a time series of a Type 1 plume are presented in Figures B.3 and B.4. On first glance at the photograph (Figure B.3), no defined particle-rich and particle-poor intrusion can be observed as only a single trailing edge is present. However, upon further assessment, there does appear to be a clear difference in colouration between the base and top of the intrusion, suggesting that a small portion of the fluid initially spreading in the particle-rich intrusion is becoming buoyant following the sedimentation of particles and is then reaching a new height of neutral buoyancy only slightly above it's original level. This is supported by the time series (Figure B.4), where it can be clearly seen that the top portion of the intrusion thickens significantly suggesting the development of a small particle-poor intrusion. By taking a vector from the end of the time series, the height of the particle-poor intrusion can be estimated as the point where the light intensity captured by the camera is at it's smallest. This is shown visually by the peak present in a plot of light intensity against height (see Figure B.5). The height of the particle-rich intrusion can simply be estimated from the left- and right-hand leading edges as indicated on Figure B.3. Alternatively, a similar light intensity vs. height plot may be produced to determine this height by taking a vector, offset from the centre of the plume at a distance where the particle-poor intrusion is not present, from a time-averaged image at steady state. This allows direct comparison of the two heights and enables the change in intrusion height to be estimated.

A second example, this time of a Type 3 plume, is shown in Figures B.6 and B.7. Unlike the Type 1 example, where two distinctly different peaks are present (allowing the two intrusions to be differentiated), the same is not the case for the Type 3 plume. Two large peaks are observed to appear in the range of 14 cm to 18 cm above the source, however, these are associated with the same (particle-poor) intrusion, with the offset measurement simply appearing thinner, and of lower magnitude, than the measurement taken at the centre of the plume. The particle-rich intrusion is faint, but visible to the naked eye when viewing photographs (see Figure B.6) and can be determined from the light intensity plots when considering the fact that, in this case, the light path of the particle-rich intrusion is less than the particle-poor intrusion, resulting in smaller light intensity peaks. This is because the majority of fluid initially spreading in the particle-rich intrusion becomes buoyant, effectively feeding the particle-poor intrusion rather than spreading further away from the edge of the plume.

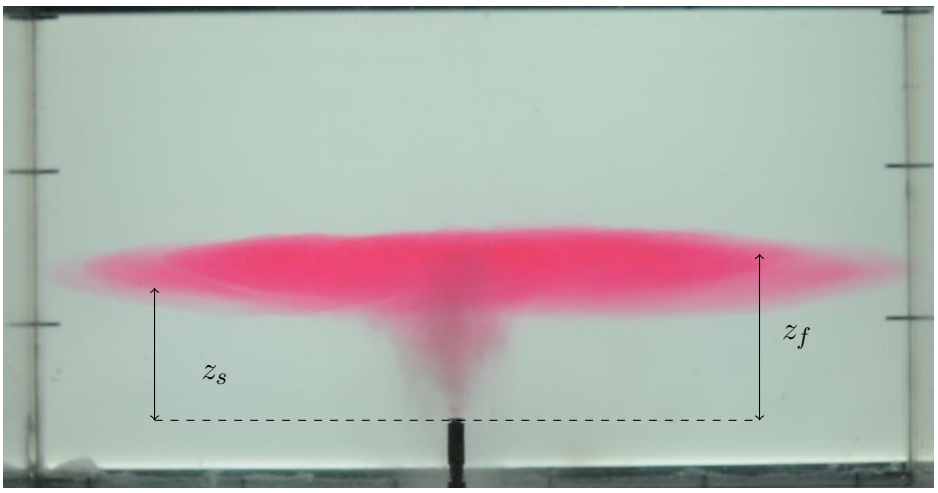

Fig. B.3 A photograph of experiment 11 taken after 300 seconds detailing the respective heights of the particle-rich (z_s) and particle-poor (z_f) intrusion. Note that the base of the intrusion appears significantly lighter in colour suggesting fluid is rising from the particle-rich intrusion to create a particle-poor intrusion above. The estimated heights correspond to those estimated in Figure B.5.

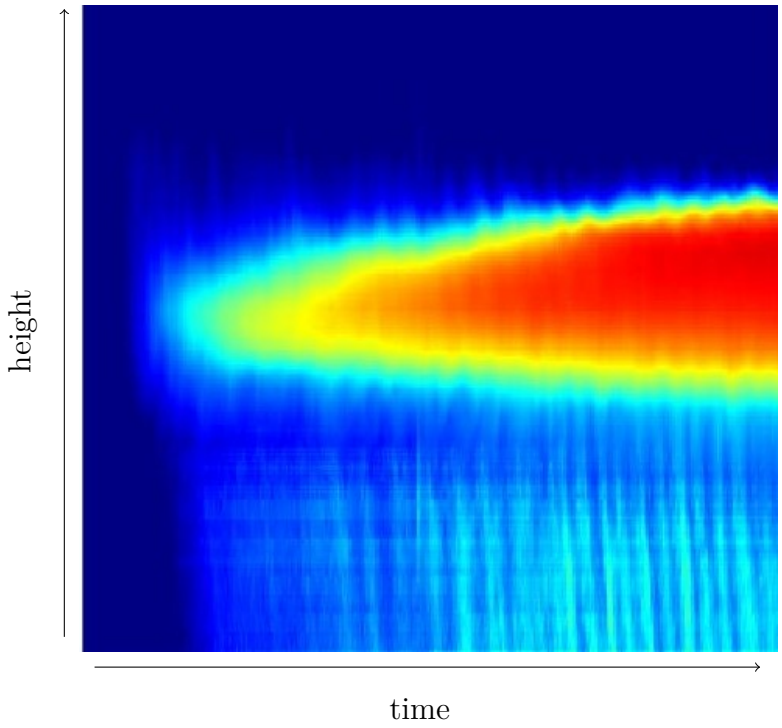

Fig. B.4 A time series of particle-laden plume experiment 11 where navy and maroon represent maximum and minimum values of light intensity. Over time, the intrusion appears to significantly thicken, with a skew towards the top of the intrusion, suggesting most fluid is spreading there rather than along the base.

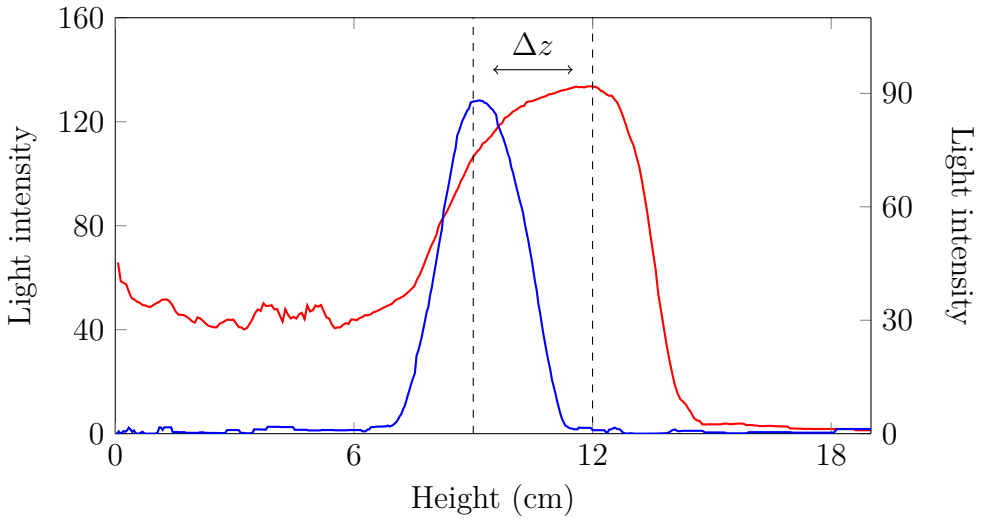

Fig. B.5 A plot of light intensity against height for experiment 11, where $\Delta z = z_f - z_s$ is the change in intrusion height. The vector taken at the centre of the plume (——) shows light is obstructed significantly between 7 cm and 14 cm, however the intensity of light is significantly skewed with the peak occurring at 12 cm (suggesting the presence of a particle-poor intrusion) before falling to a minimum value associated with the light obstructed by the plume. The offset vector (——), taken 15 cm from the left-hand edge of the plume, shows a parabolic curve of lesser intensity between 7 cm and 11 cm, with a peak around 9 cm. This peak is not associated with the same particle-poor intrusion, but the particle-rich intrusion, suggesting the two intrusions are stacked upon each other and possibly even overlap.

This means the particle-poor radius, and it's light path, increases over time, whereas the light path associated with the particle-rich intrusion remains somewhat constant for the entire length of the experiment. When looking at the smaller intensity peaks, both the central and offset vectors show either a plateau or an increase in light intensity around 12 cm above the plume source (see Figure B.7) and when compared to experimental images, gives a reasonable estimate of the particle-rich spreading height.

In all cases, irrespective of plume type, the primary intrusion heights estimated using the approach described appear to be appropriate when compared to the video footage of the experiments.

B.1.3 Secondary intrusion height

When compared to the measurement of the primary intrusions, estimating the secondary intrusion height was very straight-forward and could be done by simply measuring the

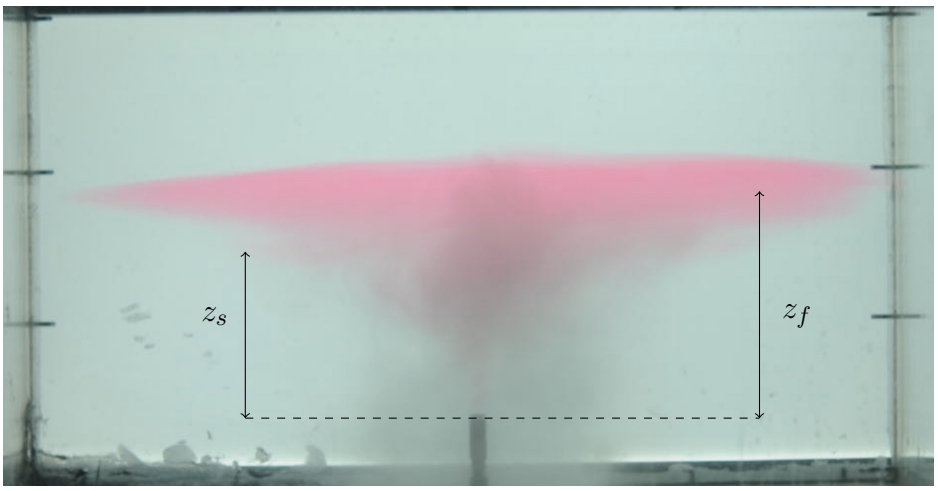

Fig. B.6 A photograph of experiment 55 taken after 300 seconds detailing the respective heights of the particle-rich (z_s) and particle-poor (z_f) intrusion. Although, the dyed fluid is very dilute, the particle-rich intrusion is visible below particle-poor intrusion.

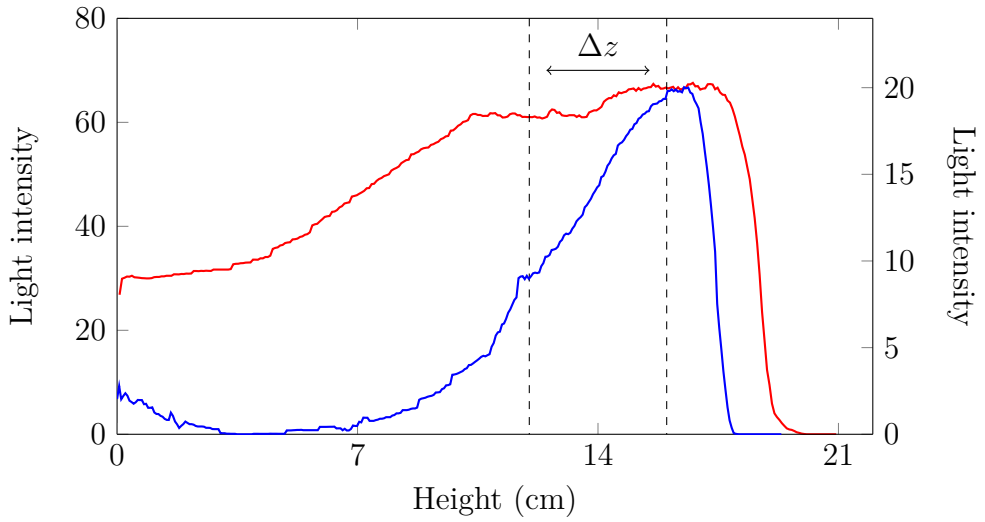

Fig. B.7 A plot of light intensity against height for experiment 55, where $\Delta z = z_f - z_s$ is the change in intrusion height. The vector taken at the centre of the plume (——) shows a maximum light obstruction between 14 and 18 cm (the thickness of the particle-poor intrusion), leading into a secondary peak between 10 and 14 cm (the thickness of the particle-rich intrusion). The light intensity then falls from this peak to a minimum value associated with the light obstructed by the plume. The offset vector (——), taken outside the convection column, shows a similar peak between 15 and 17 cm, yet of lower magnitude. This then continues to decay until reaching a plateau at 12 cm before decaying to zero. The increase in light intensity below 5 cm is simply an artifact of the image processing and is not associated with the flow. The positioning of the dashed lines correspond to the leading edge heights, as detailed on Figure B.6.

height of the left- and right-hand leading edges of the intrusion (see Figure B.8). It could also be determined by measuring the distribution of light intensity through the vertical extent of the tank in a vector located in an offset position on either the left or right of the nozzle (see Figure B.9).

B.2 Plume radius

Throughout this thesis, the plume radius appears in a number of models and is utilised to offset data when considering the extent of radial spread. Because of this, the plume radius at the spreading height was required to be measured for all the multiphase plume experiments presented. This however is not particularly straightforward as, at steady-state, the plume radius is either obscured by a trough or column of particles; or is present within a bubble plume peeling event where the inner and outer plumes cannot be differentiated experimentally.

Due to these difficulties, the exact steady-state plume radius could not be determined through image analysis. However when considering that the plume radius would either be raised to a $1/4^{\text{th}}$ power (see Chapter 3), essentially eliminating any small measurement differences, or be compared to much larger values, such as the intrusion radius (see Chapter 4 and 5), it was deemed suitable for the radius to be measured at early plume stages prior to any significant obstruction so that a value of the correct order of magnitude could be estimated.

Following this, the plume radius of both particle-laden and bubble plumes was estimated by firstly time averaging the initial stills extracted from the video footage before the plume radius became obstructed. In most cases, this was approximately over 20 seconds. A light intensity vector was then taken across the width of the tank at either the steady-state height of the particle-poor intrusion when accessing particle-laden plumes or the height of furthest radial extent for a given peeling event when accessing bubble plumes. Figures B.10 and B.11 show examples of these light intensity plots.

B.3 Intrusion volume flux

Measurement of the intrusion volume flux followed the same procedure as described by Sigurðardóttir (2019) and was used for both particle-laden and bubble plumes.

As per other image analysis methods, a single frame per second was extracted from the experimental videos and a base image was subtracted to eliminate any

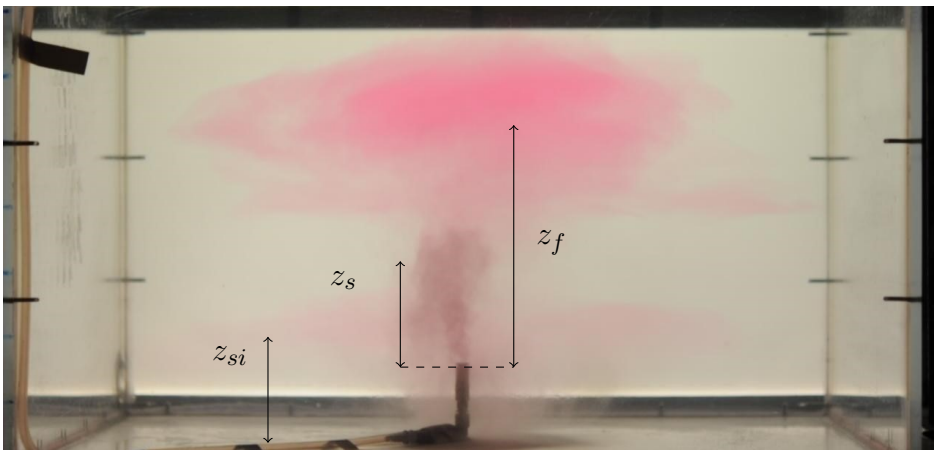

Fig. B.8 A photograph of experiment 21 taken after 300 seconds detailing the respective heights of the particle-rich (z_s), particle-poor (z_f) and secondary (z_{si}) intrusion. The estimated heights correspond to those estimated in Figure B.9.

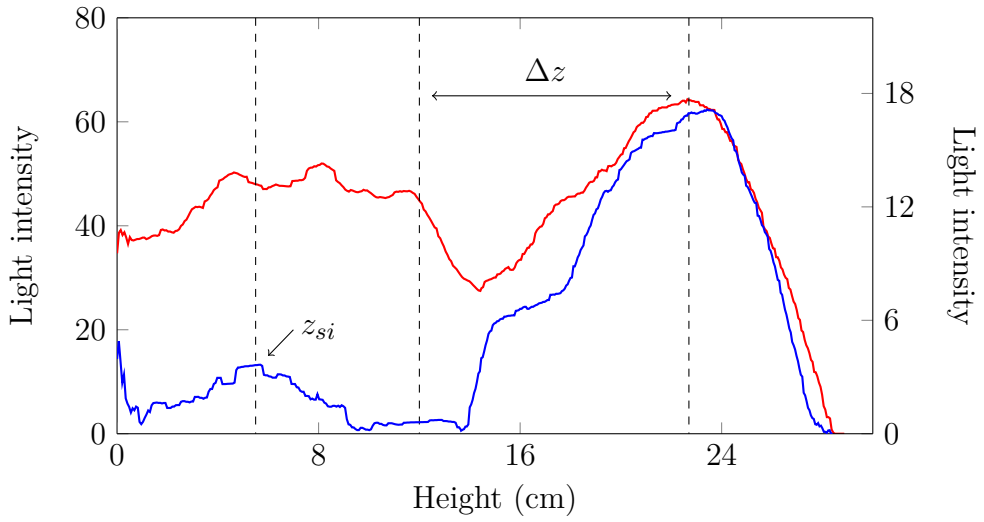

Fig. B.9 A plot of light intensity against height for experiment 21, where $\Delta z = z_f - z_s$ is the change in intrusion height. The vectors taken at both the centre of the plume (——) and outside the convection column on the left-hand side (——) show a maximum light obstruction peak at 22 cm, with an approximate particle-poor intrusion thickness between 16 and 27 cm. The second (and the smallest, in both cases) peak is observed at 12 cm and is associated with the particle-rich intrusion. The third peak of the offset vector, at a height of 5.5 cm above the source (or 12.5 cm above the tank floor), is associated with the secondary intrusion. In the case of the central intensity vector, the secondary intrusion is also identified by the plateau between 4 cm and 8 cm, with peaks at 5 cm and 7.5 cm respectively. The variation in peaks reflects the presence of smaller secondary intrusions close to the edge of the plume, whereas the offset peak represents the height where the majority of fluid is spreading radially.

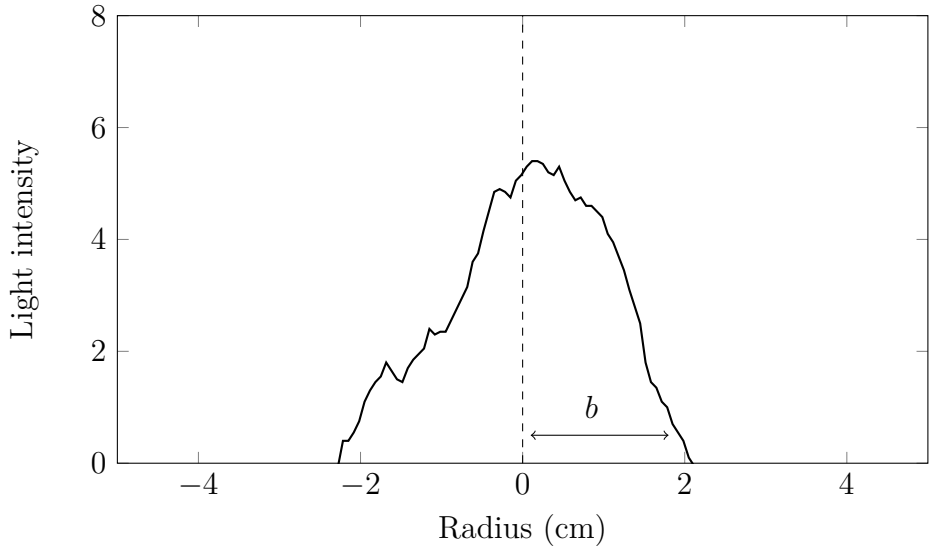

Fig. B.10 A plot of light intensity across the tank in the early stages of a bubble plume (experiment 17). The vector presented is associated with the first spreading event height above the plume source. The estimate for the radius of the plume b is shown with the double-sided arrow.

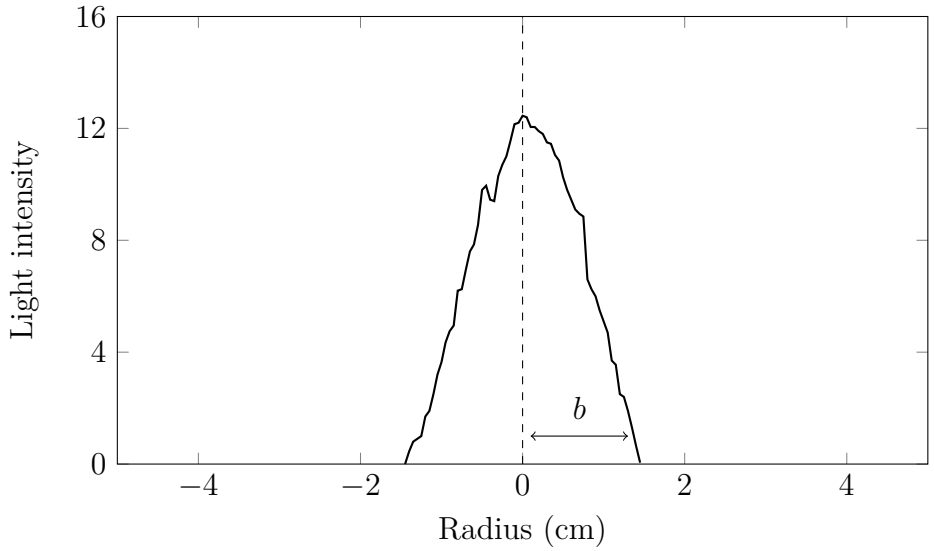

Fig. B.11 A plot of light intensity across the tank in the early stages of a particle-laden plume (experiment 55). The vector presented is associated with the steady-state particle-rich intrusion height and the estimate for the radius of the plume b is shown with the double-sided arrow.

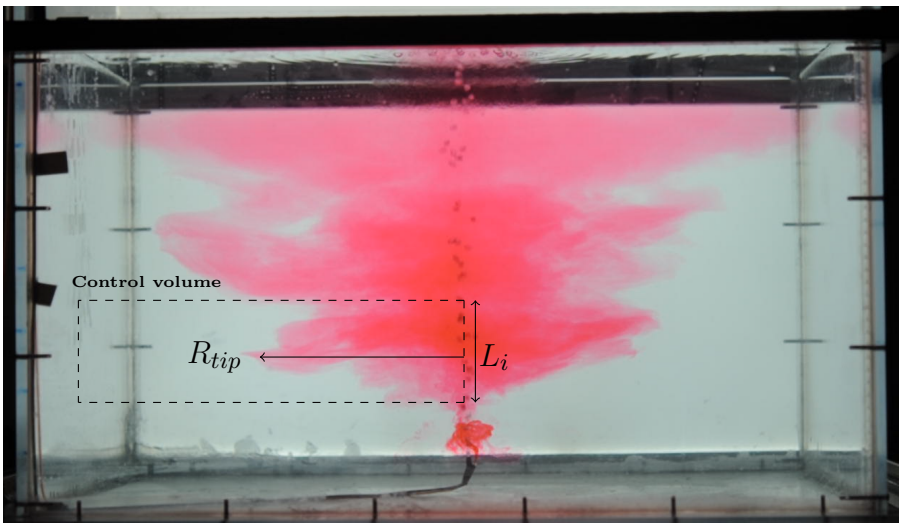

Fig. B.12 A photograph of a bubble plume (experiment 17) after 140 seconds, detailing the control volume around the first submerged intrusion above the source.

inconsistencies in the light sheet. A control volume, spanning from the centre of the plume to the tank wall, with a height equivalent to the intrusion thickness, was defined on both the left- and right-hand sides of the plume (see Figure B.12). The radius of the intrusion, R_{tip}, was then determined for each still image by firstly defining a light intensity threshold associated with the intrusion boundaries before counting the maximum number of pixels along the control volume where the light captured fell below this threshold.

The total liquid volume in the intrusion can then be determined by integrating around the axis of symmetry between the plume radius b and R_{tip},

$$V(t) = \int_b^{R_{tip}} 2\pi L_i(r) r dr. \tag{B.1}$$

This solution can be approximated through numerical integration as

$$V(t) \approx \sum_{r=1}^{R_{tip}} 2\pi L_i(r) r \Delta r. \tag{B.2}$$

Using (B.2), the volume of the intrusion at a given time can be estimated. Then, by determining the rate of change in volume over time, the volume flux of the intrusion, Q_i, may also be estimated.

Given that the intrusions produced (especially in the case of bubble plumes) are not completely symmetric, average values of both R_{tip} and Q_i (calculated from the

combination of the left- and right-hand side estimates) are presented in the body of the thesis.

Appendix C

Real source corrections

C.1 Entrainment coefficient

The entrainment coefficient, α, for each particle-laden plume was determined using the bulk parameter method, specifically by rearranging (3.3) to

$$\alpha = \left[\frac{(z_{max} - z_v)}{1.37(B_0/N^3)^{1/4}} \right]^{-2}. \tag{C.1}$$

A plot of α against σ shows the coefficient's dependence upon the buoyancy frequency parameter (Figure C.1). Konstantinidou and Papanicolaou (2003) proposed that the entrainment coefficient of a stratified forced plume varied between pure plume and pure jet values with the empirical expression,

$$\alpha = \alpha_p \exp\left[\ln\left(\frac{\alpha_j}{\alpha_p}\right) \left(\frac{\sigma}{\sigma_c}\right)^2 \right], \tag{C.2}$$

where σ_c is the critical value of the buoyancy frequency parameter where momentum begins to dominate flow behaviour. Using this expression, based upon the work of List (1982) concerning forced plumes in an unstratified environment, Konstantinidou and Papanicolaou (2003) suggested values of $\alpha_p = 0.123$, $\alpha_j = 0.035$ and $\sigma_c = 2$ to fit their experiments. More typical values of $\alpha_p = 0.118$, $\alpha_j = 0.076$ and $\sigma_c = 1$ are also plotted for comparison.

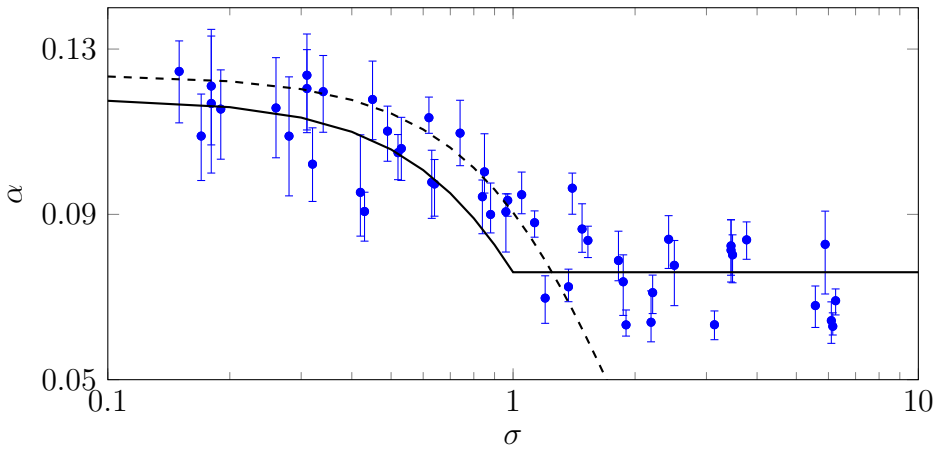

Fig. C.1 Entrainment coefficient, α, against the buoyancy frequency parameter, σ. The dashed line represents (C.2) with the model inputs of Konstantinidou and Papanicolaou (2003). The solid line has inputs of $\alpha_p = 0.118$, $\alpha_j = 0.076$, $\sigma_c = 1$.

C.2 Virtual source

Written explicitly by Hunt and Kaye (2001), the two-step virtual source correction for forced plumes consists of an exact correction, z_v, and an asymptotic correction, z_{avs}, which is only appropriate at large distances from the real source. z_v and z_{avs} are defined as

$$-\frac{z_v}{L_m} = \left(\frac{100}{16\alpha_p^2\pi}\right)^{1/4} \int_\gamma^1 v^3(v^5-\gamma^5)^{-1/2}\,dv, \tag{C.3}$$

$$-\frac{z_{avs}}{L_m} = \left(\frac{0.078}{\alpha_p^2\pi}\right)^{1/4} \gamma^{3/2}, \tag{C.4}$$

where $\gamma = (1-\Gamma_0)^5$. Note that both (C.3) and (C.4) appear in a similar form to the corrections presented in Hunt and Kaye (2001) (see their equations 12a-c), however, the constant terms differ due to the definition of L_m in this study and the use of top hat rather than Gaussian plume profiles. The asymptotic correction only becomes suitable to include in the correction when $z/L_m > 3\alpha^{-1/2}\pi^{-1/4}\gamma^{3/2}$. For all experiments, the appropriate value of z/L_m is achieved either above the maximum plume height or in between the spreading and maximum heights. Because of this, only the exact value, z_v, is utilised as the virtual source correction in these experiments.